ABSTRACT

SANDEEP KEDIA. Hydrogenation of F-nitrobenzene to F-aminophenol under kinetics and mass transfer limited regimes: Reaction Kinetics, Mass Transfer Effects and Reaction Pathway. (Under the direction of Dr. Ruben G. Carbonell and late Dr. George W. Roberts).

The heterogeneous hydrogenation of F-nitrobenzene was studied in a slurry batch reactor. One of the reduced products, F-aminophenol, is a key intermediate for the manufacture of an Active Pharmaceutical Ingredient (API) in late-stage clinical trials. Catalysts play a vital role in the hydrogenation of nitroaromatics. Heterogeneous reactions can be limited by either diffusion or kinetic control, depending upon the catalyst used or the reaction conditions. Several catalysts were rapidly evaluated using a high-throughput screening technique from a diverse group of 48 catalysts available, to choose a single catalyst for this study. The selection criteria included the reactivity, selectivity and availability of the catalyst for scale-up in pilot facilities.

Heterogeneous hydrogenation reactions exhibit a complex kinetic behavior and require a careful reaction rate control, as they produce highly energetic intermediates, such as hydroxylamines, that pose a safety concern upon scale-up. In addition, the mechanism for the formation of the dehalogenated aniline byproducts in these reactions has not been clearly identified. Such impurities can pose a potential risk for batch failure in pharmaceutical products. A detailed kinetic model was developed, elucidating the dominant pathway for the desired reaction. It was found that the hydroxylamine formation step is a mass transfer limited process, whereas the hydrogenolysis of hydroxylamine is kinetically limited. The reaction rate and the maximum concentration of hydroxylamine were both dependent on mass transfer rates and reaction temperature. Similarly, it was found that formation of a des-F impurity was also a function of both the mass transfer rate, as well as the reaction temperature. Both the temperature and mass transfer rate information were critical in order to meet the safety requirements and the product specification for the des-F impurity. It is vital to

scale such reactions from laboratory to pilot plant scale at a similar mass transfer rate of hydrogen gas. An experimental technique was developed to scale these reactions at a constant overall mass transfer coefficient. The experimental method also gave a direct measurement of hydrogen solubility in the solvent system, along with the mass transfer coefficient values.

The reactions were scaled up to pilot plant reactors by maintaining the same mass transfer coefficient k_La from the lab scale measured using a non-reactive methanol/hydrogen system. Although the reactions were scaled based on comparable k_La, the reaction rate was found to be much slower than that of the lab reaction. Upon investigation, it was found that the difference in rates was caused by the presence of a nitrogen headspace in the reactor, put in place for safety. Even though nitrogen is considered to be an innocuous substance, it resulted in catalyst inhibition. The catalyst was characterized by physi- and chemisorption techniques to understand the catalyst inhibition mechanism. Once the inhibition was well understood, then the pilot plant reactions were scaled up safely and successfully under a hydrogen atmosphere, producing good quality material required for clinical trials.

Hydrogenation of F-Nitrobenzene to F-Aminophenol under Kinetics and Mass Transfer Limited Regimes: Reaction Kinetics, Mass Transfer Effects and Reaction Pathway

by
Sandeep Kedia

A dissertation submitted to the Graduate Faculty of
North Carolina State University
in partial fulfillment of the
requirements for the Degree of
Doctor of Philosophy

Chemical Engineering

Raleigh, North Carolina

2015

APPROVED BY:

_____	_____
Dr. Ruben Carbonell Committee Chair	Dr. David Ollis
_____	_____
Dr. Saad Khan	Dr. Jack Edwards

DEDICATION

This thesis is dedicated to my late parents Mr. Babulal and Ms. Vimala Kedia, for always believing in me and teaching me everything can be achieved given enough hard work and time. I would like to also dedicate this to my grandparents (Mr. Kaluram and Ms. Kanchan Devi Kedia) who always instigated in me to always do the right thing irrespective of what it takes. My uncles and aunts (Dr. P. Ray and Sushila Kedia and Dr. Ben and Asha Kedia) for believing and supporting me in coming to USA for higher education. My sister Preeti, for standing by me and being a good friend forever. Finally, I would like to dedicate this to my wife Sheetal and our two children (Reeyan and Aryan), who has always been loving and caring all these wonderful years, and who always supported me to achieve the very best and has been my inspiration ever since.

BIOGRAPHY

Sandeep Babulal Kedia was born on the 5th of November 1974, in Bombay (Mumbai), India. In May 1995, he graduated from the University of Bombay with a Bachelors of Science in Chemistry. The following year, he came to the United States of America to study Chemical Engineering at Louisiana Tech University. While at Louisiana Tech University, he worked at the International Students Office, organizing students' arrivals, arranging their temporary accommodation, and preparing for their orientation.

He graduated from Louisiana Tech in May of 1999 with a Master of Science in Chemical Engineering. His first professional challenge was working in DSM Pharmaceuticals Inc., in Greenville, North Carolina (from 1999 to 2002). He worked as a Research and Development Engineer, scaling-up Active Pharmaceutical Ingredient (API) processes from lab to plant scale in a GMP environment. Later he worked at Pfizer Global Research and Development as a R&D engineer, responsible for scaling new chemical entities (NCE) from 2002 to 2004. He then moved to GlaxoSmithKline in 2004, in Research Triangle Park, North Carolina. He found a niche working in the field of catalysis, which he developed and led in the organization. He presented his work on palladium cross-coupling homogeneous reaction at an annual meeting of the AICHE in 2008.

He enrolled in the Chemical Engineering program at North Carolina State University in Fall of 2006. For his doctoral dissertation research, he has worked under the direction of Dr. George W. Roberts on the hydrogenation of F-nitrobenzene in a batch reactor. He later worked under the supervision of Dr Ruben G. Carbonell to complete his research work on the hydrogenation project.

ACKNOWLEDGMENTS

First and foremost, I would like to express my gratitude to my advisor, the late Dr. George Roberts, for his constant guidance, encouragement, and patience. It has been an honor to learn from him. I would like to also express my deepest gratitude to my current advisor Dr Ruben Carbonell, for accepting me as his student after the sudden passing of Dr George Roberts, his utmost patience, and continual guidance and encouragement, without which I would have not graduated. I also acknowledge my gratitude to my committee members, Dr. David Ollis, Dr. Saad Khan, and Dr. Jack Edwards, for their insightful and constant guidance towards the completion of my thesis.

I want to express my appreciation to Dr. Saad Khan for his help in guiding me through the course work and encouraging me to enroll into the graduate program at NCSU. I would also like to thank my organization, GlaxoSmithKline, for funding my research and allowing me to work on my research project during these years. I appreciate the great support of my manager, Mr. Robert Yule, who helped me to get through the professional work and research, along with proctoring my exams.

I would like thank Dr Mark Mitchell of GSK for exchanging ideas on catalyst behavior and the mechanistic behavior of such complex reactions. I am very grateful to my project leader Dr. Mike Monteith who has shown immense faith in me to solve such a complex problem, and to my project team members; Mr. Greg Erickson and Mr. Michael LeBlanc, for their support in chemistry discussion and analytical method development, in order to understand impurities on a ppm levels.

My appreciation also goes out to past and current colleagues in the Roberts research group and the Kenan CO_2 Center- particularly, Dr Laura Beth Dong, for her immense help in training me in the Quantachrome Autosorb catalyst characterization equipment.

TABLE OF CONTENTS

LIST OF TABLES

LIST OF FIGURES

CHAPTER 1: INTRODUCTION

1.1 Motivation and Objectives

Hydrogenations of halo-nitroaromatics to halo-anilines, using heterogeneous catalytic hydrogenation, are increasingly common in the chemical industry [1], as the aniline product is an essential chemical in the manufacture of dyes, antioxidants, fine chemicals and pharmaceutical intermediates. Such reactions have been extensively studied since the 1950s [2,3] in an attempt to understand the catalyst behavior and reaction rates for large-scale production [4]. The hydrogenation of a halo-nitroaromatic to halo-aniline is a key intermediate for the manufacture of an Active Pharmaceutical Ingredient (API) in late-stage clinical trials. Such a reaction involves multiple intermediate steps [1]; but, the relationships between intrinsic kinetics, mass transfer rate, and the mechanistic pathway are not well understood.

Halo-nitroaromatic reduction takes place in a slurry reactor over a heterogeneous catalyst with particle diameters typically smaller than 50 μm, and with introduction of hydrogen in the headspace of the batch reactor. Such reactions exhibit a complex kinetic behavior and require a careful reaction rate control, as they produce highly energetic intermediates, such as hydroxylamines, that pose a safety concern upon scale-up. In addition, there are significant mass transfer challenges in these reactions resulting from the need to transfer the hydrogen from the headspace of the reactor into the liquid phase, and then onto the catalyst surface. Mass transfer rates in such reactions play a key role in process safety. Previous work [5], using calorimetric measurements and hydrogen gas uptake data for these reactions, has not clearly identified the role of mass transfer and the resulting reaction pathway leading to the formation of various intermediates, such as hydroxylamine. In addition, the mechanism

for the formation of the dehalogenated aniline byproducts in these reactions has not been clearly identified. Such impurities can pose a quality risk for pharmaceutical products, thereby risking a batch failure.

Catalysts play a vital role in the hydrogenation of nitroaromatics. Heterogeneous reactions can be limited either by diffusion or kinetic control, depending upon the catalyst used or the reaction conditions. Different reaction regimes can give rise to various intermediates and impurities, which can be detrimental to the product quality and can inhibit the reaction progress (catalyst poisoning). Activated carbons are the most widely utilized supports for hydrogenation catalysts [6]. Due to their high surface area and organophilic character, they can absorb small impurities present in the reaction medium, thus preventing catalyst metal poisoning. The chemical and physical properties (mineral impurities, porosity, functional groups, etc.) for activated carbons vary widely as they are derived from naturally occurring materials, such as wood, peat, fruit kernels, etc. Precious metal catalysts, such as palladium or platinum on carbon, are the most commonly used catalysts for such hydrogenations [7]. The two most commonly available types of metal dispersions are uniform-type and egg-shell-type metal dispersion. Metal deposited at the external particle surface results in an egg-shell catalyst whereas metal deposited throughout the carbon support produces uniform catalysts. Metal deposition can be controlled either during the impregnation stage for strongly adsorbed metal, resulting in a uniform catalyst, or during the drying stage for weakly adsorbed metals [8]. In general, for catalytic hydrogenations, the carbon support and metal type, as well as the deposition profile of the metal, play a key role in reaction kinetics.

Hydrogen solubilities vary with solvents, such as alcohol, water, etc., and are strongly dependent on temperature and pressure. The overall rate of the hydrogenation reaction is determined

by the dissolved hydrogen concentrations [9]. A mixture of solvents is typically used to enhance the solubility of nitroaromatic compounds for such reactions. Some solubility data of hydrogen at various temperatures and pressures have been published [10] for single-solvent systems. It becomes an onerous task to tabulate such data for thousands of co-solvent combinations at various pressures and temperatures. Hydrogen solubility is a function of Henry's Law constant [11] at low pressures. However, these linear relationships are not valid beyond 298°K temperatures and 0.1 MPa pressures. Various equations of state have been applied to a hydrogen-solvent complex system [12,13] by treating the solvent as a mixture of pseudo-components. Vapor-liquid equilibrium (VLE) data for hydrogen in various solvents resulted in an average absolute error (AAE) between 0.5 and 2.0%. The AAE percent was calculated from the difference between the actual and predicted values, divided by the actual value. Predictions of hydrogen solubilities were variable, but resulted in AAE between 3 and 10% for three coal liquids. A detailed composition analysis of the solvent must be available for this approach to be applied but such data are rarely available. Corresponding states theory has been applied for pure- and multi-component solvent systems. The AAEs for these systems were found to be 5.8% and 6.8%, respectively [9].

The focus of this research is the hydrogenation of halo-nitroaromatics to halo-aniline over heterogeneous catalysts in a slurry batch reactor. This catalytic hydrogenation is a complex chemical process with several competing mass transfer and kinetic effects which contribute to the overall rate of the reaction. The effects of heat and mass transfer must be fully understood and quantified for a successful scale-up of the process. The control mechanisms for one of the highly energetic intermediates, hydroxylamine, pose a safety concern upon scale-up and, therefore, must be well understood. The mechanism of the de-halogenated impurity formation and its control during the course

of the reaction is not fully elucidated and, therefore, must be well understood. The hydrogenation of halo-nitroaromatic in a batch slurry reactor was investigated to obtain a mechanistic understanding and control of the various intermediates and impurities in the process. The relationship between intrinsic kinetics and mass transfer were evaluated to obtain a complete mechanistic understanding for these reactions.

1.2 Scope of Research

Chapter 2 presents a literature overview of the current state of the art in the hydrogenation of halo-nitroaromatics and the diverse approaches taken for studying these reactions, including postulated mechanisms and rate expressions. Chapter 3 focuses on the catalyst selection process, which affects the overall selectivity, reactivity and kinetics of these reactions. A high-throughput screening technique narrowed the catalyst choice from forty-eight different catalysts available from two commercial catalyst manufacturers. Chapter 4 focuses on the mass-transfer scale-up for the reaction. The reactor geometry differs widely from the lab scale to the plant scale reactors. Based on the geometric similarities, this chapter also describes the various mass-transfer models and the disadvantages of using this technique, as cited in the literature. A general procedure for scaling-up the global mass-transfer rate, independent of the reactor geometry, is outlined in this chapter. Chapter 5 illustrates the relationship between the global mass transfer coefficient and intrinsic kinetics for hydrogenation reactions. These hydrogenation reactions are often limited by one of three regimes: mass transfer limited regime; intrinsic kinetic limited regime; or both mass transfer and kinetic control regimes. Chapter 5 also describes the kinetic model for the postulated reaction mechanism. A new methodology for testing catalyst robustness, using reaction progress analysis techniques [14] is also

proposed. Chapter 6 highlights the understanding of intermediates and impurity formation. It illustrates a control mechanism for such intermediates and impurities based on process parameters. Chapter 7 describes the results from scale-up runs. During the scale-up of the process in the plant reactor, the reaction rate was observed to be slower than the lab scale reaction. Catalyst characterization techniques, such as chemisorption, revealed the cause as a special case of catalyst inhibition. Finally, Chapter 8 summarizes conclusions from these results, along with suggestions for future work.

References

1 J. Wisniak et al., Reduction of Nitrobenzene to Aniline, Ind. Eng. Chem. Prod. Res. Dev., 1984, Vol. 23 (1), p. 44–50.

2 G. S. Samuelson et al., The Hydrogenation of Nitro Compounds with Raney Nickel Treated with Chloroplatinic Acid and with Alkali, J. Am. Chem. Soc., 1950, Vol. 72, p. 3872-3874.

3 H. C. Yao, and P.H. Emmett, Kinetics of Liquid Phase Hydrogenation. IV. Hydrogenation of Nitrocompounds over Raney Nickel and Nickel Powder Catalysts, J. Am. Chem. Soc., 1962, Vol. 84, p. 1086-1091.

4 C. V. Rode et al., Hydrogenation of Nitrobenzene to p-Aminophenol in a four phase reactor, Chem. Eng. Sci., 2001, Vol. 56, p. 1299-1304.

5 F. Visentin, Study of Hydrogenations of selected Nitro compounds, Ind. Eng. Chem. Res., 2006, Vol. 45, p. 4544-4553.

6 T. Pietsch et. al., Carbons as supports for industrial precious metal catalysts, Applied Catalysis A, General, 1998, Vol. 173, p. 259-271.

7 Catalyst Guide, Hydrogenation of Aromatic Nitro Groups in Halo-nitro aromatics, Evonik Industries (http://catalysts.evonik.com/product/catalysts/en/products/technology-platforms/halo-nitroaromatic-reduction/pages/default.aspx).

8 J. G. Khinast et al., Impact of drying on the catalyst profile in supported impregnation catalysts, Chem. Eng. Sci., 2001, Vol. 56, p. 4473-4487.

9 J. M. Shah, A Correlation for Hydrogen Solubility in Acyclic and Aromatic solvents, The Canadian Journal of Chemical Engineering, 1987, Vol. 65, p. 293-298.

10 C. L. Young, IUPAC Solubility Data Series: Hydrogen and Deuterium, Pergamon Press, Oxford, England, New York, NY, 1981, Vol. 5/6.

11 W. Hayduk and W.D. Buckley, Temperature Coefficient of Gas Solubility for Regular Solutions, The Canadian Journal of Chemical Engineering, 1971, Vol. 49, p. 667-671.

12 H. M. Lin, W. A. Leet, H. Kim, and K. C. Chao, Measurement and Prediction of Vapor-Liquid Equilibrium, Ind. Eng. Chem. Process Des. Dev., 1985, Vol. 24, p. 1225-1230.

13 M. Rodasz , H. M. Lin, and K. C. Chao, High-pressure Vapor-Liquid Equilibria in Asymetric Mixtures, Ind. Eng. Chem.
Process Des. Dev., 1982, Vol. 21, p. 653-657.

14 S. Kedia and M. Mitchell, Reaction Progress Analysis: Powerful tool for understanding Suzuki-Miyaura reaction and control of Polychlorobiphenyl impurity, Org. Proc. Res. and Dev., 2009, Vol. 13, p. 420-428.

CHAPTER 2: LITERATURE REVIEW

2.1 Introduction

Historically, aniline is perhaps one of the most prominent synthetic organic chemicals ever manufactured. During the oxidation of aniline [1], a purple dye, known as mauve, was isolated by Sir William Henry Perkin in 1856. Understanding the value of his discovery, Perkin (a student at the Royal College of Chemistry in London), scaled up the process of synthesizing mauve, along with the synthesis of aniline. This synthesis became one of the first commercial processes to produce a synthetic organic chemical. Aniline is a key intermediate in the manufacture of polyurethane plastics, which have emerged over the last three decades, as a growth industry. Aniline is also a key intermediate for the manufacture of 4, 4'-diphenylmethane diisocyanate (MDI), a key commercial monomer. Aniline is also an important chemical in the manufacture of various pharmaceutical intermediates, agrochemicals, and vulcanization accelerators and antioxidants.

Aniline is formed by the reduction of nitrobenzene. Hydrogenation of nitroaromatics has been the focus of many research groups for over 60 years. Originally, the reaction of nitrobenzene with dispersed iron in the presence of HCl was found to yield aniline and iron oxide sludge. Catalytic hydrogenation was eventually introduced to overcome the large amount of iron oxide waste generated in the original process. The chemistry for the reduction of nitrobenzene to aniline was originally elucidated by Haber [2] and Debus and Jungers [3] as reported by Stratz [4]. Figure 2.1 depicts the complex mechanistic pathway, as reported by Stratz, elucidating the reduction of the halo-nitroaromatic to halo-aniline along with the dehalogenated impurity [I].

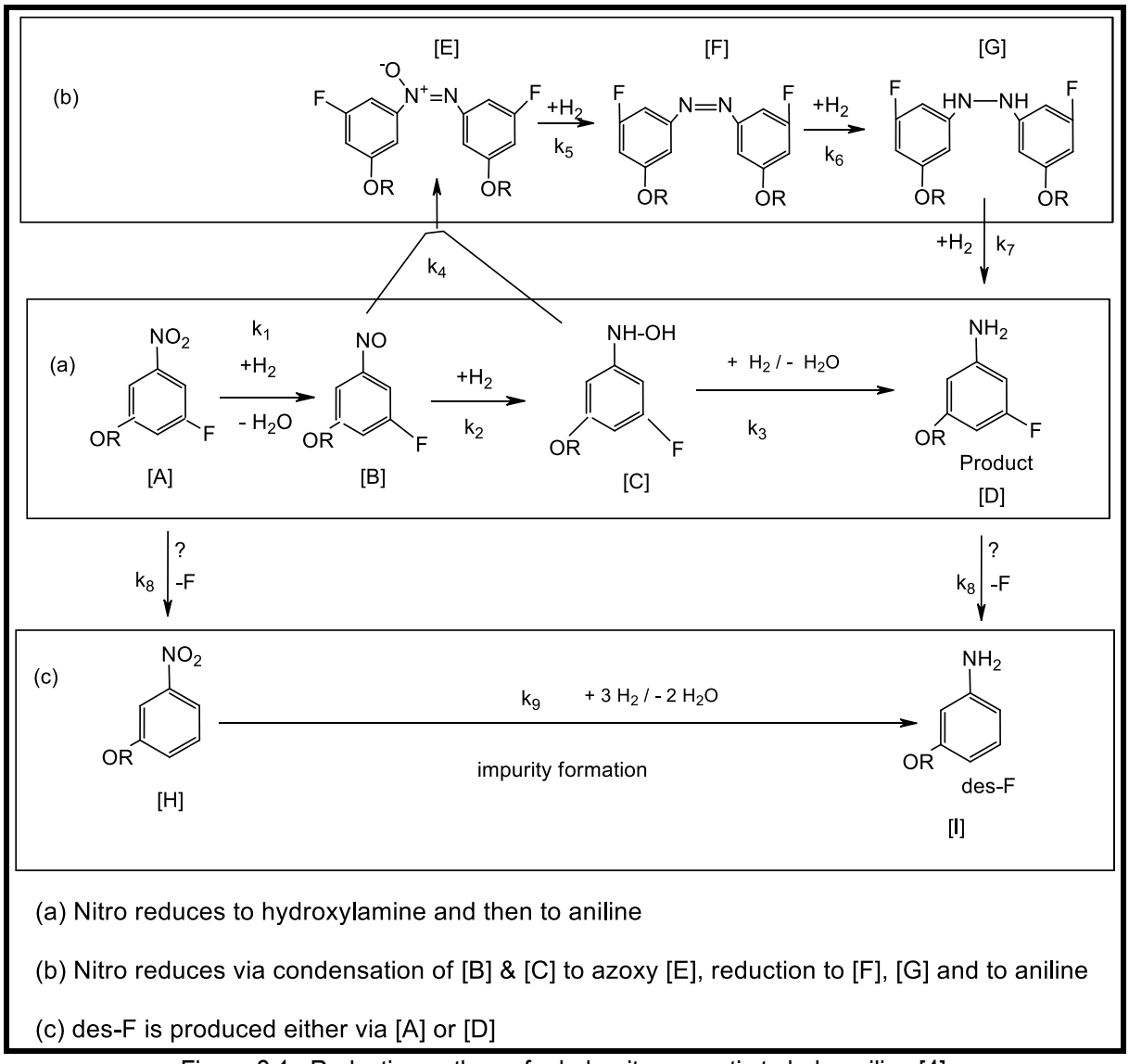

Figure 2.1: Reduction pathway for halo-nitroaromatic to halo-aniline [4]

Several papers in the literature reference the hydrogenation of nitrobenzene in the presence of catalyst and appropriate solvents to form aniline and various intermediates. Samuelsen et al. [5] hydrogenated nitrobenzene in the presence of Raney nickel as a catalyst that had been treated with chloroplatinic acid and found that quantitative conversion of nitrobenzene to aniline proceeded without the formation of intermediates. Scholnik et al. [6] hydrogenated nitrobenzene and its sodium salts, along with methyl and ethyl ester derivatives of nitrobenzoic acids, in the presence of Raney nickel, activated with

platinum chloride. Yao and Emmett [7] discovered that azoxybenzene ([E] in Figure 2.1) and aniline were formed if the catalyst (Raney nickel) was first degassed. Metcalfe and Rowden [8] found that the reaction went through stable intermediates, such as hydroxybenzene [B], phenylhydroxylamine [C], azoxybenzene [E], and azobenzene [F] in Figure 2.1 when butanol was used as a solvent with palladium-silver alloy as a catalyst. Shebaldova et al. [9] hydrogenated nitrobenzene selectively to produce phenylhydroxylamine, using catalysts such as rhodium, palladium, and cobalt complexes. Aniline was not formed; however, increasing amounts of azoxybenzene were produced. Shebaldova postulated the mechanism, illustrated in Figure 2.2, based on their results. When the reaction catalyst was changed to iron or nickel, aniline was the only product formed. Thus, depending upon the choice of the catalyst, the reduction of nitrobenzene yielded various products.

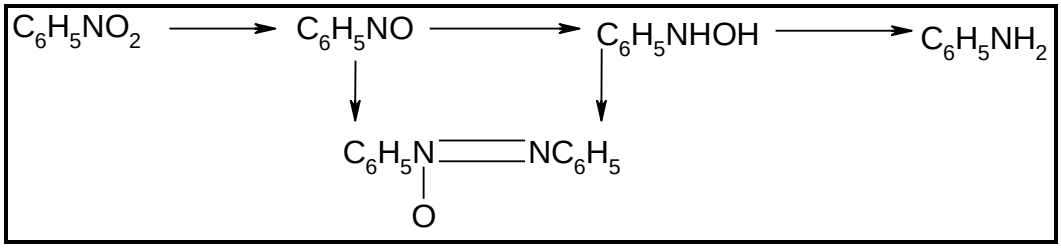

Figure 2.2: Mechanism proposed by Shebaldova for nitro reduction [9]

Debus and Jungers [3] described the hydrogenation of nitrobenzene in a complex mechanism involving several intermediates, such as nitroso-benzene, azoxybenzene, azobenzene, phenylhydroxylamine and azobenzene as shown in Figure 2.1. Nickel catalyst was found to be poisoned during the oxidation process. Debus et al. postulated a mechanism, as illustrated in Figure 2.3, similar to Haber [2], depicting the relative rates for nitro reduction.

Burge et al. [10] postulated several intermediates during the reduction of nitrobenzene. The rate of reduction of nitrobenzene was found to be zero-order when the Haber mechanism was adopted,

and the rate constants for various mechanistic pathways were calculated. Wisniak et al. [11] investigated several mechanistic pathways for nitrobenzene reduction and concluded that none of the mechanisms tested gave an accurate mechanistic description. The reaction order was markedly different when the overall reaction rates involving only the concentration of aniline or nitrobenzene were compared between the test runs.

Summarizing, the reduction of nitrobenzene has been extensively studied in a wide range of conditions: in the liquid and vapor phase, with and without solvent, and with various types of catalysts and their supports; however, its mechanism has not been fully elucidated.

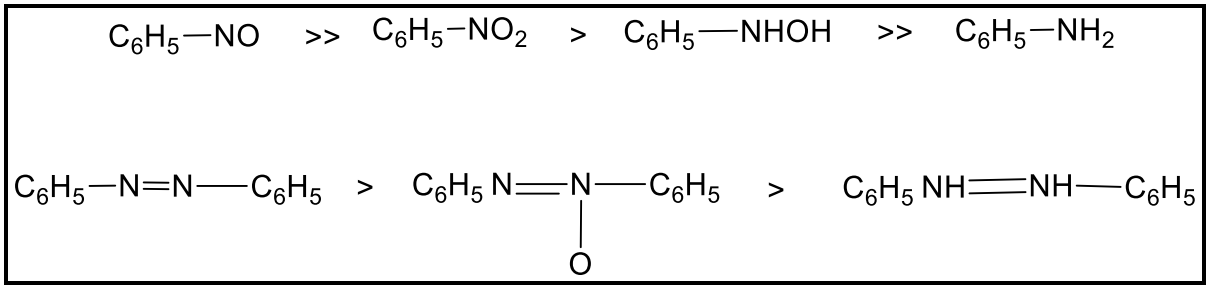

Figure 2.3: Relative rates of hydrogenation [3]

2.2 Thermal Hazard During Hydrogenation of Nitroaromatic

Thermochemistry plays a vital role in the comprehension and control of chemical process hazards [12]. Chemical process hazards originate from several factors:

- Thermal decomposition of chemical species, such as reactants, intermediates, or products. This decomposition has led to the development of several instruments such as the Differential Scanning Calorimeters and Accelerating Rate Calorimeters.

- Heat generated during the reaction, which should be removed from the reactor via heat transfer fluid (coolant) in the jacket. The rate of heat removal must match or exceed the maximum rate at which heat is generated in order to prevent a thermal runaway.
- Heat of side-reactions, which may occur in conjunction with the main reaction. These require a change in operating conditions, such as process temperature or catalyst type, and might change the selectivity of the process, thereby altering the fate of impurities or side-reactions.
- Pressure build-up due to gas evolution or vapors in the reactor, resulting from excessive heat release.

The reduction of nitroaromatics to aniline is a highly exothermic process [13], the heat of the reaction being 545 kJ/mol (or 130-kcal/mol). It was well known that the reaction proceeds via the formation of certain intermediates, as postulated in Figure 2.1; but, it was generally assumed their formation was brief, and thus little attention was paid to them. An explosion occurred during the catalytic reduction of chloronitrobenzene, which was attributed to runaway decomposition initiated by exothermic disproportionation of the hydroxylamino intermediate [14], and it has been accepted in recent years that such intermediates may cause significant process hazards. The heats of formation of these energetic intermediates were studied by Macnab [12]. The reduction of nitroaromatic to hydroxylamine was found to be an extremely fast reaction, with ΔH_{rxn} of 320-kJ/mol, and the reduction of hydroxylamine to aniline was found to be a slower reaction, with ΔH_{rxn} of 225-kJ/mol. It is well known that hydroxylamine disproportionates exothermically [12-15], leading to the formation of azo- and azoxybenzene. These reactions are not limited by mass transfer rate of hydrogen and, therefore, cannot be stopped by slowing the mass transfer rate of hydrogen. As a result, to scale-up an intrinsically safe process, a complete risk assessment is essential and should be carried out in order to evaluate the accumulation of such intermediates and determine the consequences for the thermal

safety of the process. Various heats of formation of intermediates are shown in Figure 2.4, as calculated and measured by Macnab [12]. These calculated heats of reactions have further significance: first, the overall cooling requirement for such reactions can be calculated, and second, the cooling demand must match the heats of reaction to prevent a thermal runaway of hydroxylamine reduction.

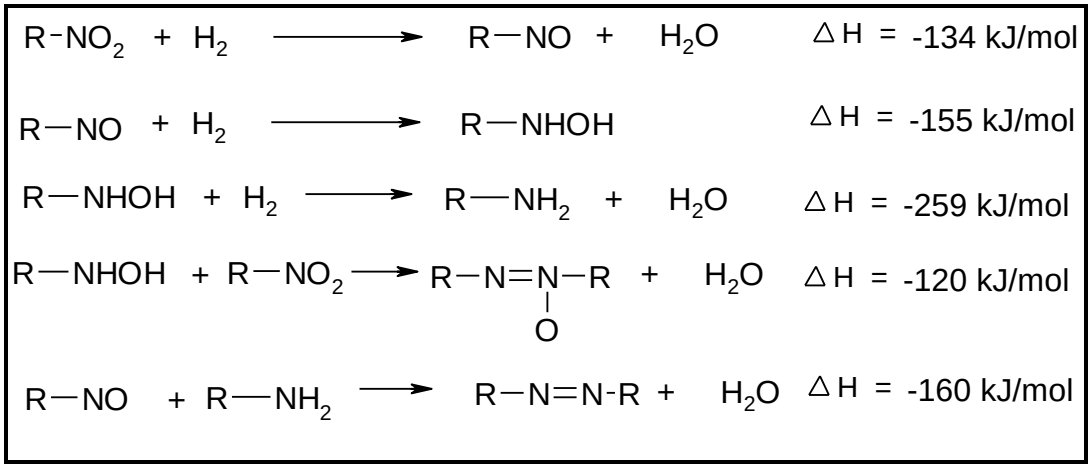

Figure 2.4: Heats of reaction during nitroaromatic reduction [12]

Stoessel [13] describes the risk of thermal explosion or time to maximum rate under adiabatic conditions (TMR_{ad}), which can be estimated by the formula published by Townsend and Tou [16]:

$$TMR_{ad}\ (seconds) = \frac{C_p\ R\ {T_o}^2}{q_o\ E_a} \qquad [2.1]$$

where R = universal gas constant = 8.314 J/mol/K; T_o = Temperature (K); q_o = reaction power per kg at T_o (W/kg); E_a = activation energy (J/mol); and C_p = specific heat of reaction mixture (J/kg/K).

In the case of loss of cooling in hydrogenation reactors, heat is accumulated inside the batch reactor so that even a slow reaction can eventually lead to a thermal runaway. Thus, measures should

be taken to prevent thermal runaway, such as: emergency cooling of the batch, slow release of pressure with condensation of solvent, or transfer of the batch to a cooling tank. For safe operation, one must ensure that the TMR_{ad} is considerably longer than the time needed for the intervention after the cooling breakdown to determine the maximum allowable temperature for the reaction.

A precise control of reaction rates and temperatures must be maintained at all times for safe plant operation. The role of hazard assessment is to define these limits of safe operation and to take corrective action to stay within the safety limits. Use of thermochemical data allows an estimate of the potential temperature rise under adiabatic conditions for given compositions. In conjunction with the thermal stability data, it is possible to predict the concentrations of nitro and phenyl hydroxylamine for a given process temperature which may bring about the maximum safe rise of reaction temperature. Additionally, based on a full understanding of the process chemistry and the possible side-reactions, thermochemical studies complement experimental thermal stability data in providing the basis for the control of chemical process hazards.

2.3 Modulation of Hydroxylamine

The catalytic hydrogenation of aromatic nitro compounds is industrially important and proceeds via several intermediates [17]. Most important is the corresponding hydroxylamine species, as elucidated by Baumeister et al. [18], and shown in Figure 2.5.

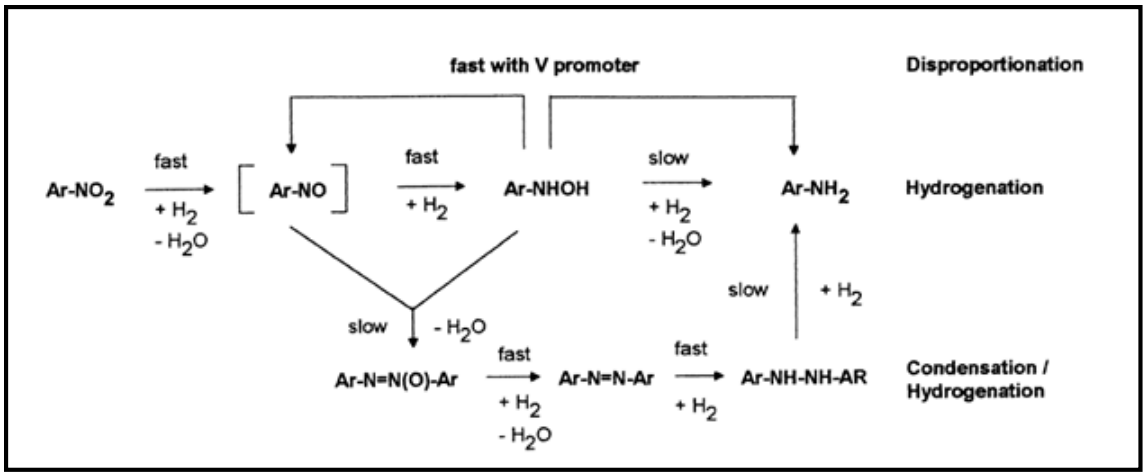

Figure 2.5: Reaction network for nitroarene hydrogenation [18]

According to Baumeister et al. [18], nitro compounds with electron-withdrawing groups, such as sulfonamide or a halogen, can accumulate aryl hydroxylamines in large quantities. The accumulation is seen when the hydrogenation is carried out in a batch reactor at low or medium temperature (<100C). Hydroxylamines are thermally unstable intermediates that can disproportionate with a strong exotherm, causing severe explosions [14]. They are also known as potent carcinogens and, therefore, are hazardous in the event of an incomplete reaction [19]. Hydroxylamines can also undergo condensation with the nitroso compound, leading to the formation of colored azo or azoxy by-products (lower part of Figure 2.5), that are detrimental to the product quality. The concentration of hydroxylamines is difficult to control and predict [20]; therefore, the product quality varies from batch to batch. Some chemical processes exist to lower the hydroxylamine accumulation [22], but better understanding and control are clearly needed. A few publications have reported the evasion of this issue by using semi-batch or continuous processes [21, 22, 23]; but, it is often impossible to employ such reactors in the production of fine chemicals and pharmaceuticals due to the multi-purpose use required in such industries.

Another approach, described by Studer et al. [24], involves the addition of a co-catalyst such as vanadium to accelerate the disproportionation of hydroxylamine. Vanadium additives were shown to decrease the accumulation of hydroxylamine. Various vanadium co-catalysts with Pt, Pd, and Ir metals, have been applied successfully to a number of processes (e.g., the hydrogenation of 2,4-dinitrochlorobenzene or 2-nitro-2',4',4'- trichlorobiphenyl ether). Minimum to zero accumulation of hydroxylamine was found; however, the role of these modifiers is still not well understood. The best combination of catalyst with vanadium is difficult to predict. In some cases, such as hydrogenation of 3,4-dichloronitrobenzene with Pt catalysts, the vanadium modifiers had a negative impact on process yields and product quality [24]. In other cases, such as Pt–Cu/C catalyst, catalyst poisoning was observed. Raney nickel (RNi) has been widely utilized due to its low cost and high chemoselectivity for the hydrogenation of nitro aromatics with several substituent groups (halogen, C=C, C≡N and others); however, RNi has been known to accumulate large amounts of hydroxylamine during the reaction, and a suitable remedy has yet to be discovered.

The results for various vanadium promoters were compared with RNi and are tabulated in Table 2.1. Studer et al. [24] showed that the reproducibility of the reaction rates and concentration of hydroxylamine (CHB) was an issue (two different batches of RNi showed a variation of the rates between batches >10%). It was also observed that the premix time of substrate and promoters was also a key process parameter for the reaction. NMR and GLC techniques were difficult to implement due to the presence of paramagnetic Ni in the sample and evaporation of anilines. Therefore, the results shown in Table 2.1 are only of a qualitative nature. The reaction system without modifiers had a maximum hydroxylamine accumulation of 71%. When vanadium was added as a modifier to the reaction mixture, the maximal hydroxylamine concentrations were found to be between 11 and 86%. Studer observed that the modifiers that reduced the amount of hydroxylamine accumulation also

lowered the overall reaction rate. Likewise, it was also observed that those modifiers that increased the overall reaction rate also showed significantly higher accumulation of hydroxylamine.

Studer investigated the use of vanadium modifiers of RNi for two additional substrates: the halo nitro phenol and the substituted nitrobenzene carrying both a COCH3 and a COOH group. He concluded the following:

- In reactions where no vanadium promoters were added, both substrates showed higher accumulation of hydroxylamine in the range of 50–70%.
- With the addition of vanadium modifiers, the hydroxylamine concentration was significantly reduced.
- Reaction screening needed to be performed to yield the best modifier combination, i.e., there was lack of understanding.
- Addition of vanadium modifiers led to lower rates in the hydrogenation of halo nitro phenol. The same was observed for substituted nitrobenzene carrying both a COCH3 and a COOH group; but, higher reaction rates with high hydroxylamine accumulation were found in some cases.
- Higher reaction rates and lower accumulation were obtained in the case of halo nitrophenol. The reason postulated for higher hydroxylamine concentration in the substituted nitrobenzene molecule, was due to the two electronic withdrawing groups [an acetyl group ($-COCH_3$) and a carboxylic acid (-COOH)] present in the molecule.

Table 2.1: Initial screening of various vanadium additives for the hydrogenation of halo nitrobenzene [a] [24]

Cat.	No.	Vanadium modifier	V / RNi ratio [b]	Relative Initial rate	[CHB] max (% HPLC)
	1.1	No	–	1.0[c]	71
I	1.2	NH4VO3	2.6	0.4	14
I	1.3	NH4VO3/clay	1.5	0.4	15
I	1.4	VO(acac)2	8	0.4	19
I	1.5	VCl3 /Beta	4	0.6	31
I	1.6	NH4 VO3/amberlite	3.6	0.6	36
II	1.7	VCl3	7	0.1	11
II	1.8	NH4VO3/Beta	1.4	0.2	14
II	1.9	V(acac)3	8	0.3	27
II	1.9	Na3PV12O40	1.7	0.4	43
III	1.1	VCl3/sepiolite	1	0.6	60
III	1.11	V–Mo/α-Al2O3	7	0.7	60
III	1.12	NH4VO3/C	3	0.4	64
III	1.13	NaVO3	2.5	1.3	75
III	1.14	V2O5	3.4	1.1	86

a Conditions: 4.8 mmol **1**, 150 mg RNi, 100 ml MeOH, 1.1 bar H_2, 30–35C.
b (mol V compound/mol nickel) *X* 100.
c 100% conversion and 100% H_2 uptake in 2 h, the initial rate was 113 mmol g^{-1} h^{-1}.

In another study, Baumeister et al. [18] speculated that a metal ion or complex may suppress the accumulation of hydroxylamine by increasing the disproportionation rate of hydroxylamine. A broad study of the effect of methanol-soluble metal salts was carried out by Studer et al. [24]. Out of the hundred metal salts screened, eleven showed an extremely fast, and fourteen showed fast, disproportionation of the hydroxylamine, mainly to nitroso, azoxy, and amine products. The most active metal salts, such as Ag, Ce, Co, Cu, Cr, Fe, Hg, Mn, Mo, Re, Ru, Ti, Tl, Th, and V, were found to disproportionate hydrogen peroxide over catalyst. Out of the twelve most reactive salts tested, eight showed fast hydroxylamine disproportionation reaction (refer to Table 2.2). It was observed that, using

most of these salts, more than 88% of the starting material was transformed into azoxy, nitroso, and aniline product. This indicated that the promoters catalyzed the disproportionation of hydroxylamine predominantly. However, the amount of product (aniline) formed varied widely from 3 - 71%. It was observed by Baumeister et al. [18] that $CuCl_2$ catalyzed the oxidation and $Tl(NO_3)_3$ the reduction of the hydroxylamine. It was also seen that $CuCl_2.2H_2O$ acted only as a disproportionation catalyst. Salts of Ag, Ce, Mn, and Ti showed slow or no reaction and, with Re, unidentified by-products were formed. The oxidation state of the metal (e.g., with iron) or the counter ion (e.g., with manganese) had an influence on the rate of decomposition; however, no clear trend was observed.

Significantly, results by Baumeister et al. [18] showed that the rate of hydrogenation accelerated in the presence of the vanadium salts, and the amount of hydroxylamine accumulation decreased substantially (refer to Figure 2.6). The hydroxylamine accumulation decreased from > 40% to < 1% with NH_4VO_3 or V/Pd/C. The addition of metal salts, such as $VOSO_4$ and V_2O_5, also resulted in the reduction of hydroxylamine concentration but was less effective. Baumeister et al. [18] observed that the reduction was faster in the presence of vanadium salts. All other additives resulted in longer reaction times and were less effective in reducing the hydroxylamine accumulation, except for $Co(NO_3)_2.6H_2O$. Baumeister et al. [18] also observed that the products obtained with efficient promoters were cleaner, with fewer intermediates and colored impurities, than the ones without promoters (see Figure 2.6 for details).

Table 2.2: Metal salt additive and hydroxylamine formation [18]

Metal salt	2	Azoxy	Nitroso	Amine
NH_4VO_3	0	30	23	46
$FeBr_2$	0	25	21	53
$Co(NO_3)_2 \cdot 6H_2O$	0	16	28	58
CuCl	3	31	60	3
$ReCl_3$ [a]	6	36	3	6
$CuCl_2 \cdot 2H_2O$	8	38	11	38
Mo(acetylacetonate)$_2$	8	37	9	34
$Tl(NO_3)_3$	11	18	4	71
no additive	89	0	0	9

[a] 39% unidentified products.

Product composition in mol% of starting material after reduction of hydroxylamine (**2)** with 3-5 mol% metal salt (methanol reflux, 3h, product analyzed by NMR)

Catalytic hydrogenations of nitroaromatic compounds often have two distinct phases. First, the nitro compound is reduced to the corresponding hydroxylamine. Then, the hydroxylamine is reduced to the corresponding aniline. With vanadium promoters, the hydroxylamine disproportionates rapidly (upper part of Figure 2.5), forming the nitroso intermediate; then, it re-enters the catalytic cycle, resulting in an acceleration of the amine formation. During various hydrogenations, Baumeister et al. [18] never observed the nitroso intermediate. This is in direct contradiction to the mechanism postulated by Debus [3] as fast hydrogenation reaction of the nitroso compound. This means that either nitroso never leaves the catalyst surface or is reacted quickly, and is therefore, not observed.

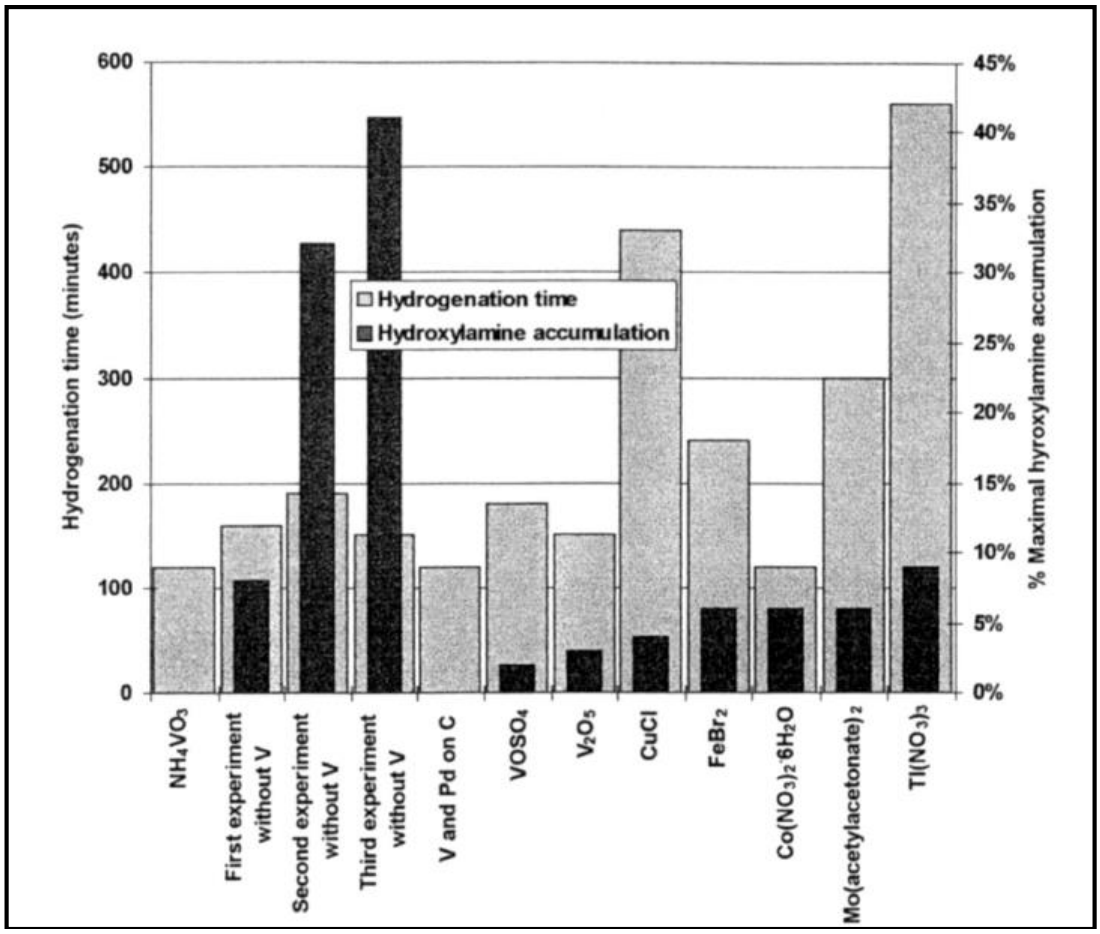

Figure 2.6: Hydrogenation of nitroarene [18]
Effect of additives on the maximum hydroxylamine accumulation (always observed after 66% hydrogen uptake) and the time needed for 100% conversion. Product analysis by NMR

2.4 Reaction Kinetics

Aromatic nitro reductions have been extensively studied over the past couple of decades. Wisniak [11] ran several experiments to understand the rates of formation of intermediates as well as their relative stability. A typical reaction profile is shown in Figure 2.7. Nitrobenzene was reduced to aniline, using RNi, and only azobenzene and azoxybenzene were observed as intermediates. For the purpose of kinetic study, it was vital to ensure that the rate data were obtained under the kinetically controlled regime. Based on the experiment, a pseudo-first order reaction rate was proposed for nitro reduction:

$$\frac{dC_{NB}}{dt} = -k\, C_{NB} \,.\left(\frac{mol}{L * min}\right) \qquad [2.2]$$

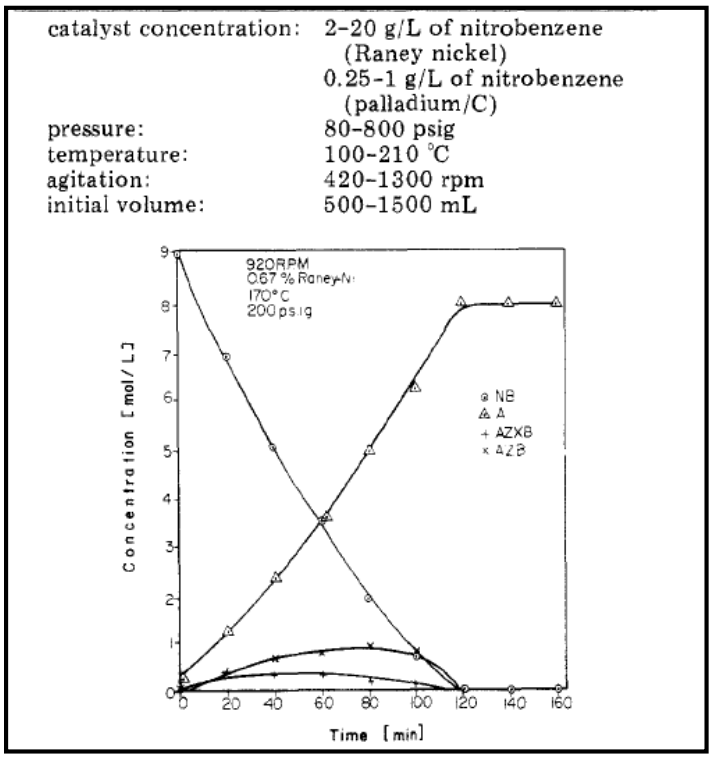

Figure 2.7: Reaction profile with Raney nickel [11]

The reaction rate was found to increase linearly with agitation rate (indicative of mass transfer limitation); however, it was found that when the agitation speed was above 900 rpm the reaction rate did not increase further, indicating the system was probably controlled by chemical reaction (as shown in Figure 2.8) under these conditions.

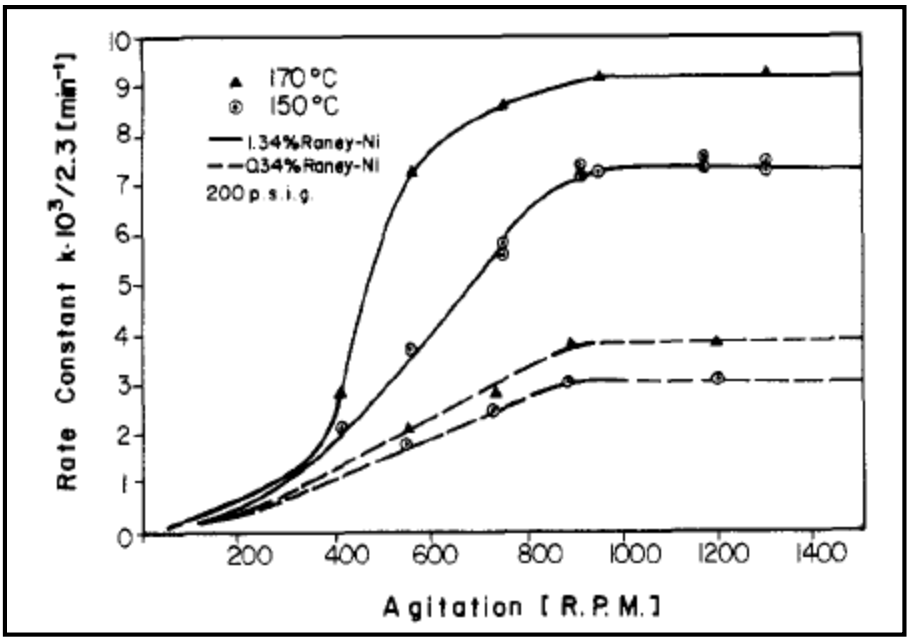

Figure 2.8: Influence of agitation rate [11]

Chaudhari et al. [25] screened various catalysts for the p-aminophenol reduction. The effects of various catalysts and solvents are elucidated in Table 2.3 and Table 2.4, respectively. The reaction rate (R_A) was calculated from the hydrogen uptake data. In this study, Chaudhari et al. [25] defined the average catalytic activity (N) [expressed as (kmol/kg*h)] as the amount of p-nitrophenol consumed per unit weight of the catalyst per hour, based on the time required to achieve more than 99% conversion of p-nitrophenol. Several precious metal catalysts were investigated for the reduction of p-nitrophenol, and the results are tabulated in Table 2.3. The catalyst activity followed the order Pt > Pd > Ni > Rh > Ru for the hydrogenation. Platinum catalysts yielded the highest catalytic reactivity, whereas ruthenium catalyst had the least activity. The catalyst activity was also investigated against various catalyst supports (Table 2.3, entries 5-8). The highest activity was observed for the carbon-supported platinum catalysts. A general trend was that increasing platinum content in the catalyst increased the overall reaction rate of the hydrogenation (Table 2.3, entries 5, 9-11).

Table 2.3: Initial rate of hydrogen and avg. catalytic activity for various hydrogenation catalysts [25]

sr.	catalyst	$R_A \times 10^3$ (kmol/m^3·s)	N (kmol/kg·h)
1	1% Pd/C	0.501	0.595
2	1% Ni/C	0.199	0.446
3	1% Rh/C	0.166	0.380
4	1% Ru/C	0.016	0.034
5	1% Pt/C	1.096	1.960
6	1% Pt/Al_2O_3	0.333	0.812
7	1% Pt/SiO_2	0.109	0.185
8	1% Pt/HY	0.082	0.131
9	0.5% Pt/C	0.524	1.347
10	2% Pt/C	2.034	2.412
11	3% Pt/C	2.895	3.017

[a] Reaction conditions: *p*-nitrophenol, 0.479 kmol/m^3; catalyst, 0.266 kg/m^3; ethanol, 30×10^{-6} m^3; hydrogen pressure, 2.72 MPa; temperature, 353 K; agitation speed, 1000 rpm.

Chaudhari et al. [25] also studied the effect of various solvents on reaction rate and catalytic activity, and the results are presented in Table 2.4. The five solvents studied were: water, methanol, ethanol, n-propanol, and n-butanol. It was observed that the average catalytic activity and the reaction rate increased with an increase in the solvent polarity, and rates were highest in water. Such enhancement in the reaction rates has been previously observed by Rajadhyaksha et al. [26] for nitro reduction and was partly attributed to the increase in activity of nitro compounds in polar solvents. Chaudhari et al. also studied the effect of catalyst loading, nitrophenol concentration, agitation speed, and H_2 pressure on the rate of hydrogenation, as shown in Figure 2.9. The reaction rate was found to increase with an increase in catalyst loading, agitation speed, and H_2 pressure. Also, saturation (zero

order) kinetics was observed at a higher concentration of nitrophenol, versus the first order at a lower concentration.

Table 2.4: Effect of solvent on the rate of hydrogenation and average catalytic activity [a] [25]

sr.	solvent	(ϵ)	$R_A \times 10^3$ (kmol/m^3·s)	N (kmol/kg·h)
1	water	78.5	1.325	3.066
2	methanol	32.6	1.170	2.160
3	ethanol	24.3	1.096	1.960
4	*n*-propanol	20.1	0.776	1.790
5	*n*-butanol	17.8	0.406	0.342

[a] Reaction conditions: *p*-nitrophenol, 0.479 kmol/m^3; catalyst (1% Pt/C), 0.266 kg/m^3; solvent, 30×10^{-6} m^3; hydrogen pressure, 2.72 MPa; temperature, 353 K; agitation speed, 1000 rpm. The values of dielectric constant (ϵ) were taken from CRC Handbook.[9]

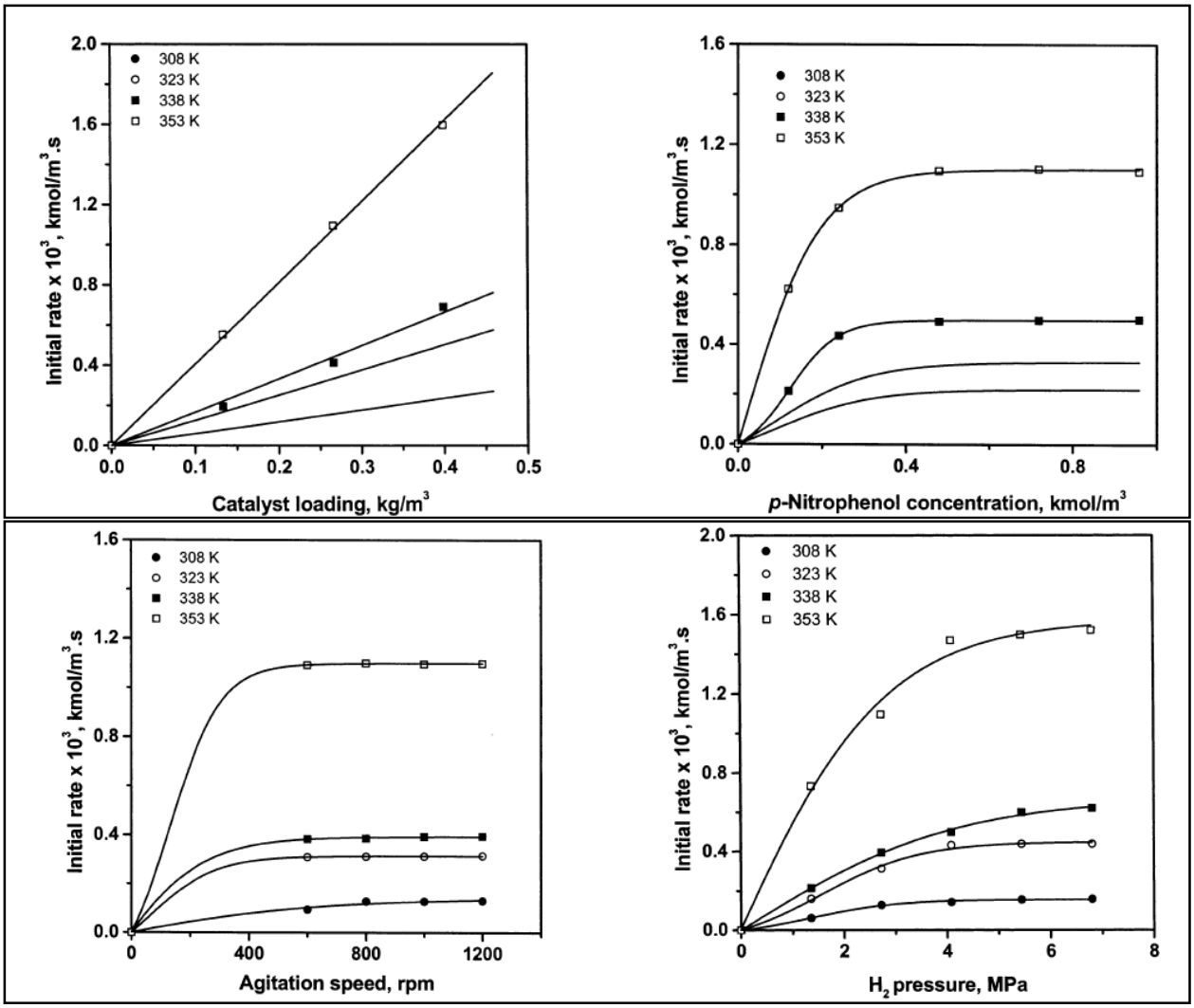

Figure 2.9: Reaction rate vs. catalyst loading, initial p-nitrophenol concentration, agitation speed, and H_2 pressure [25]

Stefoglo et al. [27] described a simplified mathematical model of a gas–liquid slurry reactor system using a suspended catalyst. The overall rate of nitro reduction is given by

$$\frac{dC_A}{dt}\left(\frac{\text{mol}}{\text{L}*\text{min}}\right) = \frac{k_A^*\ K_H\, C_{HL}}{1+\ K_H\, C_{HL}}\ \frac{K_A C_A}{K_A C_A + K_B C_B + K_C C_C} \qquad [2.3]$$

where C_A, C_B, C_C, C_{HL} are the concentrations of $ArNO_2$ (nitro aromatic), Ar-NHOH (hydroxylamine), $ArNH_2$ (aromatic aniline), and hydrogen, respectively; K_A, K_B, K_C, K_H are their respective equilibrium adsorption coefficients; and k_A and k_B are the kinetic rate constants. At a fixed hydrogen pressure, this equation simplifies further, to take the form:

$$R_A\left(\frac{\text{mol}}{\text{L} * \text{min}}\right) = -k_A \ \frac{K_A C_A \ C_{cat}}{K_A C_A + \ K_B C_B + \ K_C C_C} \qquad [2.4]$$

$$R_B\left(\frac{\text{mol}}{\text{L} * \text{min}}\right) = -k_A \ \frac{K_A C_A C_{cat}}{K_A C_A + \ K_B C_B + \ K_C C_C} + \ k_B \ \frac{K_B C_B C_{cat}}{K_B C_B + \ K_C C_C} \qquad [2.5]$$

$$R_C\left(\frac{\text{mol}}{\text{L} * \text{min}}\right) = + k_B \ \frac{K_B C_B C_{cat}}{K_B C_B + \ K_C C_C} \qquad [2.6]$$

Equations 2.4 – 2.6 are based on a Langmuir-Hinshelwood mechanism of $ArNO_2$ adsorption on catalytic sites. However, these equations lack the contributions of individual gas-liquid and liquid-solid mass transfer resistances and are coupled as one overall resistance [k_A^*] as shown in Equation 2.3.

Crezee et al. [28] describes another kinetic model of hydrogenation of D-glucose based on the number of sites involved in the reaction step. Three models based on the Langmuir-Hinshelwood rate form were postulated, assuming the reaction at the surface of the catalyst is the rate-limiting step. The first model assumed non-competitive adsorption of hydrogen and D-glucose at different catalyst sites. Hydrogen was found to be weakly adsorbed on the catalytic site, thus resulting in a linear dependency on hydrogen pressure, and was postulated as either molecular or dissociative [29]. The second model assumed competitive adsorption of hydrogen and D-glucose [30], which was found to be in direct contrast with many other hydrogenations reported in the literature involving dissociative chemisorbed

hydrogen. Nevertheless, Crezee et al. proposed this model since, for D-glucose, hydrogenation has been described to involve molecularly adsorbed hydrogen [29 - 31] by several references. The third model postulated by Crezee et al. was competitive adsorption of dissociative chemisorbed hydrogen and D-glucose [32]. Model 2 seems unlikely since it involves a reaction with molecularly adsorbed hydrogen. Furthermore, only Model 3 predicts an entropy loss for the adsorption of D-glucose as expected thermodynamically. Hence, the third model was found to be valid by Crezee et al., which was also supported by experimental data sets.

2.5 Gas-Liquid Mass Transfer

Catalytic hydrogenation reactions commonly use the surface aeration technique for gas-liquid mass transfer [33, 34, 35, 36]. It is vital to understand the gas-liquid mass transfer coefficients in the presence and absence of catalyst particles in these reactors. There are many factors affecting the volumetric mass transfer coefficient k_La, in gas-liquid and gas-liquid-solid agitated reactors, including: physical properties of the liquid (density, viscosity, surface tension, etc.); the concentration and physical properties of the solid (density, particle size, etc.); the geometry of the vessel and agitator; the power input per unit liquid, or slurry volume; the mobility of the interface; and the drop coalescence rate.

Unfortunately, the information available in the literature is limited and bewildering regarding the effects of these design variables on the mass transfer coefficient. Data for the mass transfer coefficients, power consumption, and solids suspension behavior for some gas-liquid and gas-liquid-solid systems over a wide range of some of the above-mentioned parameters are given by Schumpe et al. [37]. The mass transfer coefficient in this study was calculated for a batch agitated reactor. As reported by Topiwala [35] and indicated by Matsumara et al. [38], there was no difference observed between the performance of surface-aerated vessels and gas-sparged vessels at higher agitation

rates. Literature data indicate that the gas–liquid mass transfer is usually the rate-limiting step for industrial scale reactors [39]; and therefore, Morsi et al. [40] focused their research on determining the hydrodynamics and mass transfer parameters in agitated reactors [ARs]. Morsi et al. studied three types of agitated reactor systems, as shown in Figure 2.10. In this first reactor system, gas is introduced in the reactor headspace, and the gas absorption takes place mainly through the gas–liquid interface. This system is termed the surface-aeration reactor (SAR). In the second system, the gas is introduced from holes that are machined onto the hollow shaft of the reactor. Due to the angular velocity of the impeller, a pressure drop exists between the top and bottom of the shaft, which induces the gas into the liquid-phase interface, thus these systems are referred to as gas-induced reactors (GIRs). In the third system, the gas is bubbled from a ring located at the bottom of the reactor underneath the impeller for better mass transfer, referred to as gas-sparging reactors (GSRs). The hydrodynamic and the mass transfer parameters are expected to be different for these three operating modes. The SARs have the simplest design; however, Morsi et al. discovered that the gas absorption rate in such reactors is the lowest when compared with the other two reactor geometeries, GIRs and GSRs. The GIRs have a higher gas absorption rate when compared to SARs. The GSRs have the highest gas absorption rate; however, it is associated with significant cost to sparge the gas into these reactors. Several studies have been devoted to the determination of the hydrodynamics and mass transfer parameters in agitated reactors (ARs) [41]. Table 2.5 shows correlations of k_La in ARs. Mass transfer prediction in an agitated reactor is a challenging task, since these parameters can be affected by:

(1) Reactor geometry: reactor diameter (d_T), impeller diameter ($d_{Imp.}$), and impeller clearance from the bottom of the reactor (H_F);

(2) Operating variables: reactor mode (SAR, GIR, and GSR), mixing speed (N), liquid height (H), liquid height above the impeller (H_L), temperature (T), and gas partial pressure (P); and

(3) Physicochemical variables: liquid viscosity (μ_L), liquid and gas densities (ρ_L and ρ_G), liquid surface tension (σ_L), gas diffusivity in the liquid (DAB), and impurities/mixture composition (X_W).

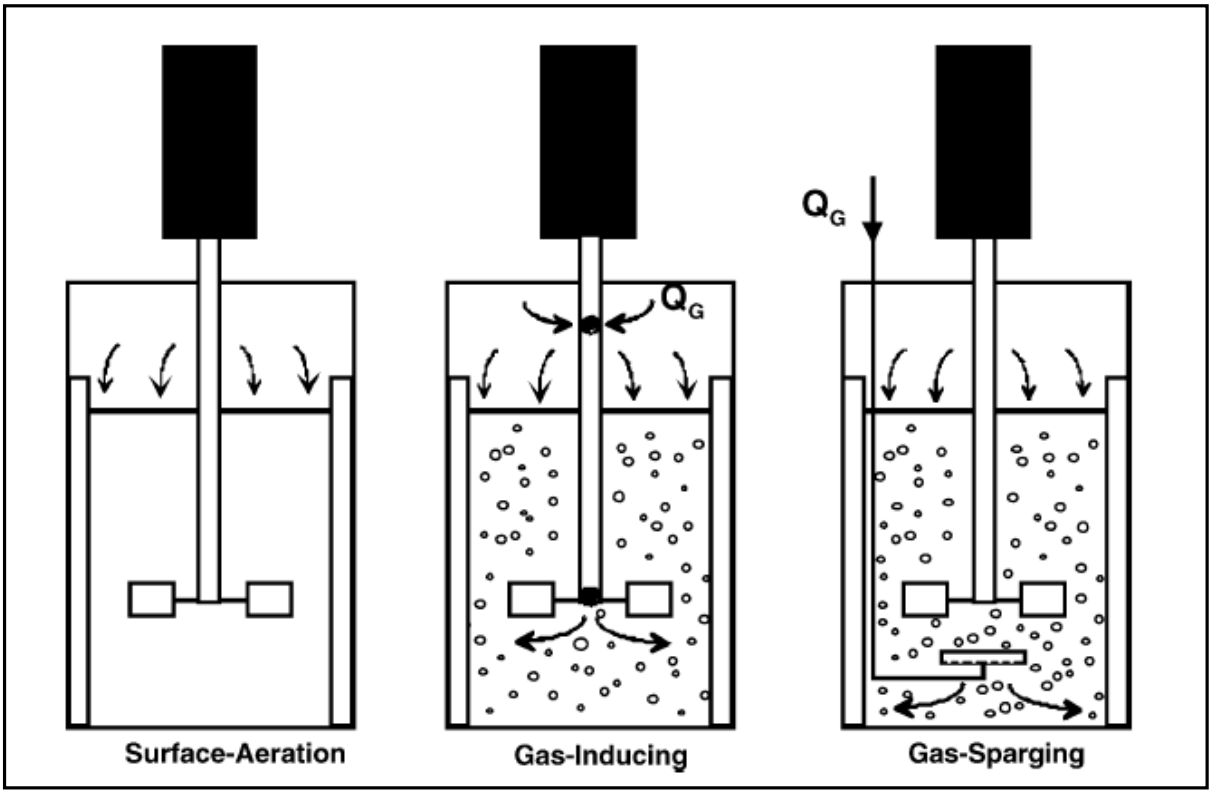

Figure 2.10: Operation modes of agitated reactors [41]

Table 2.5: Literature correlation of k_La in ARs [41]

References	Gas/liquid	Reactor	Operating conditions	Correlation
Robinson and Wilke [26]	N_2, CO_2/aqueous solutions	GSR	Atm. 303 K; N: 6.7–36.7 Hz; U_G: 1–4.6 10^{-3} m s^{-1}; P^*/V_L: 0.03–18 kW m^{-3}; d_T: 0.15 m	$k_La = 3.89 \times 10^{-3} \times \left(\frac{P^*_G}{V_L}\right)^{0.74} U_G^{0.36}$
Perez and Sandall [27]	CO_2/carbopol solution	GSR	Atm. T: 297–308 K; N: 3–8 Hz; U_G: 0.162–0.466 m s^{-1}; d_T: 0.15 m	$\frac{d^2_{Imp.}k_La}{D_{AB}} = 21.2 \times \left(\frac{N\rho_L d^2_{Imp.}}{\mu_{eff}}\right)^{1.11} \left(\frac{\mu_{eff}}{\rho_L D_{AB}}\right)^{0.5} \times \left(\frac{d_{Imp.}U_G}{\sigma_L}\right)^{0.447} \left(\frac{\mu_G}{\mu_{eff}}\right)^{0.694}$ a
Bern et al. [28]	H_2/fat	GSR	P: 0.12–0.14 MPa; T: 453 K; N: 3–12.5 Hz	$k_La = c \times \left(\frac{N^{3.15}d_T^{5.35}}{V_L^{1.81}}\right)^n U_G^m$ b
Matsumura et al. [24]	O_2, air/H_2O, various alcohols	SAR	Atm. N: 7–16.5 Hz; d_T: 0.218 m	$\frac{k_La}{\sqrt{D_{AB}}} = 309 \times \left(\frac{P^*}{V_L}\right)^{0.6} \varepsilon_G^{0.6}$
Joshi and Sharma [29]	CO_2/Na_2CO_3 + $NaHCO_3$	GIR	Atm. N: 3–11.7 Hz; U_G: 0.0003–0.032 m s^{-1}; P^*/V_L: 1–15 kW m^{-3}; d_T: 0.41–1.0 m	For $U_G < 0.005$: $k_La = 6.8 \times 10^{-3}\left(\frac{P^*}{V_L}\right)^{0.55} U_G^{0.5}$ For $U_G > 0.005$: $k_La = 3.26 \times 10^{-3}\left(\frac{P^*}{V_L}\right)^{0.55} U_G^{0.25}$
Lopes de Figueiredo and Calderbank [17]	O_2/water	GSR	Atm. N: 5–8 Hz; P_G:0.41–4.8 kW m^{-3}; U_G: 6–13 × 10^{-3} m s^{-1}; d_T: 0.91 m	$\frac{k_La V_L}{d_T} = 10^{-3} \times (P^*)^{0.58} U_G^{0.75}$
Matsumura et al. [30]	O_2, CO_2, CH_4/sodium sulfite, H_2O	GSR	Atm. N: 7–16.5 Hz; U_G: 0.5–10 × 10^{-3} m s^{-1}; d_T: 0.218 m	$\frac{k_La}{\sqrt{D_{AB}}} = 3.09 \times 10^2 \times \left(\frac{P^*_G}{V_L}\right)^{0.6} \varepsilon_G^{0.6}$
Kara [31]	H_2/tetralin SRCII	GIR	P: 7–13.5 MPa; T: 606–684 K; N: 0.8–6.6 Hz; d_T: 0.076 m	$k_La = (3.42 \pm 1.13) \times 10^{-4}\left(\frac{P^*}{V_L}\right)^{0.80\pm0.009}\left(\frac{H_L}{D_T}\right)^{-1.9\pm0.66}$
Sawant et al. [32]	Air/water + sodium sulfate	GIR	Atm. N: 5–36 Hz; d_T: 0.1 × 0.1–0.38 × 0.38 m	$k_La = 0.0195 \times \left(\frac{P^*}{V_L}\right)^{0.5}$
Judat [33]		GSR	–	$k_La = 9.8 \times 10^{-5}(B^{-0.6} + 0.81 \times 10^{-0.65/B})^{-1} \times \left(\frac{P^*}{V_L\rho_L(\mu_L g^4)^{1/3}}\right)^{0.4}\left(\frac{\mu_L}{\rho_L g^*}\right)^{-1/3}$ c
Albal et al. [25]	O_2/H_2O, CMC	SAR	Atm. N: 1.7–16.76 Hz; d_T: 0.1 m	$Sh = 1.41 \times 10^{-2} Sc^{0.5} Re^{0.67} We^{1.29}$
Karandikar et al. [34]	CO, H_2, CO_2, CH_4/F-T wax + water	GIR	P: 0.7–4.5 MPa; T: 423–498 K; N: 11.6–16.6 Hz; d_T: 0.13 m	$k_La_{CO,H_2} = 0.1607 \times (N/1000)^{3.42} \exp \times (0.108 \times P) - 0.046$ $k_La_{CO_2,CH_4} = 0.0171 \times (N/1000)^{6.05} \exp \times (0.38 \times P) + 0.00525$
Versteeg et al. [35]	CO_2, N_2O/H_2O, aq. alkanol-amine	SAR	P: 0.1–1.0 MPa; T: 291–356 K; Re: 0.2–1.2 × 10^4; Sc: 0.1–1.3 × 10^4	$Sh = 0.064 \times Sc^{0.5} Re^{0.72}$
Chang [36]	H_2,CO_2,CH_4/n-C_6, n-C_{10}, n-C_{14}	GIR	Eu: 0.5–1 × 10^4; Sc: 8–500; Re: 0.3–3 × 10^5, Fr^*: 1–3; We: 1–7 × 10^4	$Sh_{H_2} = 2.74 \times 10^{-18} Re^{3.00} Sc^{2.21} Eu^{-0.42} We^{1.29}$ $Sh_{CO,CH_4} = 5.114 \times 10^{-12} Re^{2.18} Sc^{1.63} Eu^{0.28} Fr^{*1.73}$
Hichri et al. [37]	H_2/2-propanol, o-cresol	GIR	Sh: 0.1–5 × 10^5; V_G/V_L: 1–2; Re: 0.7–13 × 10^4; Sc: 5–9 × 10^3; We: 2–6 × 10^3	$Sh = 0.123 \times Re^{0.44} Sc^{0.5} We^{1.27}\left(\frac{V_G}{V_L}\right)^{1.1}$
Dietrich et al. [38]	H_2/H_2O, ethanol, hydrogenation mixture	GIR	Atm. N: 14–33 Hz; d_T: 0.07 m	For $H/D_T = 1$: $Sh = 3 \times 10^{-4} Re^{1.45} Sc^{0.5} We^{0.5}$ For $H/D_T = 1.4$: $Sh = 1.5 \times 10^{-4} Re^{1.45} Sc^{0.5} We^{0.5}$
Koneripalli et al. [39]	H_2, CO, CO_2/methanol, ethanol	GIR	Eu: 0.3–10 × 10^3; We: 0.2–2 × 10^4; Sc: 7–200, Re: 0.6–4 × 10^5	$Sh = 4.88 \times 10^6 Re^{-3.81} Sc^{0.23} We^{4.48} Eu^{0.09}$

Table 2.5 Continued

References	Gas/liquid	Reactor	Operating conditions	Correlation
Mizan et al. [40]	H_2, C_2H_4/C_3H_6	SAR	Fr^*: 0.9–2.0; Re: 2–4.5 × 10^5; We: 741–31060	$Sh = 55.2 \times Fr^{*2.07} Re^{1.20} We^{-1.34}$
Heim et al. [20]	Air/water-fermentation mixture	GIR	Atm. Fr: 0.28–1.49; Re: 33–260 × 10^3; d_T: 0.3 m	$\frac{Sh^*}{9.5\times10^{-5}} = 1 - e^{-19.64 Re^{-0.216} Fr^{1.336}}$ d,e,f $\frac{Sh^*}{1.06\times10^{-4}} = 1 - e^{-21.63 Re^{-0.234} Fr^{1.207}}$ $\frac{Sh^*}{1.04\times10^{-4}} = 1 - e^{-1331.20 Re^{-0.557} Fr^{2.498}}$
Wu [41]	Air/H_2O + Na_2SO_3 + $CoSO_4$	SAR	Atm. P^*/V_L: 1.2–8.5 kW m^{-3}	$k_L a = 6.34 \times 10^{-2} \left(\frac{P^*}{V_L}\right)^{0.65}$
Yoshida et al. [42]	Air/water	GSR	Atm. N: 2.5–6.7 Hz; U_G: 0.004–0.06 m s^{-1}	$k_L a = 2.5 N^{1.5(1.7\times10^{-7})^{U_G}} 1.06^{n_{Imp.}} U_G^{1.29} n_{Imp.}^{0.10}$
Tekie [3]	N_2, O_2/cyclohexane	SAR; GIR	SAR; x_1: 6.67–20.0 Hz; x_2: 0.7–3.5 MPa; x_3: 330–430 K; x_4: 0.171–0.268 m; GIR; x_1: 6.67–20.0 Hz; x_2: 0.7–3.5 MPa; x_3: 330–430 K; x_4: 0.171–0.268 m	$Sh_{SAR} = 4.51 \times 10^3 We^{-0.21} Fr^{0.92}$ $\ln(k_L a_{SAR\text{-}N_2}) = -2.90 + 0.36x_1 + 0.07x_2 + 0.28x_3 - 0.18x_4 - 0.39x_1^2 - 0.06x_2^2 + 0.04x_3^2 + 0.063x_4^2 - 2.90e^{(-0.2(x_1-0.204)^2)} + 0.04e^{(0.1(x_1+3)(4-x_4))}$ $\ln(k_L a_{SAR\text{-}O_2}) = -2.93 + 0.11x_1 + 0.10x_2 + 0.23x_3 - 0.12x_4 - 0.38x_1^2 - 0.05x_2^2 - 0.03x_3^2 + 0.07x_4^2 - 2.90e^{(-0.173(x_1)^2)} + 0.11e^{(0.1(x_1+3)(4-x_4))}$ $\ln(k_L a_{GIR\text{-}N_2}) = 0.01 - 1.92x_1 + 0.10x_2 + 0.27x_3 - 0.05x_4 + 0.72x_1^2 - 0.10x_2^2 + 0.02x_3^2 + 0.01x_4^2 - 3.40e^{0.04(x_1-4.25)^2} + 0.27e^{0.1(x_1+3)(4-x_4)}$ $\ln(k_L a_{GIR\text{-}O_2}) = -3.71 + 1.23x_1 + 0.11x_2 + 0.22x_3 - 0.09x_4 + 0.09x_1^2 - 0.04x_2^2 + 0.01x_3^2 + 0.06x_4^2 - 3.75e^{-0.17(x_1-1.6)^2} + 0.21e^{0.1(x_1+3)(4-x_4)}$
Tekie et al. [43]	N_2, O_2/cyclohexane	GIR	We: 0.2–1 × 10^4, Fr^*: 1–3	$Sh_{GIR} = 4.51 \times 10^3 We^{-0.21} Fr^{*0.92} \times (1 + 1.867 \times 10^3 \varepsilon_G)$
Fillion [13]	N_2, H_2/soybean oil	GIR; GSR; SAR	GIR; x_1: 373–473 K; x_2: 10–23.3 Hz; x_3: 0.171–0.268 m; x_4: 0.1–0.5 MPa GSR; T: 373–473 K; N: 10–23.3 Hz; P: 0.1–0.5 MPa; U_G: 10.4–51.9 cm^3 s^{-1}; SAR; x_1: 373–473 K; x_2: 10–23.3 Hz; x_3: 0.171–0.268 m; x_4: 0.1–0.5 MPa	$\ln(k_L a_{GIR\text{-}N_2}) = -4.86 - 0.18x_1 + 0.71x_2 - 0.60x_3 + 0.08x_1^2 + 0.12x_2^2 - 0.23x_1x_2 - 0.08x_2x_3 - 0.34x_1x_2x_3 - 0.07x_1^3 + 0.0027 \times (x_2 + 2.5)e^{2x_3} + 1.28\tan h(0.3x_2(5.5 - x_3^2)) + 0.1(2 - 4x_3))$ $\ln(k_L a_{GIR\text{-}H_2}) = -3.87 + 0.52x_2 - 0.79x_3 + 0.22x_1^2 - 0.35e^{x_1} + 0.33e^{x_3} - 0.0038(x_2 + 3)e^{2.5x_3} - 0.93x_1e^{-\lvert x_2\rvert} + 2.10\tan h(0.3x_2(8 - x_3^2) + 0.1(2 - 6x_3))$ $k_L a_{GSR} = 1226 \times T\mu_L^{-0.10} D_{AB}^{0.62} \left(\frac{P_G^*}{V_L}\right)^{0.31} Q_G^{0.58}$ $\ln(k_L a_{SAR\text{-}N_2}) = -6.50 + 0.177x_1 + 0.474x_2 - 0.407x_3 + 0.053x_3^2 - 0.0798x_2x_3$ $\ln(k_L a_{SAR\text{-}H_2}) = -5.99 + 0.229x_1 + 0.417x_2 - 0.473x_3 - 0.0445x_1^2 + 0.0524x_3^2 - 0.126x_2x_3$

[a] $\mu_{eff} = \frac{\tau(\gamma_a)}{\gamma_a}$.
[b] $c = 0.326$, $n = 0.37 \pm 0.02$, $m = 0.32 \pm 0.10$, d_T (cm), U_S (cm s^{-1}), V_L (cm^3).
[c] $B = \frac{Q}{d_T^2} \times \left(\frac{P_*}{\mu_L g}\right)^{1/3}$.
[d] 4-pipe impeller.
[e] 6-pipe impeller.
[f] Disk impeller.

Morsi et al. [40] collected a large number of data points (7374) on the hydrodynamic and mass transfer parameters obtained in the laboratories and from the literature in ARs, covering various reactor sizes and operating conditions. These large data sets were used to develop a novel empirical and back-propagation neural network (BPNN) correlation, which was employed to construct a simple

algorithm for predicting these parameters under industrial conditions. Morsi et al. also noted that, although the developed algorithm appeared to be a useful tool for predicting the hydrodynamics and mass transfer parameters in ARs, the precision of such predictions could be further improved by diversifying and expanding the experimental data bank for large-scale reactors with various configurations and operating conditions.

Moreover Smith, Van't Riet, and Middleton [42] proposed the following general correlation for conventional, mechanically agitated reactors (SAR's) operating with coalescing systems:

$$k_L a = 0.01 \left[\frac{P_G}{V_L}\right]^{0.475} V_G^{0.4} \quad (\mathrm{s}^{-1}) \qquad [2.7]$$

where P_G (in Watt) is power consumption in the presence of gas, V_L (m^3) is total volume of liquid, and V_G (m/s) is superficial gas velocity. A good agreement, using the above empirical equation and experimental values of ± 25%, was obtained by Poncin et al. [43].

Schumpe et al. [37] and Treybal [44] proposed an experimental technique for measuring $k_L a$ for agitated systems using gas absorption (by surface aeration) of the solute gas in an initially degassed liquid or slurry. The measurement of the total pressure of the gas phase with respect to time as the absorption proceeded was utilized to determine the volumetric liquid-side, mass transfer coefficient $k_L a$. This technique has been previously utilized by Teramoto et al. [45] and Nam [46]. The equation obtained to directly measure $k_L a$ of the system takes the form:

$$\frac{P_2}{P_1} \ln\left[\frac{P_1 - P_2}{P - P_2}\right] = k_L a\,(t) \qquad [2.8]$$

where P_1 & P_2 are the initial and final equilibrium pressures, respectively; and P is the pressure of the system at time t. The mass transfer coefficient $k_L a$ is calculated from Eq. 2.8 by measuring pressure drop for the system as a function of time. The maximum errors calculated by Schumpe et al. (without accounting for the compensating errors) for the measurements of $k_L a$, equilibrium solubility, power consumption and gas holdup were found to be 3.5%, 1.3%, 7%, and 11%, respectively.

Garcia-Ochoa [47] proposed a predictive correlation, based on Higbie's penetration theory, widely accepted for the description of gas–liquid transfer [48]. For a non-stationary, gas–liquid interface, the contact or exposure time t_e for the mass transfer is related to the mass transfer coefficient by the expression:

$$k_L \left(\frac{m^2}{sec}\right) = 2\sqrt{\frac{D_L}{\pi\, t_e}} \qquad [2.9]$$

where D_L (m^2/s) is the gas diffusivity in the liquid phase, t_e (s) is given by Equation 2.10, and k_L is the mass transfer coefficient. The interfacial surface area a (1/m), is given as the ratio of the gas hold-up volume (Φ) to the average bubble diameter (d_p in m) as ($a = 6\Phi/d_p$)

It was determined by Lamont et al. [49] that k_L depends on the mixing intensity, expressed as a function of the dissipation energy, while the surface renewal rate was found to be higher than that for the bubbles in free rise under potential flow [50]. The experimental result also concluded that, at a microscopic level, the exposure time was affected by eddies or turbulence intensity. To characterize the time scale, the rate of dissipation of energy ε, defined as the energy in the liquid per unit mass, was utilized. The exposure time t_e was expressed using an adequate model to characterizes the residence time of micro-eddies at the interface. Using the Kolmogoroff's theory on isotropic turbulence, the

exposure time t_e was expressed as the ratio between two characteristic parameters of eddies, namely, the fluid density (ρ) and the kinematic viscosity (μ). For Newtonian media, the expression for the mass transfer coefficient reduces to:

$$k_L \left(\frac{m^2}{sec}\right) = 2\sqrt{\frac{D_L}{\pi}} \left[\frac{\varepsilon\,\rho}{\mu}\right]^{\frac{1}{4}} \qquad [2.10]$$

where

$$t_e = \left[\frac{\varepsilon\,\rho}{\mu}\right]^{1/2}$$

In order to determine k_L, the local energy dissipation rate ε near the interface needs to be estimated. Several correlations (as seen in Table 2.6) are indicated in the literature for calculating the volumetric mass transfer in single- and multiple-impeller systems, for various tank volumes, liquid fill level, impeller geometry, and for both Newtonian and non-Newtonian liquids.

Usually, k_La values are correlated by expression of the following form as expressed by Garcia-Ochoa [47]:

$$k_L a \left(\frac{1}{sec}\right) = C\, V_s^a \left[\frac{P}{V}\right]^b \mu^c \qquad [2.11]$$

In Eq. 2.11, the exponent values (a, b, and c) disagree appreciably in the different correlations proposed by several authors, as seen in Table 2.6. These differences can be attributed to the various tank configurations (vessel type, liquid fill level, agitator design, gas distribution system), the difference

in the liquid properties (density, surface tension, and viscosity), and the range of operating conditions studied [51] by these authors.

Table 2.6: Exponent values found by several authors on k_La for each variable in the dimensional correlations proposed in the literature [48]

System	Authors	N	P/V	V_s	μ_a	Volume (l)	Stirrer type
Newtonian	Yagi and Yoshida (1975)		0.8	0.3		12	6FBT
	Figueiredo and Calderbank (1979)	—	0.6	0.8	—	600	FBT
	Van't Riet (1979)	—	0.4	0.5	—	2–2600	Any
	Nishikawa et al. (1981)	2.4	0.8	0.33	—	2.65–170	FBT and FBP
	Chandrasekharan and Calderbank (1981)	—	0.55	$0.55D^{-1/2}$		50–1430	FBT
	Davies et al. (1985)		0.8	0.45		20–180	6FBT
	Kawase and Moo-Young (1988)		1.0	0.5			
	Linek et al. (1987)		0.6	0.4		20	6FBT
	Linek et al. (1991)		0.65	0.4		20	6FBT
	Gagnon et al. (1998)		0.6–0.8	0.5		22	6FBT
	Arjunwadkar et al.(1998)		0.68	0.58		5	FBT and PBT
	Vasconcelos et al. (2000)		0.62	0.49		5	Two-6FBT
Non-Newtonian	Yagi and Yoshida (1975)	2.2	—	0.3	−0.4	2.65	FBT and FBP
	Nishikawa et al. (1981)	2.4	0.8	0.3	−0.5	2.7–170	FBT and FBP
	Linek et al. (1991)	—	1.1	0.4	—	20	6FBT
	Pedersen et al. (1994)	2.7	—	0.5–0.7	—	15	Two-6FBT
	Garcia-Ochoa and Gomez (1998)	2.0	0.6	0.67	−0.67 to −1[a]	20	1,2-FBT, CBT, FBP, CBP, PBP
	Arjunwadkar et al. (1998)		0.68	0.4		5	FBT & PBT
	Garcia-Ochoa and Gomez (2001)	2.0	—	0.5	−0.67	2–25	FBT, CBT, BP, CBP
Prediction	This work	2.3	0.8	0.64	−0.5 to −0.9[a]		Turbines and paddles

Units: N (rps); P (W); V (m^3); V_s (m/s) and μ_a (Pa s)

Garcia-Ochoa [47] concluded that volumetric mass transfer coefficients can be predicted with reasonable accuracy, once the reactor characteristics are established, along with the physicochemical properties of the fluid. Based on Higbie's penetration theory, the proposed model has been examined, using experimental data and correlations available in the literature. A reasonable agreement has been obtained between both. The proposed model is capable of simulating the experimental data obtained in stirred tank reactors under a wide range of operating conditions, including very different vessel volumes and stirrer designs, for both Newtonian and non-Newtonian liquids.

2.6 Conclusion

Hydrogenation of halo-nitroaromatics to halo-anilines, using heterogeneous catalytic hydrogenation, is extremely common in the chemical industry, as the aniline product is an important chemical in the manufacture of dyes, antioxidants, fine chemicals, and pharmaceutical intermediates. Such reactions have been extensively studied since the 1950s to understand catalyst behavior and reaction rates critical for large-scale production. Although hydrogenation of nitrobenzene has been studied in a wide range of conditions, its effect on heat and mass transfer has not been fully elucidated.

The reduction of nitroaromatics to amine is a highly exothermic process, the heat of reaction being 545-kJ/mol (or 130-kcal/mol). In recent years, it has become evident that its intermediates can have a significant bearing on process hazards, partially, as a consequence of an explosion in the United States during the catalytic reduction of chloronitrobenzene, which was attributed to runaway decomposition initiated by exothermic disproportionation of the hydroxylamino intermediate. The risk of thermal explosion, or time to a maximum rate under adiabatic conditions (TMR_{ad}), can be estimated by the formula published by Townsend and Tou [16].

Studer et al. [24] showed that, with vanadium promoters, the hydroxylamine accumulation and the rate in the RNi-catalyzed hydrogenation of nitroarenes can be both increased or decreased. Modifiers which are able to reduce accumulation always show some deactivation of the catalysts, most likely, through the poisoning of the hydrogenation sites. It was found that modifiers, which increased the overall rate of the reaction, also led to higher hydroxylamine accumulation. The hydroxylamine accumulation can be reduced from ~ 70% to < 20% for various substrates. The vanadium modifiers were shown to work as disproportionation catalysts for CHB. It was necessary to screen modifiers for each substrate to find the optimal effect. The storage, pre-treatment, and the sequence of catalyst addition must be carefully controlled in order to guarantee reproducibility. It is vital to understand the

effect of modifiers for the current hydrogenation, along with operating conditions to minimize the amount of hydroxylamine formation during the course of the reaction.

Reaction kinetic models were proposed by various authors and found to be either zero or first order in nitro aromatic. The reaction rate was found to be the function of a solvent system, with rates increasing with solvent polarity. Agitation rates, hydrogen pressure, catalyst loading, and temperature were also assessed and were in agreement by several authors. Out of several proposed kinetic models, the Langmuir-Hinshelwood rate form (proposed by Stefoglo et al. [27] and other authors) was found to be in close agreement with measured data.

Gas-liquid mass transfer coefficients were calculated using several empirical equations and were found to be in reasonable agreement (± 25%) with measured values; however, the method proposed by Schumpe et al. [37] was found to be most accurate for measuring k_La (± 4-6%). The method described by Schumpe et al. [37] has been adopted in this thesis for accurate measurement and calculation of k_La for gas-liquid systems and will be explored to elucidate the reaction mechanism with respect to heat and mass transfer for such reacting systems.

The primary focus of this research is a full understanding of the reaction mechanism for a halo-nitroaromatic reduction to halo aniline. Understanding the reaction mechanism will further elucidate the effects of heat and mass transfer rates on the formation of various intermediate species. This is essential for controlling the concentration of highly energetic intermediates, such as hydroxylamine. The maximum concentration of hydroxylamine accumulation for a safe scale-up of the process depends upon the heat removal rate of the plant reactor; and therefore, a control mechanism must be in place in order to prevent a thermal runaway. Another impurity of concern is the dehalogenated impurity formed during the reduction. Such impurities are reported in the literature; but, there is a lack of mechanistic understanding for their formation.

Another key focus is the choice of catalyst from several commercially available catalysts for these types of hydrogenation reactions. As precious metals have various metal distribution profiles, such as egg-shell or uniform distribution, the reactivity and selectivity can be markedly influenced by the catalyst choice. Also, depending upon the metal distribution profile, gas-liquid mass transfer can significantly impact the reaction rates. Catalyst poisoning, i.e., loss in catalyst activity over the course of the reaction, is a key concern for such reactions. A mathematical model is postulated to estimate catalyst activity during the reaction course. This model will elucidate catalyst activity and postulate a new method for assessing catalyst poisoning for such reactions.

The mass transfer coefficient (k_La) is a key for all heterogeneous catalytic reactions. One needs to understand the criteria to scale k_La from lab-scale to plant-scale reactors. Mass transfer coefficients vary widely from reactor to reactor, based on the reactor geometry, agitation types, speed of agitation, liquid fill level, and pressure in the reactor. Also, evaluating k_La for a reactive system is a tedious task, as the reaction and mass transfer coefficient must be separated out at various scales. A generic, non-reactive model for evaluating k_La will be postulated to evaluate k_La at all scales, which can be applied to all reactions without the need to evaluate k_La for each reactive system.

Another key aspect of this research is the focus on elucidating the reaction mechanism using kinetic rate law equations. Such a reaction exhibits a complex mechanism, and various reaction conditions yield to various mechanistic pathways, as shown in Figure 2.1. Understanding the rate-limiting step and the saturation state of the catalyst can also aid in understanding the stability of the catalyst system. Observed reaction kinetics will also highlight the relationship between intrinsic kinetics and mass transfer rates for control of energetic intermediates, as well as impurities for the reactive system. A full scale-up model is developed for the reduction of a halo-nitro aromatic to halo-aniline compound.

References

1 J. McMurry, Organic Chemistry, Brooks/Cole Publishing Company, Monterey, Calif., 1984, p. 961-968.

2 F. Haber, Z. Elektrochem. Angew. Phys. Chem., 1898, Vol. 22 (4), p. 506-511.

3 H. Debus and J. C. Jungers, Reduction of Nitrobenzene, Bull. Soc. Chim. Fr., 1959, p. 785-793.

4 A. M. Stratz, Catalysis of Organic Reactions, Chem. Ind. (Marcel Dekker), 1984, Vol. 18, p. 335-337.

5 G. S. Samuelsen, V. L. Garlc, and G. B. Smith, The Hydrogenation of Nitro compounds with Raney Nickel Treated with Chloroplatanic Acid and with Alkali, J. Am. Chem. Soc., 1950, Vol. 72 (9), p. 3872-3874.

6 S. S. Scholnik, J. R. Reasenberg, E. Leiber, and G. B. L. Stein, The Promoter Effect of Platinic Chloride on Raney Nickel. III. Hydrogenation of the Nitrobenzoic Acids and the Nitrobenzene-Aniline Intermediates, J. Am. Chem. Soc., 1941, Vol. 63 (5), p. 1192-1193.

7 H. C. Yao and P. H. Emmett, Kinetics of Liquid Phase Hydrogenation. IV. Hydrogenation of Nitrocompounds over Raney Nickel and Nickel Powder Catalysts J. Am. Chem. Soc., 1962, Vol. 84, p. 1086-1091.

8 A. Metcalfe and M. W. Rowden, Hydrogenation of nitrobenzene over palladium-silver catalysts, J. Catal., 1971, Vol. 22 (1), page 30-34.

9 A. D. Shebaldova, V. N. Krawtsova, T. A. Bolshinkova, E. V. Selyaeva, and M. L. Khldekel, Nitrobenzene Reduction, Russian Chemical Bulletin, 1975, Vol. 24 (7), p. 1556-1557.

10 H. D. Burge, D. J. Collins, and B. H. Davis, Intermediates in the Raney Nickel Catalyzed Hydrogenation of Nitrobenzene to Aniline, Ind. Eng. Chem. Prod. Res. Dev., 1980, Vol. 19 (3),

p. 389-391.

11 J. Wisniak et al., Reduction of nitrobenzene to aniline, Ind. Eng. Chem. Prod. Res. Dev., 1984, Vol. 23 (1), p. 44–50.

12 J. I. Macnab, The Role of Thermochemistry in Chemical Process Hazards: Catalytic Nitro Reduction Process, I. Chem. E. Symposium Series, 1981, No. 68.

13 F. Stoessel, Experimental study of thermal hazards during hydrogenation of nitroaromatics; J. Loss. Prev. Process Ind., 1993, Vol. 6 (2), p. 79-85.

14 W. R. Tong, R.L. Seagrove, and R. Wiederhorn, 3-4-Dichloroaniline Autoclave Incident, AIChE Loss Prev., 1977, Vol. 11, p. 71-75.

15 P. Cardillo, A. Quattrini, E. Vanjna de Pava, and A. Girelti, Reduction of Amines, J. Calorim. Anal. Therm. Thermodyn. Chim., 1986, Vol. 17, p. 394-397.

16 D. I. Townsend and J. C. Tou, Thermal Hazard Evaluation by an Accelerating Rate Calorimeter, Thermochimica Acta, 1980, Vol. 37, p. 1-30.

17 R. S. Downing, P. J. Kunkeler and H. van Bekkum, Catalytic syntheses of aromatic amines, Catal. Today, 1997, Vol. 37 (2), p. 121-136.

18 P. Baumeister, H. -U. Blaser and M. Studer, Strong reduction of hydroxylamine accumulation in the catalytic hydrogenation of nitroarenes by vanadium promoters, Catal. Lett., 1997, Vol. 49, p. 219-222

19 J. A. Miller, Carcinogenesis by chemicals, Cancer Res., 1970, Vol. 30 (3), p. 559-576.

20 J. R. Kosak, in Catalysis of Organic Reactions, Marcel Dekker, New York, 1988, Chp. 18, p. 135-138.

21 U. Birckenstock, B. Lachmann, J. Metten and H. Schmidt, DE2849002 (1978)

22 K. Halcour, W. Schwerdtel and W. Swondenk, DE2519838 (1975)

23 H. Thelen, W. Schwerdtel, K. Halcour and W. Swondenk DE2214056 (1972), assigned to Bayer AG.

24 M. Studer, S. Neto, and H. -U. Blaser, Modulating the hydroxylamine accumulation in the hydrogenation of substituted nitroarenes using vanadium-promoted RNi catalysts, Topics in Catalysis, 2000, Vol. 13, p. 205–212.

25 R. V. Chaudhari, M. S. Kulkarni, M. J. Vaidya, M. J., Synthesis of p-Aminophenol by Catalytic Hydrogenation of p-Nitrophenol, Organic Process Research & Development, 2003, Vol. 7, p. 202-208.

26 R. Rajadhyaksha and S. Karwa, Solvent effects in catalytic hydrogenation, Chem. Eng. Sci., 1986, Vol. 41 (7), p. 1765-1770.

27 E. F. Stefoglo, O. P. Zhukova, I. V. Kuchin, The influences of the gas rate dissolution and mass-transfer limitation at the interfaces on selectivity of gas–liquid processes in stirred reactors with a suspended catalyst, Catalysis Today, 2001, Vol. 66, p. 397–402.

28 E. Crezee, B. W. Hoffer, R. J. Berger, M. Makkee, F. Kapteijn, and J. A. Moulijn, Three-phase hydrogenation of D-glucose over a carbon supported ruthenium catalyst – mass transfer and kinetics; Applied Catalysis A: General, 2003, Vol. 251, p. 1-17.

29 F. Turek, R. K. Chakrabarti, R. Lange, R. Geike, and W. Flock, On the experimental study and scale-up of three-phase catalytic reactors: Hydrogenation of glucose on nickel catalyst, Chem. Eng. Sci., 1983, Vol. 38 (2), p. 275-283.

30 N. Déchamp, A. Gamez, A. Perrard, P. Gallezot, Kinetics of glucose hydrogenation in a trickle-bed reactor, Catalysis Today, 1995, Vol. 24, p. 29-34.

31 P. H. Brahme and L. K. Doraiswamy, Modeling of a slurry reaction. Hydrogenation of glucose on Raney nickel, Ind. Eng. Chem. Process Des. Dev., 1976, Vol. 15 (1), p. 130-137.

32 J. Wisniak, R. Simon; Hydrogenation of glucose, fructose, and their mixtures, Ind. Eng. Chem. Prod. Res. Dev., 1979, Vol. 18, p. 50-57.

33 J. B. Joshi, A. B. Pandit, and M. M. Sharma, Mechanically agitated gas-liquid reactors, Chem. Eng. Sci., 1982, Vol. 37, p. 813 - 844.

34 R. Fuches, D. D. Ryu, and A. E. Humphrey, Effect of surface aeration on scale-up procedures for fermentation processes; Ind. Eng. Chem. Process Des. Dev., 1971, Vol. 10 (2), p 190-196.

35 H. H. Topiwala, J. Ferment. Technol., Surface aeration in a laboratory fermenter at high power inputs, 1972, Vol. 50, p. 668-675.

36 J. A. Wiedmann, A. Steiff, and P. M. Weinspach, Chem. Eng. Commun., Experimental investigations of suspension, dispersion, power, gas hold up, and flooding characteristics in stirred gas-liquid-solid systems (slurry reactors), 1980, Vol. 6 (4), p. 245-256.

37 A. Schumpe, Y. T. Shah, and R. S Albal, Mass transfer in multiphase agitated contractors, The Chemical Engineering Journal, 1983, Vol. 27, p. 61-80.

38 M. Matsumara, H. Masunga, and J. Kobayashi, J. Ferment. Technol., 1979, Vol. 57, p.107-112.

39 P.L. Mills, R.V. Chaudhari, Reaction engineering of emerging oxidation processes, Catalysis Today, 1999, Vol. 48, p.17–29.

40 B. I. Morsi, and R. Lemoine, An algorithm for predicting the hydrodynamic and mass transfer parameters in agitated reactors, Chemical Engineering Journal, 2005, Vol. 114, p. 9–31.

41 A. Behkish, R. Lemoine, L. Sehabiague, R. Oukaci and B.I. Morsi, Prediction of the gas holdup in industrial-scale bubble columns and slurry bubble column reactors using back-propagation neural

networks, International Journal of Chemical Reactor Engineering, 2005, Vol. 3, p. 53-57.

42 J. M. Smith, K. Van't Riet, and J, C. Middleton, Scale-up of agitated gas–liquid reactors for mass transfer, Proceedings of the second European conference on mixing, Cambridge, UK, 1977, Vol. F4, p. 51–66.

43 S. Poncin, C. Nguyen, N. Midoux, and J. Breysse, Hydrodynamics and volumetric gas–liquid mass transfer coefficient of a stirred vessel equipped with a gas-inducing impeller; Chemical Engineering Science, 2002, Vol. 57, p.3299 – 3306.

44 R. E. Treybal, Mass Transfer operation, McGraw-Hill, 1980, New York, N.Y.

45 M. Teramoto, S. Tai, K. Nishi, and H. Teranishi, Effects of pressure on liquid-phase mass transfer coefficients, Chem. Eng. J., 1974, Vol. 8, p. 223-226.

46 N. D. Nam, The oxidation of ethylene on a supported silver catalyst in a liquid phase, Thesis, University of Ottawa, Ottawa, 1975.

47 F. Garcia-Ochoa, and E. Gomez, Theoretical prediction of gas–liquid mass transfer coefficient, specific area and hold-up in sparged stirred tanks; Chemical Engineering Science, 2004, Vol. 59, p. 2489 – 2501.

48 Y. Kawase, B. Halard, and M. Moo-Young, Theoretical prediction of volumetric mass transfer coefficients in bubble columns for Newtonian and non-Newtonian fluids, Chemical Engineering Science, 1987, Vol. 42, p. 1609–1617.

49 J. C. Lamont and D. S. Scott, An Eddy cell model of mass transfer into the surface of a turbulent liquid, A.I.Ch.E Journal, 1970, Vol. 16, p. 513–519.

50 L. M. Figueiredo and P. H Calderbank, The scale-up of aerated mixing vessels for specified oxygen dissolution rates, Chemical Engineering Science, 1979, Vol. 34, p. 1333–1338.

51 F. Garcia-Ochoa and E. Gomez, Mass transfer coefficient in stirrer tank reactors for xanthan solutions, Biochemical Engineering Journal, 1998, Vol. 1, p. 1–10.

CHAPTER 3: CATALYST SELECTION

3.1 Introduction

Catalysts play a vital role in the hydrogenation of nitroaromatics. Heterogeneous reactions can be limited by mass transfer or kinetic control, depending upon the catalyst used or the reaction conditions. Different reaction regimes can give rise to various intermediates and impurities, as shown in Figure 2.1. Precious metals, such as palladium or platinum are deposited on the support structure, i.e. carbon, during the catalyst preparation process. Supported catalysts allow for the fine dispersion of precious metal on their surfaces. The support type varies widely in the chemical industry, ranging from carbon, aluminum, and bismuth, among which, carbon is the most commonly used support type for such organic reactions [1].

Three types of carbon are typically used as supports for the precious metal: activated carbon, carbon black, and graphite [2-3]. Activated carbon is the most widely used support type due to its high surface area. The raw materials used for the manufacturing of activated carbon are derived from wood, coal, lignite, coconut shell, and peat, although, other materials, such as fruit pits and synthetic polymers are also used. Chemically-activated carbons are produced by simultaneously carbonizing and activating raw material at 600-800°C. Typically, phosphoric acids or zinc chlorides are used as activating agents in the raw material prior to heating. Steam-activated carbon utilizes decomposition of raw materials at 600-800°C in the absence or addition of air at a controlled rate [1]. The activation step is then performed in the presence of steam or CO_2 at 800-1100°C. The physical and chemical properties of activated carbon vary widely due to the various types of raw materials, activating agents and processes used in its manufacture.

Precious metals, such as palladium or platinum on carbon, are the most commonly used metals for nitro reductions [4]. The two most commonly available types of metal dispersions are uniform and egg-shell type. Metal deposited at the external particle surface results in an egg-shell catalyst, whereas, metal deposited throughout the carbon support produces uniform catalysts. Metal deposition can be controlled during the impregnation stage for strongly adsorbed metal, resulting in a uniform catalyst, or during the drying stage for weakly adsorbed metals [5].

Figure 3.1 shows various metal deposition patterns onto the carbon support. Egg-shell catalysts typically enhance the selectivity of intermediates of consecutive, irreversible, or diffusion-limited reactions. Egg-yolk catalysts are advantageous for reactions in which diffusion limitation increases the reactivity and selectivity for the reaction. Egg-white catalysts are typically used for a reaction that favors kinetic limitation but can be prone to metal poisoning when deposited onto external surfaces. For example, egg-yolk catalysts are reported to have best activity for CO oxidation over Pt at low Thiele modules [6], whereas the egg-white catalyst was shown to be optimal under kinetic control regime [7]. Uniform catalysts are the best choice for reactions subject to diffusion limitation, and the catalyst is not easily poisoned under the reaction conditions [8, 9, 10, 11, and 12]. The choice of optimal metal support is determined by the required selectivity, activity, and chemical kinetics of the desired reaction. In general, for catalytic hydrogenations, both carbon support and metal type, along with deposition profile of the metal, play a key role in reaction kinetics.

Catalysts were purchased from two commercial vendors for evaluation: Johnson Matthey and Evonik Industries. A set of forty-eight such catalysts were commercially available to choose from for the current hydrogenation example. In this chapter, a high-throughput screening methodology is employed to narrow the catalyst selection from forty-eight to one. Catalysts characteristics differed as follows: the precious metal type (Pd or Pt); the percent metal loading on the support (5 wt%, 10 wt% or 20 wt%); support type (activated carbon from various raw materials); and the metal distribution on the

support (egg-shell, egg-yolk, egg-white, or uniform). As catalyst manufacturers seldom reveals the various characteristics of such catalysts (due to intellectual property claims and competitiveness), all forty-eight available catalysts were screened to find the optimum catalyst. In section 3.5 below, the characterization of the chosen catalyst using chemisorption and physisorption techniques, is described.

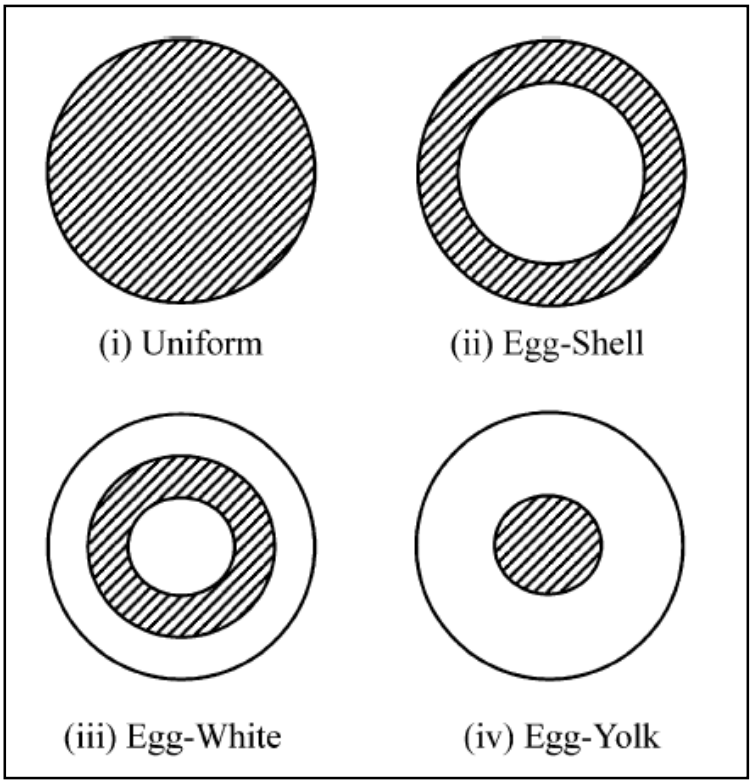

Figure 3.1: Main types of precious metal distribution on carbon support [1]

3.2 High-Throughput Screening Equipment

The high-throughput catalyst screening equipment consisted of a pressurized metal block with 96-well plates. See Figure 3.2 for details. The reaction block [13] was purchased from the HEL group in the UK, and equipped with fully automated controls for temperature and pressure inside the block with a magnetic plate that rotates the magnetic stir bar placed inside each vial, at a fixed speed of 700 rpm. The pressure block is rated for 100 barg (bar gauge pressure) at 150°C. Using the electrical

heater, the metal block can be heated to achieve the desired temperature; however, it can only be air cooled by convection. The reactor block is pressurized by two solenoid valves, which are hooked to the nitrogen and hydrogen gas supply lines, respectively. The reaction block is also equipped with a pressure relief valve, set at a maximum pressure of 110 barg. A specialized, 2-ml HPLC glass vial, rated at 20 barg, is placed in each well, which acts as a single reactor. The reaction mixtures containing various catalysts were added to each vial and placed inside each of the 48 wells. These vials were then crimped capped and a small puncture was made in the septa of the crimped vials to enable the flow of gas inside the vial for the reaction to commence. All of the magnetic stir bars inside the vials were stirred at a constant speed of 700 rpm (single speed), and maintained at the desired temperature and pressure for the reaction.

3.3 Materials and Reagents

High-purity hydrogen and nitrogen gas cylinders (purity of 99.999%) purchased from Airgas Inc., were connected to the high-throughput screening reaction block. The starting material, nitroaromatic [A] in Figure 2.1, is an advanced intermediate prepared by GlaxoSmithKline. Concentrated hydrochloric acid (HCl) was purchased from Sigma-Aldrich Co., with an assay of 37% HCl. Solvents used for the process; ethanol (200-proof) and distilled water were also purchased from Sigma-Aldrich. Forty-eight different catalysts were used, primarily from the two vendors: Evonik Industries and Johnson Matthey. The properties of these catalysts were considered proprietary information, which the vendors did not reveal. Out of the 48 catalysts, thirty five were single-metal catalysts (25 Pd and 10 Pt); and thirteen were bimetallic catalysts (8 bimetallic with platinum and another metal, and 5 bimetallic catalysts with palladium and another metal) which were chosen for screening. The metal composition for both single and bimetallic catalysts varied from 2.5 wt% to

20 wt% metal loading. High-performance liquid chromatography (HPLC) grade water and acetonitrile were used as mobile phases for the HPLC analysis.

48-vial tray

Reactor block

HEL Cat 96 system

Computer controls

Figure 3.2: HEL Cat 96 Reaction Block

3.4 Procedure

The method used to identify the catalyst that would meet the desired reactivity and selectivity for the reaction is described in the following section. Then, the desired catalyst was further characterized by Quantachrome Autosorb instrument to understand its chemical and physical properties.

3.4.1 Reaction Set-up

In a 2-mL HPLC vial, 50 mg of halonitroaromatic [A] was charged with 280-µL of 200-proof ethanol, 300-µL of distilled water, and 39-µL of concentrated hydrochloric acid. Five milligrams (10 wt% loading by weight) of catalyst were added to the individual vial. A magnetic stir bar was then inserted into the vial before the vial was crimped capped. Forty-eight [14] such vials, containing the same reaction solution but different catalysts, were prepared. Once all of the reaction vials were crimped capped, a small puncture was made in the septa of the vial to enable the flow of gas inside the vial for the reaction to commence. The vials were then inserted into the well plate, and the reactor block was sealed. The reaction block was set to the desired temperature of 25°C and a stirring speed of 700 rpm. Using nitrogen gas, a pressure check was performed at 60 psig to ensure that there were no leaks from the block. Upon passing the pressure check, the reactor was pressurized with nitrogen and held at 30-psig for two minutes, at which time it was vented to the atmosphere to release the pressure. This procedure was repeated twice to ensure that the headspace was free of oxygen. During the pressure purge cycle the agitation was turned off. The reaction block was then purged twice with hydrogen at 60 psig to evacuate nitrogen from the head space in a similar manner, after which the block was again pressurized with hydrogen to 60 psig and stirred at 700 rpm for approximately 7 hours at 25°C. The reaction block was then vented to the atmosphere and pressure purged twice with nitrogen to evacuate hydrogen from the reactor headspace prior to pulling HPLC samples. The vials were then un-crimped and analyzed by HPLC for reaction completion.

3.4.2 HPLC Method and Analysis

Reaction mixtures were analyzed by HPLC for the extent of conversion and impurity formation. An Agilent 1200 series diode-array detector was used for analysis. A Sunfire C18 column (4.6 mm X 150 mm) with 3.5 micron porosity was purchased from Water Corp., and used for peak separation.

Water and acetonitrile in a 30:70 ratio was used as the mobile phase. The temperature of the column was set to 30°C, and a flow rate of 1.5 mL/min was chosen for the analysis. Sample preparation consisted of 0.5 mg sample diluted in 1 mL of acetonitrile with an analysis time of 20 minutes. The optimum region was found to be at 245 nm wavelength number. The retention times for the product, des-F impurity (refer to Figure 2.1) and the starting material were found to be 7.44, 7.75, and 9.24 minutes respectively. A typical HPLC chromatogram is shown in Figure 3.5. Other impurities observed in the chromatogram, were easily purged during the crystallization of the product and were not considered critical for analysis purposes.

3.4.3 Catalyst Characterization

The chosen catalyst, E101NE/W, was classified as an eggshell catalyst by Evonik Industries. Eggshell catalyst is characterized by metal deposition on or near the surface of the catalyst rather than being evenly distributed among the catalyst particles. Such catalysts do not have intra-particle mass transfer issues, as the reaction takes place on or near the surface of the catalyst, and the intraparticle diffusion mechanism is absent [7]. Catalyst characterization was performed by using an Autosorb automated gas sorption system (1-C), purchased from Quantachrome Instruments [15]. The Autosorb equipment consisted of a sample preparation area and an analysis station. It was also connected to the helium, nitrogen, and hydrogen gas supply lines. The Autosorb analysis station was also connected to a high-performance vacuum pump and a mass spectrometer for off-gas analysis. The system was fully automated and was computer controlled. See Figure 3.3 and Figure 3.4 for schematic details of the system.

3.4.3.1 Physisorption Analysis

Physisorption is a process by which gas molecules are adsorbed onto a solid surface, usually performed at cryogenic temperatures. The molecules rely on Van-der Waals forces of attraction, to

form a thin layer that covers the entire adsorbent surface. Based on the well-known Brunauer, Emmett and Teller (B.E.T.) theory, the total number of molecules N_m required to cover the adsorbent surface with a monolayer of adsorbed molecules can be calculated. Multiplying N_m by the cross-sectional area of an adsorbate molecule results in the total sample surface area [16]. The pores become filled with adsorbate molecules as the equilibrium adsorbate pressure reaches saturation. The total pore volume of the sample can be estimated by the density of the adsorbate and the total volume which is occupied.

The catalyst samples were outgassed at 300°C for at least one hour before nitrogen physisorption measurements were taken. The results for the surface area and total pore volume for several lots of catalysts are summarized in Table 3.3.

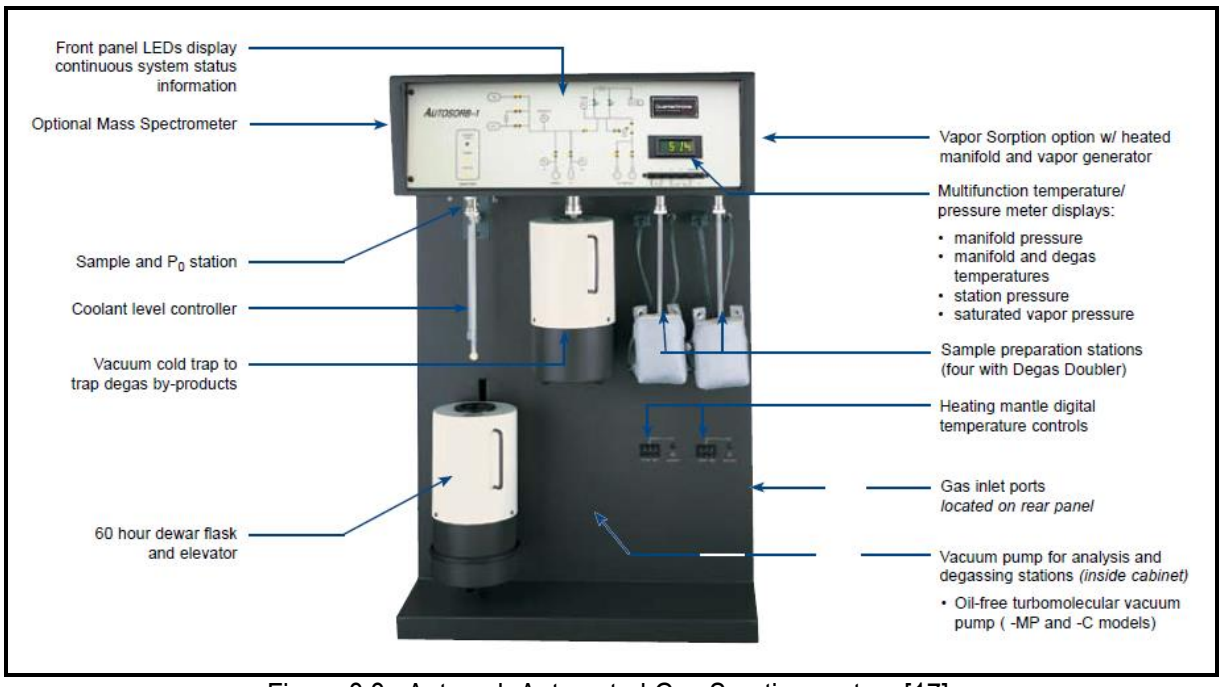

Figure 3.3: Autosorb Automated Gas Sorption system [17]

3.4.3.2 Chemisorption Analysis

The aim of chemisorption experiments is to determine the number of active sites present on a given sample. In practice, what is measured is the sample's chemisorption capacity at different adsorbate pressures, from which one can estimate the volume of adsorbate needed to form a monolayer of chemisorbed gas (*V_m in cc/g*). Based on reasonable assumptions, the active surface area (ASA in m^2/g), the percent dispersion (D) and the average crystallite size (d) [17] can be calculated using V_m. For H_2 chemisorption measurements, the catalyst was dried at 120°C and then reduced with hydrogen at 400°C. The sample was then cooled down to 25°C prior to chemisorption analysis. Then, a preselected amount of hydrogen gas was sequentially added to the sample. Thus, adsorbed volume (*V*) versus equilibrium pressure (*P*) isotherm was generated. The monolayer volume V_m can be estimated from Equation 3.1 [17]:

$$\frac{1}{V}\left(\frac{g}{cc}\right) = \frac{1}{V_m} + \frac{1}{V_m\,[\,P^{\left(\frac{1}{S}\right)}]\;K_C} \qquad [3.1]$$

where *S* is the adsorption stoichiometry (assumed two Pd atoms per H_2 molecule), and K_c is the adsorption equilibrium constant (adsorption/desorption). A plot of *1/V* vs. *$1/P^{(1/S)}$* results in the values of the inverse of the monolayer volume V_m (as the y-intercept). Pressure is defined in mm of Hg. The monolayer uptake N_m is then calculated from V_m, as shown in Equation 3.2 [17]:

$$N_m(\mu mol/g) = 44.61\,V_m\ (\mathrm{cc/\ g}) \qquad [3.2]$$

For the supported metal catalysts, it is vital to know the fraction of active metal atoms exposed. The metal dispersion (D), defined as the fraction of metal atoms found on the surface of active metal

particles, is expressed as a percentage of all active metal atoms present in the sample, and its value is calculated from N_m ($\mu mol/g$), as shown in Equation 3.3 [17]:

$$D\ (\%) = \frac{N_m\ S\ M}{L}\ (100) \qquad [3.3]$$

where M and L are the molecular weight (g/mol) and fraction loading (0-1) of the supported metal, respectively. The active surface area (ASA) and the average crystallite size (d in $°A$) can be calculated using Equations 3.4 and 3.5, respectively [17]:

$$ASA\ \left(\frac{m^2}{g}\right) = \frac{N_m\ S\ A_m}{166} \qquad [3.4]$$

$$d\ (°A) = \frac{100\ L\ f}{ASA\ \ Z} \qquad [3.5]$$

where 'A_m' (m^2) is the cross-sectional area occupied by each active surface atom; *S* is the adsorption stoichiometry, 'f' is the particle shape factor (~6 for spheres); and 'Z' is the density of the support (i.e. Carbon).

Figure 3.4: Quantachrome Autosorb Catalyst Characterization Equipment

3.5 Results and Discussion

The various catalysts screened will be discussed below, in terms of their performances for reactivity and selectivity. The physical and chemical property for the chosen catalyst will be further discussed herein.

3.5.1 Catalyst Selection

The results of the 48 catalysts, with respect to aniline formation (product) and des-F impurity [I] formation, are shown in Table 3.1 and Figure 3.6. Figure 3.6 shows a plot of percent aniline (product) on the y-axis and the percent des-F (impurity) on the x-axis. The screening data in Figure 3.6 is visualized in Spotfire [18], where the spread of the result is apparent, ranging from 0-100% conversion and des-F ranging from 0-0.6%. In the figure, the primary metal was colored blue for Pd and red for Pt, and the catalysts were labeled by manufacturer's reference (Manf Ref.) numbers. This experiment was performed twice to confirm the results, which were found to be reproducible with a standard deviation of 0.14% for the product formation, 0.01% for the des-F formation, and with an instrument variability of 0.01%. To narrow the catalyst choice, selection criteria were arbitrarily set for the desired conversion of > 96% of product formation (aniline) and < 0.25% of des-F impurity formation. The plot in Figure 3.6 gives the overall performances of the product formation versus des-F, for the various catalysts screened. Figure 3.7 is drawn with des-F on a reverse scale on the x-axis, with catalysts meeting > 96% aniline formation on the y-axis. The plot shows that, out of the 48 catalysts screened, only nine met the selection criteria (as shown in Table 3.2).

Further, out of the nine catalysts, only one catalyst (E101 NE/W) was chosen for further development, primarily due to the cost and availability of that catalyst required for the scale-up studies. Table 3.2 and Figure 3.7 also indicate that all the catalysts that met the selection criteria contained palladium as their precious metal type. Additionally, there was only one platinum metal catalyst (CF1082BV/W) that was in top 20; however, it resulted in an incomplete reaction. This outcome contradicts the findings in the literature [19-20] that indicates platinum is superior when compared to palladium for selectively reducing the halonitroaromatic to its respective halo-amino aromatic. This could be due to the acidic environment under which the reaction is run, which is known to cause excessive and uncontrollable dehalogenated byproducts [21]. Also, from the information available from

these vendors Evonik Industries and Johnson Matthey, the nine catalysts that met the criteria were either egg-shell or uniform catalysts, indicating that the metal distribution was not significant. Utilizing the high-throughput screening technique narrowed the catalyst choice from forty-eight catalysts to one, expediting the catalyst selection with minimal time and resources.

Analysis Details

Injection date: Mon, 29. Jun. 2009 at 11:08:02
Vial position: Vial 94
Raw data file: C:\HPCHEM\1\DATA\OPEN_ACC\29061106.D
Method: C:\HPCHEM\1\METHODS\917_HPLI.M
Sample reference: Vial 4
Sample identity: 6.5 hrs 5baraH2

Results

Signal 1: DAD1 A, Sig=245,8 Ref=off

Peak #	RT (min)	Width (min)	Height	Area	Area %
1	5.28	0.035	1.876	4.312	0.08
2	5.79	0.037	5.419	12.808	0.23
3	5.94	0.039	4.473	11.264	0.20
4	6.85	0.040	0.405	1.060	0.02
5	6.95	0.083	0.216	1.207	0.02
6	7.31	0.058	0.420	1.736	0.03
7	7.44	0.042	1938.141	5333.336	96.48
8	7.55	0.061	9.440	41.805	0.76
9	7.75	0.094	1.799	12.663	0.23
10	7.92	0.068	0.816	4.040	0.07
11	8.04	0.089	1.151	7.743	0.14
12	8.30	0.082	0.932	5.608	0.10
13	8.50	0.069	0.451	2.190	0.04
14	8.97	0.052	0.209	0.741	0.01
15	9.24	0.048	2.557	8.116	0.15
16	9.38	0.051	0.839	2.980	0.05
17	9.55	0.043	6.451	17.726	0.32
18	9.61	0.043	2.582	7.455	0.13
19	9.75	0.050	1.099	3.658	0.07
20	10.12	0.053	0.389	1.337	0.02
21	10.26	0.049	2.447	7.794	0.14
22	11.19	0.046	10.199	30.193	0.55
23	11.97	0.055	0.196	0.692	0.01
24	12.40	0.051	1.660	5.367	0.10
25	13.04	0.163	0.156	1.861	0.03

Figure 3.5 HPLC chromatogram result for E 101NE/W catalyst (Reaction Completion)
RT (mins) – 7.44 (product); 7.75 (des-F impurity); and 9.24 nitroaromatic (starting material)

Table 3.1: Catalyst Screening Results for all forty-eight catalysts

Vial #	% Aniline	% Des-F aniline	Manfacture Reference	1st Metal	2nd Metal	1st Metal %	2nd Metal %
1	95.12	0.12	E105N/W	Pd	none	5	0
2	95.46	0.14	E105O/W	Pd	none	5	0
3	93.71	0.12	E105NN/W	Pd	none	5	0
4	96.48	0.23	E101NE/W	Pd	none	10	0
5	97.66	0.27	E101NE/W	Pd	none	20	0
6	97.29	0.19	E196R/W	Pd	none	5	0
7	84.31	0.09	E1518NN/W	Pd	none	5	0
8	95.34	0.13	E107MA/W	Pd	none	5	0
9	95.6	0.15	E105R/W	Pd	none	5	0
10	95.85	0.18	E101B/W	Pd	none	5	0
11	97.62	0.25	E196NN/W	Pd	none	10	0
12	94.17	0.11	E213R/D	Pd	none	5	0
13	55.94	0.06	E407R/D	Pd	none	5	0
14	96.72	0.18	EF101R/W	Pd	Pt	4	1
15	1.31	0.00	CE407R/D	Pd	Pb	5	3.5
16	94.31	0.33	F105R/W	Pt	none	5	0
17	89.87	0.12	F105N/W	Pt	none	5	0
18	95.92	0.31	F1015RE/W	Pt	none	5	0
19	94.09	0.17	F1015RCB/W	Pt	none	3	0
20	94.85	0.41	F105R/W	Pt	none	10	0
21	69.38	0.05	CF105RA/W	Pt	Bi	5	5
22	4.21	0.00	F1082QHA/W	Pt	none	3	0
23	90.11	0.11	CF105BV/W	Pt	V	1	2
24	94.67	0.23	CF1082BV/W	Pt	V	1	2
25	56	0.05	CF105RA/W	Pt	Cu	1	0.1
26	98.14	0.23	E106N/W	Pd	none	5	0
27	98.06	0.20	E101O/W	Pd	none	5	0
28	97.87	0.16	E101NN/W	Pd	none	5	0
29	93.94	0.33	F1002RE/W	Pt	none	5	0
30	93.85	0.52	F101KYA/W	Pt	none	5	0
31	86.06	0.08	F1932RBSH/W	Pt	Sulfide	3	1
32	97.62	0.19	CE105XRC/W	Pd	Fe	5	0.5
33	76.9	0.06	CF1082RA/W	Pt	Cu	1	0.1
34	93.83	0.34	CF105R/W	Pt	Fe	5	0.5
35	95.89	0.13	CE1097XRC/W	Pd	Fe	5	1
36	97.72	0.18	JM 5	Pd	none	5	0
37	95.87	0.19	JM A402028-10	Pd	none	10	0
38	96.18	0.25	JM19	Pd	Pt	2.5	2.5
39	96.56	0.31	JM2	Pd	none	10	0
40	98.07	0.31	AE13	Pd	none	10	0
41	96.15	0.31	AE7	Pd	none	10	0
42	97.48	0.33	AE2	Pd	none	10	0
43	97.35	0.31	JM3	Pd	none	10	0
44	97.37	0.24	JM1	Pd	none	10	0
45	96.72	0.31	JM30	Pt	Sulfide	5	0
46	95	0.36	AE6	Pt	none	1	0
47	96.91	0.25	JM7	Pd	none	5	0
48	81.28	0.10	JM B101 038/1	Pt	none	1	0

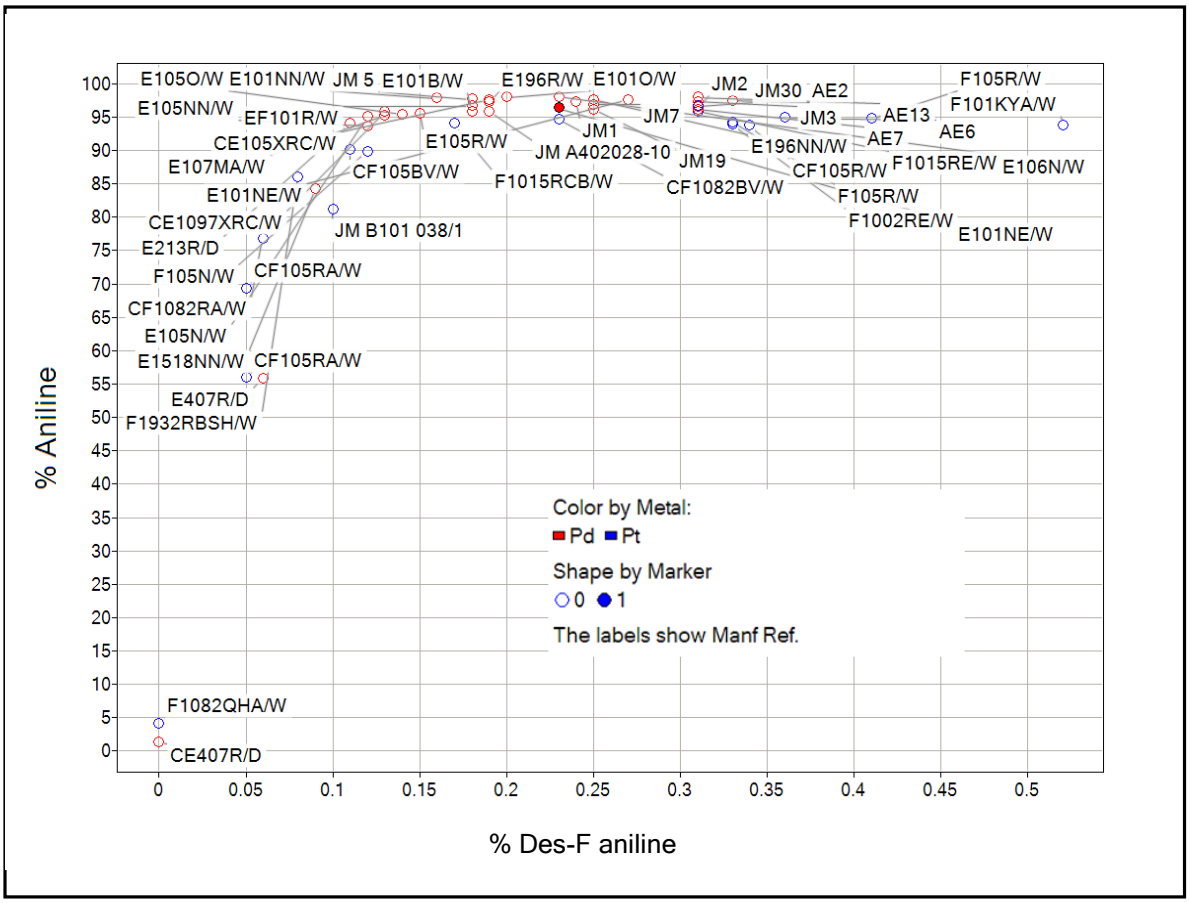

Figure 3.6: Catalyst Screening Result

Table 3.2: Catalysts that resulted in > 96% product and < 0.25% impurity

Vial #	% Aniline	% Des-F aniline	Manfacture Reference	1st Metal	2nd Metal	1st Metal %	2nd Metal %
4	96.48	0.23	E101NE/W	Pd	none	10	0
6	97.29	0.19	E196R/W	Pd	none	5	0
14	96.72	0.18	EF101R/W	Pd	Pt	4	1
26	98.14	0.23	E106N/W	Pd	none	5	0
27	98.06	0.20	E101O/W	Pd	none	5	0
28	97.87	0.16	E101NN/W	Pd	none	5	0
32	97.62	0.19	CE105XRC/W	Pd	Fe	5	0.5
36	97.72	0.18	JM 5	Pd	none	5	0
44	97.37	0.24	JM1	Pd	none	10	0

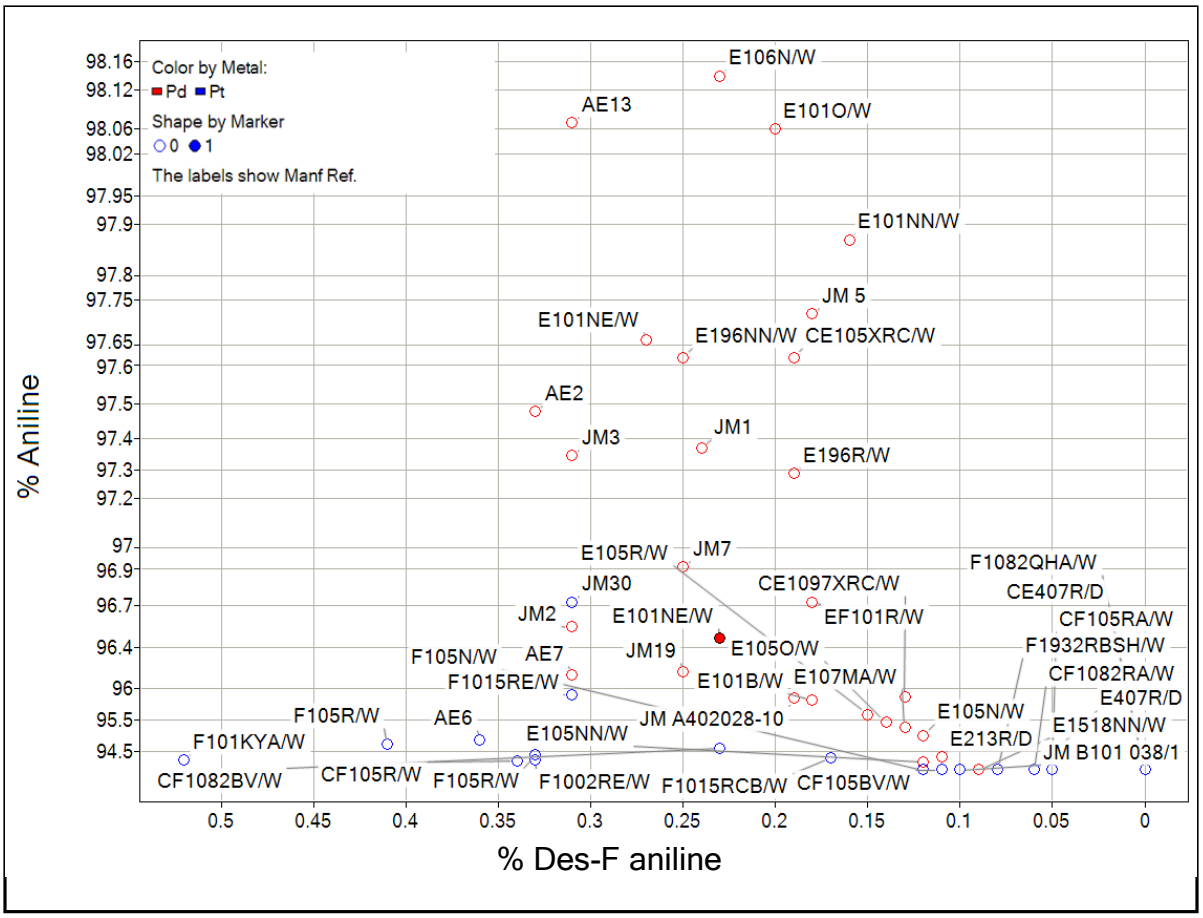

Figure 3.7: Catalysts that resulted in > 96% product and < 0.25% impurity

3.5.2 Catalyst Characterization

Several lots of E101NE/W catalyst were characterized and found to be identical with respect to metal dispersion, active surface area, and crystallite size, as summarized in Table 3.3. The catalyst manufacturer (Evonik Industries) provided the catalyst shape to be spherical in nature with a diameter of 28 μm (d_{50}). The catalyst was again tested once the reaction was completed. The catalyst was filtered and vacuum dried to remove any organic material. The spent catalyst was then analyzed and compared to the fresh (virgin) catalyst, indicating that the spent catalysts gave the same percent metal dispersion of 2.5% Pd, along with a crystallite size of ~454°A, compared to the virgin catalyst, thus confirming that the catalyst did not lose its activity during the course of the reaction. Due to the proprietary nature of these catalysts, very little published data exists. However, analysis shows greater degree of agglomeration of active metal, which is evident by large crystal size and low percent metal dispersion [22]. The BET surface area is well within the published range for activated carbons of 800-1200 m^2/g [23], and the total pore volume of 0.8 cm^3/g suggests that the carbon has been physically or steam activated with predominantly micro-pore structures for greater adsorption [24, 25].

Table 3.3: Catalyst Characterization Summary for E101NE/W

Lot #	ASA (m^2/g)	Dispersion (% D)	Avg. cryst. size d (°A)	Multi-point BET surface area (m^2/g)	Total Pore Volume (cm^3/g)
U26046-1	1.10	2.46	454	854.9	0.7948
U26046-2	1.09	2.40	452	855.3	0.8013
U26046-3a	1.12	2.53	453	850.8	0.7987
U26046-3b*	1.11	2.51	451	853.3	0.8028

*U26046-3b is the spent catalyst compared to the input virgin catalyst U26046-3a.

3.6 Conclusion

Catalysts were evaluated using a high-throughput screening technique from a diverse group of 48 catalysts available, down to a single catalyst. The selection criteria were based on the reactivity, selectivity and availability of the catalyst for scale-up. The catalyst screening results showed that the catalysts containing palladium metal were superior in terms of reactivity and selectivity of the reaction, when compared to platinum or other bimetallic catalysts, which was in direct contradiction to the published literature for such reactions [19]. One postulated theory could be that the acidic nature of the reaction solution resulted in this deviation from the norm [21]. The chosen catalyst (E101NE/W) was classified as an egg-shell catalyst by Evonik Ind., which was further characterized using Autosorb equipment by chemisorption and physisorption techniques. Several lots of the catalysts were compared in terms of the active surface area, metal dispersion, crystallite size, BET surface area, and pore volume of the catalyst, and were found to be comparable to one another. The catalyst was also compared, pre- and post reaction, and found to be comparable, thus confirming that the catalyst did not lose its activity during the course of the reaction.

References

1 T. Pietsch et. al., Carbons as supports for industrial precious metal catalysts, Applied Catalysis A, General, 1998, Vol. 173, p. 259-271.

2 A. J. Bird and A. B. Stiles (Ed.), Catalyst supports and supported catalysts, Butterworths, Boston, 1987, p. 107-137.

3 L. R. Radovic, F. RodrõÂguez-Reinoso, and P. A. Thrower (Ed.), Chemistry and Physics of Carbon, Marcel Dekker, New York, 1997, Vol. 25, p. 243-358.

4 Catalyst Guide, Hydrogenation of aromatic nitro groups in halo-nitro aromatics, Evonik Industries (http://catalysts.evonik.com/product/catalysts/en/products/technology-platforms/halo-nitroaromatic-reduction/pages/default.aspx).

5 J. G. Khinast et al., Impact of drying on the catalyst profile in supported impregnation catalysts, Chem. Eng. Sci., 2001, Vol. 56, p. 4473-4487.

6 J. Wei and E. R. Becker, The optimum distribution of catalytic material on support layers in automotive catalysis, Advances in Chemistry Series, 1975, Vol. 143, p. 116–132.

7 E. R. Becker and J. Wei, Non-uniform distribution of catalysts on supports: I Bimolecular Langmuir reactions, Journal of Catalysis, 1977, Vol. 46, p. 365–371.

8 S. Y. Lee and R. Aris, The distribution of active ingredients in supported catalysts prepared by impregnation, Catal. Rev. Sci. Eng., 1985, Vol. 27 (2), p. 207-340.

9 M. Komiyama, Design and preparation of impregnated catalysts, Catal. Rev. Sci. Eng., 1985, Vol. 27 (2), p. 341-372.

10 A. V. Nelmark, L. I. Khelfez and V. B. Fenelonov, Theory of preparation of supported catalysts, Ind. Eng. Chem. Prod. Res. Dev., 1981, Vol. 20, p. 439-450.

11 E. Iglesia, Design, synthesis, and use of cobalt-based Fischer-Tropsch synthesis catalysts, Applied Catalysis A, General, 1997, Vol. 161 (1), p. 59-78.

12 F. Shadman-Yadzi and E. E. Petersen, Changing catalyst performance by varying the distribution of active catalyst within porous supports, Chem. Eng. Sci., 1972, Vol. 27, p. 227-237.

13 Reaction block as shown in Figure 3.2 was purchased from the HEL group in the UK.

14 Forty-eight catalysts were combined from two different vendors, Evonik Industries and Johnson Matthey Catalyst Corporations.

15 Autosorb 1C was purchased from Quantachrome Instruments, Boynton Beach, FL.

16 S. Brunauer, P. H. Emmett and E. Teller, Adsorption of gases in multimolecular layers, J. Am. Chem. Soc., 1938, Vol. 60 (2), p. 309-319.

17 Autosorb 1C operation manual, Quantachrome instruments, 2007.

18 Spotfire decision suite available from TIBCO Software, Sommerville, MA; http://spotfire.tibco.com. For a discussion on the use of Spotfire in data visualization and mining, see: P. D. Higginson and N. W. Sach, High-Throughput experimentation in pharmaceutical process R&D: Developing a new software workflow to overcome downstream data-analysis bottlenecks and improve productivity, Org. Process Res. Dev. 2004, Vol. 8, p. 1009-1014.

19 The Catalyst Technical Handbook, Johnson Matthey Plc (2009).

20 H. Greenfield, Platinum metal sulfides in catalytic hydrogenations, Annals New York Academy of Sciences, 1967, Vol. 145, p. 108-115.

21 J. Kosak, Catalytic hydrogenation of aromatic halo-nitro compounds, Annals New York Academy of Sciences, 1970, Vol. 172, p. 175-184.

22 A. Borodzinski and M. Bonarowska, Relationship between crystallize size and dispersion on supported metal catalysts, Langmuir, 1997, Vol. 13, p. 5613-5620.

23 E. Auer, A. Freund, J. Pietsch, and T. Tacke, Carbons as supports for industrial precious metal catalysts, Applied Catalysis A: General, 1998, Vol. 173, p. 259-271.

24 L.R. Radovic, Carbon Materials as Adsorbents, Reactants and Catalyst Supports: Some Examples of Remarkable Flexibility and a Suggestion of Macroscopic Complementarity, Hemijska Industrija (Chemical Industry, Belgrade, Yugoslavia), 1996, Vol 50, p.225.

25 S. M. Manocha, Porous carbons, Sadhana, 2003, Vol. 28 (Parts 1 & 2), p. 335-348.

CHAPTER 4: MASS TRANSFER EFFECTS

4.1 Introduction

Catalytic hydrogenation reactions commonly use the surface aeration technique for gas-liquid mass transfer [1, 2, 3, 4]. It is vital to understand the gas-liquid mass transfer coefficients in the presence and absence of catalyst particles in these reactors. The factors affecting the volumetric mass transfer coefficient k_La in gas-liquid and gas-liquid-solid agitated reactors consist of many parameters: the physical properties of the liquid (density, viscosity, surface tension, etc.); the concentration and physical properties of the solid (density, particle size, etc.); the geometry of the vessel and agitator; the power input per unit liquid, or slurry volume; the mobility of the interface; and the coalescence rate.

A direct experimental technique required for measuring k_La for agitated systems using gas absorption (by surface aeration) is described herein following the approach described by Shah et al. [5]. For this method, hydrogen gas is introduced into the headspace of the batch reactor. Using surface aeration techniques, such as agitation, hydrogen is mixed with the liquid phase and reaches equilibrium over time. The rate at which the hydrogen concentration reaches equilibrium with the liquid phase is directly proportional to k_La. The goal was to establish a simple, non-reacting solvent system to calculate k_La based on various agitation rates and liquid volumes in the lab batch reactor for process development. As the reactor geometry varies widely from lab to production scale, the volumetric mass transfer rate would be determined using the same process for the production scale reactors.

4.2 Theoretical Background

This section describes in detail the background on measuring mass transfer coefficient (k_La) experimentally, along with discussing the theoretical method for calculating hydrogen solubility in solvent system utilizing Corresponding States Theory.

4.2.1 Mass Transfer Coefficient (k_La)

The mass transfer rate (k_La) can be measured experimentally, as described by Shah et al. [5]. The experimental technique involves a batch reactor in which gas absorption in the liquid takes place due to surface aeration. The liquid is added to the batch reactor, and the reactor is pressurized with the gas (hydrogen) and sealed. Upon initiation of agitation in the reactor, the pressure in the reactor headspace decreases with time because of the absorption of gas in the liquid phase. This decrease in pressure with time allows the estimation of mass transfer rate and volumetric mass transfer coefficient (k_La). The total pressure decrease, until equilibrium is reached, gives us the dissolved equilibrium concentration (C^*). The following assumptions were used by Shah to derive k_La and (C^*) equations:

1. In the pressure range of operation, the ideal gas assumption is valid.
2. Absorption of gas in the liquid phase can be described by Henry's Law.
3. The temperature of the gas and liquid are equal and constant.
4. While pressurizing the reactor with gas, there is no absorption of gas before the stirrer is set in motion and aeration takes place.
5. The time required for the achievement of constant gas entrainment and gas holdup during the start of the absorption process is negligibly short compared to the absorption time required for saturation.
6. The vapor pressure of the solvent is small compared to total system pressure (usually less than five percent of the total pressure).

7. Mass transfer resistance in the gas phase is negligible.
8. The liquid in the reactor is well mixed and has a uniform concentration (C_L) at any given time.

With these assumptions, the equilibrium concentration (C^*) can easily be obtained from the total uptake of gas by the liquid and can be calculated by using the ideal gas law as follows:

$$P_1 - P_2 = \left(n_{G_1} - n_{G_2}\right)\frac{RT}{V_G} \ \text{(psi)} \qquad [4.1]$$

where P denotes the system pressure, n_G denotes the moles of hydrogen, V_G is the molar gas volume of hydrogen, R is the universal gas constant and T is the temperature. The initial and final conditions are denoted by subscripts "1" and "2", respectively.

The drop in number of moles of hydrogen in the gas phase into the liquid phase is given by:

$$\left(n_{G_1} - n_{G_2}\right) = C^* V_L \ \text{(moles)} \qquad [4.2]$$

where V_L denotes the liquid volume and C^* is the equilibrium hydrogen concentration.

Re-arranging Equations 4.1 & 4.2 above gives us a way to measure the equilibrium solubility of hydrogen:

$$(C^*) = (P_1 - P_2)\frac{V_G}{V_L}\frac{1}{RT} \ \left(\frac{\text{moles}}{\text{L}}\right) \qquad [4.3]$$

The kinetics of the adsorption process can be analyzed using a differential macroscopic mass balance for hydrogen in the liquid phase during the adsorption process

$$\frac{dC_L}{dt}\left(\frac{\text{mol}}{\text{L} * \text{min}}\right) = k_L a(C^* - C_L) \qquad [4.4]$$

Since $C_L = n_L/V_L$ moles of gas in the liquid volume, and using Henry's Law (C^*) = P/H, we rewrite this expression in the form

$$\frac{dn_L}{dt}\left(\frac{\text{mol}}{\text{min}}\right) = V_L\, k_L a\, \left(\frac{P}{H} - \frac{n_L}{V_L}\right) \qquad [4.5]$$

A differential form of Equation 4.1 gas law can be used to relate pressure changes in the gas phase to liquid concentration changes as:

$$\frac{dP}{dt}\left(\frac{\text{psi}}{\text{min}}\right) = \left(\frac{RT}{V_G}\,\frac{dn_G}{dt}\right) = -\left(\frac{RT}{V_G}\,\frac{dn_L}{dt}\right) \qquad [4.6]$$

Equation 4.6 can be integrated to derive an expression for the time dependence of the total pressure P as follows:

$$(n_L - n_{L0})mol = \frac{V_G}{RT}\,(P_1 - P) \qquad [4.7]$$

where P and P_1 are the pressures at time 't=t' and at t=0, respectively. The subscripts "L_0" and "L" denotes the moles of hydrogen at time 't=t' and at t=0, respectively.

Inserting Equations 4.6 and 4.7 into Eq. 4.5, we obtain

$$\frac{dP}{dt}\left(\frac{\text{psi}}{\text{min}}\right) = -k_L a\; V_L \frac{RT}{V_G}\left[\frac{P}{H} - \frac{1}{V_L}\frac{V_G}{RT}\,(P_1 - P) - \frac{n_{L0}}{V_L}\right] \qquad [4.8]$$

Integrating the above Equation 4.8 from t=0 to t, and rearranging terms, as shown in Appendix, (Section 9.1 Mass Transfer Coefficient ($k_L a$)) results in a simplified expression to determine $k_L a$

$$(k_L a)\,\mathrm{t} = \frac{(P_2 - P_0)}{(P_1 - P_0)} \ln\left[\frac{P_1 - P_2}{P - P_2}\right] \text{ (Valid for } P_1 < P < P_2) \qquad [4.9]$$

where P_1 & P_2 are the initial and final pressures, respectively; P is the pressure of system at time t; and P_0 is the pre-saturation pressure (or vapor pressure of solvent at the system temperature). This vapor pressure is usually very small and can be neglected. The volumetric mass transfer rate ($k_L a$) can be calculated from Equation 4.9 by measuring the pressure drop of the system as a function of time.

4.2.2 Hydrogen Gas Solubility based on Corresponding States Theory (CST)

Hydrogen solubility in simple and mixed solvent systems can be calculated as described by Shaw [6] and Sebastian et al. [7]. Hydrogen gas solubility cannot be expressed by simple relationships, such as Henry's Law, at temperatures and pressures above 298ºK and 0.10 MPa, or when one of the components is supercritical, as described by Brandani and Prausnitz [8]. A hydrogen solubility correlation, employing corresponding states theory (CST), was developed by Shaw, by equating the fugacity of the dissolved hydrogen to the fugacity of the gas in equilibrium

$$[C^*]\frac{\mathrm{mol}}{\mathrm{L}} = \frac{P}{\rho_{ref}^2}\, S^* \left[\frac{f}{P}\right]^{-1} \qquad [4.10]$$

where Shaw defined ρ_{ref} (in kg/m^3) as the density of liquid phase at 25ºC, P is the hydrogen partial pressure (in atm), and the normalized solubility (S^*) (in mols of H_2 $L^{-2}_{solvent}$ atm^{-1} $kg_{solvent}$) for hydrogen as:

$$\ln(S^*) = \frac{A_1}{\rho_{ref}^{0.5}}\, T^* + \frac{A_2}{\rho_{ref}^{0.5}} + A_3 + A_4\, \Delta\rho_s \qquad [4.11]$$

The constants were regressed using experimental values by Shaw and found to be; A_1 = 2.17587; A_2 = -1.81836; A3 = -5.23139; A4 = 1.500; and $\Delta\rho_s$ is the density difference between the two phases set to zero for simple solvent systems.

An expression for the fugacity was further derived by Shaw [6] as:

$$\left[\frac{f}{P}\right] \cong exp\left[\frac{(\Omega_b - \ \Omega_a \ F_{Soave})}{\frac{T_r}{2\ P_r} + \frac{T_r}{2\ P_r}\left[1 - \frac{P_r}{T_r}\ \Omega_a \ F_{Soave}\right]^{0.5}}\right] \qquad [4.12]$$

where; $\Omega_a \ and \ \Omega_b$ are constants 0.42748 and 0.08664, respectively; Tr and Pr and the reduced temperatures and pressures, respectively; and F_{Soave} (fugacity function defined by Soave) should approach zero asymptotically at elevated temperatures,

$$F_{Soave} = \ T_r^{-1}\left[1 + (0.48 + 1.574\omega - 0.176\ \omega^2)\ (1 - T_r^{0.5})\right]^2 \qquad [4.13]$$

where ω = Pitzer acentric factor (= - 0.22 for hydrogen); and Tr and Pr are the reduced temperature and pressure, respectively.

Equations 4.10 through 4.13 are used to calculate hydrogen solubility in the given solvent system. A detailed derivation for Equations 4.10-4.13 is given in Appendix, Section 9.2: Hydrogen Gas Solubility based on Corresponding States Theory (CST).

4.3 Factors Affecting Mass Transfer Coefficient (k_La) and Gas Solubility (C*)

In order to understand and scale-up the three-phase gas-liquid-solid system, it is vital to understand the factors that influence both the equilibrium gas solubility and mass transfer coefficient

(k_La). This section describes the literature findings of these critical factors, i.e. temperature, pressure, and agitation rate, and its impact on k_La and gas solubility (C*).

4.3.1 Mass Transfer Coefficient (k_La)

The volumetric liquid-side mass transfer coefficient, k_La is one of the important parameters in Equation 4.9. The k_La is commonly measured either by chemical or physical methods. The various factors affecting the k_La values are discussed as follows:

4.3.1.1 Effect of Agitation on k_La

Several authors reported that increasing the agitation rate tends to increase in k_La values [9,12,13,14,15,and 19]. Both the gas holdup and gas-liquid interfacial area 'a', increase with an increase in agitation rate. Increasing the mixing speed increases the shear rate applied at the gas-liquid interface, which reduces the liquid film diffusion thickness thus increasing the k_L values. Several investigators [10,11], however, reported that at very high agitation rates there was no significant increase in k_La observed. It was postulated that at higher agitation rates the pumping capacity of the impeller reaches its maximum and would not provide any further increase in the gas holdup volume and subsequently k_La values.

4.3.1.2 Effect of Pressure on k_La

It has been reported by several investigators that k_La increases with increasing pressure [12, 13, 14, and 15], while others also reported that k_La remains unaffected [16, 17, and 18]. However, the majority of these authors have agreed that the effect of pressure on k_La is related to the variation of the liquid-phase physico-chemical properties due to the increase of gas solubility with pressure, which tends to the decrease of the viscosity and surface tension of the liquid-phase.

4.3.1.3 Effect of Temperature on k_La

Resembling the effects of pressure, increasing temperature could lead to an increase [13,14,18, and 19]; no effect [15,20]; or even reduce [13] k_La values. With increasing temperature, the liquid viscosity and surface tension decreases, whereas the diffusivity of the gas in the liquid phase increases. The decrease of viscosity and surface tension leads to a decrease of the average bubble size, and therefore the gas-liquid interfacial area, a, increases. The increase of the gas diffusivity into the liquid increases k_L since it is proportional to the diffusivity. Therefore, increasing temperature should increase k_La. Depending on the gas-liquid system, however, since the gas solubility decreases with increasing temperature, the solubility effect on k_La could offset the expected increase of k_La with increasing temperature of the liquid.

4.3.2 Gas Solubility (C*)

In a two-phase gas-liquid system, the equilibrium solubility (C*) is an important factor in determining the mass transfer rate. It is documented in the literature that for many gas-liquid systems, the solubility tends to increase [14,15,17, and 19] linearly with pressure, and therefore, Henry's Law is applicable within the pressure range examined by these authors. Also, the solubilities of gases were reported to decrease [12,13] with increasing molecular weight and/or carbon number of organic liquids. Depending on the gas-liquid system and the temperature range used, (C*) values can either tend to increase or decrease with increasing temperature.

4.4 Equipment

The lab scale hydrogenator [21] was purchased from the HEL group in the UK. It is equipped with fully automated temperature, pressure, and stirring control. The reactor was made with hastelloy C-276, with a maximum reaction volume of 100-mL and total volume of 185-mL (total liquid +

headspace volume). See Figure 4.1 for details. The batch reactor was fitted with a temperature transducer (T_r), a pressure transducer (P), and a pitched blade turbine agitator (down-flow) with speed control (M). Gas inlet and outlet (vent) valves (for hydrogen and nitrogen) were located in the headspace of the vessel. Syltherm was used as a heat transfer fluid in the jacket for temperature control. The reactor is also equipped with a React IR (high pressure infrared detection system from Mettler Toledo) for reaction monitoring and a sampling port for taking manual HPLC samples. A three-way ball valve separates the hydrogen and nitrogen gas in the reactor headspace. The rupture disc was set at 110-barg pressure in case of over pressurization. The hydrogen and nitrogen cylinders are hooked up to gas regulators; and, the regulators are manually adjusted to obtain a pressure slightly higher than the desired reaction pressure. The total hydrogen uptake, as well as temperature difference between the jacket and reactor, is recorded every few seconds in the control software.

4.5 Materials and Reagents

High purity hydrogen and nitrogen gas cylinders (purity of 99.999%) were purchased from Airgas Co. and were connected to the reactor. As most of the nitro reductions are carried out in water and/or alcohol systems, methanol was chosen as the standardized solvent to conduct the mass transfer studies, due to its high dielectric values and hydrogen solubility [22]. Methanol along with ethanol (200-proof) and high purity water were purchased from Aldrich Chemical Company.

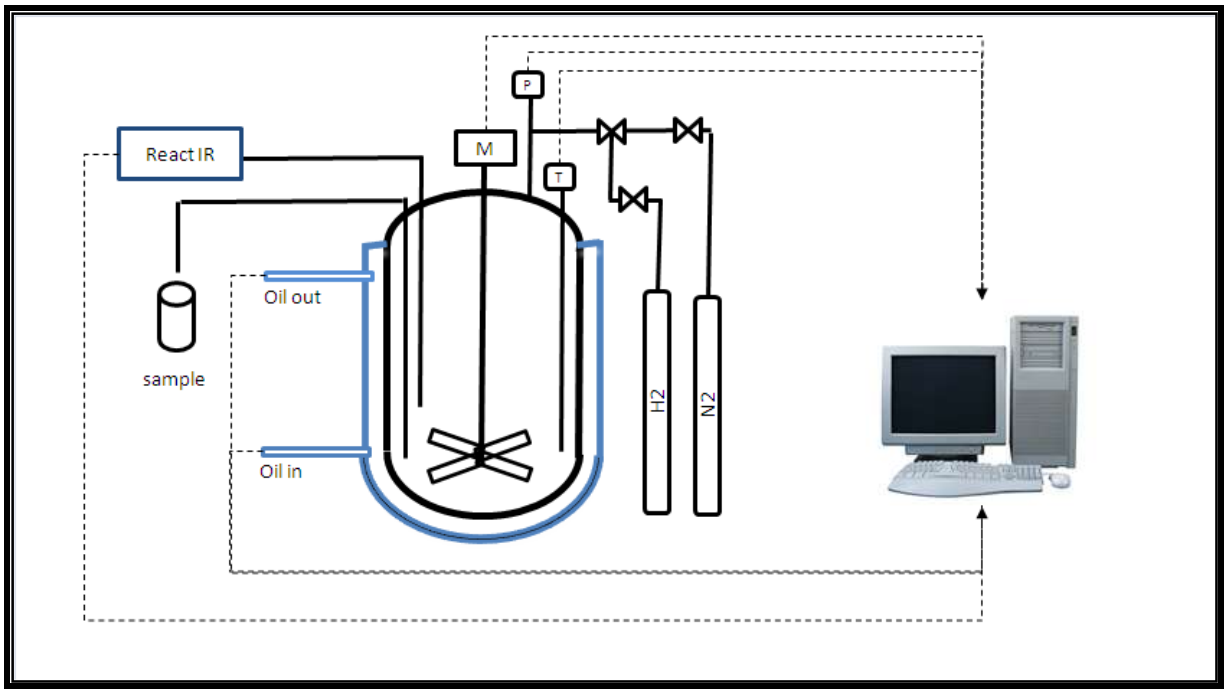

Figure 4.1: Lab scale 100-mL Hydrogenator

Hydrogenator is a hastelloy vessel, which is completely computer controlled. It is also equipped with a down flow 45° pitched impeller [M], temperature [T], and pressure [P] controller. The jacket is filled with syltherm oil for heat transfer. The "React IR" is an in-situ high-pressure infrared concentration measurement instrument from Mettler Toledo. HPLC samples are pulled through the sample port for the reaction progress. Hydrogen and nitrogen cylinders are provided with the regulator for the desired pressure in the vessel. A batch recipe is fed into the vessel for control and operations.

4.6 Procedure for k_La and (C*) Measurement

Most of the industrial hydrogenation is conducted in polar protic solvents, such as water and/or alcohols, i.e., methanol [23]. Polar protic solvents are solvents with high dielectric solvents which have the ability to donate H-atoms and form strong hydrogen bonding. Methanol was charged to the reactor, and the batch temperature was adjusted to 25°C. Once the desired temperature was reached, the reactor was inerted with nitrogen (agitation was turned off during the inertion process), after which it was twice pressure purged with hydrogen to evacuate nitrogen from the headspace. Then, the reactor was pressurized again with hydrogen, to an initial pressure (P_1), and the inlet valve was closed. The reactor was agitated at a constant rpm at t=0, and the pressure drop from the headspace was

measured as a function of time. As the hydrogen was being absorbed into the liquid phase, the total hydrogen uptake was calculated from the pressure drop in the headspace using the ideal gas law. The experiment was completed once the equilibrium pressure was reached in the reactor headspace (final pressure = P_2). Several experiments were run (using virgin methanol for each experiment) varying agitation rates and liquid level to get a correlation for k_La versus the agitation rate (rpm) and the reaction liquid volume (mL). Experiments were also run using virgin ethanol or water to measure the H_2 equilibrium solubility (C*) in these solvents.

4.7 Results and Discussion

In this section, the mass transfer coefficient (k_La) and the equilibrium gas solubility data obtained for 100-mL reactor are presented and discussed.

4.7.1 Mass Transfer Coefficient (k_La)

The volumetric liquid-side mass transfer coefficient k_La for pure hydrogen was measured in methanol (50-100 mL) in the temperature range of 25-45°C, pressure range of 2-4 barg, and agitation rate of 700-1150 RPM. The data obtained are discussed in the following section.

4.7.1.1 Effect of Agitation Rate and Liquid Volume on k_La

Hydrogen pressure drop from the headspace was measured as a function of time, and the data was collected and stored in HEL software [21] every two seconds. Figure 4.2 shows the pressure drop in the headspace for the experiment run with 50-mL methanol liquid level at an initial hydrogen pressure of 4-barg, when stirred at various rpm. The pressure in the headspace reaches equilibrium over time, depending upon the agitation speed, as observed in Figure 4.2 (a) through (d). The higher the agitation rate, the faster the pressure reaches equilibrium. The overall equilibrium concentration of hydrogen in methanol was calculated using Equation 4.3 and was found to be in close agreement with

each other at 1.74 x 10^{-2} mol/L with a standard deviation of 9.03 x 10^{-4} mol/L (refer to Table 4.1). The measured solubility is found to be in close agreement with literature values [22], thereby, validating the methodology used.

Table 4.1: Estimation of equilibrium concentration of hydrogen in methanol at 25°C using Eq. 4.3

RPM	P_1 (barg)	P_2 (barg)	(P_1-P_2) (barg)	C* (mol/L)
700	4.023	3.8637	0.1593	1.74E-02
800	3.9785	3.8295	0.149	1.62E-02
900	3.9976	3.8283	0.1693	1.84E-02
1150	4.1235	3.9642	0.1593	1.74E-02
V_G/V_L	2.7	-	Std Dev.	9.03E-04
1/RT	0.040342	mol/L/bar		

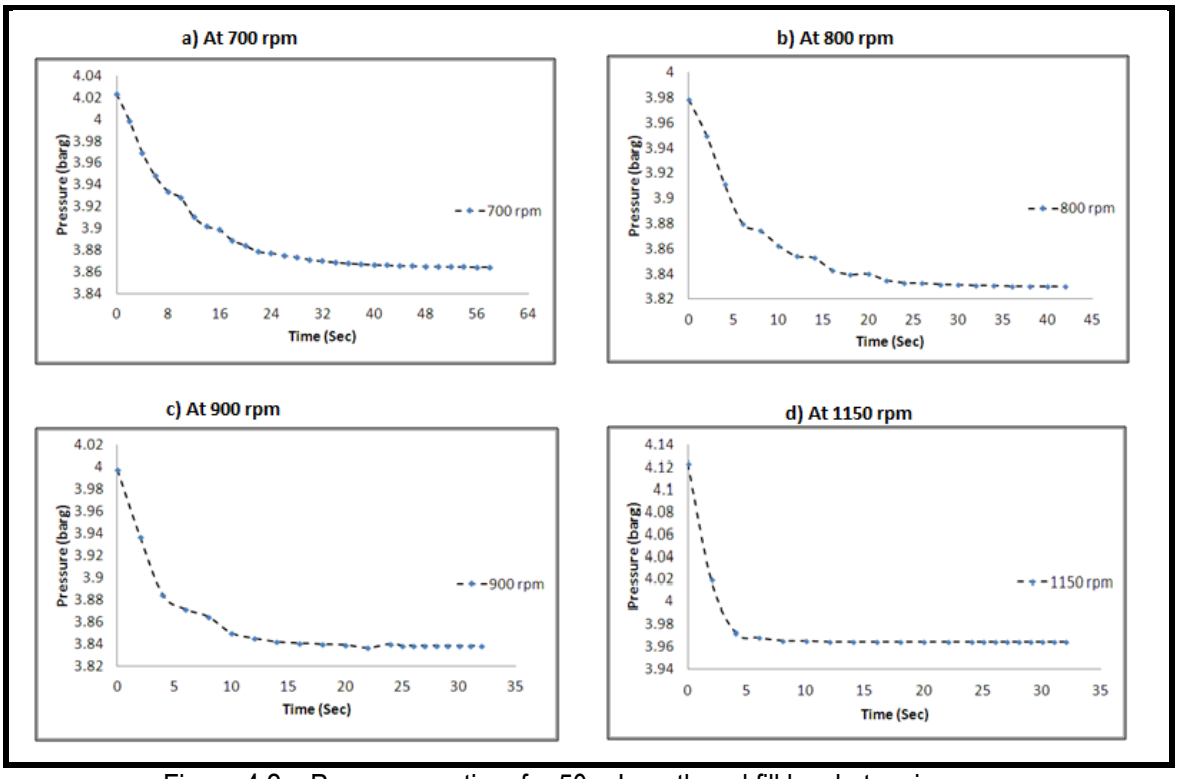

Figure 4.2: Pressure vs. time for 50-mL methanol fill level at various rpm

The overall volumetric mass transfer coefficient (k_La) was calculated from the slope of Eq. 4.9, shown in Figure 4.3. The right-hand side of Eq. 4.9 is plotted on the y-axis, with time (in seconds) on the x-axis. The slope of the plot gives the value of the overall volumetric mass transfer coefficient (k_La). These experiments were each repeated three times, and the k_La values were found to be in close agreement with each other as shown in Table 4.2.

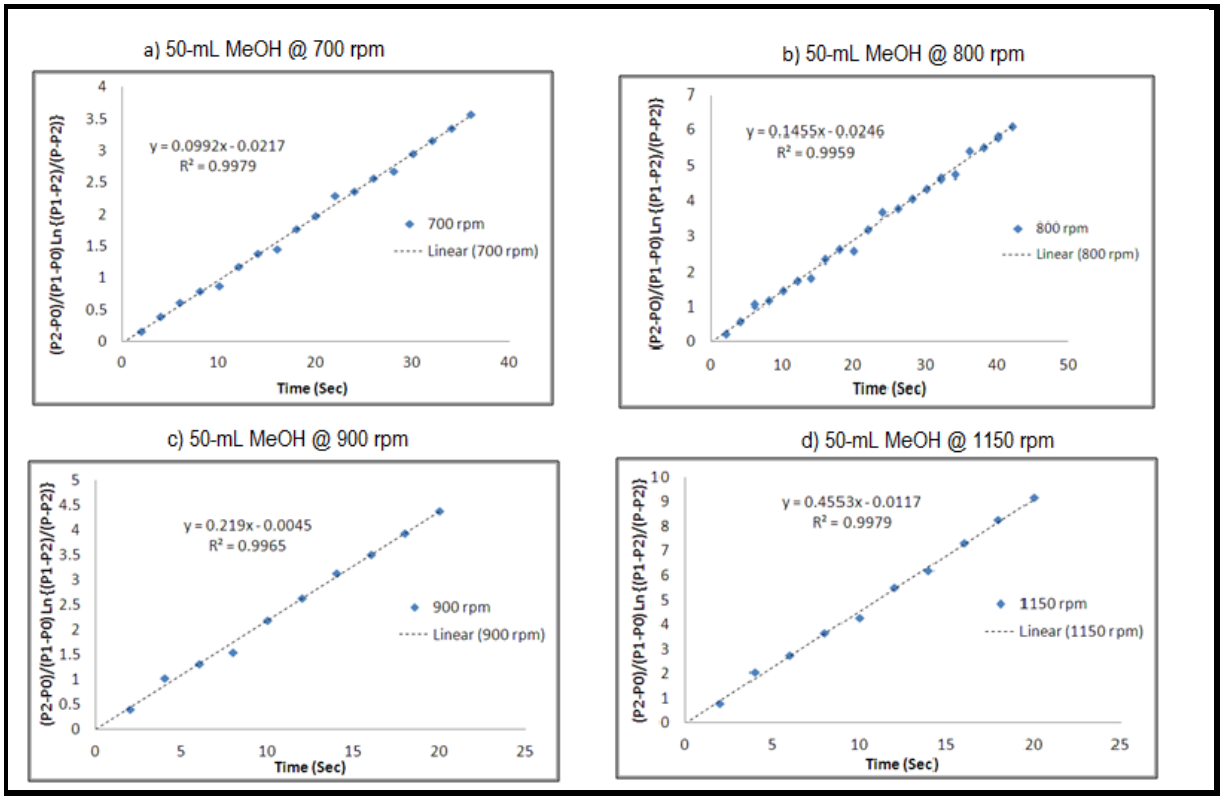

Figure 4.3: Estimation of k_La for 50-mL MeOH volume using Equation 4.9

Table 4.2: k_La values for 50-mL MeOH calculated from Eq. 4.9

RPM	k_La 1/sec (exp 1)	k_La 1/sec (exp 2)	k_La 1/sec (exp 3)	Std Dev
700	0.071	0.069	0.076	0.0037
800	0.135	0.128	0.143	0.0077
900	0.219	0.200	0.250	0.0252
1150	0.455	0.430	0.499	0.0348

The overall volumetric mass transfer coefficient was found to depend linearly on rpm, as shown in Figure 4.4, which is in agreement with the result of numerous authors [9-20]. This is a critical finding as, due to the linearization of the plot, one can calculate the rpm required to run the reaction at a desired k_La value for this reaction and volume. Similarly, the measurements were carried out for various fill levels of methanol and at various agitation rates. For each measurement, a fresh solvent (methanol) was charged and then degassed, as per the procedure described earlier.

Figure 4.5 shows the plot of k_La (on the y-axis) versus rpm (on the x-axis) for 50-, 75- and 100-mL methanol fill levels. It was observed that k_La is linearly proportional to rpm at all fill levels. As it can be seen, a higher agitation rate is required as the liquid volume increases to achieve the same k_La value.

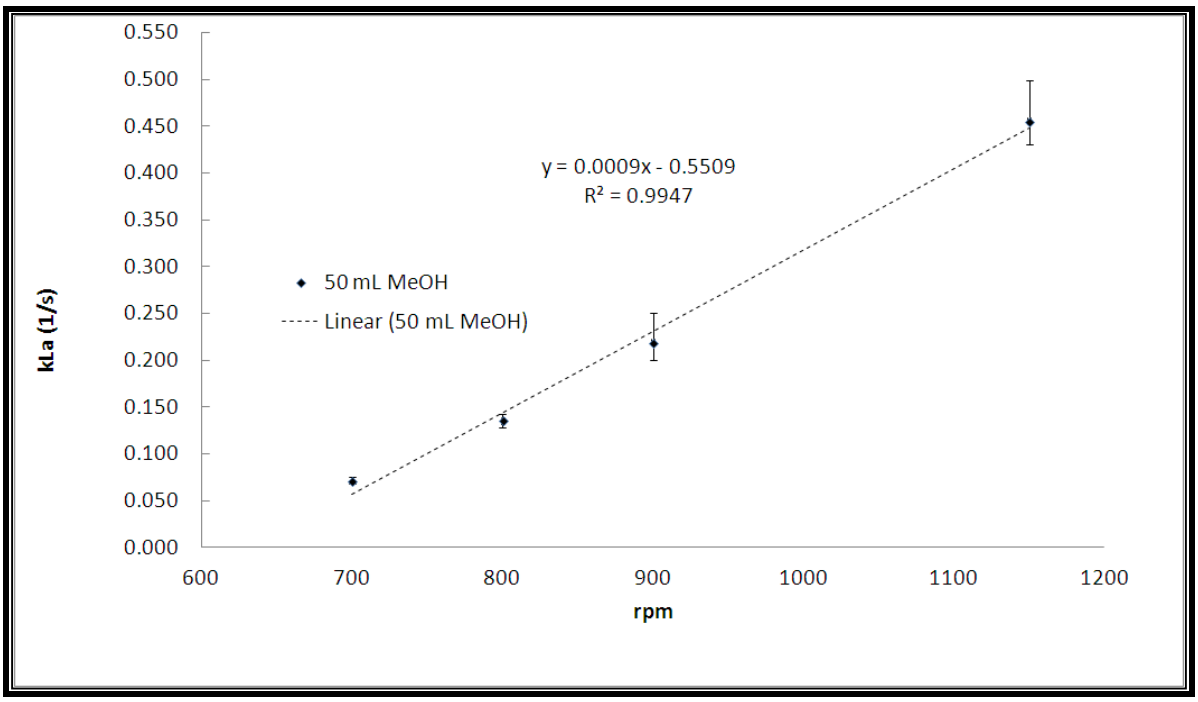

Figure 4.4: The overall volumetric mass transfer coefficient vs. rpm (for 50-mL MeOH fill level)

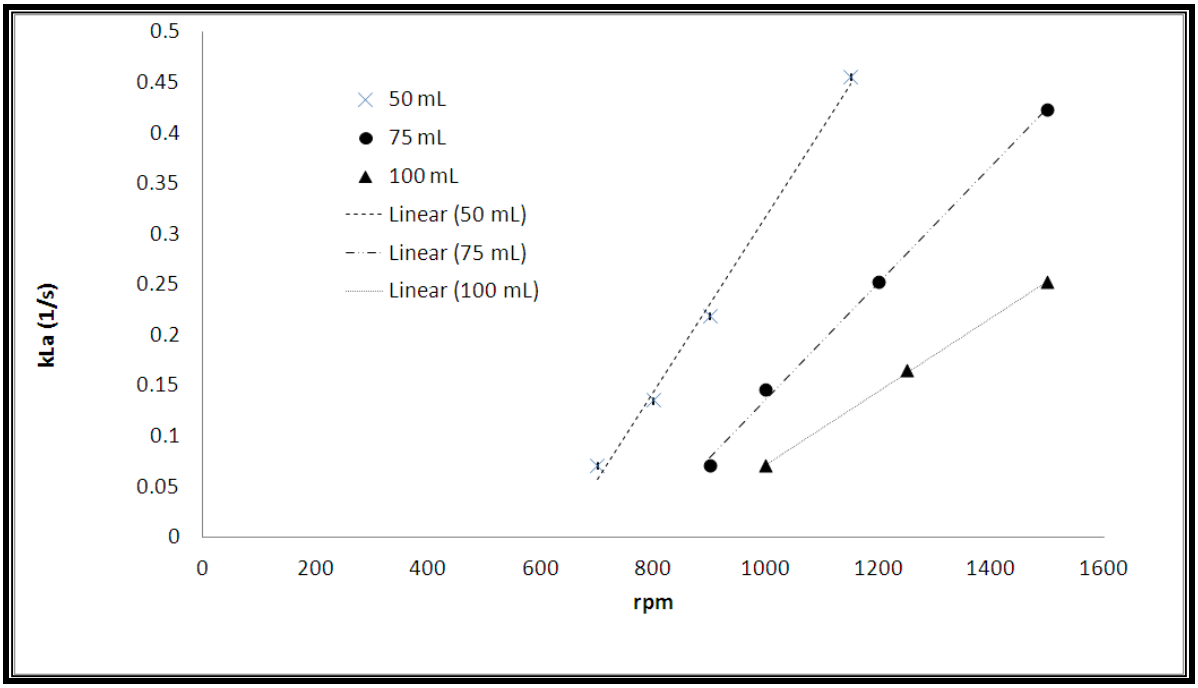

Figure 4.5: k_La vs. rpm for various MeOH fill levels

4.7.1.2 *Effect of Pressure on k_La*

Experiments were run under the reaction pressure conditions to understand the k_La effect in methanol (50-mL) as described earlier. The effect of pressure on k_La was measured at 25°C for pressures between 3-5 bar as shown in Figure 4.6. Under the reaction conditions; temperature is 25°C; agitation rate between 700-900 rpm; and pressure ranging from 3-5 bar (absolute), there appears to be negligible effect of pressure on the k_La measurement. Our results concur that under small pressure variation (1-3 MPa), there is negligible increase in gas solubility (see Section 4.7.2 below) or gas-liquid interfacial area 'a', to have an appreciable effect of pressure on k_La.

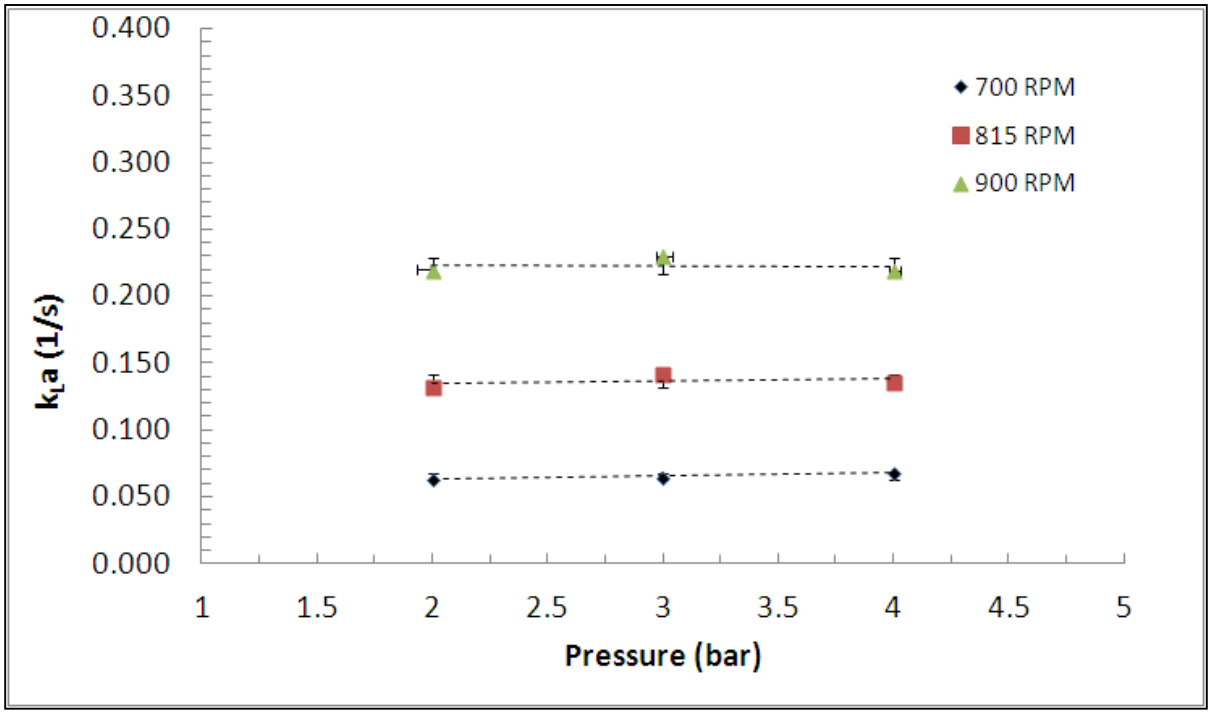

Figure 4.6: Effect of Pressure on k_La in 50-mL MeOH at 25°C

4.7.1.3 *Effect of Temperature on k_La*

Experiments were run under the reaction temperature conditions to understand the k_La effect in methanol (50-mL) as described earlier. The effect of temperature on k_La was measured at 4 barg H_2

head-space pressure, varying temperature and agitation speeds between 25-45°C and 700-900 RPM, respectively, as shown in Figure 4.7. The plot shows that the k_La value decreases with increase in temperature, and the effect is larger at the higher agitation speeds.

It is known that at higher temperature the diffusivity increases, and the surface tension between the gas-liquid interface decreases, leading to the creation of many small gas bubbles which increases the interfacial area 'a'. This should result in increase in k_La values. However, at higher temperatures the partial pressure of solvent also increases, resulting in more resistance to gas component for diffusing into the liquid phase (counter flux), i.e. 'k_L'. Thus, the overall effect of temperature on k_La will be the combination of 'a' and 'k_L' at elevated temperatures. Thus, we observe that increasing temperature reduces the k_La values due to the increase in counter flux to mass transfer created by the increase in partial pressure of the solvent system.

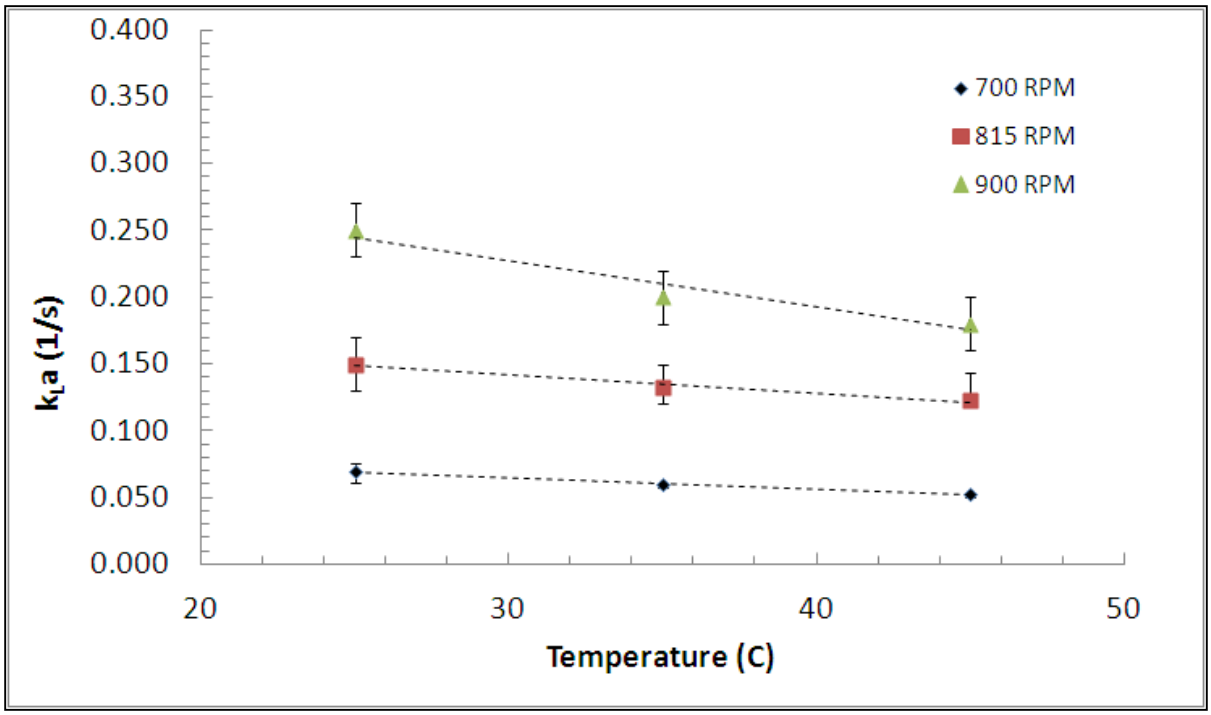

Figure 4.7: Effect of Temperature on k_La at 4-barg H_2 pressure in methanol

4.7.2 Hydrogen Solubility (Equilibrium measurements compared to CST)

The equilibrium solubility was measured by Eq. 4.3 as described by Shah et al. [5]. Critical properties for common solvents (i.e., methanol, ethanol, and water) and hydrogen are found in Reid et al. [24] as shown in Table 4.3. Hydrogen solubility was calculated using corresponding states theory (CST) as described by Shaw in Eq. 4.10 and given in Table 4.4.

Table 4.3: Critical properties of common solvents derived from Reid et al. [12]

	Critical Temperature Tc (K)	Critical Pressure Pc (Pa)	Density (ρ) in g/cc at 25C	MW	Tr	Pr
Hydrogen	33.23	1316000		2.00	8.82	0.38
Methanol	512.64	8092000	0.791	32.04	0.57	0.64
Ethanol	513.92	6137000	0.789	46.07	0.57	0.64
Water	647.12	22055000	0.999	18.01	0.45	0.49

Table 4.4: Hydrogen solubility comparison between CST and experimental procedure (T=25ºC)

	Experimental				Calculated		
Solvent	Initial Pressure (barg)	Final Pressure (barg)	dP (bar)	moles of H_2 dissolved - eq 4.8 (mol/m3)	Ln[S*] - eq 4.36	$[C_{H2}]$ eq 4.37 (mol/m^3)	% Deviation
Methanol	1.36	1.22	0.14	8.47	-5.71	8.19	3.3%
Methanol	3.99	3.70	0.29	16.94	-5.71	17.31	-2.2%
Methanol	5.99	5.58	0.41	24.81	-5.71	24.25	2.3%
Ethanol	1.54	1.39	0.15	9.07	-5.72	8.92	1.7%
Ethanol	4.20	3.90	0.30	17.85	-5.72	18.26	-2.3%
Ethanol	6.20	5.80	0.40	24.20	-5.72	25.29	-4.5%
Water	2.20	2.06	0.14	8.47	-5.98	8.12	4.1%
Water	6.20	5.89	0.31	18.75	-5.98	18.23	2.8%
Total Reactor Vol (mL)	1000 mL		Vol. of liquid (mL)	400 mL		Vol. of gas (mL)	600 mL

The percent difference found between the experimental and calculated values is less than five percent; hence, the CST method can be applied with confidence to a wide variety of solvent systems, and the hydrogen solubility can be calculated, thereby, expediting the solvent selection. In addition, this method can also be used to calculate Henry's constant for solvents that are not readily available by using the correlation given by Eq. 4.15.

$$[C^*]\left(\frac{mol}{L}\right) = \frac{P}{\rho_{ref}^2} S^* \left[\frac{f}{P}\right]^{-1} = \frac{P}{H} \qquad [4.14]$$

$$H\left(Pa\frac{m^3}{mol}\right) = \left[\frac{f}{P}\right]\frac{\rho_{ref}^2}{S^*} \qquad [4.15]$$

The equilibrium solubility of hydrogen in methanol (C*) was also measured as a function of temperature and pressure and compared with the CST model as shown in Figure 4.8 below, and is found to increase with increases in pressure and temperature. The increase in solubility with pressure can be related to the increase in driving force (concentration difference of hydrogen gas between the two phases) when increasing the system pressure. This behavior is in good agreement with the reported literature [12,16,18, and 19].

Several potential causes for the increase in solubility of H_2 with increasing temperature were postulated by Y. Rakymkul [25]:

1. During the dissolution of gas into a liquid phase, heat is absorbed by the liquid phase to create a cavity for the gas to dissolve. Once the gas molecule enters the pocket of solvent, energy is then released.

2. Heat is released as the intermolecular forces of attractions between the gas and the solvent molecules lowers its energy. The stronger the attraction (H-bonding), the larger the heat released. There is a net absorption of heat when gases are dissolved in liquid phase. According to Le Chatelier's principle, higher temperature will favor the heat absorption process of the gases into the liquid phase. Thus, the solubility was expected to increase due to increase in temperature for hydrogen with polar solvents (i.e. Methanol, Ethanol, etc.).

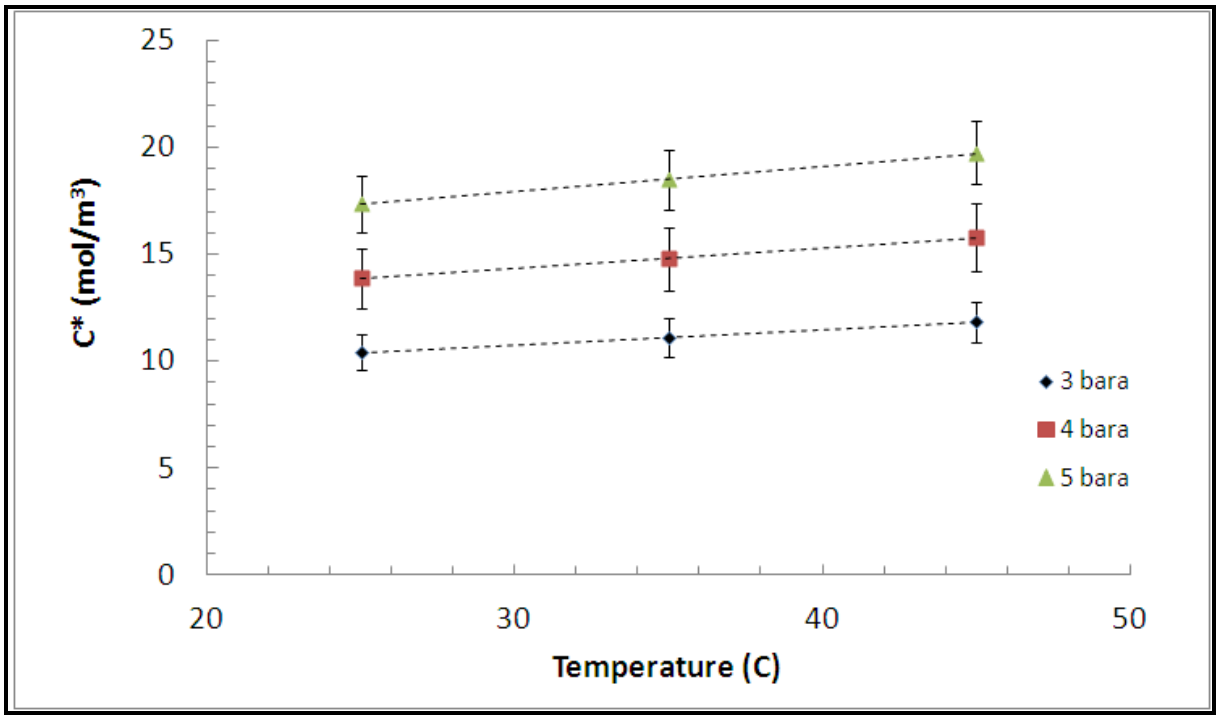

Figure 4.8: Equilibrium Solubility as a function of Temperature and Pressure

4.8 Conclusion

An experimental technique was utilized to measure the overall mass transfer coefficient as described by Shah et al. [5]. Furthermore, as most of the nitro reductions are carried out in a water and/or alcohol system, methanol was chosen as the standardized non-reactive solvent to conduct the mass transfer studies, due to its high dielectric values and high hydrogen solubility [22]. The experimental method also gave a direct measurement of hydrogen solubility in the solvent system, along with k_La values. The overall equilibrium concentration of hydrogen in methanol was calculated (at T=25ºC and P = 5-Bara) using Equation 4.3 and found to be 1.74×10^{-2} mol/L with a standard deviation of 9.03×10^{-4} mol/L. The measured solubility was found to be in close agreement with literature values [22], validating the methodology used. The overall volumetric mass transfer coefficient was calculated from experimental data using Eq. 4.9 and was found to increase linearly with reactor agitation rate at all liquid volumes. This is particularly useful, as one can predict the k_La values for the desired liquid fill volume and rpm. For the given system, it was found that k_La was constant over the pressure range, however, was found to decrease with increasing temperature.

For simple systems, the CST method is in agreement with the measured value of hydrogen solubility in the solvent system (i.e. MeOH), even for the systems (i.e., MeOH, Ethanol and water) which do not have readily available Henry's constant data. Also, the hydrogen solubility in methanol was found to increase with increase in temperature and pressure. With the degree of accuracy for hydrogen solubility, such data can be generated very quickly without the need to do experiments, and then can be verified in the lab for the system of interest, thus saving process development timelines.

References

1 J. B. Joshi, A. B. Pandit, and M. M. Sharma, Mechanically agitated gas-liquid reactors, Chem. Eng. Sci., 1982, Vol. 37, p. 813 - 844.

2 R. Fuches, D. D. Ryu, and A. E. Humphrey, Effect of surface aeration on scale-up procedures for fermentation processes; Ind. Eng. Chem. Process Des. Dev., 1971, Vol. 10 (2), p 190-196.

3 H. H. Topiwala, J. Ferment. Technol., Surface aeration in a laboratory fermenter at high power inputs, 1972, Vol. 50, p. 668-675.

4 J. A. Wiedmann, A. Steiff, and P. M. Weinspach, Experimental investigations of suspension, dispersion, power, gas hold up, and flooding characteristics in stirred gas-liquid-solid systems (slurry reactors), Chem. Eng. Commun., 1980, Vol. 6 (4), p. 245-256.

5 Y.T. Shah, A. Deimling, B.M. Karandikar, and N.L. Carr, Solubility and mass transfer of CO and H_2 in Fischer—Tropsch liquids and slurries, The Chemical Engineering Journal, 1984, Vol. 29 (3), p. 127-140.

6 J. M. Shaw, A correlation for hydrogen solubility in alicyclic and aromatic solvents; The Canadian Journal of Chemical Engineering, 1987, Vol 65, p. 293-298.

7 H. M. Sebastian, H. M. Lin and K. C. Chao, Correlation of solubility of hydrogen in hydrocarbon solvents, AIChE J., 1981, Vol. 27, p. 138-148.

8 V. Brandani and J. M. Prausnitz, Thermodynamics of gas solubility in liquid solvents and solvent mixtures, Fluid Phase Equilibria, 1981, Vol. 7, p. 259-274.

9 S. Ledakowicz, H. Nettelhoff, and W.D. Deckwer, Gas-liquid mass transfer data in a stirred autoclave reactor, Industrial & Engineering Chemistry Fundamentals, 1984, Vol. 23(4), p. 510-512.

10 Y.-C Hsu, R.Y. Peng, and C.-J. Huang, Onset of gas induction, power consumption, gas holdup and mass transfer in a new gas-induced reactor, Chemical Engineering Science, 1997, Vol. 52(21-22), p. 3883-3891.

11 T. Sridhar and O.E. Potter, Interfacial areas in gas--liquid stirred vessels, Chemical Engineering Science, 1980, Vol. 35(3), p. 683-695.

12 M.Y. Chang and B.I. Morsi, Solubilities and mass transfer coefficients of carbon monoxide in a gas-inducing reactor operating with organic liquids under high pressures and temperatures, Chemical Engineering Science, 1992, Vol. 47 (13-14), p. 3541-3548.

13 A. Deimling, B.M. Karandikar, and Y.T. Shah, Solubility and mass transfer of CO and H2 in Fischer—Tropsch liquids and slurries, The Chemical Engineering Journal, 1984, Vol. 29(3), p. 127-140.

14 Z. Tekie, J. Li, and B.I. Morsi, Mass transfer parameters of O_2 and N_2 in Cyclohexane under elevated pressures and temperatures: A statistical approach, Industrial & Engineering Chemistry Research, 1997, Vol. 36, p. 3879-3888.

15 J.R. Inga and B.I. Morsi, Effect of catalyst loading on gas/liquid mass transfer in a slurry reactor: A statistical experimental approach, Canadian Journal of Chemical Engineering, 1997, Vol. 75(5), p. 872-881.

16 S.A. Miller, A. Ekstrom, and N.R. Foster, Solubility and mass-transfer coefficients for hydrogen and carbon monoxide in n-octacosane, Journal of Chemical and Engineering Data, 1990, Vol. 35(2), p. 125-127.

17 R.S. Albal, Y.T. Shah, N.L. Carr and A. Schumpe, Mass transfer in multiphase agitated contactors, The Chemical Engineering Journal, 1983. 27(2), p. 61-80.

18 R.S. Albal, Y.T. Shah, N.L. Carr, and A.T. Bell, Mass transfer coefficients and solubilities for hydrogen and carbon monoxide under Fischer-Tropsch conditions, Chemical Engineering Science, 1984, Vol. 39(5), p. 905-907.

19 B.M. Karandikar, B.I. Morsi, Y.T. Shah, N.L. Carr, Effect of water on the solubility and mass transfer coefficients of CO and H_2 in a Fischer-Tropsch liquid, The Chemical Engineering Journal, 1986, Vol. 33(3), p. 157-168.

20 A. L. Zaidi, M. Ralek and W.D. Deckwer, Mass transfer in the liquid phase Fischer-Tropsch synthesis, German Chemical Engineering, 197, Vol. 2, p. 94-102.

21 Reaction block as shown in Figure 4.1 was purchased from HEL group in UK.

22 A. Z. Francesconi and J. H. dAngelo, Gas-liquid solubility of hydrogen in n-alcohols; J. Chem. Eng. Data, 2001, Vol. 46, p. 671-674.

23 R. V. Chaudhari, M. S. Kulkarni, M. J. Vaidya, M. J., Synthesis of p-aminophenol by catalytic hydrogenation of p-nitrophenol, Organic Process Research & Development, 2003, Vol. 7, p. 202-208.

24 R.C. Reid, The properties of gases and liquids, McGraw-Hill Publications, 1977, 3rd Edition.

25 Y. Rakymkul, Solubilities and mass transfer coefficients of gases in heavy synthetic hydrocarbon liquids, University of Pittsburg, 2011.

CHAPTER 5: REACTION KINETICS

5.1 Introduction

Halo-nitroaromatic reduction takes place in a slurry reactor over a heterogeneous catalyst with particle diameters typically smaller than 50 μm, with the introduction of hydrogen in the headspace of the batch reactor. Such reactions exhibit a complex kinetic behavior and require a careful reaction rate control, as they produce highly energetic intermediates, such as hydroxylamines, that pose a safety concern upon scale-up. In addition, there are significant mass transfer challenges in such reactions resulting from the need to transfer the hydrogen from the headspace of the reactor into the liquid phase, and then onto the catalyst surface. Mass transfer rates in such reactions play a key role in process safety. Previous work of F. Visentin [1], using calorimetric measurements and hydrogen gas uptake for such reactions, has not clearly identified the role of mass transfer and the resulting reaction pathway, along with the formation of various intermediates, such as hydroxylamine. In addition, the mechanism for the formation of the dehalogenated aniline byproducts in these reactions has not been clearly identified. Such impurities can pose a quality risk for pharmaceutical products, thereby, risking a batch failure.

In order to understand and control the intermediates concentrations (such as hydroxylamine), as well as the impurity (des-F), it is essential to understand the overall reaction mechanism as shown in Figure 5.1. The reaction mechanism is sub-divided into the following three main pathways:

a) Formation of aniline [D] via conversion of nitro aromatic [A] and hydrogenolysis of hydroxylamine [C] ([C] to [D] directly)
b) Formation of azo-oxy intermediate [E] and subsequent hydrogenation to make azo [F], di-azo- [G], and final reduction to aniline [D] ([C] through [E], [F], [G] to [D])

c) Formation of the des-F impurity [I] by de-fluorination of the nitro [A] followed by reduction to form the des-F aniline [I] , or des-F of aniline product [D] to [I]

To establish a kinetic model, it was essential to understand the dominant pathway the reaction takes for the product formation. It was also critical to understand the reaction order with respect to hydrogen and catalyst concentration. Finally, it was important to understand whether the reaction was in mass transfer limited regime, intrinsic kinetic limited regime, or both mass transfer and kinetic control regimes. A series of experiments were performed to address these questions.

The scope of this chapter is, therefore, to discuss the general model for the three-phase nitro reduction and to investigate the role of reaction kinetics, mass transfer rate, and the resulting reaction pathway such reactions exhibit. In addition, a kinetic rate model is postulated, based on several assumptions, and the validity of this model will be investigated, either by calculations or by kinetic measurement, as described in the latter part of this chapter.

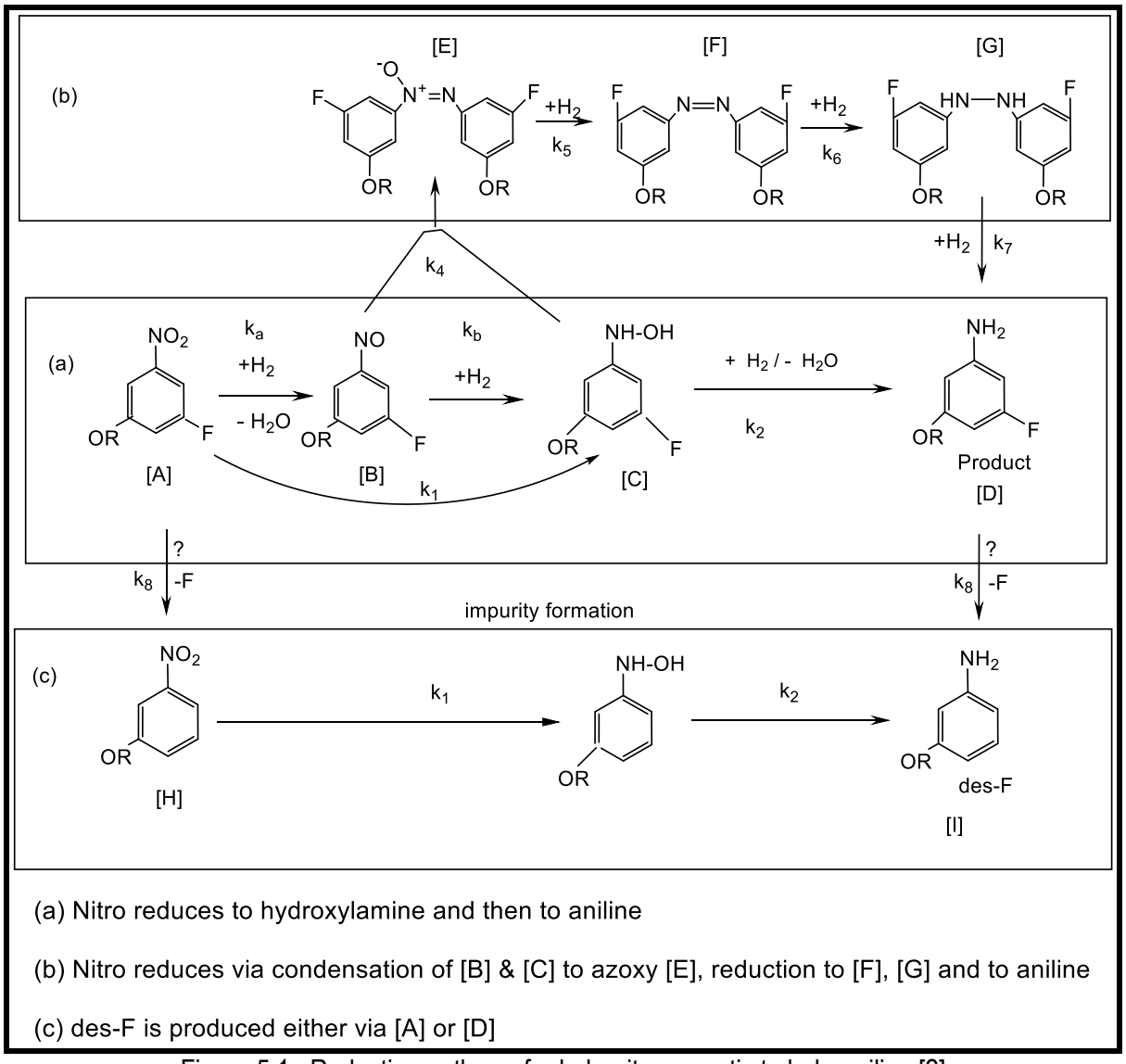

(a) Nitro reduces to hydroxylamine and then to aniline

(b) Nitro reduces via condensation of [B] & [C] to azoxy [E], reduction to [F], [G] and to aniline

(c) des-F is produced either via [A] or [D]

Figure 5.1: Reduction pathway for halo-nitroaromatic to halo-aniline [2]

5.2 Theoretical Background

For a given three-phase slurry reactor, a general model for nitro reduction over a Pd/C catalyst with hydrogen in the liquid phase was developed. The model incorporates various physical and chemical steps that can occur in a three-phase reaction system (Figure 5.2). The chemical reaction rate expression is based on Langmuir-Hinshelwood theory, with adsorption of hydrogen and nitro aromatic [A] on different active sites of the catalyst.

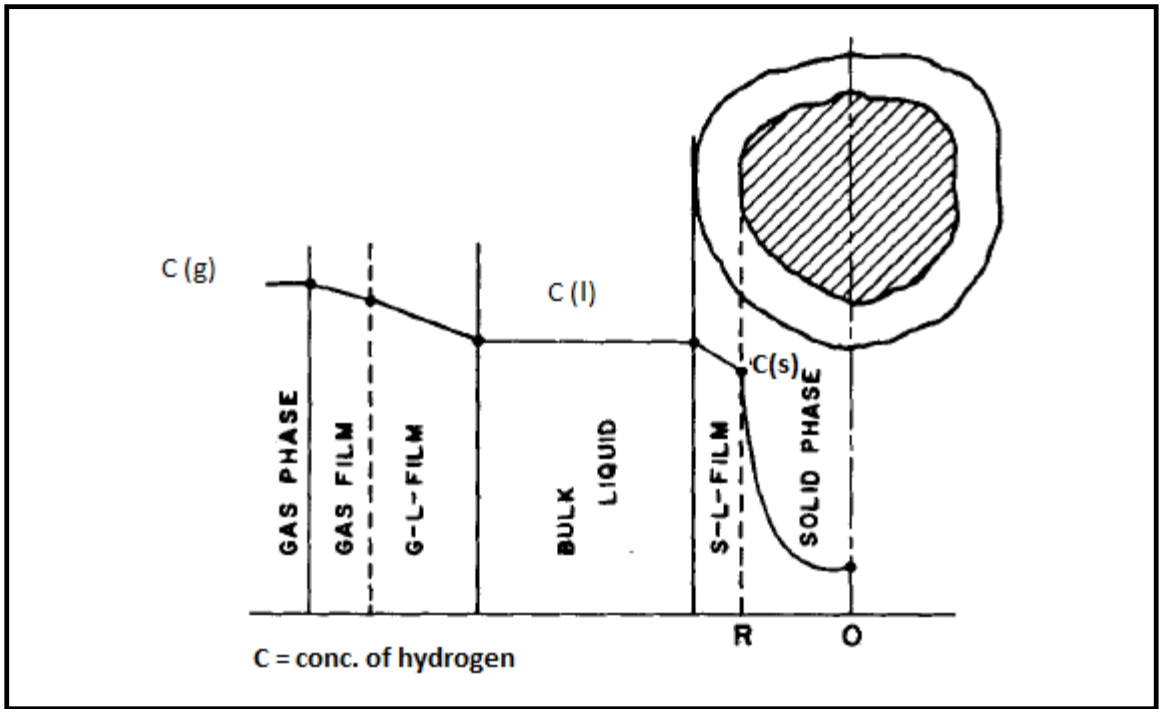

Figure 5.2: Physical and chemical steps of a three-phase hydrogenation [**3**]

5.2.1 Kinetic Model

For the reduction of nitro aromatic [A] to aniline [D], the only major intermediate (>2%) identified was hydroxylamine [C], as shown in Figure 5.1. For such reaction, the reaction steps can be written as:

$$[A] + [H_2] \xrightarrow{k_a/-H_2O} [B] + [H_2] \xrightarrow{k_b/+H_2} [C] + [H_2] \xrightarrow{k_c/-H_2O} [D] \quad [5.1]$$

In this kinetic analysis, it will be assumed that all intrinsic adsorption/desorption steps on the catalyst surface for all species (H_2, A, B, C and D) are much faster than the chemical reaction steps involving adsorbed aromatic species and hydrogen in the liquid phase. As a result, all adsorption/desorption steps are assumed to be in equilibrium.

It is also assumed that hydrogen adsorbs to the catalyst surface to catalytic sites that are different from those to which all the aromatic species can bind [4 - 5]. The aromatic species A, B, C, and D are all assumed to bind to the same binding type of binding sites for aromatics.

The elementary step for adsorption/desorption of [A] on active catalytic site $[\theta_*]$ can be written as:

$$A + \theta_{1*} \overset{K_A}{\leftrightarrow} \theta_A \quad [5.2]$$

where K_A is the equilibrium constant for adsorption of [A], $[\theta_{1*}]$ is the fraction of aromatic binding sites that are vacant, and $[\theta_A]$ is the is the fraction of aromatic binding sites occupied by [A].

Similarly, the adsorption/desorption of [B], [C], and [D] on the aromatic sites can be written as:

$$B + \theta_{1*} \overset{K_B}{\leftrightarrow} \theta_B \quad [5.3]$$

$$C + \theta_{1*} \overset{K_C}{\leftrightarrow} \theta_C \quad [5.4]$$

$$D + \theta_{1*} \overset{K_D}{\leftrightarrow} \theta_D \qquad [5.5]$$

where K_B, K_C and K_D are the equilibrium constants for adsorption of [B], [C] and [D], respectively.

Similarly, the adsorption/desorption of hydrogen from the liquid phase to the surface of the catalyst can be written as:

$$H_2 + \theta_{2*} \overset{K_H}{\leftrightarrow} \theta_H \qquad [5.6]$$

Where K_H is the adsorption equilibrium constant, [θ_{2*}] is the fraction of hydrogen binding sites that are vacant and [θ_H] is the fraction of hydrogen binding sites occupied by hydrogen.

Once [A] is absorbed onto the active catalyst aromatic site [θ_A], it is assumed that it can react with hydrogen to form the intermediate (nitroso – [B]) that is then instantaneously reacts with another mole of hydrogen and forms hydroxylamine – [C], which remains bound on the aromatic binding site. Finally, one mole of hydrogen reacts with [C] to form the product [D].

$$\theta_A + \theta_H \overset{k_a}{\rightarrow} \theta_B + H_2O \qquad [5.7]$$

$$\theta_B + \theta_H \overset{k_b}{\rightarrow} \theta_C \qquad [5.8]$$

$$\theta_C + \theta_H \overset{k_c}{\rightarrow} \theta_D \qquad [5.9]$$

The reaction rate for hydrogenation of [A] can be written as:

$$-r_A \left(\frac{mol}{L\ min}\right) = \eta\, m_k\, k_a\, [\theta_A]\, [\theta_H] \qquad [5.10]$$

Where $\eta = 1$(for egg shell catalyst) and m_k is defined as the amount of catalyst (wt% of catalyst per gram of [A])

The reaction rate for hydrogenation of [B] can be written as:

$$r_B \left(\frac{mol}{L\ min}\right) = \ m_k\ k_a\ [\theta_A]\ [\theta_H] - \ \ m_k\ k_b\ [\theta_B]\ [\theta_H] \qquad [5.11]$$

Furthermore, since the intermediate [B] is not observed under HPLC conditions in any appreciable quantity (<0.1%), it is assumed that it reacts rapidly with one mole of hydrogen to form the hydroxylamine [C] intermediate. The above equation is written as:

$$r_B \left(\frac{mol}{L\ min}\right) \cong 0 \quad and \quad k_a\ [\theta_A]\ [\theta_H] = \ k_b\ [\theta_B]\ [\theta_H] \qquad [5.12]$$

Similarly, the reaction rates for hydrogenation of [C] and [D] are written as:

$$r_C \left(\frac{mol}{L\ min}\right) = \ m_k\ k_a\ [\theta_A]\ [\theta_H] - \ \ m_k\ k_c\ [\theta_C]\ [\theta_H] \qquad [5.13]$$

$$r_D \left(\frac{mol}{L\ min}\right) = \ \ \ m_k\ k_c\ [\theta_C]\ [\theta_H] \qquad [5.14]$$

By definition, the fraction of all aromatic catalyst binding sites that are free and bound to A, C, D add up to one:

$$1 = [\theta_{1*}] + [\theta_A] + \ [\theta_C] + \ [\theta_D] \qquad [5.15]$$

Similarly, the fractions of all hydrogen binding sites that are free and bound to hydrogen also, add up to one:

$$1 = [\theta_{2*}] + [\theta_H] \qquad [5.16]$$

The equilibrium binding constants for the adsorption of [A], [C] and [D], are defined according to these equations:

$$[\theta_A] = K_A * [\theta_{1*}] * [C_{Al}] \qquad [5.17]$$

$$[\theta_C] = K_C * [\theta_{1*}] * [C_{Cl}] \qquad [5.18]$$

$$[\theta_D] = K_D * [\theta_{1*}] * [C_{Dl}] \qquad [5.19]$$

where C_{Al}, C_{Cl}, and C_{Dl} are the bulk liquid concentration for species [A], [C] and [D], respectively.

Combining and rearranging Equations 5.15-5.19, we get an expression for the fraction of 'vacant' aromatic catalyst binding site $[\theta_{1*}]$ surface concentration as:

$$[\theta_{1*}] = \frac{1}{(1 + \mathrm{K}_{\mathrm{A}} C_{Al} + \mathrm{K}_{\mathrm{C}} C_{Cl} + \mathrm{K}_{\mathrm{D}} C_{Dl})} \qquad [5.20]$$

Similarly, the fraction of hydrogen binding sites that are bound to hydrogen is give as:

$$[\theta_H] = \frac{\mathrm{K}_H C_{Hl}}{(1 + \mathrm{K}_H C_{Hl})} \qquad [5.21]$$

where C_{Hl} is the bulk liquid concentration for [H_2] species.

Substituting for $[\theta_A]$ from Eq. 5.17 and 5.20, and $[\theta_{1*}]$ from Eq. 20 into Eq. 5.11, we get:

$$-r_A \left(\frac{\text{mol}}{\text{L min}}\right) = \left[\frac{m_k \ k_1 \ \text{K}_\text{A} \ C_{Al}}{1 + \text{K}_\text{A} C_{Al} + \ \text{K}_\text{C} \ C_{Cl} + \ \text{K}_\text{D} \ C_{Dl}}\right] \quad [5.22]$$

Similarly, the rate of disproportionition (r_c) of hydroxylamine and the rate of product formation (r_D), from Eq. 5.18 through 5.20 and inserting into Eq. 13 and Eq. 14, respectively, can be written as:

$$r_C \left(\frac{\text{mol}}{\text{L min}}\right) = \ m_k \left[\frac{k_1 \ \text{K}_\text{A} \ C_{Al} \ - \ k_2 \ \text{K}_\text{C} \ C_{Cl}}{1 + \text{K}_\text{A} C_{Al} + \ \text{K}_\text{C} \ C_{Cl} + \ \text{K}_\text{D} \ C_{Dl}}\right] \quad [5.23]$$

$$r_D \left(\frac{\text{mol}}{\text{L min}}\right) = \ m_k \left[\frac{k_2 * \text{K}_\text{C} \ C_{Cl}}{1 + \text{K}_\text{A} C_{Al} + \ \text{K}_\text{C} \ C_{Cl} + \ \text{K}_\text{D} \ C_{Dl}}\right] \quad [5.24]$$

where k_1 and k_2 are the rate constant written as:

$$k_1 = k_a \theta_H \quad = \ k_a \left[\frac{K_H C_{Hl}}{1 + K_H \ C_{Hl}}\right] \quad [5.25]$$

$$k_2 = k_c \ \theta_\text{H} = \ k_c \ \left[\frac{K_H C_{Hl}}{1 + K_H \ C_{Hl}}\right] \quad [5.26]$$

where k_1 *and* k_2 contains the intrinsic rate constants ($k_a \ and \ k_c$), and the hydrogen term as described earlier.

Also, C_{Al}, C_{Cl}, C_{Dl}, and K_A, K_C, K_D are the concentrations in the liquid phase and the equilibrium constants for A, C or D, respectively; k_1 and k_2 are the reaction rate constants as described in Equations 5.25 and 5.26, respectively; k_a and k_c are intrinsic rate constants, and m_k is the concentration of the catalyst in the reaction mixture. Table 5.1 summarizes the kinetic rate equation and the rate constants for the kinetic control regime.

Table 5.1: Kinetic Control Rate Model

$$-r_A\left(\frac{\text{mol}}{\text{L min}}\right) = \left[\frac{m_k\ k_1\ \text{K}_\text{A}\ C_{Al}}{1 + \text{K}_\text{A} C_{Al} + \text{K}_\text{C}\ C_{Cl} + \text{K}_\text{D}\ C_{Dl}}\right] \qquad r_C\left(\frac{\text{mol}}{\text{L min}}\right) = m_k\left[\frac{k_1\ \text{K}_\text{A}\ C_{Al} - k_2\ \text{K}_\text{C}\ C_{Cl}}{1 + \text{K}_\text{A} C_{Al} + \text{K}_\text{C}\ C_{Cl} + \text{K}_\text{D}\ C_{Dl}}\right]$$

$$r_D\left(\frac{\text{mol}}{\text{L min}}\right) = m_k\left[\frac{k_2\ \text{K}_\text{C}\ C_{Cl}}{1 + \text{K}_\text{A} C_{Al} + \text{K}_\text{C}\ C_{Cl} + \text{K}_\text{D}\ C_{Dl}}\right] \qquad [\theta_A] = \frac{K_A\ C_{Al}}{(1 + \text{K}_\text{A} C_{Al} + \text{K}_\text{C}\ C_{Cl} + \text{K}_\text{D}\ C_{Dl})}$$

$$[\theta_C] = \frac{K_C\ C_{Cl}}{(1 + \text{K}_\text{A} C_{Al} + \text{K}_\text{C}\ C_{Cl} + \text{K}_\text{D}\ C_{Dl})} \qquad [\theta_D] = \frac{K_D\ C_{Dl}}{(1 + \text{K}_\text{A} C_{Al} + \text{K}_\text{C}\ C_{Cl} + \text{K}_\text{D}\ C_{Dl})}$$

$$[\theta_H] = \frac{\text{K}_H C_{Hl}}{(1 + \text{K}_H C_{Hl})} \qquad C_{Hl} = C_{Hg}\,\text{f}(\text{P}, \text{T})$$

$$k_1 = k_\text{a}\,\theta_H \qquad k_2 = k_\text{c}\,\theta_\text{H}$$

Where K_A, K_C, K_D, K_H, k_1 and k_2 are the equilibrium and reaction rate constants.

5.2.2 Mass Transfer Limited Regime

In a steady state chemical reaction, the molar rate of reaction should equal the stoichiometric rates of adsorption and mass transfer for the individual specie. The steady state reaction rate for the mass transfer limited regime based upon the physical and chemical steps for the nitro reduction to aniline, as shown in Figure 5.1, can be derived using the following assumptions:

1) The rate of [H_2] mass transfer across the gas-liquid interface is given by:

$$-r_H \left(\frac{mol}{L * min}\right) = [k_L a]_H \left[C_{Hg} - C_{Hl}\right] \qquad [5.27]$$

where $r_H, k_L a, C_{Hg}, and\ C_{Hl}$ are the rate of hydrogenation, gas-liquid mass transfer coefficient, the concentration of H_2 in gas and bulk liquid phases, respectively.

2) From equation 5.21, the fraction site absorbed by hydrogen $[\theta_H]$ is given as:

$$\theta_H = \left[\frac{K_H C_{Hl}}{1 + K_H\ C_{Hl}}\right] \qquad [5.28]$$

where, K_H and C_{Hl} are the equilibrium adsorption constant and the concentration of hydrogen in the liquid phase, respectively.

Under the mass transfer regime, the gas-liquid mass transfer resistance for H_2 across the interface is large (i.e. C_{Hl} <<< C_{Hg}), hence $-r_H$ and θ_H simplifies to (as $1 \gg K_H\ C_{Hl}$):

$$-r_H \left(\frac{mol}{L * min}\right) = [k_L a]_H \left[C_{Hg}\right]\ and\ \ \theta_H = K_H C_{Hl} \qquad [5.29]$$

3) Furthermore, there are three moles of H_2 consumed for every mole of D formed. For every mole of A reacting, two moles of H_2 are consumed. As a result, the rates of reaction of A and D can be related to the rate of disappearance of H_2 in the reaction as:

$$-r_A = \frac{2}{3}\,(-r_H) \qquad [5.30]$$

$$r_D = \frac{1}{3}\,(-r_H) \qquad [5.31]$$

4) From Equations 5.22, 5.29 and 5.30, we get :

$$\left[\frac{m_k\ k_1\,\mathrm{K_A}\,C_{Al}}{1+\mathrm{K_A}C_{Al}+\ \mathrm{K_C}\,C_{Cl}+\ \mathrm{K_D}\,C_{Dl}}\right] = \frac{2}{3}\ \left[k_L a\right]_H \left[C_{Hg}\right]$$

$$k_1 = \frac{2}{3}\ \ \frac{1+\mathrm{K_A}C_{Al}+\ \mathrm{K_C}\,C_{Cl}+\ \mathrm{K_D}\,C_{Dl}}{m_k\ \ \mathrm{K_A}\,C_{Al}}\left[C_{Hg}\right]\ \left[k_L a\right]_H$$

$$k_1 = G_1'\ \left[k_L a\right]_H \qquad [5.32]$$

Where, the kinetic terms are grouped along with the constants into G_1', and now substituting for k_1 from Eq. 5.25 and simplifying θ_H from Eq. 5.29 we get:

$$-r_A\left(\frac{\mathrm{mol}}{\mathrm{L\ min}}\right) = \left[\frac{m_k\ k_1\,\mathrm{K_A}\,C_{Al}}{1+\mathrm{K_A}C_{Al}+\ \mathrm{K_C}\,C_{Cl}+\ \mathrm{K_D}\,C_{Dl}}\right] \qquad [5.33]$$

Where $k_1 = G_1'\ \left[k_L a\right]_H$ in mass transfer limited regime;

Similarly, Equation 5.23 and 5.24 equates to:

$$r_C \left(\frac{\text{mol}}{\text{L min}}\right) = m_k \left[\frac{k_1 \ \text{K}_\text{A} \ C_{Al} \ - \ k_2 \ \text{K}_\text{C} \ C_{Cl}}{1 + \text{K}_\text{A} C_{Al} + \ \text{K}_\text{C} \ C_{Cl} + \ \text{K}_\text{D} \ C_{Dl}}\right] \qquad [5.34]$$

$$r_D \left(\frac{\text{mol}}{\text{L min}}\right) = m_k \left[\frac{k_2 \ \text{K}_\text{C} \ C_{Cl}}{1 + \text{K}_\text{A} C_{Al} + \ \text{K}_\text{C} \ C_{Cl} + \ \text{K}_\text{D} \ C_{Dl}}\right] \qquad [5.35]$$

Where $k_1 = G_1' \ [k_L a]_H$ and $k_2^{"} = G_2' \ [k_L a]_H$; and $G_1' \ and \ G_2'$ are the constants summarized in the Table 5.2.

Table 5.2 summarizes the kinetic rate equation and the rate constants for the mass transfer limited regime.

Table 5.2: Mass Transfer Limited Rate Model

$$-r_A\ (\frac{\text{mol}}{\text{L min}}) = \left[\frac{m_k\ k_1\ \text{K}_\text{A}\ C_{Al}}{1 + \text{K}_\text{A} C_{Al} + \text{K}_\text{C}\ C_{Cl} + \text{K}_\text{D}\ C_{Dl}}\right] \qquad r_C\ (\frac{\text{mol}}{\text{L min}}) = m_k \left[\frac{k_1\ \text{K}_\text{A}\ C_{Al} - k_2\ \text{K}_\text{C}\ C_{Cl}}{1 + \text{K}_\text{A} C_{Al} + \text{K}_\text{C}\ C_{Cl} + \text{K}_\text{D}\ C_{Dl}}\right]$$

$$r_D\ (\frac{\text{mol}}{\text{L min}}) = m_k \left[\frac{k_2\ \text{K}_\text{C}\ C_{Cl}}{1 + \text{K}_\text{A} C_{Al} + \text{K}_\text{C}\ C_{Cl} + \text{K}_\text{D}\ C_{Dl}}\right] \qquad [\theta_A] = \frac{K_A C_{Al}}{(1 + \text{K}_\text{A} C_{Al} + \text{K}_\text{C}\ C_{Cl} + \text{K}_\text{D}\ C_{Dl})}$$

$$[\theta_C] = \frac{K_C\ C_{Cl}}{(1 + \text{K}_\text{A} C_{Al} + \text{K}_\text{C}\ C_{Cl} + \text{K}_\text{D}\ C_{Dl})} \qquad [\theta_D] = \frac{K_D C_{Dl}}{(1 + \text{K}_\text{A} C_{Al} + \text{K}_\text{C}\ C_{Cl} + \text{K}_\text{D}\ C_{Dl})}$$

$$[\theta_H] = \text{K}_H C_{Hl} \qquad C_{Hl} = C_{Hg}\, \text{f}\,(\text{P}, \text{T}, \text{k}_\text{L}\text{a})$$

$$k_1 = G_1'\ \ [k_L a]_H \qquad k_2 = G_2'\ \ [k_L a]_H$$

$$G_1' = \frac{2}{3}\ \frac{1 + \text{K}_\text{A} C_{Al} + \text{K}_\text{C}\ C_{Cl} + \text{K}_\text{D}\ C_{Dl}}{m_k\ \ \text{K}_\text{A}\ C_{Al}} [C_{Hg}] \qquad G_2' = \frac{1}{3}\ \frac{1 + \text{K}_\text{A} C_{Al} + \text{K}_\text{C}\ C_{Cl} + \text{K}_\text{D}\ C_{Dl}}{m_k\ \ \text{K}_\text{D}\ C_{Dl}} [C_{Hg}]$$

$$-r_A = \frac{2}{3}\ (-r_H) \qquad r_D = \frac{1}{3}\ (-r_H)$$

Where K_A, K_C, K_D, K_H, k_1 and k_2 are the equilibrium and reaction rate constants.

5.3 Experimental Procedure

This section describes the equipment; materials and reagents; and procedure used for estimating the kinetic and equilibrium rate constants.

5.3.1 Materials and Reagents

High purity hydrogen and nitrogen gas cylinders (purity of 99.999%) were purchased from Airgas Co. and were connected to the reactor. Ethanol, methanol and high purity water were purchased from Aldrich Chemical Company. Halo-nitroaromatic [A] was a GSK proprietary intermediate that was used for these experiments to reduce to aniline. Catalyst (10% Pd/C) was purchased from Evonik Industries.

5.3.2 Equipment (100-mL Reactor)

The lab scale hydrogenator [6] as described in Section 4.4 was used for these experiments. It is equipped with fully automated temperature, pressure, and stirring control. The reactor was made with hastelloy C-276, with a maximum reaction volume of 100-mL and total volume of 185-mL (total liquid + headspace volume). See Figure 4.1 and Section 4.4 for more details. The reactor also had capability to measure hydrogen gas-uptake directly, and was hooked-up with an Infrared high-pressure detection instrument (ReactIR) for online spectra measurements. Offline High Pressure Liquid Chromatography (HPLC) was used to aid and quantify ReactIR concentration profiles.

5.3.3 React IR

React IR (high-pressure infrared instrument a product of Mettler Toledo) was used to analyze individual concentrations in real time for species [A], [C] and [D]. ReactIR is a Fourier Transform Infrared (FTIR) spectroscopy based, high performance, in situ reaction analysis system. React IR is used directly to measure the liquid phase reactant concentrations during hydrogenations. The solid catalyst is often not observed in the spectra, even though the dispersions can be fully opaque (due to carbon-black-supported metal catalysts), and the gas bubbles do not interfere with the measurements (mid-infra red instruments are only affected by solid coating on the window and can see through gas

bubbles). React IR consists of an FTIR instrument box where the data is collected and transferred to the computer for analysis, a fiber optic conduit, and a hastelloy probe with Dicomp diamond sensor. React IR uses the mid-infrared portion of the spectrum for concentration changes over time for a range of wave numbers. This change of the mid-infrared region over time gives us information of real-time concentration profiles. Concentration profiles are further regressed by Chemometrics software (Intelliform), using a curve resolution method (as described in Section 5.3.4.2), and then fitted to the measured HPLC data to give us real-time information of each species concentration. The mid-IR region for the instrument was between 800 and 2000 cm^{-1}, and the peaks are typically well resolved so that the concentration of the chemical species present can be readily determined by measuring the peak height relative to a nearby baseline region that contains no peaks. Mid-IR regions for the nitro aromatic can be found to be around 1530 cm^{-1}, whereas, for the aniline, the mid IR region is around 1620 cm^{-1} [7]. Using advance chemometrics analysis, experiments revealed a new change in the spectra at 1500 cm^{-1}, which was not readily visible from the React IR plot below. This component corresponds to the hydroxylamine intermediate. A typical waterfall-plot of React IR spectra showing the various reaction components can be found in Figure 5.13. Using principal component analysis on the React IR spectra, hydroxylamine was identified by the Intelliform software.

5.3.4 Procedure

This section describes in detail the procedure and analytical method used to estimate the equilibrium and rate constants for the given reaction.

5.3.4.1 Reaction Set-up

In a batch reactor (as shown in Figure 4.1), halo-nitro aromatic [A] was charged (5 grams) along with 10 wt% Pd on C [8] (0.5 grams) catalyst, 22.4 mL of 200-proof ethanol, 24.1 mL of purified water, and 3.1 mL of concentrated HCl. Concentrated HCl was added to dissolve the halo-nitro

aromatic in the reaction solution. The reactor was stirred for 5 minutes at 25°C to dissolve [A] into the solution. The reactor was then purged with nitrogen, followed by hydrogen, to evacuate the reactor headspace from air and nitrogen, respectively. During the pressure purge cycle, the agitation rate was set to zero. The reactor was then pressurized to 60-psig (4-barg) of H_2 pressure, and then agitation was started to allow the reaction to commence. The species concentrations were measured by HPLC grab samples (every 10-30 mins) during the reaction; also, the reaction spectra was collected using the mid-infrared React IR [9] instrument. The hydrogen uptake was directly measured based on the pressure drop in the headspace of the reactor with time. The reaction was deemed complete once the HPLC profile showed less than 0.20% area under curve (AUC) for residual [A] and greater than 98% (AUC) for product [D]. Once the reaction was completed, the reactor was vented off and inerted once again with nitrogen. The catalyst was then filtered off from the reaction solution, for further processing.

A set of experiments were run at different conditions to understand the following:

1. The order of reaction with respect to hydrogen concentration (varying only the pressure between 3-5 bara of hydrogen gas in the headspace), while keeping the agitation rate (815 rpm), the temperature (25°C), the catalyst loading (10 wt%), and the nitro aromatic concentration (0.0109 mol) constant.
2. The order of reaction with respect to catalyst loading (varying only the catalyst loadings from 2.5 - 10.0 wt%) while keeping the agitation rate (815 rpm), the temperature (25°C), the pressure (5 bara of hydrogen gas in the headspace), and the nitro aromatic concentration (0.0109 mol) constant.
3. Mass transfer effects by varying the k_La between 0.10 – 0.60 (1/s), while keeping the temperature (25°C), the pressure (5 bara of hydrogen gas in the headspace), the catalyst loading (10 wt%) and the nitro aromatic concentration (0.0109 mol) constant.

4. Activation energy by varying the temperature between 25-45°C for each set of k_La (from 0.10 – 0.60 1/s), while keeping the pressure (5 bara of hydrogen gas in the headspace), the catalyst loading (10 wt%) and the nitro aromatic concentration (0.0109 mol) constant.
5. The data was fitted to the kinetic model developed previously to test the assumptions.

5.3.4.2 Chemometrics Analysis

React IR spectra were further analyzed using a chemometrics package (Intelliform [10-11]). Analysis involves regressing the data using principal component analysis (PCA) across the spectra for each time interval (between the spectra collection). Three components were identified by the chemometrics techniques, and, then, the species were normalized with respect to the mass balance for each spectrum, so that the sum of the three equals one. This technique is commonly referred to as curve resolution technique. Once the spectra concentration profiles were obtained, they were further analyzed from the measured HPLC concentration to obtain the concentration values with respect to time.

5.4 Results and Discussion

In order to estimate the equilibrium and reaction rate constants, it is vital to understand the reaction order with respect to hydrogen concentration and catalyst loading. Once that is well understood, it becomes imperative to understand whether the reaction is gas-liquid; liquid-solid; and/or kinetically limited. As seen earlier, the governing rate equations would vary depending upon the rate limiting step. In addition, activation energies were also measured at these reaction conditions. The results indicated that for a heterogeneous catalytic reactions that have activation energy (Ea) ≤ 5 kJ/mol are often diffusion-limited processes; Ea in the range of 5-15 kJ/mol can be either kinetic-limited

or diffusion-limited processes; and Ea ≥ 15 kJ/mol are intrinsic kinetic-limited processes (base on work from Bartholomew and Farrauto [12]). Finally the reaction equilibrium and rate constants are evaluated and fitted against the experimentally data to evaluate the kinetic understanding mentioned earlier.

5.4.1 Reaction Order

A reaction order with respect to hydrogen headspace pressure and catalyst concentration is established in this section.

5.4.1.1 Hydrogen Pressure Effects

A series of experiments was run, varying the hydrogen pressures in the headspace (3, 4, and 5 bar absolute (bara), respectively), while keeping the agitation rate (815 rpm), temperature (25°C), catalyst loading (10 wt%), and the nitro aromatic concentration (0.0109 mol) constant. The overall reaction rate was calculated from the hydrogen uptake measurements, as shown in Equation 5.36 as:

$$-r_H\left(\frac{mol}{L\ min}\right) = \frac{d[H_2]}{dt} \qquad [5.36]$$

The plot of hydrogen uptake vs. time shows a linear H_2 uptake for the reaction, as shown in Figure 5.3. The global reaction rate is given by the slope of the line as given by Eq.5.36, and shown in Table 5.3 and Figure 5.4. It was shown that, for the operating conditions studied, Henry's law was valid [13-14]. Figure 5.4 shows that the reaction rate is a linear function of H_2 pressure passing through the origin, thereby, indicating first-order behavior of hydrogen at tested pressures.

Table 5.3: Rate of reaction at varying H_2 pressure

H_2 Pressure (bara)	rate (-rH) mol /(L*min) X 10 -4
5	12.4
4	9.7
3	7.5

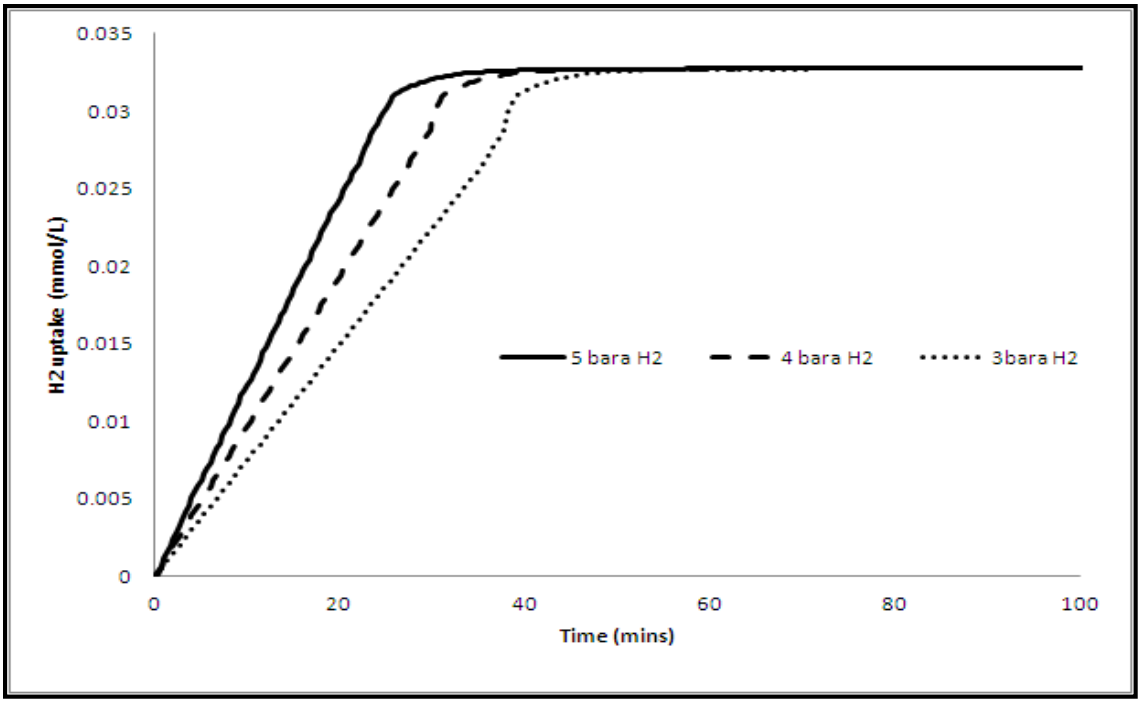

Figure 5.3: Hydrogen uptake rate for various experiments at different H_2 pressure

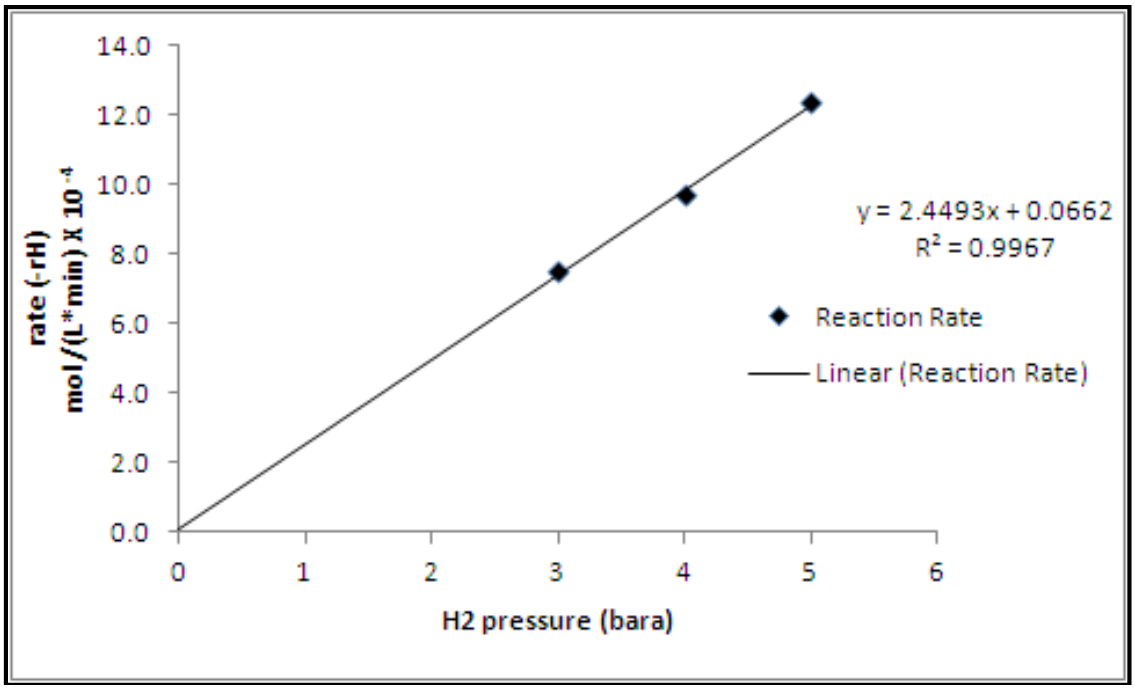

Figure 5.4: Rate of reaction at varying H_2 pressure

5.4.1.2 Catalyst Loading Effects

In another set of experiments, the amount of catalyst was varied (2.5 wt%, 5 wt%, 10 wt%) to understand the order of reaction with respect to catalyst concentration, by keeping the substrate concentration (0.0109 mol), agitation rate (815 rpm), reaction temperature (25°C), and hydrogen pressure (5 bara) constant. The overall reaction rate was calculated from the hydrogen uptake measurements, as shown in Equation 5.36.

Figure 5.5 shows the hydrogen uptake vs. time for different catalyst loading experiments, and it is a linear function of catalyst loading. Also, it can be seen in Figure 5.6 that the reaction rate doubles when the catalyst loading is doubled from 2.5 wt% to 5.0 wt%, and then from 5.0 wt% to 10.0 wt% loading. This confirms the first-order behavior in the catalyst. This further indicates that gas-liquid mass transfer resistance is not significant under these reaction conditions as described by Chaudhari et. al [15].

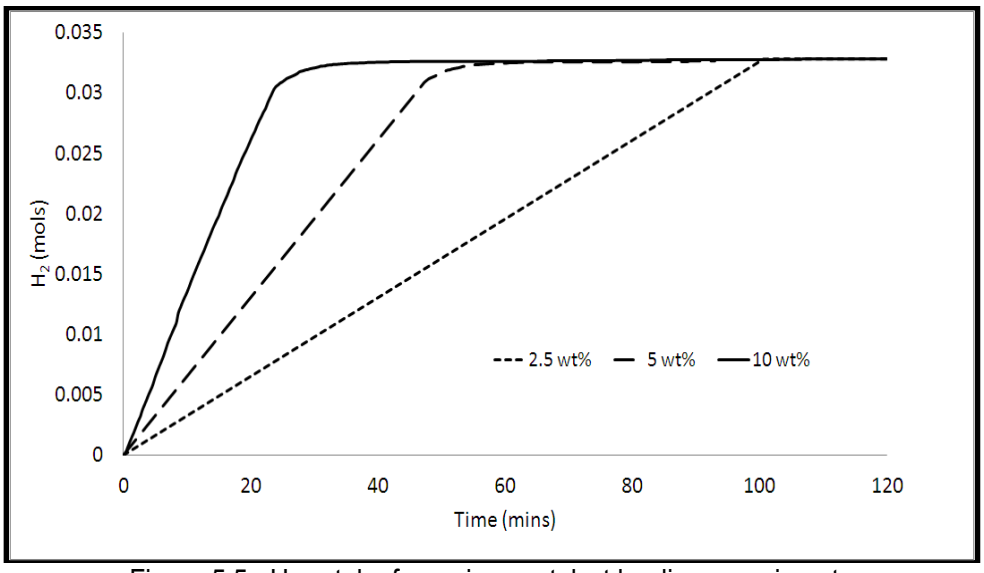

Figure 5.5: H_2 uptake for various catalyst loading experiments

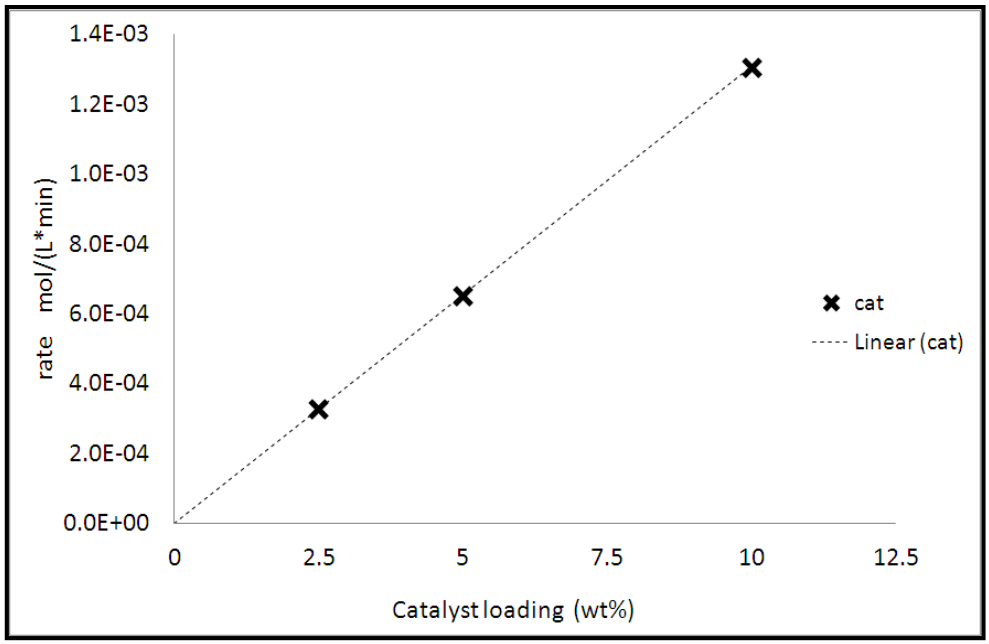

Figure 5.6: Reaction rate vs. catalyst loading

5.4.2 Gas-Liquid (G-L) Mass Transfer Effect

In order to understand whether the reaction was kinetically or gas-liquid mass transfer limited, several reactions were run varying mass transfer coefficient (k_La), while keeping the other parameters (H_2 pressure 4 barg, temperature at 25°C, catalyst loading at 10 wt%, and substrate concentration at 0.0109 mols) constant. The mass transfer coefficients were varied between 0.10 - 0.60 (1/s). Figure 5.7 shows the hydrogen uptake vs. time for various k_La runs. The reaction rate was calculated from the overall hydrogen uptake, as given in Equation 5.36.

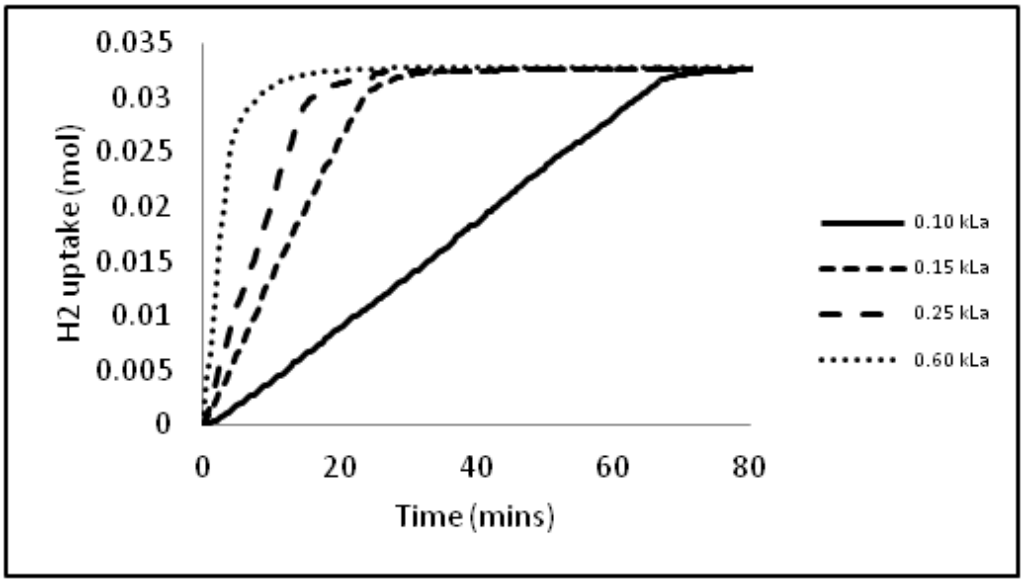

Figure 5.7: Hydrogen uptake vs. time for various k_La at 25°C

Figure 5.7 shows that there is a large increase in reaction rate observed when k_La is increased from 0.10 to 0.60 (1/s). Figure 5.8 shows that the reaction rate is almost constant between the k_La values of 0.15 and 0.60 (1/s), but it sharply decreases below a k_La of 0.15 (1/s). The results indicate:

a) Reaction is mass transfer limited (H_2 concentration in the liquid phase) when $k_La < 0.15$ (1/s);

b) The reaction rate appears to be constant as the k_La was increased from 0.15 to 0.60 (1/s), indicative of a kinetic control regime.

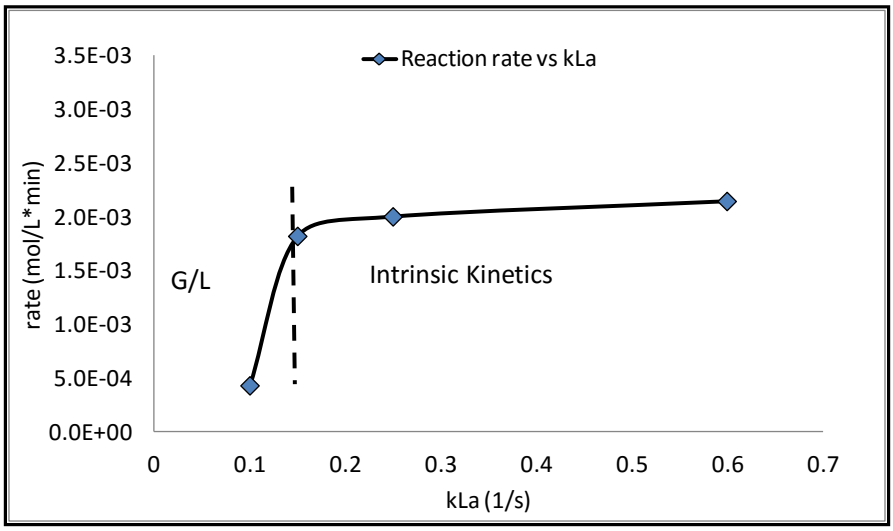

Figure 5.8: Reaction rate vs. k_La at 25°C

To further test this conclusion, calculations suggested by Mills and Chaudhari [16] were used, as seen in Equation 5.37. The gas-liquid mass transfer can be neglected if the ratio of the observed reaction rate (r_H) to the maximum gas-liquid mass transfer rate (γ_1) is < 0.1. The hydrogen solubility for the reaction solvent system (ethanol and water), was calculated using Equation 4.3 as described by Shah et. al [17] (see Chapter 4 Section 4.2.1).

Table 5.4 shows the ratio of the observed reaction rate to the maximum gas-liquid mass transfer rate for various values of k_La. Also, as concluded previously, γ_1 is greater than 0.1 for the reaction that is run at a k_La of 0.10 (1/s), and less than 0.1 for reactions that are run between a k_La of 0.15 to 0.60 (1/s), indicative of a reaction starved of hydrogen at lower than 0.15 k_La (1/s). The maximum gas-liquid mass transfer rates were found to be 74-200 times higher than the observed rate of H_2 consumption for these experiments. Therefore, it can be said that the effect of G-L mass transfer rate on the reaction is insignificant for k_La of 0.15 1/s or higher.

Gas-liquid mass transfer is insignificant if:

$$\gamma_1 = \frac{r_H}{k_L a\ H_2\ [sat]} < 0.1 \qquad [5.37]$$

Table 5.4: Reaction rate versus diffusion rates as suggested by Mills and Chaudhari [15]

k_La (min-1)	rate (-rH) mol /(L*min)	H_2 sat (mol/L) - Eq. [4.3]	k_La^* H_2 sat [mol /(L*min)]	γ_1 rate / (k_La^* H_2 sat)
6	4.29E-04	5.54E-04	0.0033	1.288E-01
9	1.82E-03	4.32E-03	0.0389	4.676E-02
15	2.00E-03	1.30E-02	0.1944	1.029E-02
36	2.14E-03	1.51E-02	0.5443	3.937E-03

5.4.3 Liquid-Solid (L-S) Mass Transfer Effect

Mills and Chaudhari [12] proposed that the liquid-solid (L-S) mass transfer can be neglected, if the ratio of the observed reaction rate (r_H) to the maximum L-S mass transfer rate (γ_2) is < 0.1. The ratio (γ_2) is expressed as:

L-S mass transfer is insignificant if:

$$\gamma_2 = \frac{r_H}{[k_L s]_{A\ or\ H2} * a_p * H_2\ [sat]} < 0.1 \qquad [5.38]$$

where a_p is the ratio of the external surface of the catalyst to the slurry volume (cm^2/cm^3) and was calculated, as given by Bartholomew and Farrauto [8]:

$$a_p = \frac{6 * \text{g of catalyst}}{\rho_a * d_p * \text{Slurry Volume}} \left(\frac{cm^2}{cm^3}\right) \qquad [5.39]$$

$$a_p = 18.55 \frac{cm^2}{cm^3} \text{(For the given system)}$$

A detailed calculation of diffusivities and k_Ls for [A] and [H_2] can be found in Appendix, Section 9.3. Similarly to the G-L resistance, Table 5.5 shows the ratio of the observed reaction rate to the maximum liquid-solid mass transfer rates (for [A] and [H_2]) at various values of k_La. The maximum liquid-solid mass transfer rates were found to be 250-1200 times higher than the observed rate of H_2 consumption for these experiments. Therefore, it can be said that the effect of L-S mass transfer rate on the reaction is insignificant. In addition, the L-S mass transfer rates are 2-4 orders of magnitude larger, when compared to the G-L mass transfer rates, concluding that the L-S is not the rate-limiting step for the reaction.

Table 5.5: Calculation of Gas-Liquid/ Liquid-Solid resistances at various rpm

k_La (min-1)	rate (-rH) mol /(L*min)	H_2 sat (mol/L) - Eq. [4.3]	γ_1 rate / (k_La* H_2 sat)	γ_2 [A] rate / (k_Ls (ap)* [A] sat)	γ_2 [H_2] rate / (k_Ls (ap)* [H_2]sat)	L-S / G-L resistance (k_Ls/k_La)
6	4.29E-04	5.54E-04	1.29E-01	4.01E-05	2.17E-06	5.95E+04
9	1.82E-03	4.32E-03	4.68E-02	1.70E-04	9.19E-06	5.09E+03
15	2.00E-03	1.30E-02	1.03E-02	1.87E-04	1.01E-05	1.02E+03
36	2.14E-03	1.51E-02	3.94E-03	2.01E-04	1.08E-05	3.63E+02
	[A] sat	1.09E-02	mol/L	[H2]sat	0.01512	mol/L

5.4.4 Activation Energy

Another method used to determine the reaction limitation is the measurement of the activation energy, which gives an indication of whether the reaction is mass transfer or kinetically limited, as described by Bartholomew and Farrauto [8]. Three different sets of experiments, varying k_La and temperatures, were used to evaluate this phenomenon. Mass transfer coefficients of 0.10, 0.15, and 0.60 (1/s) were selected, and for each selected k_La, three experiments were run at 25°C, 35°C, and 45°C, respectively, to obtain activation energy values at those agitation rates. The rate constant was obtained from the slope of hydrogen uptake, as given by equation 5.36. The activation energy was calculated by plotting Ln (k) vs. 1/T, and is given in equation 5.33 and plotted in Figure 5.9:

$$Slope = Ln\ \frac{k}{\left[\frac{1}{T}\right]} = \frac{Ea}{R} \qquad [5.40]$$

where Ea= Activation energy, R=gas constant = 8.314 J/mol*K, k= rate constant, and T is temperature in Kelvin.

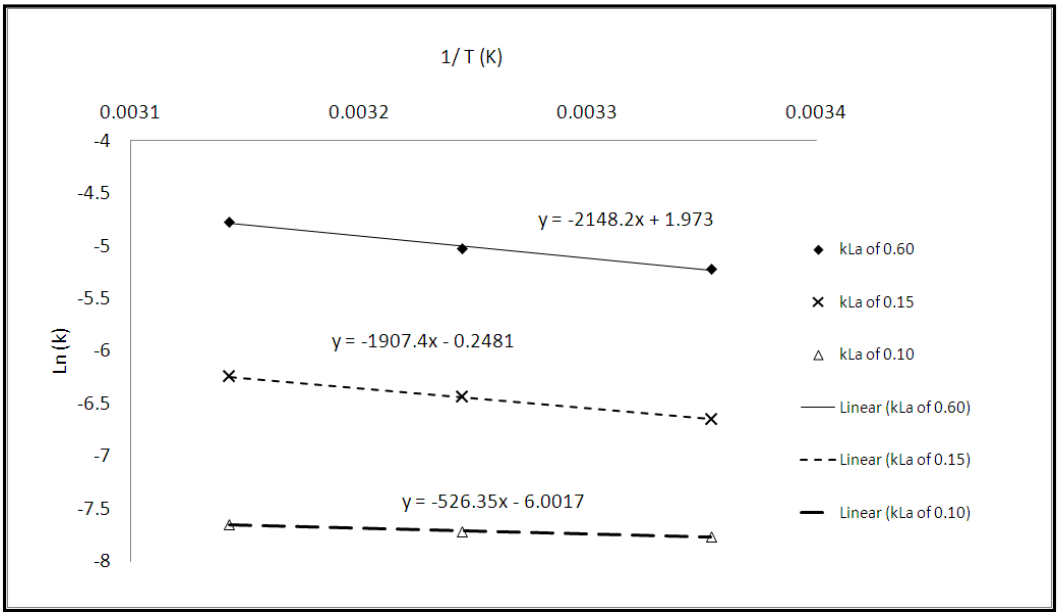

Figure 5.9: Ln[k] versus 1/T

Figure 5.10 (a) through (c) show hydrogen uptake rate versus time for 0.10, 0.15, and 0.60 (1/s) k_La, respectively. At a k_La of 0.10 (1/s), it can be observed that, the hydrogen uptake rate is similar for the three temperature runs (25-45°C). Similarly, at a higher k_La's (0.15 1/s and 0.60 1/s), the hydrogen uptake rate increases as the temperature increases. Activation energies calculated for various sets of k_La experiments are tabulated in Table 5.6. A plot of activation energy versus G-L mass transfer coefficient is also shown in Figure 5.11. It can be concluded that Figure 5.11 has a very similar profile compared to Figure 5.8, thereby, defining the gas-liquid mass transfer control regime below 0.15 (1/s) k_La and a kinetic control regime above 0.15 (1/s) k_La.

Figure 5.10: Hydrogen uptake vs. time at various k_La's

a) Hydrogen uptake rate vs. time at 0.10 (1/s) k_La

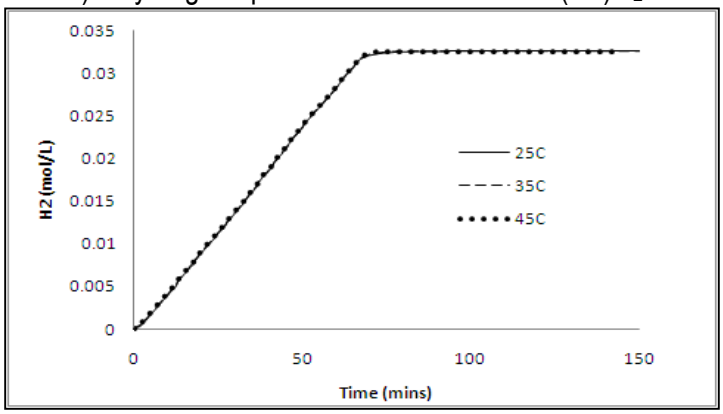

b) Hydrogen uptake rate vs. time at 0.15 (1/s) k_La

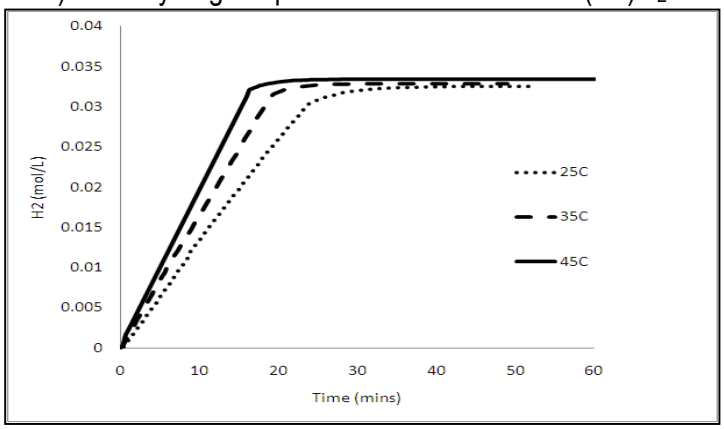

c) Hydrogen uptake rate vs. time at 0.60 (1/s) k_La

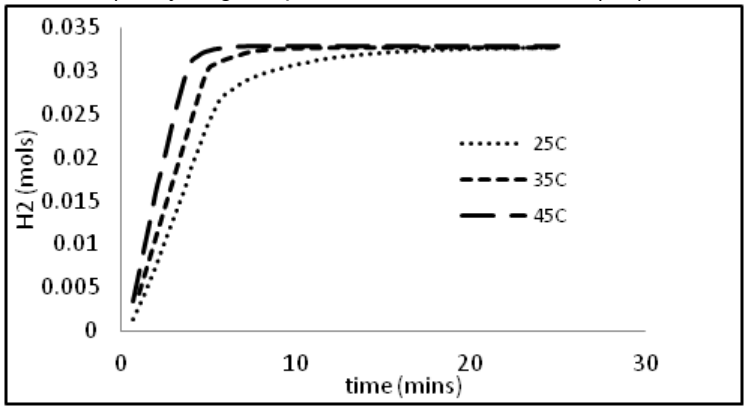

Table 5.6: Activation Energies versus k_La (1/s)

k_La (1/s)	Ea (kJ/mol)
0.10	4.38
0.15	15.85
0.60	17.86

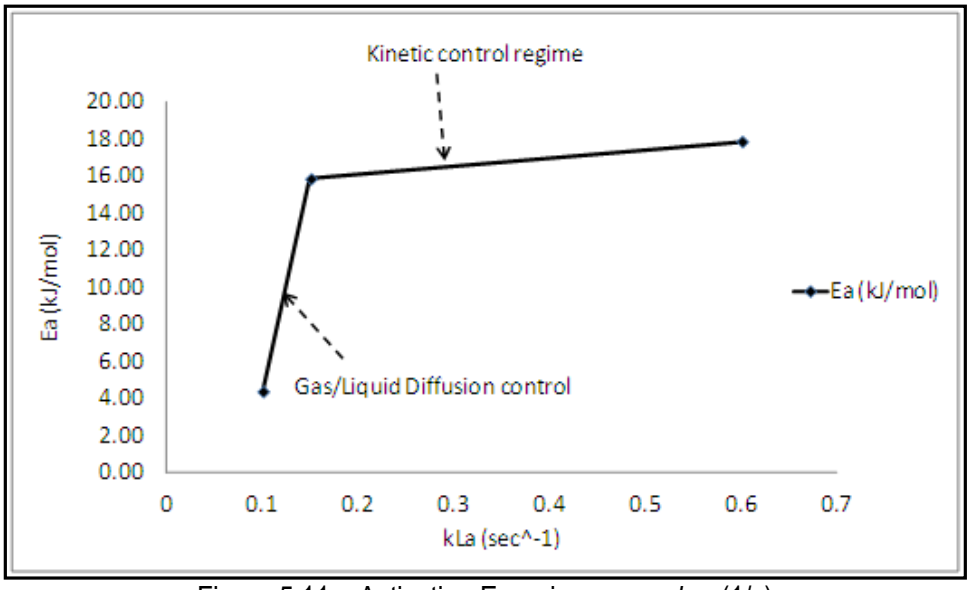

Figure 5.11: Activation Energies versus k_La (1/s)

5.4.5 Kinetic Modeling

As reaction kinetic is found to be the rate limiting step for mass transfer coefficient (k_La) region 0.15 (1/s) and higher, kinetic modeling will be performed in this region between 0.15-0.60 (k_La) 1/s using the equations shown in Table 5.1.

5.4.5.1 Reaction Profile

A typical reaction profile is shown in Figure 5.12. The conditions for the reaction were 4-barg H_2 pressure, temperature of 25°C, and 1150 rpm (~0.60 1/s k_La). The individual species concentrations were obtained from React IR along with HPLC [18] analysis. The reaction profile shows three main components (>2% AUC for HPLC analysis): the nitro aromatic [A], hydroxylamine [C], and the aniline [D] product. The sum for the remaining species ([E], [F], and [G]), as described in Figure 5.1, were under two percent (AUC) and were being ignored from the kinetic model. Similarly, the impurity [I], typically found to be less than 0.5% AUC, was also ignored for kinetics modeling, leaving for consideration only the main reaction of [A] converting to [D] via [C].

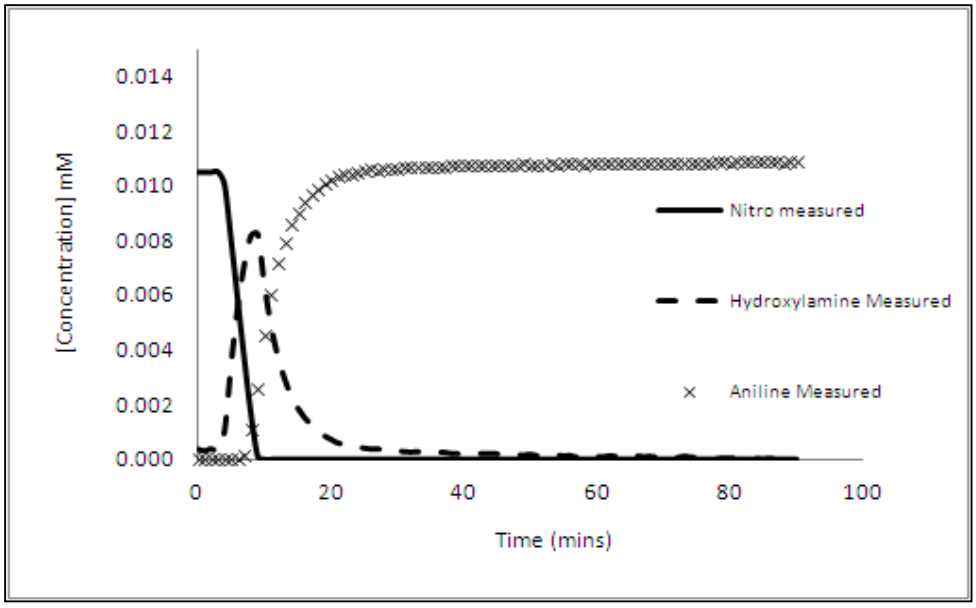

Figure 5.12: Reaction profile showing various concentrations vs. time (at 25°C, 0.60 1/s k_La)

A typical React IR plot is as shown in Figure 5.13. Chemometrics analysis is performed on the spectra data sets to obtain the concentration versus time as shown in Figure 5.14. Pure component spectrums for these three reacting species (nitroaromatic [A], hydroxylamine [C], and aniline [D]) are obtained from chemometrics analysis as shown in Figure 5.15.

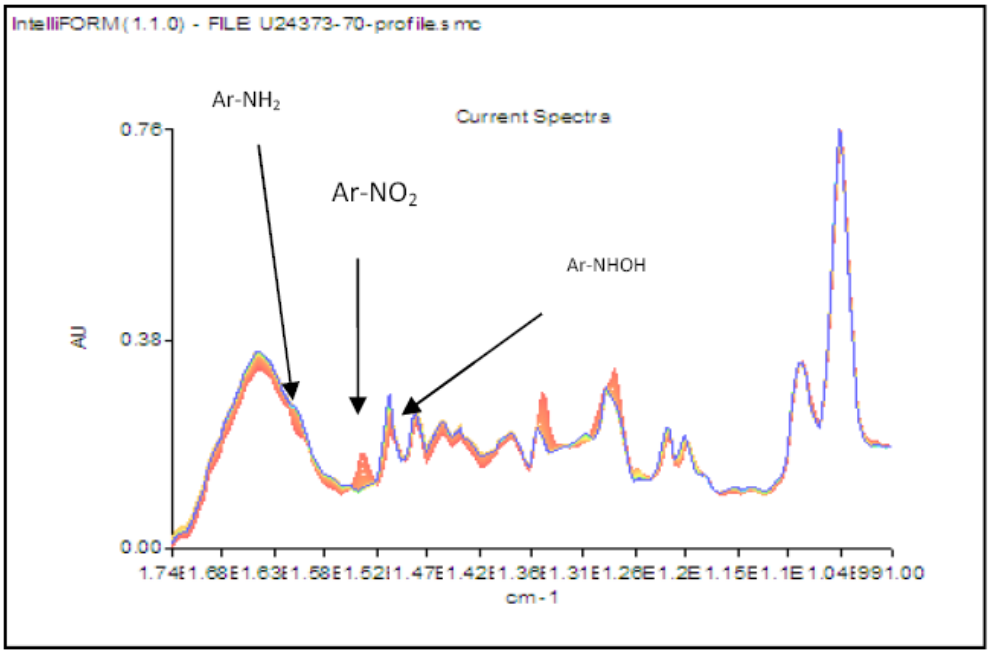

Figure 5.13: Waterfall plot of React IR showing the mid-infrared for nitro reduction

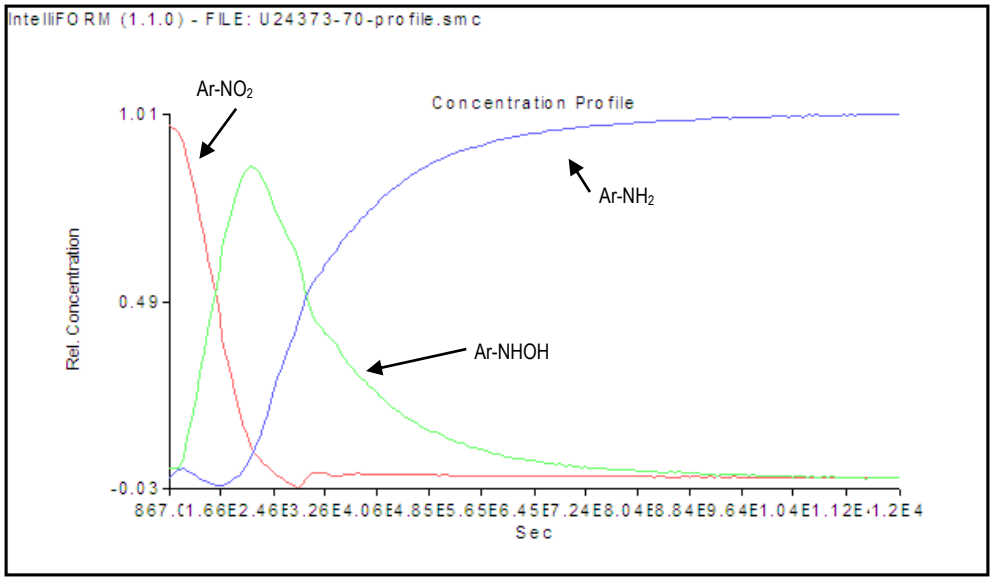

Figure 5.14: Pure component concentration over time resulting from chemometrics analysis

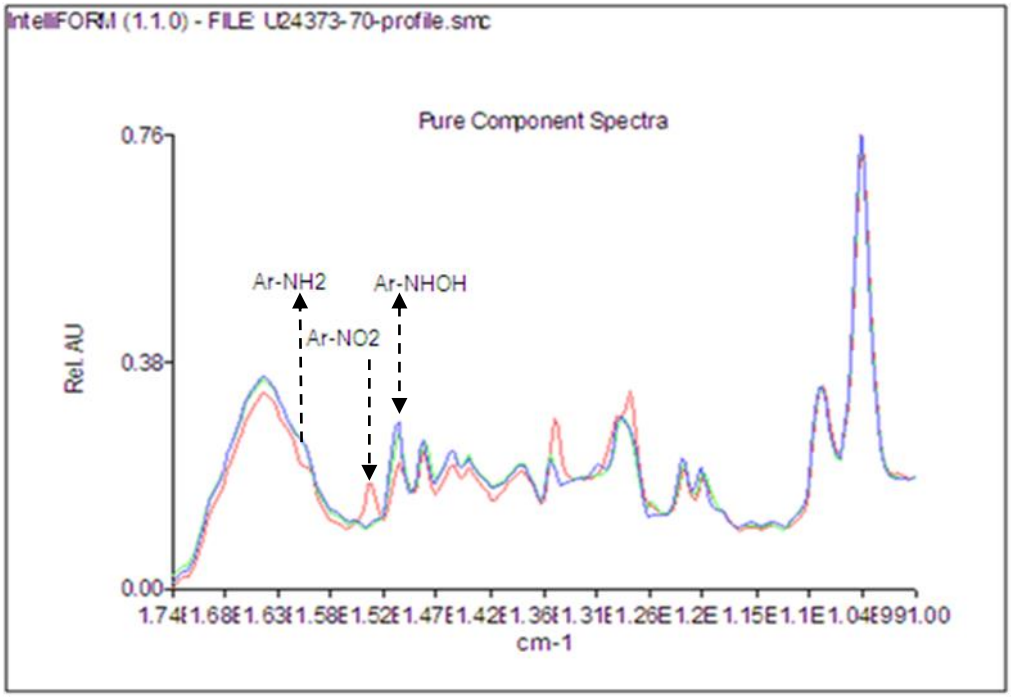

Figure 5.15: Pure component spectra results from PCA

5.4.6 Kinetic Rate Constants

Rate constants, as defined in equations 5.22, 5.23, and 5.24 were obtained from a set of three experiments varying catalyst amounts (as stated earlier). All three experiments were run at 0.60 (1/s) k_La, 4 barg H_2 reactor headspace pressure, 25°C batch temperature, but varying in catalyst amount, 2.5, 5.0, and 10.0 wt%, respectively. These three sets of experiments yielded nine known concentrations as a function of time plots (each experiment with three reacting species [A], [C], and [D]). From the kinetic rate law model, we have five unknown rate and equilibrium constants (k_1, k_2, K_A, K_C, and K_D). Using the Least Mean Square method (equation 5.41) it was possible to regress the measured concentrations of the individual species with the appropriate rate law equations (equation 5.22 for [A], 5.23 for [C], and 5.24 for [D]) simultaneously, to fit these unknown rates and equilibrium constants. This was achieved by using solver function in MS Excel, and calculating the concentration at time t_2 with known concentration of the species (i.e., [A]) at time t_1. Solver is used to fit

these rate constants simultaneously across all three data sets, by regressing the measured concentration at various time intervals (t), such that the error, as defined in equation 5.42, is minimized.

$$[X]_{calc,2} = [X]_{calc,1} - \left(r_{X,1} + r_{X,2}\right) * \left[\frac{t_2 - t_1}{2}\right] \quad [5.41]$$

$$\sum_{n=1}^{N} [[X]_{measured} - [X]_{calculated}]^2 \cong 0 \quad [5.42]$$

where [X]= [A], [C] and [D].

Thus, by fitting the above three equations 5.22, 5.23, and 5.24, simultaneously, for three different catalyst loading experiments, we obtain the unknown rate and equilibrium constants: k_1 (Eq.5.25), k_2 (Eq. 5.26), K_A, K_C, and K_D. The constants obtained by this method, along with their corresponding errors, are given in Table 5.7. The individual concentration profiles are given in Figure 5.16, Figure 5.17, and Figure 5.18.

Table 5.7: Rate constants using LMS method and Data Fitting for 0.6 k_La, 25°C and 10 wt% catalyst loading

	Constant	**Units**	**Error**
k_1	0.79	1/min	±2.8 X 10^{-4}
K_A	1.4 X 10^{13}	L/mol	± 32
k_2	5.5 X 10^{10}	1/min	± 20
K_C	19.7	L/mol	± 0.34
K_D	2.0 x 10^{12}	L/mol	± 24

It can be clearly seen that $[K_A C_{Al} K_A\ C_A\ + K_D\ C_D\ K_D C_{Dl}] \gg 1$ (max $C_{A,D}$ = 0.010 mol/L), indicating that the catalyst is saturated by liquid phase substrate. In Figure 5.16, the concentration profiles are plotted for 10 wt% catalysts loading. Nitroaromatic [A], plotted in (a), shows that the calculated concentration is in reasonable agreement with the measured value (by React IR, Chemometrics and HPLC grab samples). This behavior is also observed in figure (b) for hydroxylamine [C] and in figure (c) for aniline [D] concentration.

Similarly, the concentration profiles for 5.0 and 2.5 wt% catalysts loading are plotted in Figure 5.17 and Figure 5.18, respectively, using the rate constants obtained in Table 5.7. Similar to the 10 wt% catalyst loading, the measured and calculated concentrations for nitroaromatic [A], hydroxylamine [C], and aniline [D] are in close agreement with each other.

Figure 5.16: Concentration profiles for 10 wt% catalyst loading

a) Nitroaromatic concentration measured vs. calculated

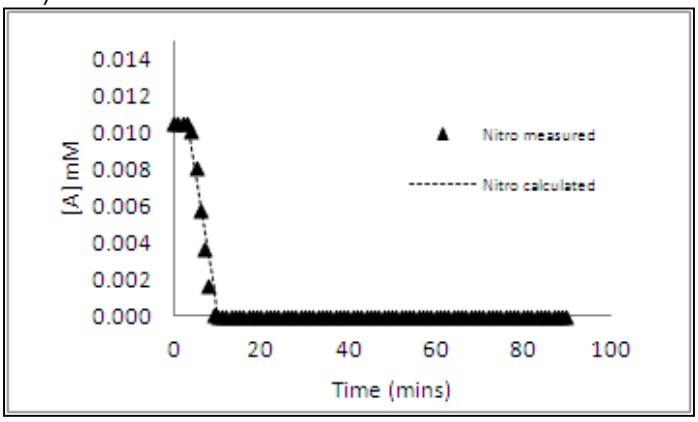

b) Hydroxylamine concentration measured vs. calculated

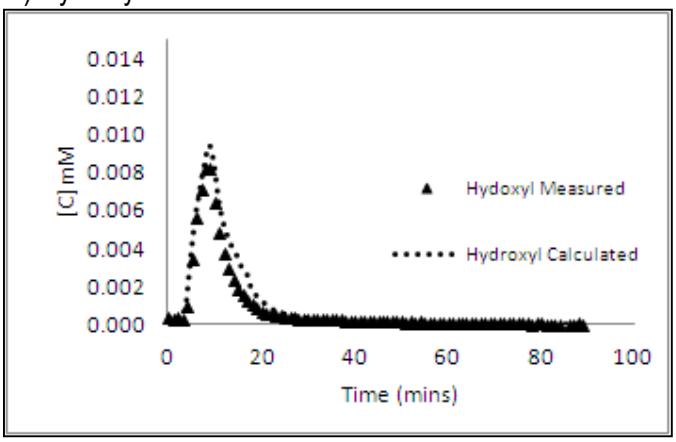

c) Haloaminoaromatic concentration measured vs. calculated

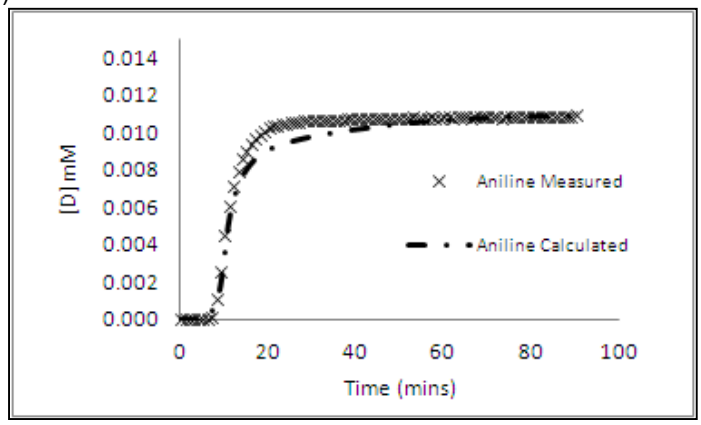

Figure 5.17: Concentration profiles for 5 wt% catalyst loading

a) Nitroaromatic concentration measured vs. calculated

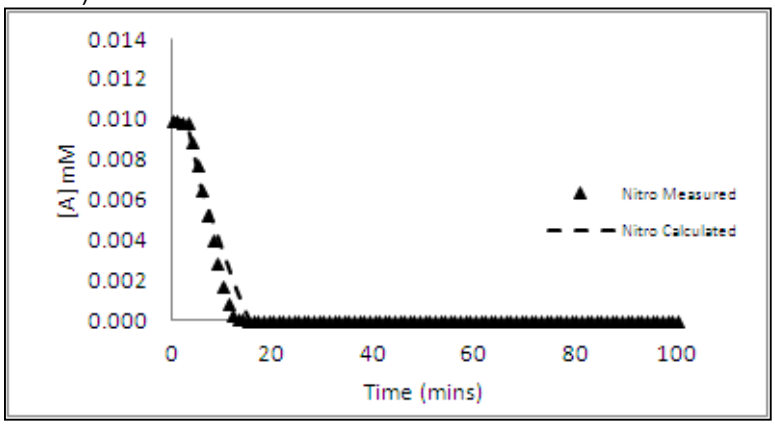

b) Hydroxylamine concentration measured vs. calculated

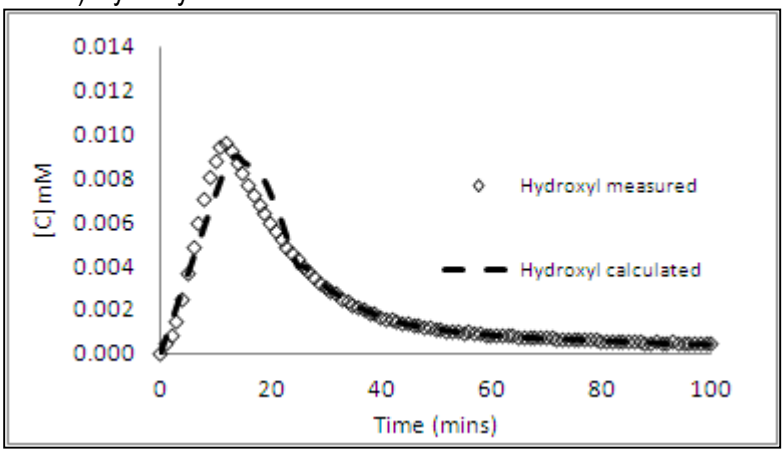

c) Haloaminoaromatic concentration measured vs. calculated

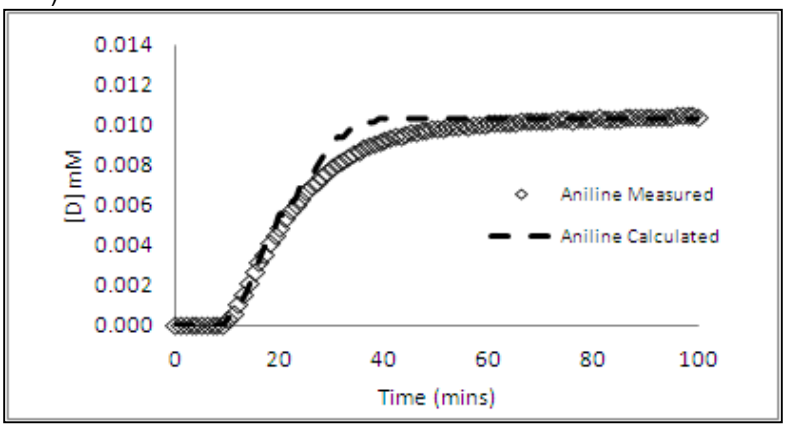

Figure 5.18: Concentration profiles for 2.5 wt% catalyst loading

a) Nitroaromatic concentration measured vs. calculated

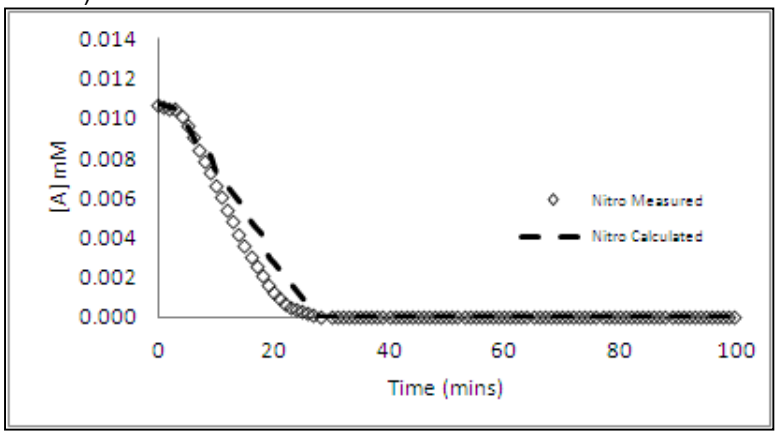

b) Hydroxylamine concentration measured vs. calculated

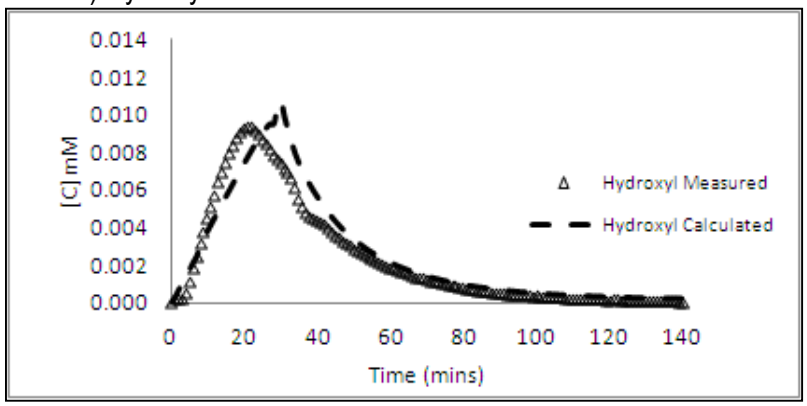

c) Haloaminoaromatic concentration measured vs. calculated

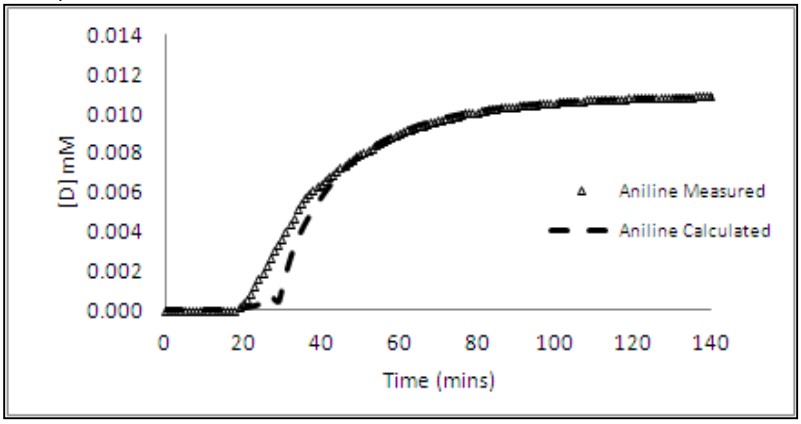

5.4.7 Catalyst Order using Kinetics Analysis

In order to confirm that these reactions are indeed first order in catalyst as shown previously, we compare these three experiments using earlier rate law equations 5.22 – 5.24. The reaction progress analysis technique as described by Kedia et al. [19] was used to describe the catalyst activity. The overall reaction rate for reduction of halonitroaromatic [A] to haloaminoaromatic [D] can be related to the rates of reaction of A and D according to Eq. 5.36:

$$R_A\left(\frac{mol}{L\ min}\right) = -r_H\ =\ -r_A + r_D \qquad [5.43]$$

where r_A, r_D, and r_H are obtained from equations 5.22, 5.24 and 5.36, respectively.

A plot of concentration of nitroaromatic vs. the overall rate (R_A) is shown in Figure 5.19. It can be seen that, as the nitroaromatic concentration decreases, the rate of the reaction does not change; i.e., it is constant for a major part of the reaction (90%). From Figure 5.19, it can be said that saturation kinetics is observed for the most part of the reaction, i.e., zero order with respect to [A] from the commencement of the reaction, up to 90% [A] is consumed. Then, there is a small transient behavior observed, before the reaction rate becomes first order in [A] toward the end.

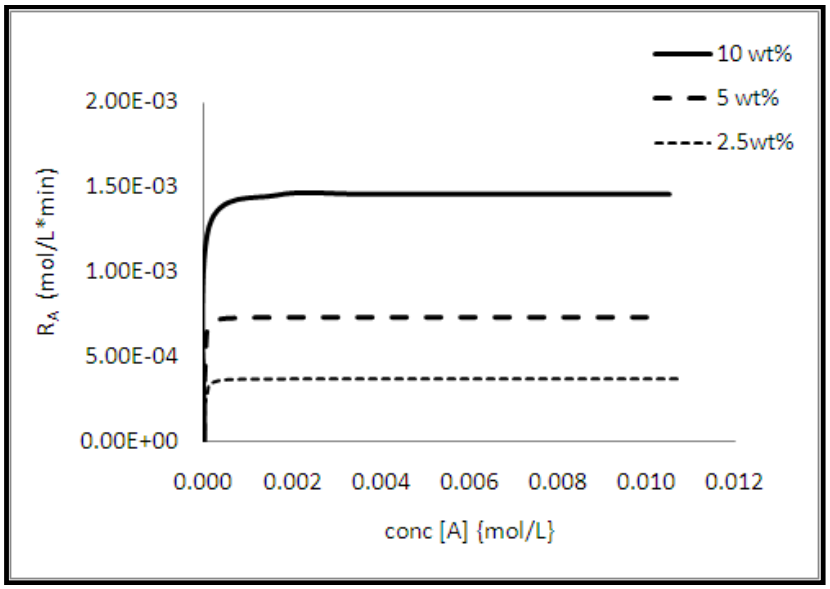

Figure 5.19: Overall Reaction rate vs. Nitroaromatic Concentration [A]

The overall rate of reaction [R_A], is divided by catalyst concentration [cat] to normalize the reaction rate with respect to the catalyst, and it is plotted in Figure 5.20.

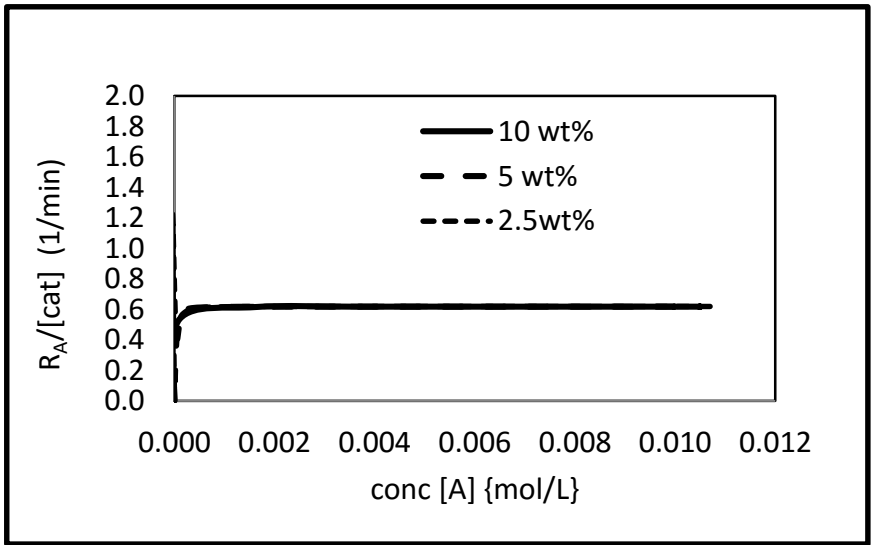

Figure 5.20: Normalized rate vs. [A]

From these results, it can be concluded that:

a) As seen from Figure 5.19, the reaction was indeed first order in catalyst concentration, when the catalyst concentration was doubled, the reaction rate also doubled.

b) In addition, it can also be seen that, when the overall reaction rate was normalized with the catalyst concentration from Figure 5.20, all the three reactions overlay each other. If the reactions were not first order in catalyst, this behavior would not have been observed. The total number of active sites, as seen from mass balance (Eq. 5.15), has to be constant for them to overlay, i.e., the number of active sites/gm-catalyst have to be the same for all three experiments, as the concentrations of [A], [C], and [D] are the same in these reactions. Thus, it can be concluded that the catalyst is not poisoned, or inhibited with substrates or product, during the course of the reaction. If the catalyst sites were poisoned or it lost its active sites (due to binding of various species), the reaction rate would be different for all three experiments; and when the normalized reaction rate with respect to catalyst was plotted, the rates would not overlay each other.

5.5 Conclusions

This chapter elucidates the dominant pathway for the desired reaction, to establish a kinetic model. Results proved that the dominant pathway for the generic reaction schematic, as shown in Figure 5.1, was the reduction of nitroaromatic to hydroxylamine and, then, the hydrogenolysis of hydroxylamine to aniline. This mechanistic pathway was then utilized to postulate a kinetic model, considering the various kinetic reactions: gas-liquid mass transfer and liquid-solid mass transfer that need to take place during such heterogeneous catalysis.

In addition, the postulated kinetic rate model, based on several calculations and by kinetic measurement, established that intrinsic kinetics rather than gas-liquid or liquid-solid mass transfer resistances limited the reaction rate. Furthermore, results show that the reaction behaves first order in both the hydrogen concentration (i.e., partial pressure of hydrogen in the reactor headspace) as well as the catalyst concentration. A new methodology to test catalyst robustness (i.e., catalyst poisoning, inhibition, or degradation) was established, using reaction progress analysis, which showed that the given catalyst was robust for the given reaction conditions. Rate constants obtained from reaction data sets were used to validate catalyst robustness, by normalizing the reaction rate w.r.t. catalysts. Later Chapters will discuss the control mechanism for hydroxylamine and the impurity [I] formation.

References

1 F. Visentin, Study of the hydrogenation of selected nitro compounds by simultaneous measurements of calorimetric, FT-IR, and gas-uptake signals, Ind. Eng. Chem. Res., 2006, Vol. 45 (13), p. 4544-4553.

2 A. M. Stratz, Catalysis of Organic Reactions, Chem. Ind. (Marcel Dekker), 1984, Vol. 18, p. 335-337.

3 R. V. Chaudhari and P. A. Ramachandran, Three Phase Slurry Reactors, AICHE Journal, 1980, Vol. 26 (2), p. 177- 202.

4 E. F. Stefoglo, O. P. Zhukova, I. V. Kuchin, The influences of the gas rate dissolution and mass-transfer limitation at the interfaces on selectivity of gas–liquid processes in stirred reactors with a suspended catalyst, Catalysis Today, 2001, Vol. 66, p. 397–402.

5 E. Crezee, B. W. Hoffer, R. J. Berger, M. Makkee, F. Kapteijn, and J. A. Moulijn, Three-phase hydrogenation of D-glucose over a carbon supported ruthenium catalyst – mass transfer and kinetics; Applied Catalysis A: General, 2003, Vol. 251, p. 1-17.

6 Reaction block as shown in Figure 4.1 was purchased from HEL group in UK.

7 Socrates, George, Infrared and Raman Characteristic Group Frequencies, Tables and Charts, John Wiley and Sons

8 Catalyst Screening was performed to find the optimum selectivity and reactivity. Refer to Chapter 3 for details on catalyst selection.

9 React IR is a mid-infrared spectra measurement instrument, purchased from Mettler Toledo Inc. For more details please refer to Mettler Toledo website (http://us.mt.com/us/en/home/products/L1_AutochemProducts/L2_in-situSpectrocopy.html).

10 Intelliform uses principle component analysis to determine the number of individual spectroscopically identifiable components. Intelliform was developed by H&A Scientific Inc., East Carolina University, and Glaxo Wellcome, Inc.

11 P. Gemperline, M. Zhu, E. Cash, and D. Walker, Chemometric characterization of batch reactions, ISA Transactions., 1999, Vol. 38, p. 211-216.

12 C.H. Bartholomew and R.J. Farrauto, Fundamentals of Industrial Catalytic Processes, John Wiley & Sons, Inc., 2006, 2nd edition.

13 P.H. Brahme, L. K. Doraiswamy, Modeling of a Slurry reaction: Hydrogenation of glucose on Raney Nickel, Ind. Eng. Chem. Process Des. Dev., 1976, Vol. 15 (1), p. 130-137.

14 J. Wisniak, M. Hershkowitz, R. Leibowitz, and S. Stein, Hydrogen solubility in aqueous solutions of sugars and sugar alcohols, J. Chem. Eng. Data, 1974, Vol. 19 (3), p 247-249.

15 C. V. Rode, M. J. Vaidya, R. Jaganathan, and R. V. Chaudhari, Hydrogenation of nitrobenzene to p-aminophenol in a four-phase reactor: Reaction kinetics and mass transfer effects, Chem. Eng. Sci., 2001, Vol. 56, p. 1299-1304.

16 P. L. Mills and R. V. Chaudhari, Multiphase catalytic reactor engineering and design for pharmaceuticals and fine chemicals, Catalysis Today, 1997, Vol. 37, p. 367-404.

17 Y.T. Shah, A. Deimling, B.M. Karandikar, and N.L. Carr, Solubility and mass transfer of CO and H_2 in Fischer—Tropsch liquids and slurries, The Chemical Engineering Journal, 1984, Vol. 29 (3), p. 127-140.

18 Agilent HPLC was used to analyze the reaction species, using Zobrax SB-C-18 column, run with water and acetonitrile as mobile phases. The method was run isocratic with 10% acetonitrile at time t=0 to 100 % acetonitrile at t=8 mins. Column temperature of 40C was achieved prior to run and flow rate of 1.5 mL/min was used

19 S. Kedia and M. Mitchell, Reaction Progress Analysis: Powerful tool for understanding Suzuki-Miyaura reaction and control of Polychlorobiphenyl impurity, Org. Proc. Res. and Dev., 2009, Vol. 13, p. 420-428.

CHAPTER 6: CONTROL OF HYDROXYLAMINE AND DES-F IMPURITY

6.1 Background

Catalytic hydrogenation of nitroaromatic proceeds through intermediate formation, such as hydroxylamine, which further reduces to its corresponding aniline. Accumulating intermediates, i.e., hydroxylamine, can undergo side reactions that result in lower selectivity to the aniline. It is well known that hydroxylamine disproportionates exothermically [1, 2, 3, 4], leading to the formation of azo- and azoxybenzene, reactions which are not limited by the mass transfer rate of hydrogen and, therefore, cannot be stopped by slowing the mass transfer rate of hydrogen. An explosion occurred during the catalytic reduction of chloronitrobenzene, which was attributed to runaway decomposition initiated by exothermic disproportionation of the hydroxylamine intermediate [5]. Therefore, to scale up an intrinsically safe process, it is critical to understand and control the accumulation of these intermediates in the process. Furthermore, they are often carcinogenic and allergenic, therefore, hazardous in the event of an incomplete reaction [6]. Hydroxylamines can also undergo condensation with the nitroso compound, leading to the formation of colored azo- or azoxy- by-products, which are detrimental to the product quality. Clearly, for these reasons, the accumulation of hydroxylamine should be minimized. Various methodologies, such as adding a co-catalyst, as proposed by Studer et al. [7], may accelerate the rate of hydroxylamine disproportionation. Another approach proposed by Birckenstock et al. [8] is to use a semi-batch or continuous process in order to minimize the accumulation of hydroxylamine. However, this is often not possible in pharmaceutical manufacturing plants, which prefers to use flexible equipment to run multi-purpose batch processes. In addition, the current literature does not provide information on the rates of formation of hydroxylamine under reaction conditions, as well as the

impact of heat and mass transfer rates on the formation of such energetic intermediates. The primary focus of this chapter is to illustrate a complete understanding of the reaction mechanism for a halo-nitroaromatic reduction to halo aniline, which will further elucidate the effects of heat and mass transfer rates on the formation of various intermediate species, including the formation of hydroxylamine. The maximum concentration of hydroxylamine accumulation for a safe scale-up of the process depends upon the heat removal rate of the plant reactor; and, therefore, a control mechanism must be in place in order to prevent a thermal runaway. For the current project, the maximum hydroxylamine concentration that can be tolerated safely in the process should be < 70% area under curve (AUC) on the HPLC analysis.

Another impurity of concern is the dehalogenated impurity formed during the reduction. Such impurities are reported in the literature [9]; but, there is a lack of mechanistic understanding for its formation. The rates of formation of such impurities are not well understood and could result in a batch failure. For the current project, the maximum dehalogenated aniline that can be tolerated safely in the process should be < 0.15% AUC.

6.2 Experimental Procedure

This section describes the equipment; materials and reagents; and procedure used for estimating the kinetic and equilibrium rate constants.

6.2.1 Materials and Reagents

High purity hydrogen and nitrogen gas cylinders (purity of 99.999%) were purchased from Airgas Co. and were connected to the reactor. Ethanol, methanol and high purity water were purchased from Aldrich Chemical Company. Halo-nitroaromatic [A] was a GSK proprietary

intermediate that was used for these experiments to reduce to aniline. Catalyst (10% Pd/C) was purchased from Evonik Industries.

6.2.2 Equipment (100-mL Reactor)

The lab scale hydrogenator [10] described in Section 4.4 was used for these experiments. It is equipped with fully automated temperature, pressure, and stirring control. The reactor was made with hastelloy C-276, with a maximum reaction volume of 100-mL and total volume of 185-mL (total liquid + headspace volume). See Figure 4.1 and Section 4.4 for more details. The reactor also had capability to measure hydrogen gas-uptake directly, and was hooked-up with an Infrared high-pressure detection instrument (ReactIR) for online spectra measurements. Offline High Pressure Liquid Chromatography (HPLC) was used to aid and quantify ReactIR concentration profiles.

6.2.3 React IR

React IR (high-pressure infrared instrument a product of Mettler Toledo) was used to analyze individual concentrations in real time for species [A] - nitroaromatic, [C] - hydroxylamine and [D] - aniline. ReactIR is a Fourier Transform Infra-red (FTIR) spectroscopy based, high performance, in situ reaction analysis system. React IR is used directly to measure the liquid phase concentrations during hydrogenations. Refer to Section 5.3.3 for details.

6.2.4 Procedure

In a batch reactor (as shown in Figure 4.1), halo-nitro aromatic [A] was charged (5 grams) along with 10-wt % Pd on C [11] (0.5 grams) catalyst, 22.4 mL of 200-proof ethanol, 24.1 mL of purified water, and 3.1 mL of concentrated HCl. Concentrated HCl was added to dissolve the halo-nitro aromatic in the reaction solution. The reactor was stirred for five minutes at 25°C to dissolve [A] into

the solution. The reactor was then purged with nitrogen, followed by hydrogen, to evacuate the reactor headspace from air and nitrogen, respectively. During the pressure purge cycle, the agitation rate was set to zero. The reactor was then pressurized to 60-psig (4-barg) of H_2 pressure, and then agitation was started to allow the reaction to commence. The species concentrations were measured by HPLC grab samples (every 10-30 mins) during the reaction; also, the reaction spectra was collected using the mid-infrared React IR [12] instrument. The hydrogen uptake was directly measured based on the pressure drop in the headspace of the reactor with time. The reaction was deemed complete once the HPLC profile showed less than 0.20% area under curve (AUC) for residual [A] and greater than 98% (AUC) for product [D]. Once the reaction was completed, the reactor was vented off and inerted once again with nitrogen. The catalyst was then filtered off from the reaction solution, for further processing.

A set of experiments were run at different conditions In order to understand the impact of temperature and mass transfer rates on the formation of hydroxylamine and des-F impurity as follows:

1. Mass transfer effects by varying the k_La between 0.10 – 0.60 (1/s), while keeping the temperature (25°C), the pressure (5 bara of hydrogen gas in the headspace), the catalyst loading (10 wt%) and the nitro aromatic concentration (0.0109 mol) constant.
2. Varying the temperature between 25 to 45°C, while keeping the k_La (0.15 1/s), the pressure (5 bara of hydrogen gas in the headspace), the catalyst loading (10 wt%) and the nitro aromatic concentration (0.0109 mol) constant.
3. Kinetic model was build using the data from the above set of experiments

6.3 Results and Discussion

This section is divided into two parts: (a) the hydroxylamine formation and control, and (b) the des-F impurity formation and control.

6.3.1 Hydroxylamine Formation

Hydroxylamine formation and control were analyzed by varying reaction conditions, including mass transfer rates, temperature, and addition of additives, such as vanadium promoters, as described herein.

6.3.1.1 Vanadium Promoters

In order to investigate the role of vanadium promoters, as described by Studer et al. [13], to reduce the maximum accumulation of the hydroxylamine formed during such nitro reductions, reactions were run using vanadium pentoxide and vanadium trichloride as additives. These reactions were run at 25°C with 10-wt percentage catalyst and 0.15 k_La (1/s), and compared to the standard reaction with no additives. Refer to Table 6.1 for the effect of vanadium promoters on the concentration of hydroxylamine formation.

Table 6.1: Vanadium promoters for the hydrogenations

	Vanadium Modifers	Relative Reaction Rate	Maximum Hydroxylamine (%)
1	None	1.00	52.0%
2	V_2O_5	0.95	49.8%
3	VCl_3	0.98	50.7%

Although a slight decrease in the formation of the hydroxylamine was observed for the reactions with vanadium additives, the overall reduction in the hydroxylamine was not found, as reported by Studer et al. [7]. One of the potential causes could be due to the varying amount of the

unsupported vanadium modifier on the catalyst surface; neither reduced the hydroxylamine accumulation nor deactivated the catalyst significantly. A wider screen of catalyst-vanadium modifier is required to find the optimum combination in order to reduce the hydroxylamine accumulation. However, the catalyst was chosen earlier in the screen due to its availability on a commercial scale.

6.3.1.2 Mass Transfer Effect

Hydroxylamines are highly energetic intermediates formed during the nitro reduction. The hydroxylamine concentration was required to maintain AUC < 70% in the reaction mixture, due to its high thermal decomposition energy of 487-kJ/mol, and due to the limited heat removal rates of the pilot plant reactors. Although the overall reaction is kinetically limited (at a k_La of 0.15 1/s and above), as shown in Chapter 5 (Figure 5.8), the rate of intermediate formation (hydroxylamine) and by-products (des-F impurity) are not well understood. In order to understand the rate of formation of intermediate species with respect to mass transfer rates, several reactions were run varying gas-liquid mass transfer coefficient (k_La), keeping temperature (25°C) and catalyst loading (10-wt %) constant for these experiments. Refer to Figure 6.1 for details of hydroxylamine formation (as seen by React IR) at various mass transfer coefficients (k_La).

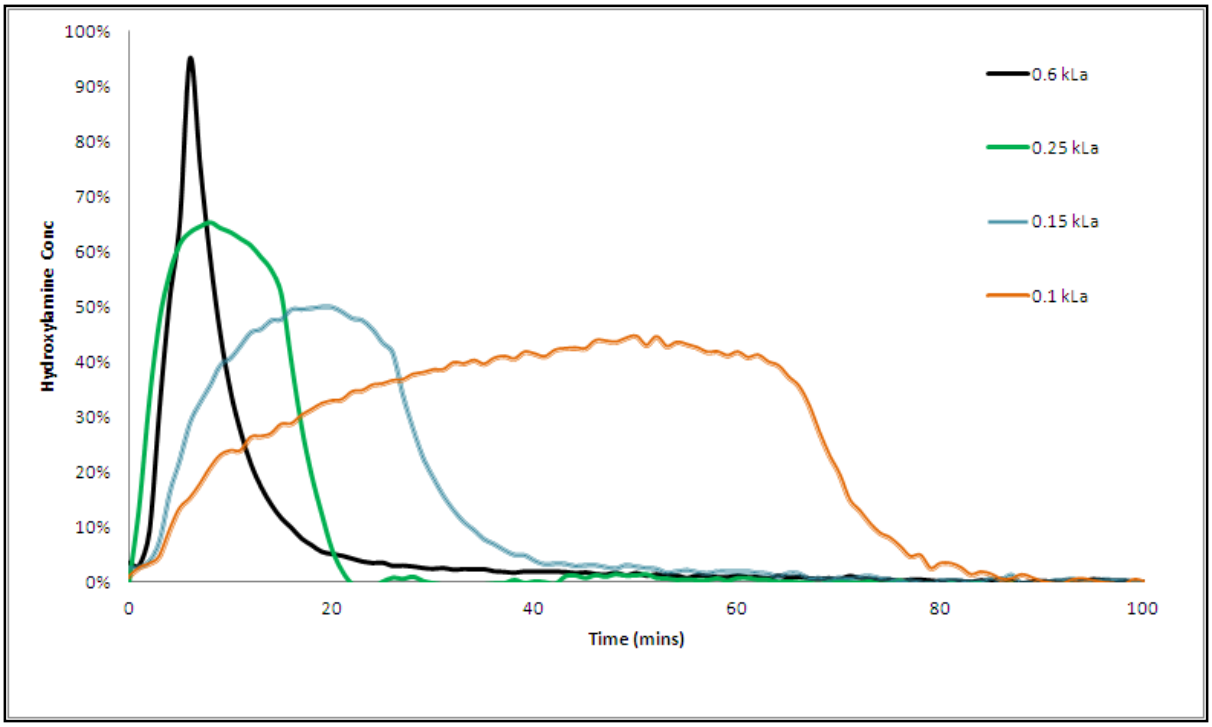

Figure 6.1: Hydroxylamine concentration vs. time at various k_La values (25°C and 10-wt % catalyst loading)

As can be seen from Figure 6.1, the rate of formation of the hydroxylamine [C], increases rapidly with increases in k_La from 0.10 to 0.60 (1/s), indicative of mass transfer control regime at 25°C. The amount of accumulation of [C] also increases with the increase in k_La; as the hydrogen transfer rate in the liquid increases, more and more of nitro aromatic is converted to hydroxylamine. Thus, the rate of nitro reduction to hydroxylamine can be said to be mass transfer limited at all k_La studied. Based on the accumulation of hydroxylamine, the mass transfer coefficient of 0.25 (1/s) k_La or less is desired for maintaining the concentration of hydroxylamine to ≤ 70% for a safe process scale-up as, described earlier.

6.3.1.3 Temperature Effects

In order to understand the formation of hydroxylamine with respect to reaction temperature, several reactions were run varying the temperature from 25°C to 45°C, keeping mass transfer rate of

0.15 (1/s) and catalyst loading (10-wt %) constant for these experiments. Figure 6.2 shows the concentration profile (as seen by React IR) for nitro reduction at 25°C. From the profile, it can be seen that the nitro aromatic is reduced to hydroxylamine, which, in turn, upon hydrolysis reduces to the corresponding aniline. Also, the reaction profiles reveal that the nitro is completely depleted prior to the end of the reaction, and the rate-limiting step of the reaction is the hydrogenolysis of the hydroxylamine to its corresponding aniline. The kinetic model as shown below was also in agreement with the React IR data, with a maximum 10% deviation. The rate constants are shown in Table 6.2 for various k_La [0.15 k_La (1/s)]. See Section 6.3.1.4 on Kinetic Modeling for details.

Figure 6.3 shows no accumulation of the hydroxylamine in the reaction system, as observed by React IR, at a reaction temperature of 35°C. The rate of aromatic nitro reduction is directly proportional to the rate of formation of its corresponding aniline. Hence, one can postulate that the rates of formation of hydroxylamine and reduction of hydroxylamine are equal at these temperatures; additionally, no appreciable accumulation was observed in the reaction media by HPLC. In addition, it can be seen that the reaction kinetic and the mass transfer rate model, described in Chapter 5, are in good agreement with the experimental data, with a maximum deviation of 10%. These results are verified by HPLC samples, and the maximum hydroxylamine concentration observed was < 2% AUC. A similar result (no accumulation of hydroxylamine) was obtained at 45°C.

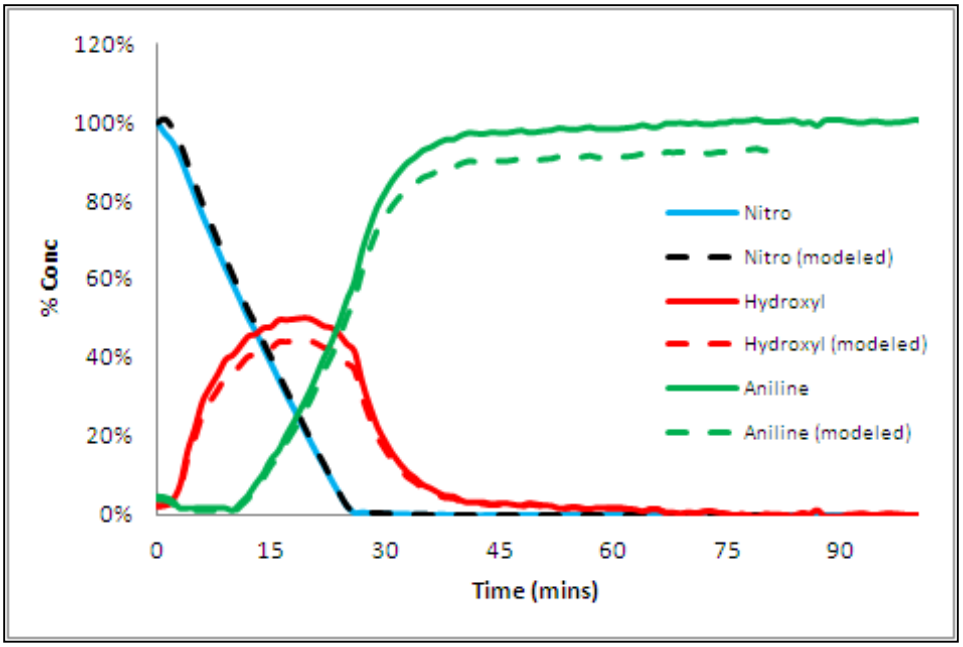

Figure 6.2: Concentration profile at 0.15 (1/s) k_La, 25°C and 10 wt% catalyst loading

As it can be observed from the reaction profile that there is a shift in rate limiting step from 25°C to 35°C and higher. For the reaction that is run at 25°C the rate limiting step was the hydrogenolysis of hydroxylamine to its respective aniline, whereas, for the reaction that was run at 35°C or higher, the rate limiting step appears to be the nitro aromatic reduction (as no appreciable amounts of hydroxylamine is observed in the reaction mixture). This will be further evaluated under the kinetic modeling section below.

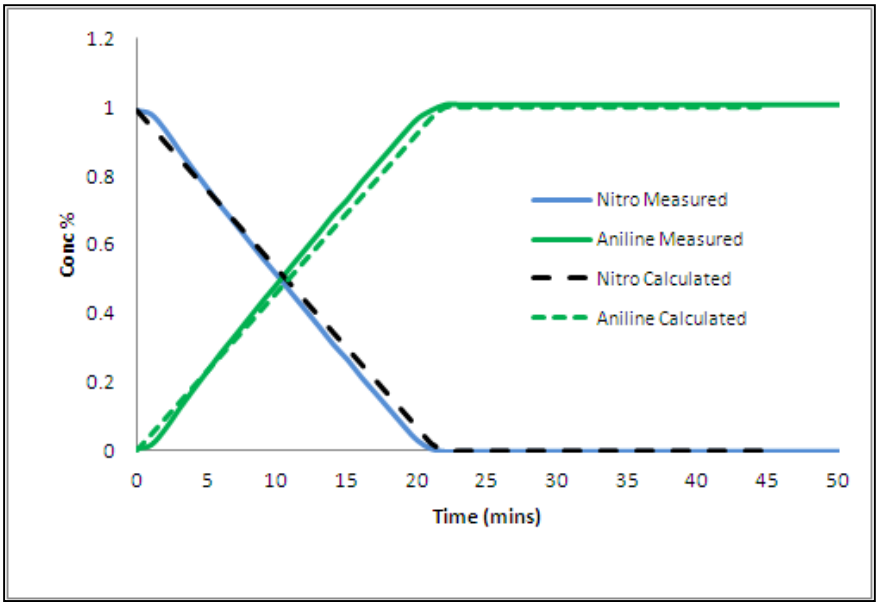

Figure 6.3: Concentration profile at 0.15 (1/s) k_La, 35°C, and 10 wt% catalyst loading

6.3.1.4 Kinetic Modeling

In order to establish the relationships between the rate of hydroxylamine formation and the effects of temperature and k_La, several reactions were run and a reaction rate model was postulated below. This section is divided into two sub-sections: the mass transfer effects and the temperature effects on the hydroxylamine formation.

6.3.1.4.1 Mass Transfer Effect on Hydroxylamine Formation

In order to obtain the apparent reaction rate constants $k_1 and\ k_2$ (as defined in Table 5.1) for kinetic controlled regime and in and Table 5.2 for mass transfer controlled regime, a set of four experiments varying k_La were run (0.10, 0.15, 0.25 & 0.60 1/s). Chapter 5 has already shown that the overall rate for reactions performed at or above 0.15 (1/s) k_La was kinetically limited, and the reaction that was run at 0.1 (1/s) k_La was mass transfer limited process limited. The adsorption/de-sorption coefficients; K_A for [A], K_C for [C] and K_D for [D] were kept constant (as defined in Table 5.7). All these experiments were run at 10.0 wt% catalyst loading, 4 barg H_2 reactor headspace pressure, and 25°C

batch temperature. These set of experiments yielded 12 known concentrations as a function of time plots (each experiment with three reacting species [A], [C], and [D]), and two unknown rate constants (k_1 and k_2 as defined in Table 5.1 and Table 5.2). Albeit the global reaction rate was in the kinetically controlled regime for k_La values at and above 0.15 1/s, the rates of formation and disappearance of hydroxylamine may still vary as function of k_La, i.e. $k_1 and\ k_2 = f(k_La)$. It was possible to regress the measured concentrations of the individual species with the appropriate rate law equations (Equations 5.22 for [A], 5.23 for [C], and 5.24 for [D]) simultaneously, to fit these unknown rates constants using the Least Mean Square method (as described in Equation 5.41). This was done using the solver function in MS Excel, and calculating the concentration at time t_2 with known concentration of the species (i.e., [A]) at time t_1. Solver is used to fit these rate constants simultaneously across all four data sets, by regressing the measured concentration at various time intervals (t), such that the error, as defined in Equation 5.42, is minimized.

Thus, by solving the above three Equations 5.22, 5.23, and 5.24, simultaneously, for three different k_La experiments (0.15-0.60 1/s), we obtain the two unknown rate constants: $k_1$and k_2 (for kinetic limited regime). Similarly, Equations 5.33, 5.34 and 5.35 were regressed for $k_1$and k_2 (for mass transfer limited regime) for a k_La value of 0.10 1/s. The constants obtained by this method, along with their corresponding errors, are given in Table 6.2. The individual concentration profiles are given in Figure 6.4 through Figure 6.7 For all higher k_La values the reactions are kinetically controlled. The values of adsorption rate constants K_A, K_C and K_D are taken from the results shown in Table 5.1.

Figure 6.4: Concentration profiles for 0.60 k_La (1/s)

a) Nitroaromatic concentration measured vs. calculated

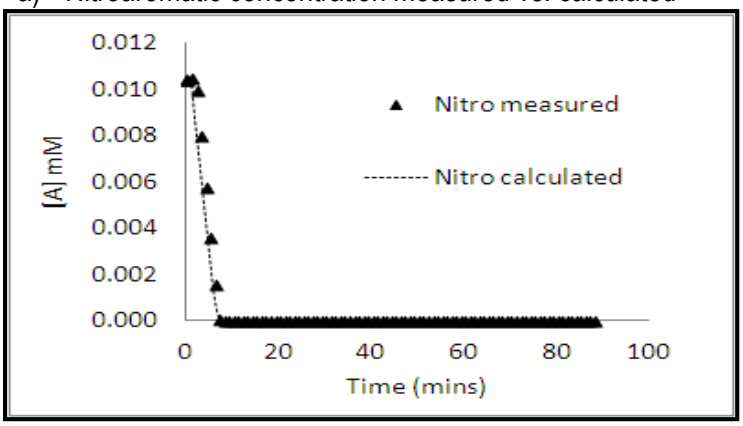

b) Hydroxylamine concentration measured vs. calculated

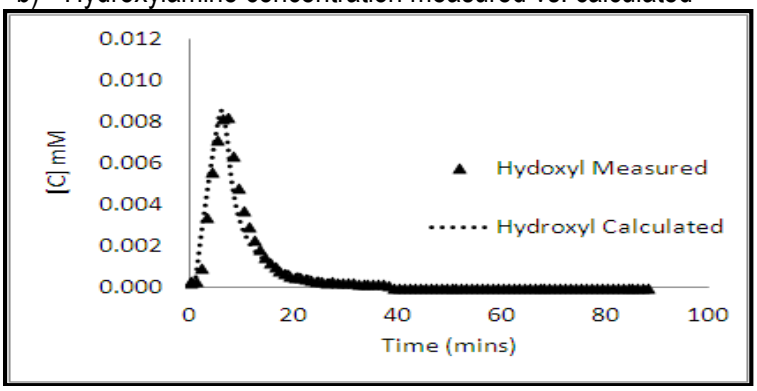

c) Aniline concentration measured vs. calculated

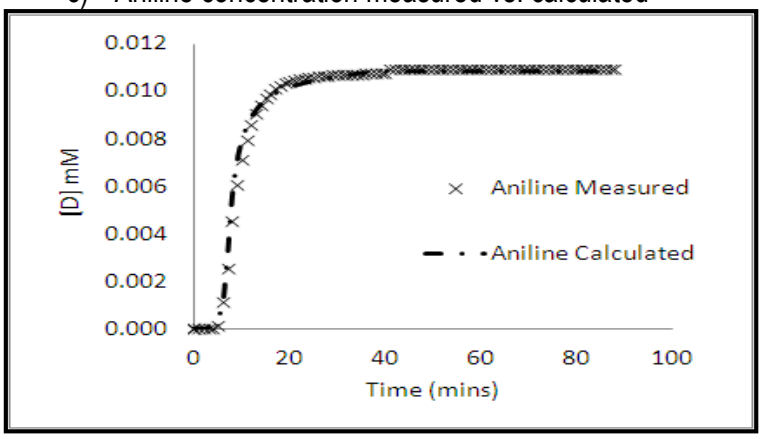

Figure 6.5: Concentration profiles for 0.25 k_La (1/s)

a) Nitroaromatic concentration measured vs. calculated

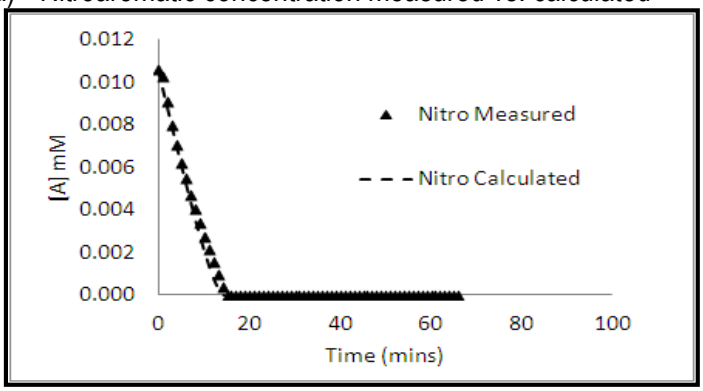

b) Hydroxylamine concentration measured vs. calculated

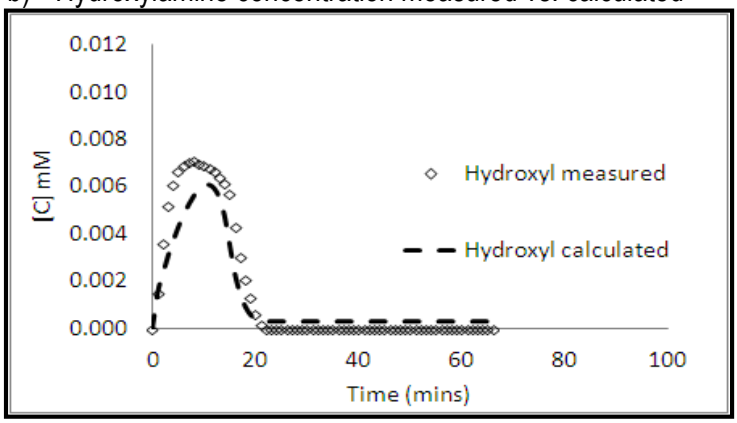

c) Aniline concentration measured vs. calculated

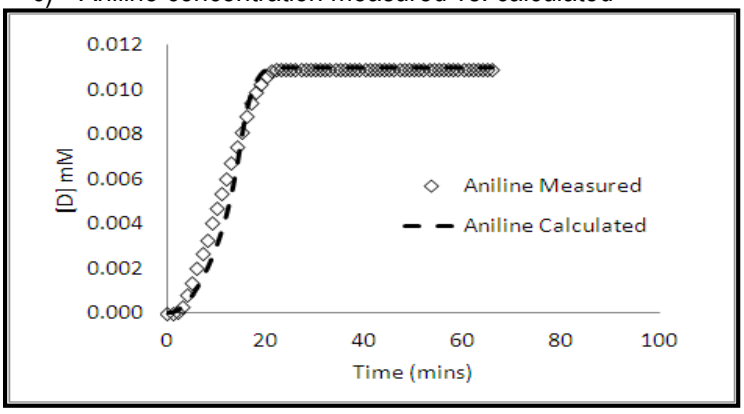

Figure 6.6: Concentration profiles for 0.15 k_La (1/s)

a) Nitroaromatic concentration measured vs. calculated

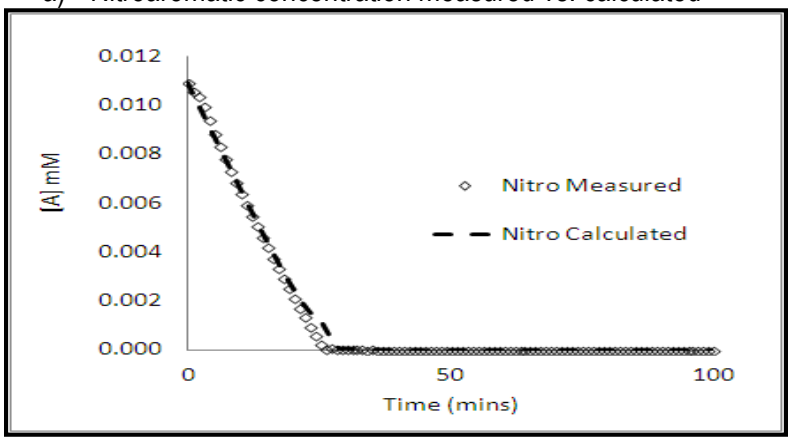

b) Hydroxylamine concentration measured vs. calculated

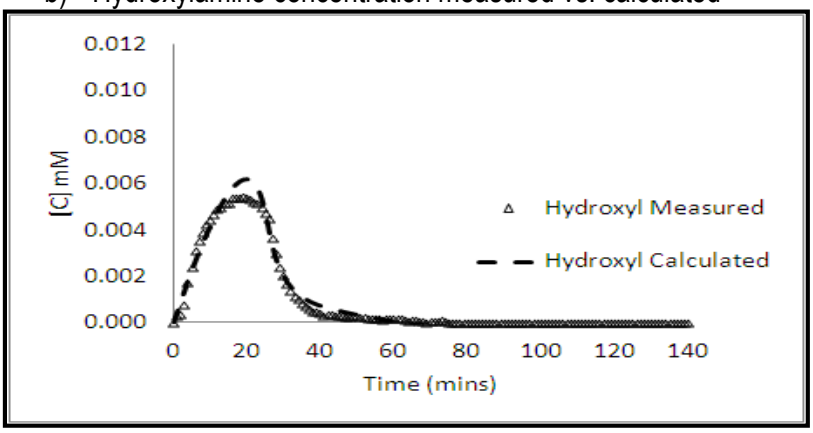

c) Aniline concentration measured vs. calculated

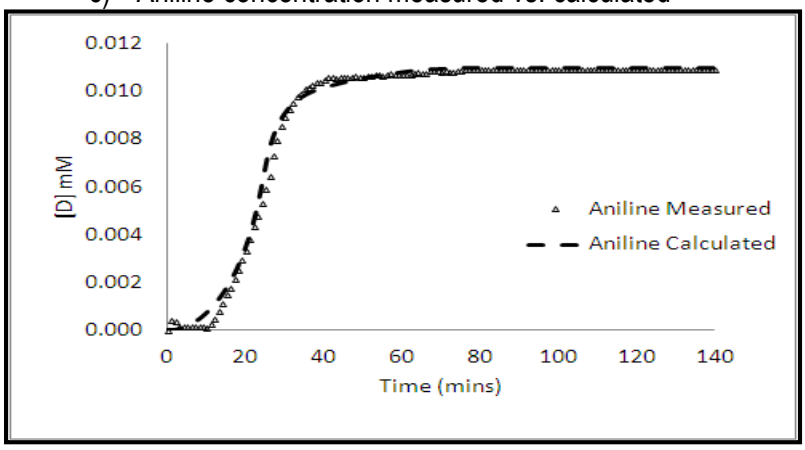

Figure 6.7: Concentration profiles for 0.10 k_La (1/s)

a) Nitroaromatic concentration measured vs. calculated

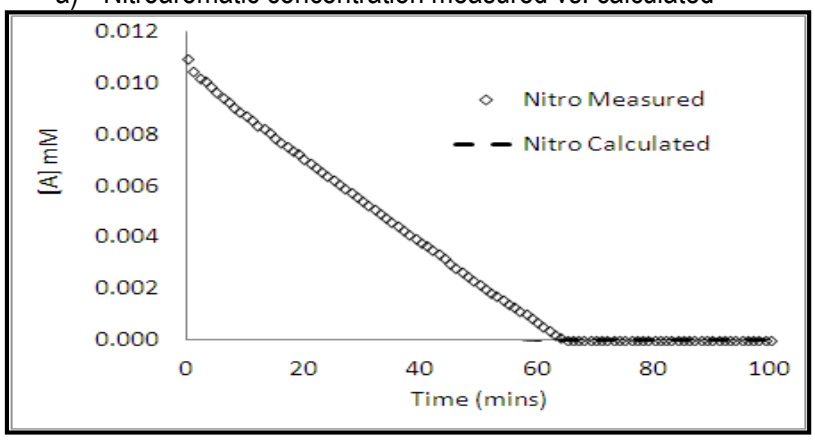

b) Hydroxylamine concentration measured vs. calculated

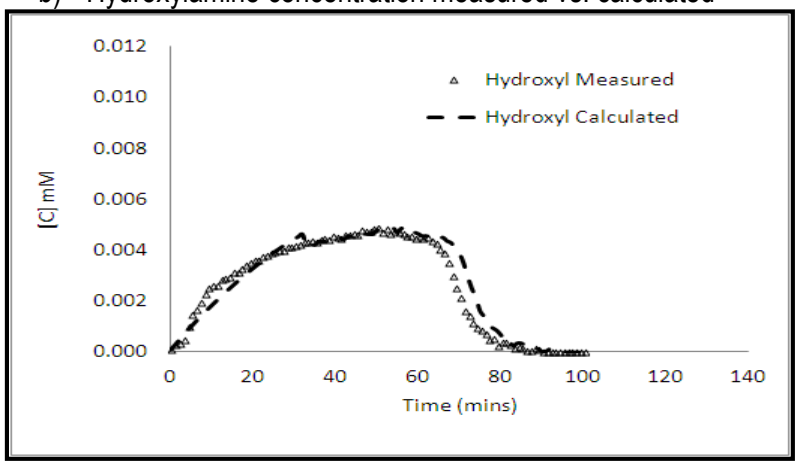

c) Aniline concentration measured vs. calculated

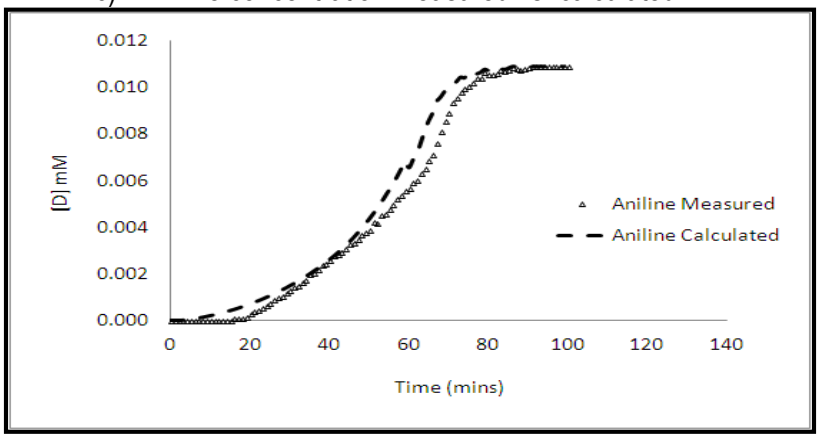

Table 6.2: Rate Constants using LMS method and Data Fitting a 25°C

k_La (1/sec)	0.6	0.25	0.15	0.1
k_La (1/min)	36	15	9	6
k_1 (1/min)*	0.79	0.37	0.20	0.12
k_1 (error ±)	2.8×10^{-4}	2×10^{-3}	1.74×10^{-3}	2.12×10^{-4}
K_A (L/mol)	1.4E+13	1.4E+13	1.4E+13	1.4E+13
k_2 (1/min)*	5.5E+10	6.0E+10	5.6E+10	3.5E+11
k_2 (error ±)	20	52	78	37
K_C (L/mol)	19.7	19.7	19.7	19.7
K_D (L/mol)	2.0E+12	2.0E+12	2.0E+12	2.0E+12

From Table 6.2 it is observed that the apparent rate constants k_1 is a function of k_La, i.e., as k_La decreases, the apparent 'k_1" decreases (see Figure 6.8). This concurs with the finding described under Figure 6.1, that the nitro aromatic reduction is entirely influenced by the mass transfer rate of hydrogen across the gas-liquid interface. The error (in Table 6.2) is calculated as the mean difference between the values obtained from three individual experiments run under identical reaction conditions. The apparent rate constants ($k_1$and k_2) are products of intrinsic rate constants ($k_a$and k_c) and the hydrogen constant term ($\frac{\mathrm{K}_H C_{Hl}}{1+\mathrm{K}_H C_{Hl}}$) for the kinetic limited regime (Table 5.1) for k_La between 0.15 and 0.60 1/s, where $C_{Hl} = C_{Hg}\,\mathrm{f}\,(\mathrm{P},\mathrm{T})$. Similarly, the apparent rate constants ($k_1$and k_2) are products of rate constants (G_1' and G_2') and the mass transfer coefficient k_La, for the mass transfer limited process (Table 5.2) at 0.10 1/s k_La. Thus, it can be concluded (from Figure 6.8) that the rate of nitro reduction to hydroxylamine can also be said to be mass transfer limited at all k_La studied due to linear relationship with k_La

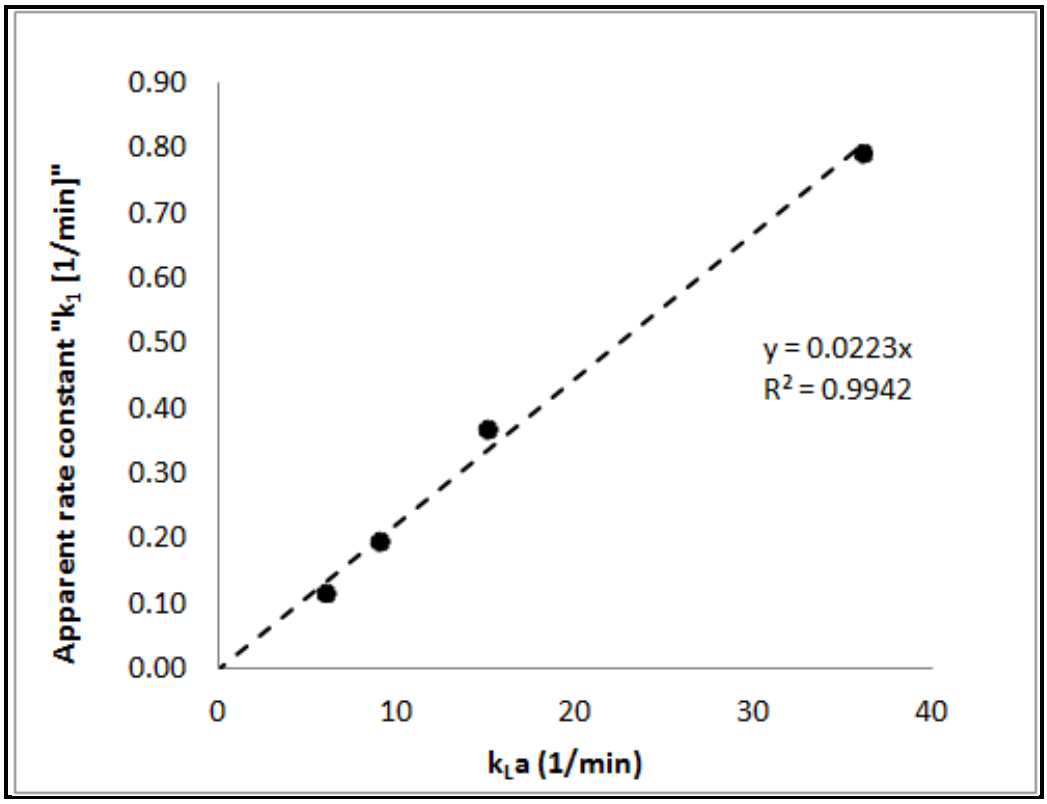

Figure 6.8: Apparent rate constant k_1 vs. k_La at 25°C

In addition, from the Table 6.2 it is observed that the apparent rate constant k_2 for hydrogenolysis of hydroxylamine to its respective aniline, is nearly constant for k_La values from 0.15 - 0.60 1/s. However, the k_2 value increases sharply at k_La of 0.10 1/s. See Figure 6.9 for the corresponding plot. As described earlier, the intrinsic rate constant (k_c) should be a constant (for both mass transfer and intrinsic kinetic limited regimes). However, it is seen from Figure 6.9 that there is no effect of increase in k_La (from 9 - 36 1/min) on k_2 values, but, at a k_La value of 6 (1/min), k_2 increases dramatically. When this intrinsic rate constant k_c (at k_La (1/min) = 6) is normalized ($k_c = k_2/k_La$), then the intrinsic rate constant (k_c) remains nearly constant across the k_La ranges examined (6 - 36 1/min). See Figure 6.10 for details. We can summarize the kinetic findings at 25°C below:

1) The nitro aromatic reduction to hydroxylamine is limited by mass transfer at all measured k_La values between 6 - 36 1/min.

2) The hydrogenolysis of hydroxylamine is limited by mass transfer rate only for a k_La value of 6 1/min and below.

3) The overall rate limiting step is the hydrogenolysis of the hydroxylamine to its respective aniline ($k_2 K_C << k_1 K_A$) at 25°C for k_La ranges between 9 – 36 1/min.

4) The overall rate limiting step for a k_La value of 6 1/min, is the reduction of nitro aromatic (mass transfer limited) as $k_2 K_C >> k_1 K_A$ at 25°C

To understand the temperature effect on the intermediate steps, a set of temperature experiments were also run.

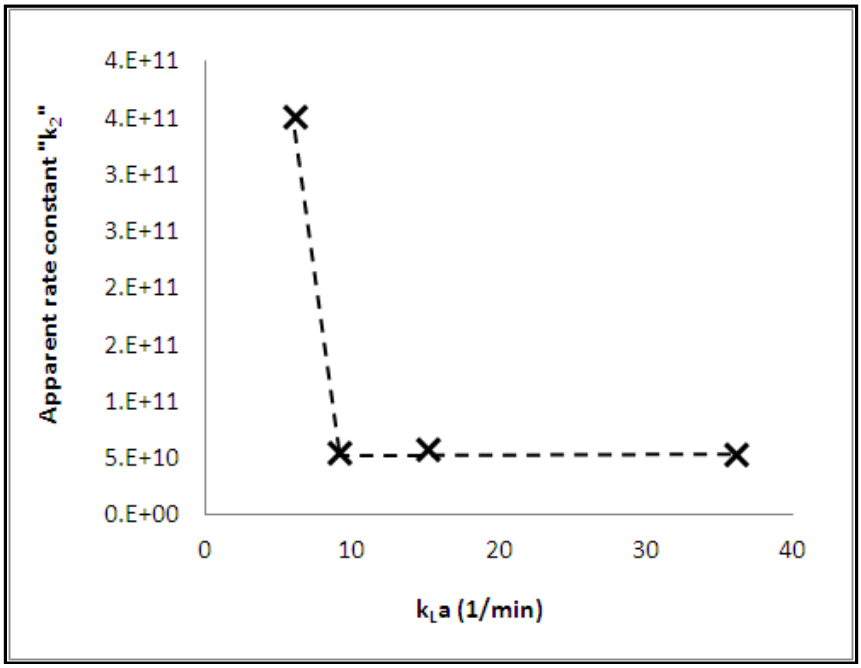

Figure 6.9: Apparent rate constant 'k_2' vs. k_La at 25°C

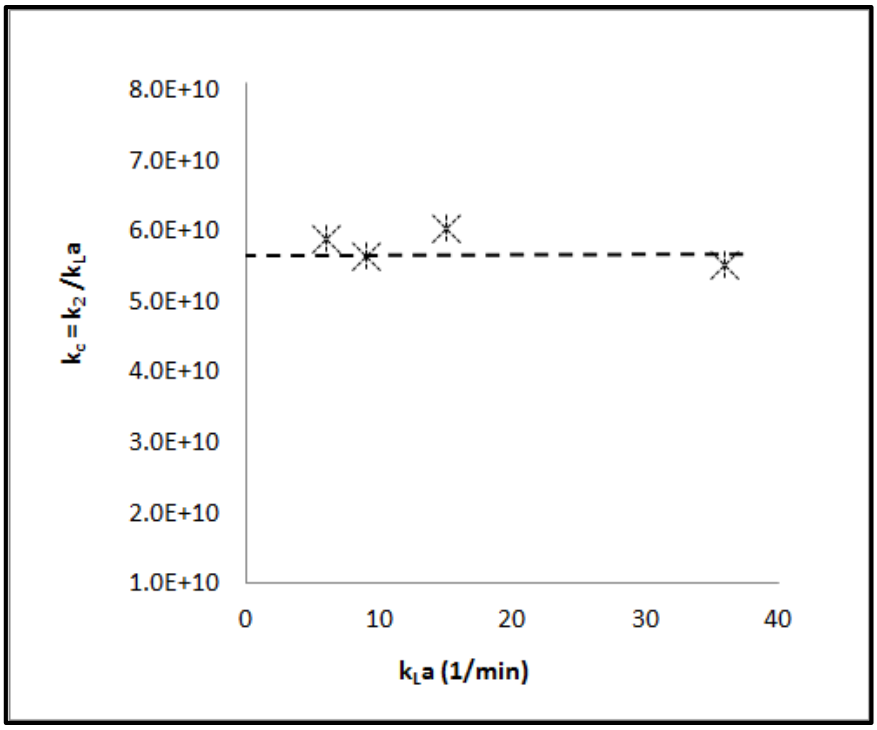

Figure 6.10: Apparent intrinsic rate constant k_2' vs. k_La at 25°C.

6.3.1.4.2 Temperature Effects on Hydroxylamine Formation

In order to calculate the activation energies and the apparent rate constants, three different sets of experiments, varying k_La and temperatures were run. Mass transfer coefficients of 0.10, 0.15, and 0.60 (1/s) were selected, and for each selected k_La, three experiments were run at 25°C, 35°C, and 45°C, respectively, to obtain activation energy values at those agitation rates. From Figure 6.3 it can be observed that there was no hydroxylamine detected or accumulated in the reactor at a temperature ≥ 35°C (at 0.15 1/s), hence, the rate of formation of aniline now equals the rate of disappearance of nitro aromatic [A] ($r_D = r_A$). A similar trend was observed for all k_La ranges evaluated between 0.10 to 0.60 1/s (no hydroxylamine observed at a temperature ≥ 35°C).

In order to obtain the apparent reaction rate constant (k_1) [as defined in Equation 5.22; three sets of experiments varying the temperature between 25-45°C for the k_La of 0.10, 0.15 and at 0.60 1/s,

were executed. The activation energies [Ea] and the pre-exponential factor (A) were also calculated and compared to the data obtained in Section 5.4.4 and in Table 5.6. The adsorption/de-sorption coefficients; K_A for [A], K_C for [C] and K_D for [D] were kept constant (as defined in Table 5.7). All these experiments were run at 10.0 wt% catalyst loading and at 4 barg H_2 reactor headspace pressure. These set of experiments yielded three known concentrations (for nitro reduction) as a function of time plots, and three unknown rate constants (k_1 for various k_La's). It was possible to regress the measured concentrations of the individual species with the appropriate rate law equations (Equations 5.22 for [A] and $r_D = r_A$), to fit these unknown rates constants using the Least Mean Square method (as described in Equation 5.41). This was computed by using solver function in MS Excel, and calculating the concentration at time t_2 with known concentration of the species (i.e., [A]) at time t_1. Solver is used to fit these rate constants simultaneously across all three data sets, by regressing the measured concentration at various time intervals (t), such that the error, as defined in Equation 5.42, is minimized. Thus, by solving the Equations 5.22, simultaneously, for three different temperature experiments (for each set of k_La), we obtain the unknown rate constant: k_1. A plot and data for the constants obtained by this method are given in Figure 6.12 and Table 6.3, respectively. From the plot it can be seen that the apparent rate constant 'k_1' increases with the increase in temperature at all k_La values studied. The activation energy was calculated by plotting Ln (k) vs. 1/T, and is given in equation 5.40 and plotted in Figure 6.13. The activation energies obtained are compared to the overall activation energies obtained using the hydrogen uptake rate as shown in Table 5.6, and found to be in agreement with a maximum deviation of 14% as shown in Table 6.3. This validates the findings in Chapter 5 for the rate limiting steps and the activation energies obtained via hydrogen uptake method. It also validates the findings that at higher temperatures (≥35°C) there is no hydroxylamine formed as $k_1 = 0$ (similar activation energies obtained for k_1 when compared to H_2 uptake rate). Thus, for the overall reaction it can be said

that the gas-liquid mass transfer rate controls the regime below 0.15 (1/s) k_La and the reaction is kinetically controlled above a k_La of 0.15 (1/s) as summarized in Section 6.3.1.5.

Table 6.3: Apparent rate constant 'k_1' at various temperature and activation energies

Temperature [C]	25	35	45	Ea (from k_1)	Ea (from Table	%
k_La (1/s)	k_1 [1/min]			[kJ/mol]	5.4) [kJ/mol]	Difference
0.10	0.12	0.13	0.14	3.76	4.38	14.2%
0.15	0.15	0.19	0.23	16.00	15.85	0.9%
0.60	0.79	1.03	1.24	19.64	17.86	9.9%

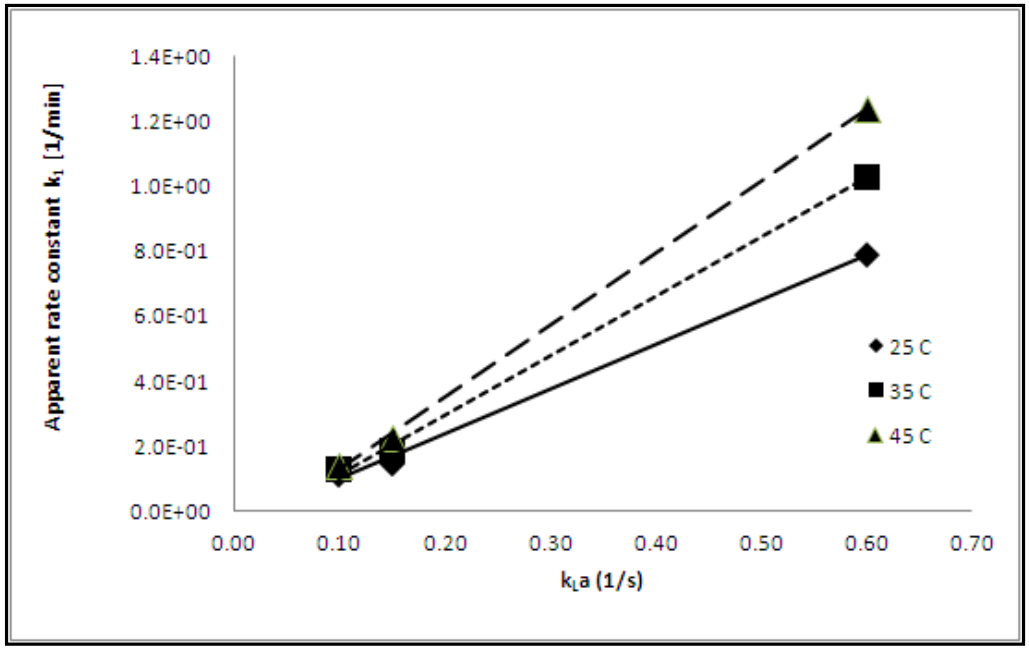

Figure 6.12: Apparent rate constant 'k_1' at various temperature

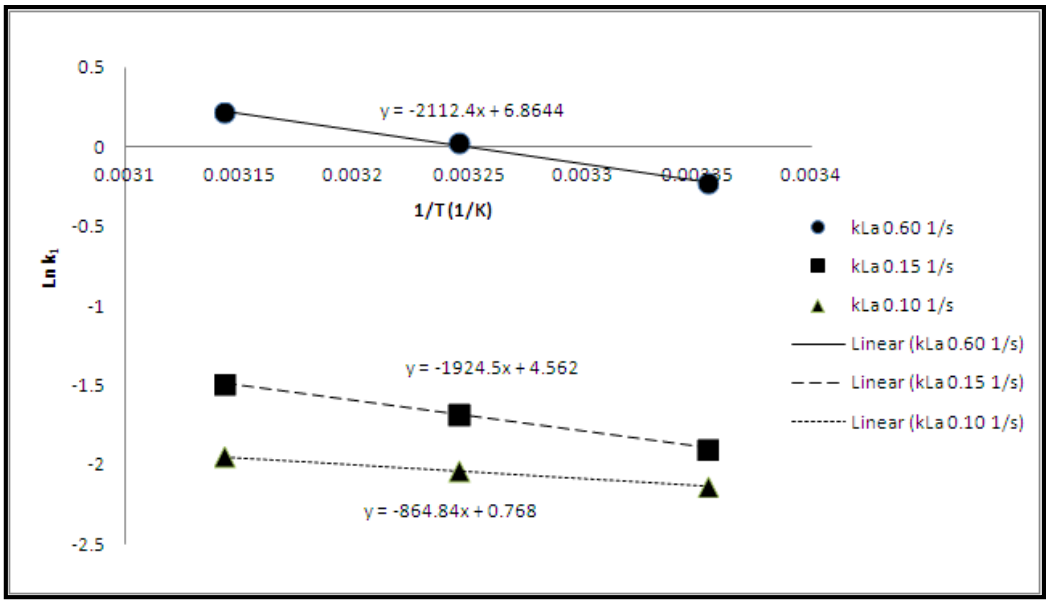

Figure 6.13: Activation energy for k_1 at various k_La's

6.3.1.5 Rate-Limiting Step

The rate of formation of hydroxylamine [C] increases rapidly with increase in k_La from 0.10 to 0.60 (1/s) at 25°C, indicative of mass transfer control regime as mentioned earlier; whereas, the rate of consumption of hydroxylamine [C] increases rapidly with increase in temperature from 25°C to 45°C, indicative of intrinsic kinetic control regime, as seen previously. Results show that the hydroxylamine is only formed when reactions are run at 25°C or lower (see Figure 6.1); whereas, the nitro aromatic and aniline products were observed at temperatures equal to and greater than 35°C (refer to Figure 6.2 and Figure 6.3). Thus, experiments specify that the rate of consumption of hydroxylamine is a temperature dependent phenomena, i.e., intrinsic kinetics; whereas, the rate of formation of hydroxylamine is a mass transfer dependent phenomena.

These results proved to be a critical step towards understanding the reaction mechanism. Also, for the reactions that were run at 25°C and between 0.15 to 0.60 (1/s) k_La, the hydrogenolysis was found to be the rate-limiting step (hydroxylamine reduction to aniline), which is a kinetically limited

phenomena (see Figure 6.14). Whereas, for the reactions that were run at 35°C and between 0.15 to 0.60 (1/s) k_La (see Figure 6.15), nitro reduction was found to be the rate-limiting step, i.e., mass transfer limited phenomena. The reaction was found to be rate-limiting in nitro-reduction at all temperatures (25-45°C) that were run at 010 k_La (1/s). Thus, it can be concluded that for reaction that were run between a k_La of 0.15-0.60 1/s, hydrogenolysis of hydroxylamine controls the overall reaction rate at 25°C; whereas, at 35°C or higher, the nitro reduction is the overall rate-limiting step in the process. For reactions that were run at 0.10 1/s k_La, the nitro reduction is the overall rate-limiting step at all temperatures (25-45°C). Therefore, it can be seen that the rate-limiting step is switched from hydrogenolysis of the hydroxylamine (Figure 6.14) to the hydrogenation of nitrophenol (Figure 6.15) by raising the reaction temperature from 25°C to 35°C (for a k_La of 0.15-0.60 1/s).

This was a critical finding, as most nitro reductions are perceived to be limited by the hydrogen concentration alone, irrespective of the reaction temperature or the mass transfer rate. It is, therefore, vital to understand the rate-limiting step of the process. In order to control the accumulation of hydroxylamine in the reactor, the reaction can be run at a higher temperature for accelerating the rate of hydrogenolysis to its corresponding aniline or at a lower mass transfer rate in order to match the heat removal rate of the plant reactor which would prevent the thermal runaway. The overall conditions would depend upon the desired selectivity and reactivity of the process.

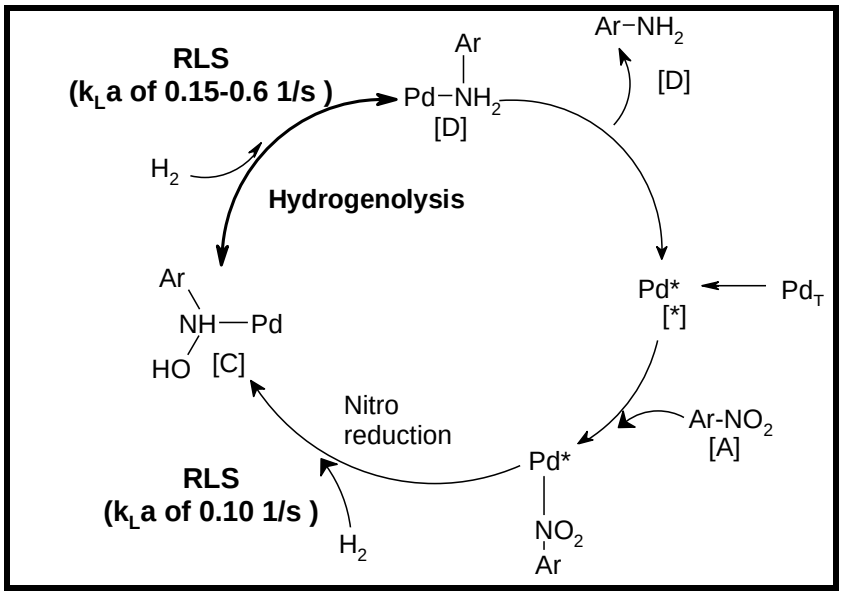

Figure 6.14: Rate-Limiting Step at 25°C]

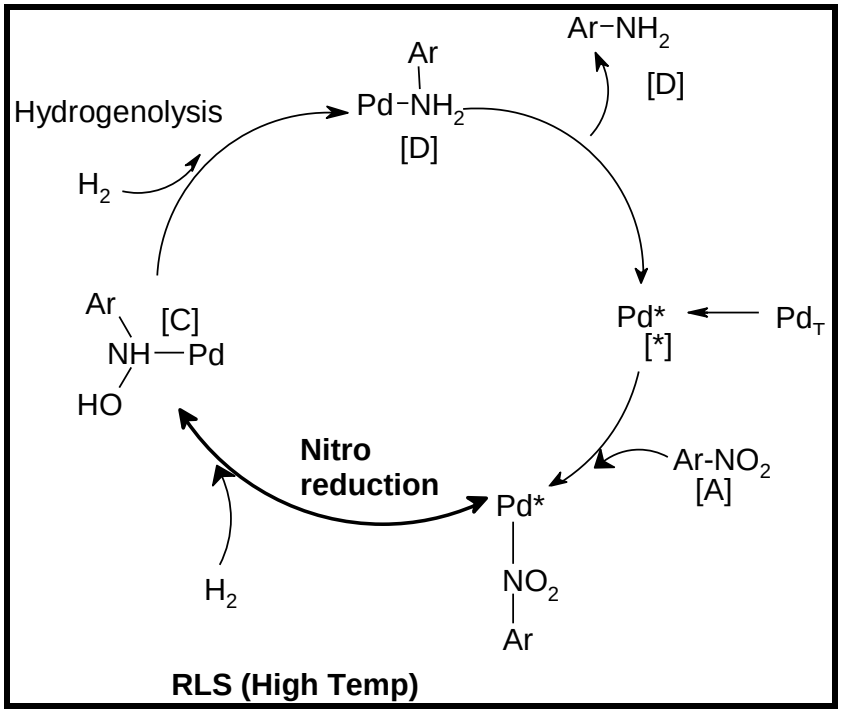

Figure 6.15: Rate-Limiting Step at 35°C and higher [at 0.1 to 0.6 (1/s) k_La]

6.3.2 Des-F Formation

Dehalogenation during the reduction of halo nitroaromatic to halo aniline has been well known in the literature. Kosak [9] studied the reduction of p-chloroaniline and suggested that the dehalogenation is a function of reaction pressure and temperature. However, the operating conditions would need to be optimized differently for each catalyst and substrate system, and Kosak demonstrated no clear understanding of the mechanistic pathway for the formation of the dehalogenated impurity. In order to understand the formation of des-F impurity, several experiments were run varying temperature, mass transfer rates, and catalyst loading.

6.3.2.1 Mass Transfer Effect

In order to understand the effect of mass transfer on the formation of the dehalogenated impurity, a reaction was run at 0.10 (1/s) k_La at 25°C, while keeping the catalyst loading at 10-wt percentage. Concentrations of individual species were measured over time by HPLC; additionally, the reaction profile was plotted using React IR spectra, measured every two minutes, as shown in Figure 6.16.

The plot indicates that the rate of formation of the des-F impurity is directly proportional to the rate of disappearance of the halo nitroaromatic compound. Once the halo nitroaromatic is completely depleted from the reaction mixture, no further increase in des-F is observed, thereby confirming that des-F is not formed from the halo aniline but originates either from the halo nitroaromatic or from the de-halogenation of the intermediates, such as the hydroxylamine.

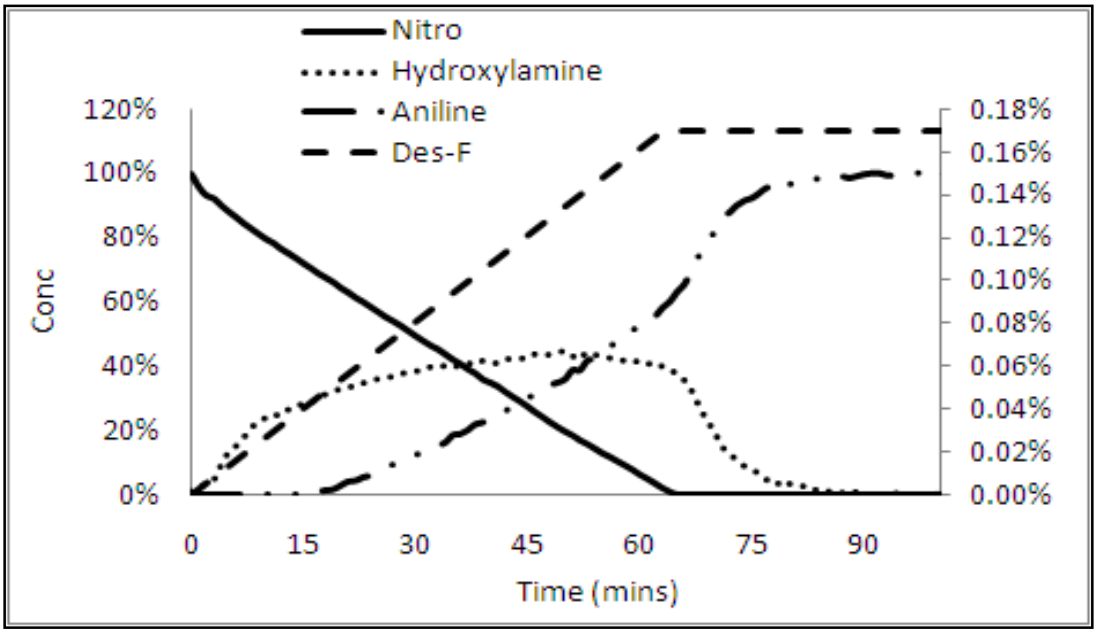

Figure 6.16: Dehalogenation (des-F) impurity formation at 0.10 (1/s) k_La at 25°C and 10-wt % Cat.

To further de-convolute the mechanism for the formation of the des-F impurity, several reactions were run, varying the gas-liquid mass transfer coefficients (k_La) and keeping the temperature (25°C) and the catalyst loading (10-wt %) constant for these experiments. Refer to Figure 6.17 for details of the des-F formation (as measured by HPLC analysis) for various mass transfer coefficients (k_La). It can be seen that, as the rate of mass transfer coefficients (k_La) increases from 0.10 to 0.25 (1/s), the overall percent des-F formation decreases from 0.18% to 0.02%. At a k_La value of higher than 0.25 (1/s), the des-F formation remains unchanged from a value of 0.02%. Note that the input starting material contains a 0.02% of des-F nitro aromatic. However, as it can be seen in Figure 6.18 that the rate of des-F formation is independent on the k_La, thereby indicating apparent "first order" behavior in [A]. The postulate rate law for des-F formation can be written as:

$$r_{des-F}\left(\frac{mol}{L\ min}\right) = k'_8[A] \qquad [6.1]$$

Where, $k'_8 = k_8 [\theta_H]$ = overall rate constant for des-F formation. See Figure 5.1 for details. It is presumed that once des-F nitroaromatic is formed, it further hydrogenates at the same rate to form des-F hydroxylamine (with rate constant k_1), and des-F aniline [I] (with rate constant k_2).

The calculated value for the rate constant (k'_8) was found to be 2.3 X 10^{-7} (1/min). This rate constant was used to calculate percent des-F formed for various k_La values assuming 'first-order' behavior in [A], and knowing des-F is only formed during the nitro reduction, is also plotted in Figure 6.17. The plot validates the conclusions made, as the modeled data for des-F concentrations are found to be in good agreement with the experimentally measured values with a maximum 10% deviation.

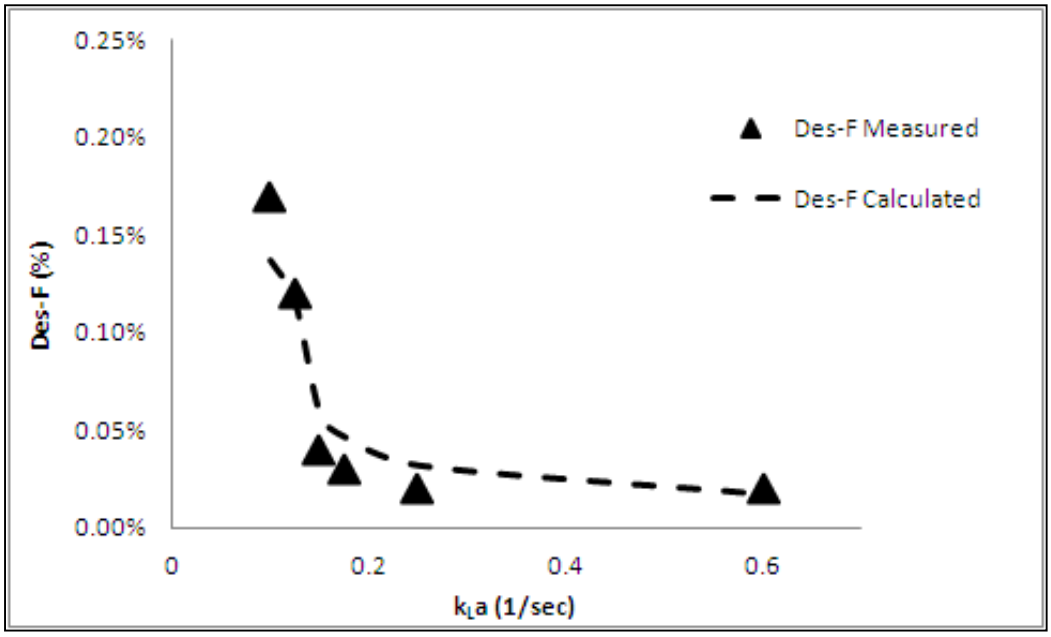

Figure 6.17: Des-F formation vs. k_La at 25°C and 10-wt % catalyst loading

In addition, as seen in Figure 6.1, the rate and net accumulation of hydroxylamine concentration increases with an increase in the overall mass transfer coefficients (k_La). This effect indicates that the des-F formation is inversely proportional to the hydroxylamine formation, thereby,

confirming that the des-F formation is a result of the reduction of the halo group during the halo nitro reduction, and not the result of the dehalogenation of hydroxylamine. Therefore, the des-F formation results from a competitive reaction between the nitro group and the fluorine atom on the molecule. The faster the nitro is reduced to its corresponding hydroxylamine, the lower the amounts of the des-F formation are seen in the reaction. Also, as concluded earlier, there is no des-F formation observed at a k_La of 0.25 (1/s) and higher, nor after all of the nitro is converted to hydroxylamine or to its corresponding aniline.

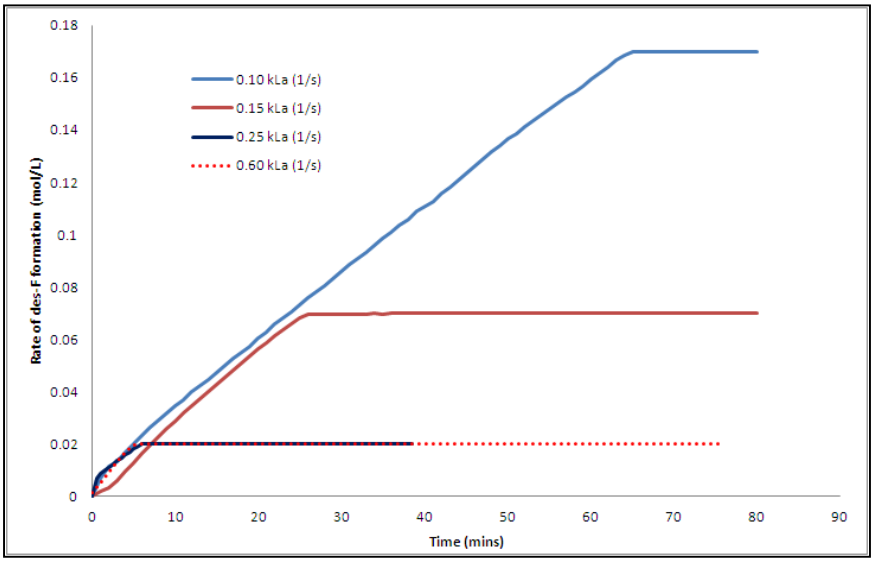

Figure 6.18: Rate of des-F impurity formation vs. time at 10 wt% cat and 25ºC

6.3.2.2 Catalyst Loading

In order to understand the catalyst loading effects on the formation of the dehalogenated impurity, several reactions were run at 0.15 (1/s) k_La and at 25°C; varying the catalyst loading between 2.5 and 10-wt % loading. Concentrations of the individual species were measured over time by HPLC; and, the reaction profile was plotted using React IR spectra, measured every two minutes, as shown in Table 6.4.

Table 6.4: Catalyst Loading vs. des-F Formation

Catalyst Loadings (wt %)	des-F Formation (AUC %)
10.0	0.08
5.0	0.17
2.5	0.26

Table 6.4 shows that as the catalyst loading decreases from 10-wt % to 2.5-wt %, the des-F impurity increases from 0.08% to 0.26%. In addition, as the catalyst loading is decreased from 10-wt % to 2.5-wt %, the rate of nitro reduction also decreases due to fewer available active sites, thereby, resulting in lower overall reaction rate. Similarly, in a separate experiment, a reaction was run as described above in absence of catalyst for five hours. During the course of the reaction, samples were pulled to analyze the species concentration using HPLC; but, no des-F or reduction of nitro aromatic was observed. The resultant conclusion is that the formation of des-F occurs during the competitive reduction of the nitroaromatic.

6.3.2.3 Temperature Effects

In order to understand the temperature effect on the formation of the dehalogenated impurity, several reactions were run at 0.15 (1/s) k_La, varying the temperature between 25°C and 45°C, and keeping the catalyst loading of 10-wt percentage constant. Concentrations of the individual species were measured over time by HPLC; and, the reaction profile was plotted using React IR spectra, measured every two minutes, as seen in Figure 6.19 .

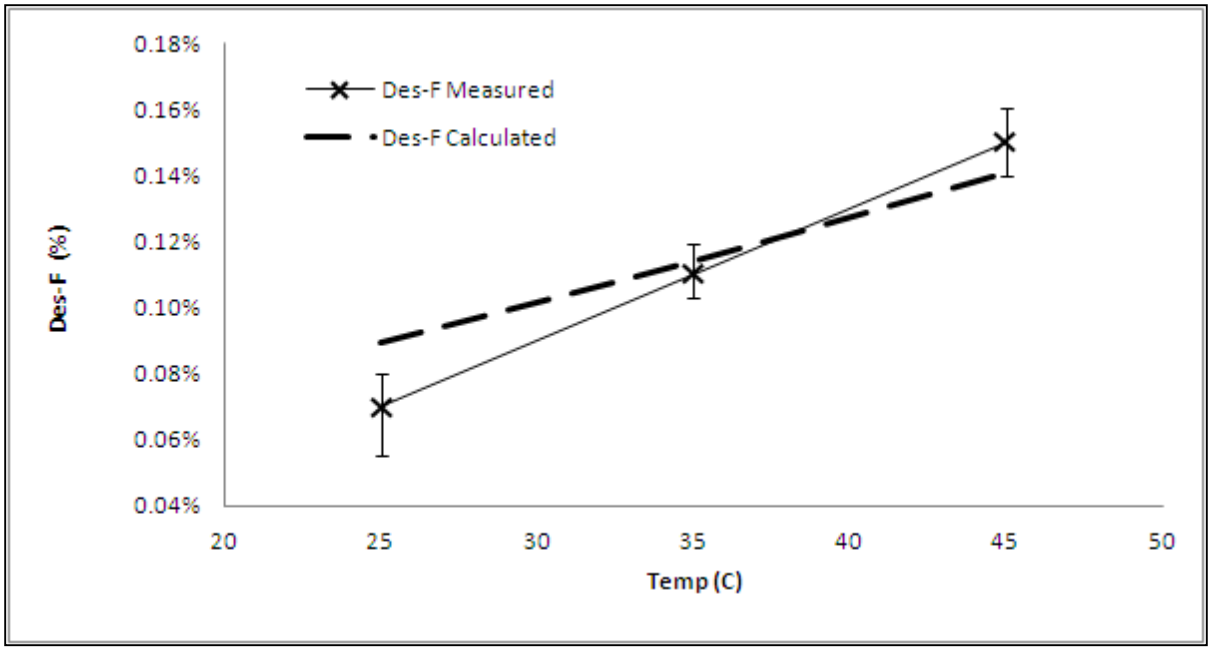

Figure 6.19: Des-F formation vs. the temperature at 0.15 k_La (s^{-1}) and 10-wt % catalyst loadings

The plot shows that the rate of formation of des-F increases linearly with temperature (25-45ºC at 0.15 1/s k_La). The percent des-F was also calculated using Eq. 6.1. It can be observed from the Figure 6.19 that the modeled data for des-F concentrations are found to be in good agreement with the experimentally measured values with a maximum 10% deviation, for the temperature range under investigation.

Also, from Figure 6.20 the activation energy of 36.4 kJ/mol is obtained for des-F formation. It can be said that the des-F formation is a kinetically limited process based on Bartholomew et al. [14] with an activation energy greater than 20 kJ/mol for a catalytic process.

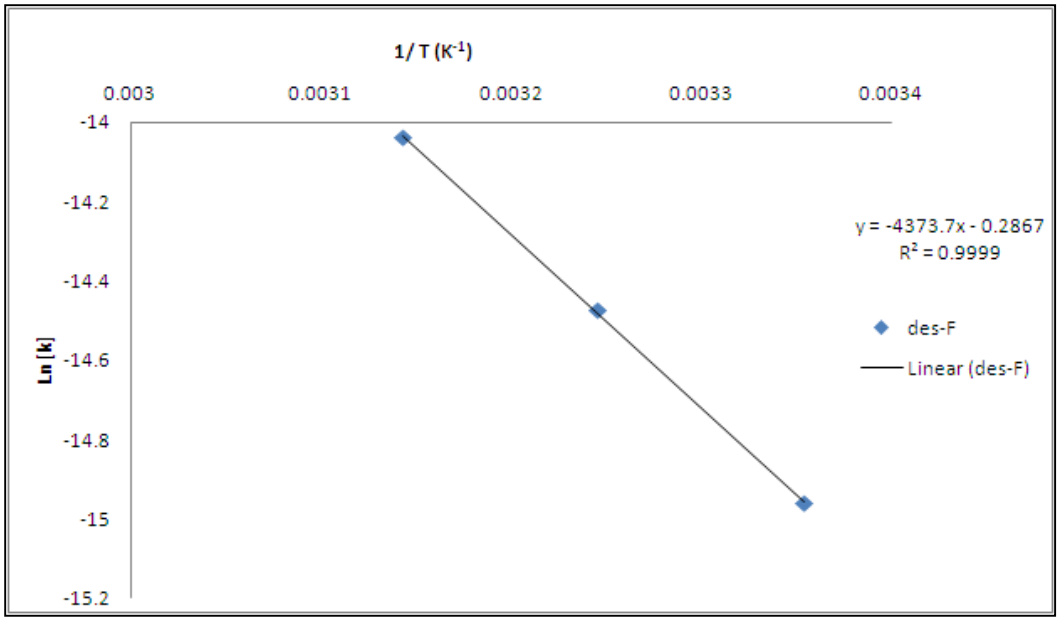

Figure 6.20: Activation energy plot for des-F formation

6.3.2.4 Des-F Impurity Postulation

From the des-F impurity formation experiments, the findings can be summarized as follows:

a) Initially the catalyst sites were pre-saturated with nitroaromatic due to the strong nitroaromatic adsorption rate (very high K_A compared to K_c).

b) At higher k_La values (≥ 0.25), no des-F was observed during the course of the reaction (refer to Figure 6.17).

c) At lower k_La values (≤ 0.20), des-F was found to increase in proportion to the rate of the nitroaromatic reduction.

d) In addition, at lower catalyst loadings, higher amounts of des-F formation were observed; and in the absence of the catalyst, no further des-F or nitroaromatic reduction took place in the reaction mixture.

e) It was also noted that the des-F formation increases linearly with an increase in temperature from 25°C to 45°C.

Therefore, it can be postulated that the dehalogenation takes place due to competitive reduction between the nitroaromatic and the halo- functional group on the nitroaromatic ring. The dehalogenation was only observed in the presence of the catalyst, because the catalyst lowers the overall activation energy for the system. During the reaction, the nitro adsorbs onto the catalyst site, and the hydrogen is adsorbed onto the adjacent site in order for the reduction to occur (single-site model from the reaction kinetics chapter). If the reaction conditions are such that the rate of nitro reduction is suppressed from the lack of hydrogen, then the halogen on nitroaromatic has time to react with the dissolved hydrogen gas in the liquid phase and forms the dehalogenated impurity. The rate of dehalogenation increases with the lower catalyst loadings and lower mass transfer rates (i.e., lower adsorption of hydrogen onto the catalyst site available to reduce the nitro group), as well as, increasing the reaction temperature.

Initially, due to the presence of the electron-withdrawing group on the aromatic ring, such as the nitro-, it stabilizes the incipient negative charge developed on the aromatic ring during the hydrogenolysis of carbon sp^2-substituted halogen bond. Once the electron-withdrawing group is reduced to the electron-rich group, such as the hydroxylamine, aniline, etc., then the rate of hydrogenolysis of C-X (halogen) drops. A similar observation was cited by Moreau [15], where the rate of hydrogenolysis of carbon sp^2–substituted bond resulted due to the hydride ion attack onto the C-X. The rate of hydrogenolysis was calculated by quantum chemical calculations and found to correlate with the π-electron density charge on the carbon substituent. The hydrogenolysis rate was found to increase with an increase in π-electron density on the carbon substituent (C-X). Refer to Figure 6.21 for des-F postulation.

Hence, it can be concluded that the de-halogenation results only during the presence of the nitroaromatic group which stabilizes the negative charge on the aromatic ring. Once the nitro aromatic

is consumed completely, the rate of hydrogenolysis of C-X bond drops, and no further dehalogenated impurity is generated in the reaction mixture.

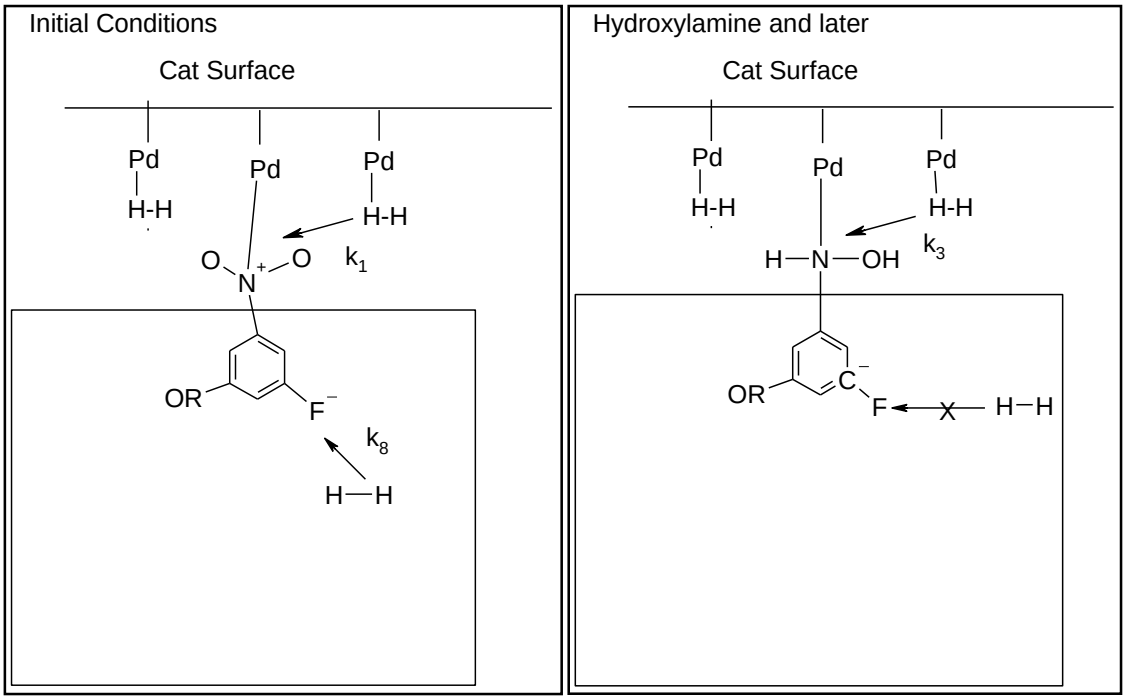

Figure 6.21: Postulation of des-F formation

6.4 Conclusions

Hydroxylamine formation was found to be a mass transfer limited process, whereas, the hydrogenolysis of hydroxylamine was found to be kinetically limited. In order to control the rate and the maximum concentration of hydroxylamine in the reaction, both mass transfer rates and the desired reaction temperature were required. A shift in the rate-limiting step was postulated for the mass transfer limited process, which resulted in hydroxylamine formation as rate limiting, to a kinetically limited process, which resulted in hydrogenolysis as the rate-limiting step. For the current example and choice of the catalysts system, vanadium promoters were found to be ineffective in reducing the overall accumulation of hydroxylamine in the reaction mixture. A detail kinetic model was also presented in

order to understand and control the hydroxylamine formation with respect to both, the mass transfer coefficient and the intrinsic kinetics.

Des-F impurity formation was found to be a function of both the mass transfer rate, as well as the reaction temperature. The dehalogenated impurity was formed as a result of competitive reduction between the nitroaromatic and the halo- functional group on the nitroaromatic ring during the mass transfer limited process. The rate of dehalogenation was found to increase with lower catalyst loadings or lower mass transfer rates (i.e., lower adsorption of hydrogen onto the catalyst site available to reduce the nitro group), as well as with the increase in the reaction temperature. Initially, due to the presence of the electron-withdrawing group on the aromatic ring, such as the nitro-, it stabilizes the incipient negative charge developed on the aromatic ring during the hydrogenolysis of carbon sp^2-substituted halogen bond. Once the electron-withdrawing group was reduced to the electron-rich group, such as the hydroxylamine, aniline, etc., then the rate of hydrogenolysis of C-X (halogen) drops. It was found that the dehalogenated impurity only occurred in the presence of nitroaromatic, and it did not increase during the hydrogenolysis of hydroxylamine or in the presence of aniline under the reaction conditions. Both the temperature and mass transfer rates were critical in order to meet the product specification for the des-F impurity. A kinetic model was also postulated in order to understand and control the des-F formation with respect to both, the mass transfer coefficient and the intrinsic kinetics.

References

1 J. I. Macnab, The Role of Thermochemistry in Chemical Process Hazards: Catalytic Nitro Reduction Process, I. Chem. E. Symposium Series, 1981, No. 68.

2 F. Stoessel, Experimental study of thermal hazards during hydrogenation of nitroaromatics; J. Loss. Prev. Process Ind., 1993, Vol. 6 (2), p. 79-85.

3 W. R. Tong, R.L. Seagrove, and R. Wiederhorn, 3-4-Dichloroaniline Autoclave Incident, AIChE Loss Prev., 1977, Vol. 11, p. 71-75.

4 P. Cardillo, A. Quattrini, E. Vanjna de Pava, and A. Girelti, Reduction of Amines, J. Calorim. Anal. Therm. Thermodyn. Chim., 1986, Vol. 17, p. 394-397.

5 W. R. Tong, R.L. Seagrove, and R. Wiederhorn, 3-4-Dichloroaniline Autoclave Incident, AIChE Loss Prev., 1977, Vol. 11, p. 71-75.

6 J. A. Miller, Carcinogenesis by chemicals, Cancer Res., 1970, Vol. 30 (3), p. 559-576.

7 M. Studer, S. Neto, and H. -U. Blaser, Modulating the hydroxylamine accumulation in the hydrogenation of substituted nitroarenes using vanadium-promoted RNi catalysts, Topics in Catalysis, 2000, Vol. 13, p. 205–212.

8 U. Birckenstock, B. Lachmann, J. Metten and H. Schmidt, DE2849002 (1978)

9 J. R. Kosak, in Catalysis of Organic Reactions, Marcel Dekker, New York, 1988, Chp. 18, p. 135-138.

10 Reaction block as shown in Figure 4.1 was purchased from HEL group in UK.

11 Catalyst Screening was performed to find the optimum selectivity and reactivity. Refer to Chapter 3 for details on catalyst selection.

12 React IR is a mid-infrared spectra measurement instrument, purchased from Mettler Toledo Inc. For more details please refer to Mettler Toledo website (http://us.mt.com/us/en/home/products/L1_AutochemProducts/L2_in-situSpectrocopy.html).

13 M. Studer, S. Neto, and H. -U. Blaser, Modulating the hydroxylamine accumulation in the hydrogenation of substituted nitroarenes using vanadium-promoted RNi catalysts, Topics in Catalysis, 2000, Vol. 13, p. 205–212.

14 C.H. Bartholomew and R.J. Farrauto, Fundamentals of Industrial Catalytic Processes, John Wiley & Sons, Inc., 2006, 2nd edition.

15 C. Moreau, J. Joffre, C. Saenz, J. C. Afonso, and J-L. Portefaix, Mechanism of carbon sp^2 – heteroatom bond clevage in hydroprocessing of substituted benzenes over unsupported transition metal sulfides, Journal of Molecular Catalysis A: Chemical, 2000, Vol. 161, pages 141-147.

CHAPTER 7: SCALE-UP OF NITROAROMATIC AND CATALYST ROBUSTNESS

7.1 Background

Hydrogenation of halonitroaromatic is a highly energetic process with a heat of reaction of 545-kJ/mol [1]. The reaction mechanism was found to proceed by the reduction of halonitroaromatic to its corresponding hydroxylamine, which is a highly energetic intermediate that poses a safety concern upon scale-up, followed by the hydrogenolysis of hydroxylamine to its corresponding halo aniline. The formation of hydroxylamine was found to be both a function of both the reaction temperature, as well as mass transfer rate of the hydrogen gas into the reaction solution. In addition, another impurity was formed during such reaction: the dehalogenated aniline. It was also found to be a function of reaction rate that needed to be controlled upon scale-up in order to meet the final product specifications.

In order to establish the volumetric mass transfer coefficient for the pilot plant reactor, similar to the lab process, the method described by Shah et al. [2] was utilized. The hydrogen gas is introduced into the headspace of the batch reactor and, using surface aeration techniques such as agitation, hydrogen is mixed with the liquid phase and reaches equilibrium over time. The rate at which the hydrogen concentration reaches equilibrium with the liquid phase is directly proportional to the volumetric mass transfer coefficient (k_La). The volumetric mass transfer coefficient depends upon several factors, such as the liquid state properties, agitation rate and mechanism, pressure of the system, and liquid volume (hydrogen solubility). By using a simple, non-reacting solvent system to calculate k_La based on various agitation rates and liquid volumes in the plant reactor, the process could be scaled up from lab to plant reactors by maintaining the reactions at similar k_La values.

An explosion occurred during the catalytic reduction of chloronitrobenzene, which was attributed to runaway decomposition initiated by exothermic disproportionation of the hydroxylamine intermediate [3], and it has been accepted in recent years that such intermediates may cause significant process hazards. In order to safely scale-up and prevent the thermal runaway during such hydrogenations, the heat removal rate would be required to exceed the heats of reaction. Also, the reaction profile for the intermediate species, along with the impurity, would require scaling up of both the mass and heat transfer from lab to pilot scale in order to meet the desired specification.

Catalyst behavior is always in question during scale-up of any heterogeneous reaction and will be evaluated. The catalyst is said to be robust when it has the same turnover frequency (TOF) as the lab scale reactions during plant runs. External factors, such as plant operation, which can sometimes cause the catalyst to perform differently from lab scale runs, will also be evaluated, as elucidated earlier.

7.2 Experimental Setup

This section details in the pilot scale reactor used for scaling-up the nitroaromatic reaction. It details in the procedure for measuring k_La values and scaling-up reactions from laboratory scale to pilot scale using this information. A procedure for the scale-up reaction of nitroaromatic is also detailed herein.

7.2.1 Equipment

The plant scale hydrogenator was purchased from the Precision Stainless group in the USA. It is equipped with fully automated temperature, pressure, and stirring control. The reactor was made with hastelloy C-22, with a maximum reaction volume of 947-L and total volume of 1247-L (total liquid + headspace volume). See Figure 7.1 for details. The batch reactor was fitted with a temperature gauge (T), a pressure transducer (P), and a pitched blade turbine agitator (down-flow) with speed control (M). Gas inlet and outlet (vent) valves for hydrogen and nitrogen, were located in the headspace of the vessel. Syltherm was used as a heat transfer fluid in the jacket for temperature control. A three-way automatic valve separates the hydrogen and nitrogen gas in the reactor headspace. The rupture disc is set at 15-barg pressure in case of over pressurization. Both the hydrogen and the nitrogen cylinders are hooked up to the gas regulators; and the regulators are manually adjusted at a rate slightly higher than the desired reaction pressure. The total hydrogen uptake, as well as temperature difference between the jacket and reactor, are recorded every few seconds in the control software.

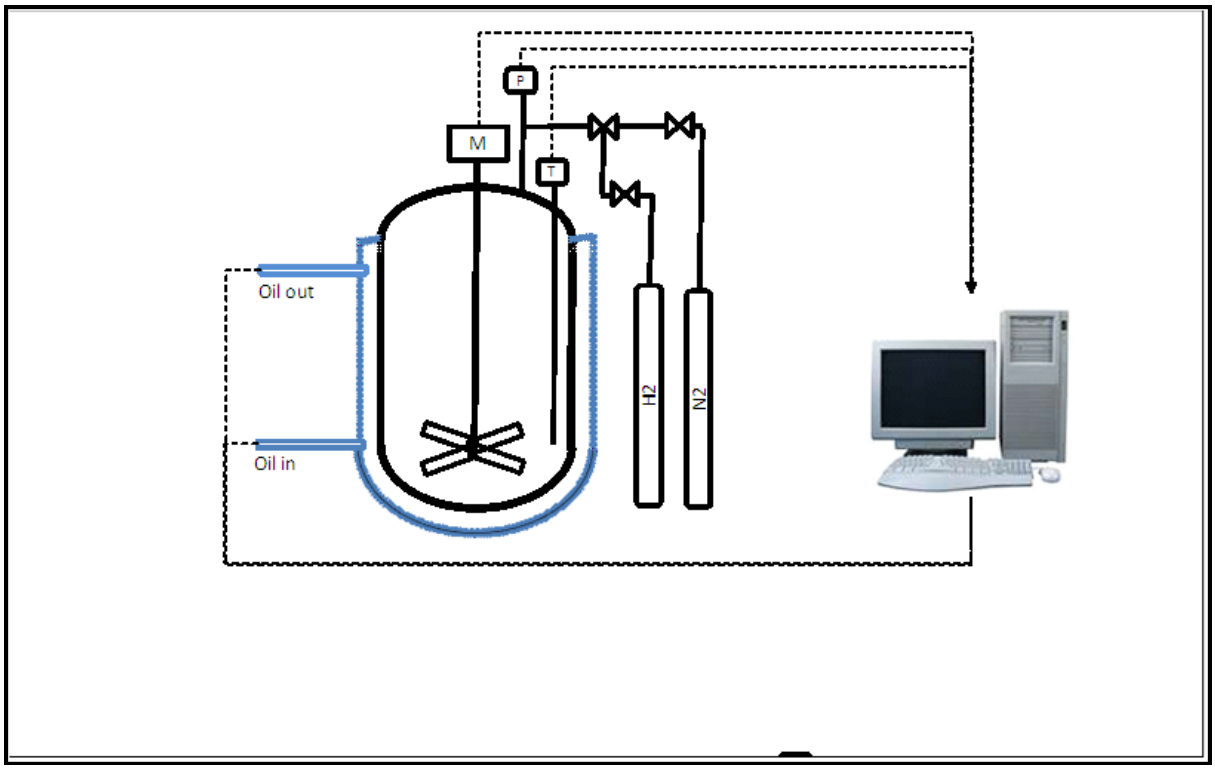

Figure 7.1: Pilot Plant Reactor Configuration

7.2.2 Materials and Reagents

The materials and reagents used for measuring the mass transfer coefficient and for scaling up the reaction are given as follows:

7.2.2.1 Mass Transfer Coefficient Measurement (k_La)

High-purity hydrogen and nitrogen gas cylinders (purity of 99.999%), purchased from Airgas Co.; were connected to the reactor. As most of the nitro reductions are carried out in water and/or alcohol systems, methanol was chosen as the standardized solvent to conduct the mass transfer studies due to its high dielectric values and hydrogen solubility [4]. Methanol was purchased from Aldrich Chemical Company.

7.2.2.2 Reaction Scale-up

High-purity hydrogen and nitrogen gas cylinders (purity of 99.999%) purchased from Airgas Inc., were connected to the pilot plant reactor. The starting material, nitroaromatic [A] in Figure 5.1, is an advanced intermediate prepared by GlaxoSmithKline. Concentrated hydrochloric acid (HCl) was purchased from Sigma-Aldrich Co., with an assay of 37% HCl. Solvents used for the process; methanol, ethanol (200-proof) and distilled water were also purchased from Sigma-Aldrich company. The catalyst (10% Pd/C) was purchased from Evonik Industries.

7.2.3 Procedure

This section describes in detail the procedure used for both measuring the k_La and scaling-up the reaction to produce halo-aniline product in the pilot scale reactor.

7.2.3.1 Mass Transfer Coefficient (k_La) Measurement

Most of the industrial hydrogenations are conducted in polar protic solvents, such as water and/or alcohols, i.e., methanol [5]. Polar protic solvents are solvents with high dielectric solvents which have the ability to donate H-atoms and form strong hydrogen bonding. Methanol (400-L) was charged to the reactor, and the batch temperature was adjusted to 25°C. Once the desired temperature was reached, the reactor was inerted with nitrogen (agitation was turned off during the inertion process). The reactor was then pressure purged twice with hydrogen to evacuate nitrogen from the headspace. Subsequently, the reactor was pressurized again with hydrogen to 60 psig, and the inlet valve was closed. Initial agitation was set to 80 RPM at t=0, and the pressure drop from the headspace was measured as a function of time every two seconds. As the hydrogen was being absorbed into the liquid phase, the total hydrogen uptake was calculated from the pressure drop in the headspace using the ideal gas law. Several experiments were run (using virgin methanol for each experiment) while varying agitation rates and maintaining a constant liquid level in order to get a correlation for k_La versus the

agitation rate (rpm). The liquid level was calculated from the reaction volume to be run in the plant vessel. By virtue of maintaining similar k_La values between the lab and the plant scale reactor, the overall mass transfer rate can be kept constant.

7.2.3.2 Reaction Scale-up Procedure

In a batch reactor (as shown in Figure 7.1), halonitroaromatic [A] was charged (40-kg), along with 10-wt% Pd on C [6] catalyst (4-kg), 179.2-L of 200-proof ethanol, 192.8-L of purified water, and 24.8-L of concentrated HCl. The reactor was stirred for 30 minutes at 25°C to dissolve [A] into the solution. The reactor was then purged with nitrogen to evacuate the reactor headspace from air and inert the reactor. Unlike the lab reactions, the reactor was not purged with hydrogen after the nitrogen purge cycle but was maintained under 2-psig of nitrogen pressure in order to avoid the potential runaway reaction. Secondly, the presence of small amounts of nitrogen prevents the reaction from consuming the entire amount of hydrogen present in the headspace and creating an unsafe environment by creating a vacuum. This was the normal safety procedure followed in the pilot plant for such hydrogenation reactions. During the pressure purge cycle, the agitation rate was set to zero. The reactor was then pressurized to 60-psig (4-barg) of H_2 pressure, and then the agitation was started (120 rpm or a k_La of 0.15 1/s) to allow the reaction to commence. During the scale-up of such reactions, the k_La was kept constant (using methanol/hydrogen k_La, as described earlier) from lab to pilot plant reactors. The hydrogen uptake was directly measured based on the pressure drop in the headspace of the reactor with time. The species concentrations were measured by HPLC grab samples (at 30 minute intervals and upon cessation of the hydrogen uptake) during the reaction. The reaction was deemed complete once the HPLC profile showed < 0.20% area under curve (AUC) for residual [A] and greater than 98% (AUC) for product [D]. Once the reaction was completed, the reactor was vented off and inerted once again with nitrogen. The catalyst was then filtered off from the reaction solution for further processing.

7.2.3.3 Catalyst Characterization

Catalyst characterization of virgin and spent catalyst, was performed by using an Autosorb automated gas sorption system (1-C), purchased from Quantachrome Instruments (as described in Section 3.4.3). The Autosorb equipment consisted of a sample preparation area and an analysis station. It was also connected to the helium, nitrogen, and hydrogen gas supply lines. The Autosorb analysis station was also connected to a high-performance vacuum pump and a mass spectrometer for off-gas analysis. The system was fully automated and was controlled by the computer system. See Figure 3.3 and Figure 3.4 for schematic details of the system. By measuring physi- and chemisorption for the catalyst, one can understand the differences in catalyst performances for the virgin and spent catalysts (refer to Sections 3.4.3.1 and 3.4.3.2 for physisorption and chemisorption techniques, respectively).

The Quantachrome Autosorb Automated Gas sorption system was also equipped with mass spectrometry, for outlet gas analysis. The catalyst was loaded into the quartz tube and then dried under helium atmosphere for six hours under vacuum, as the catalyst was water wet. The catalyst was then reduced with hydrogen gas in order to determine the dispersion and crystallite size of Pd/C. Once the reduction was complete, the catalyst was filtered off and dried under vacuum. The spent catalyst was then analyzed (by various purging sequences with and without N_2 atmosphere in the headspace), along with a fresh catalyst (virgin).

7.3 Results and Discussion

This section details in the results for the k_La experiments and the reaction scale-up data in the pilot plant reactor. Catalyst activity and performance will also be evaluated and compared with the lab scale reactions. Finally, this section discusses the reaction performances along with any catalyst inhibition observed on scale.

7.3.1 Pilot Plant Reactor k_La Measurement

Hydrogen pressure drop from the headspace was measured as a function of time, and the data was collected and stored in Delta V (pilot plant software) every two seconds. Figure 7.2 illustrates the pressure drop in the headspace for the experiment run with 400-L methanol liquid level and at an initial hydrogen pressure of 9-barg, when stirred at 110 rpm.

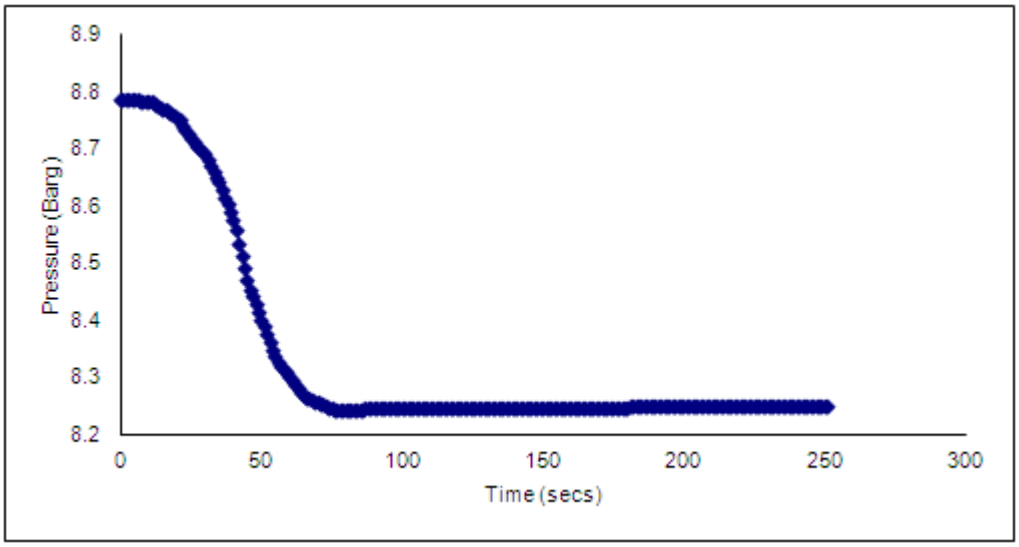

Figure 7.2: Pressure vs. Time for 400-L Methanol at 110 rpm

The overall volumetric mass transfer coefficient (k_La) was calculated as the slope of Equation 4.9, and plotted in Figure 7.3. The right-hand side of Equation 4.9 is plotted on the y-axis, with time on the x-axis. The slope of the plot gives the value of the overall volumetric mass transfer coefficient (k_La). These experiments were replicated three times, and the k_La values were found to be in close agreement with each other, as illustrated in Figure 7.4.

The overall volumetric mass transfer coefficient was plotted versus the rpm and was found to be linear, as observed in Figure 7.4. This is a critical result as, due to the linearization of the plot, one can calculate the rpm required to run the reaction at a desired k_La value. Similarly, the measurements

were carried out at various agitation rates for 400-L methanol volume. For each measurement, a fresh solvent (methanol) was charged and then degassed, as per the procedure stated earlier.

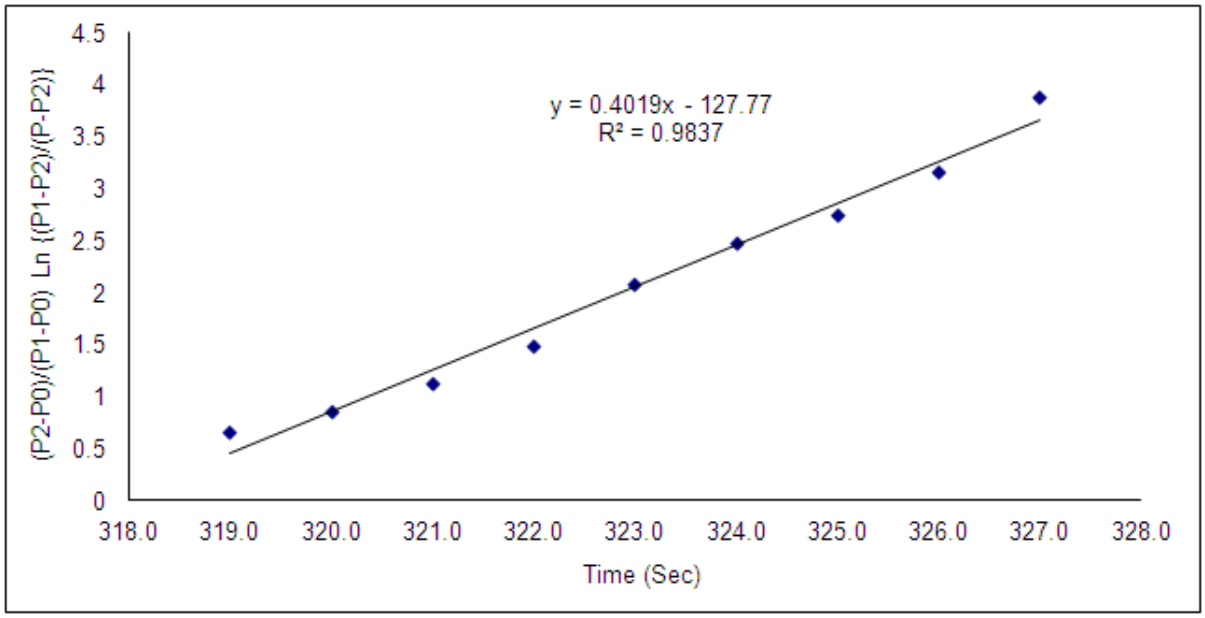

Figure 7.3: Estimation of k_La using Eq. 4.9

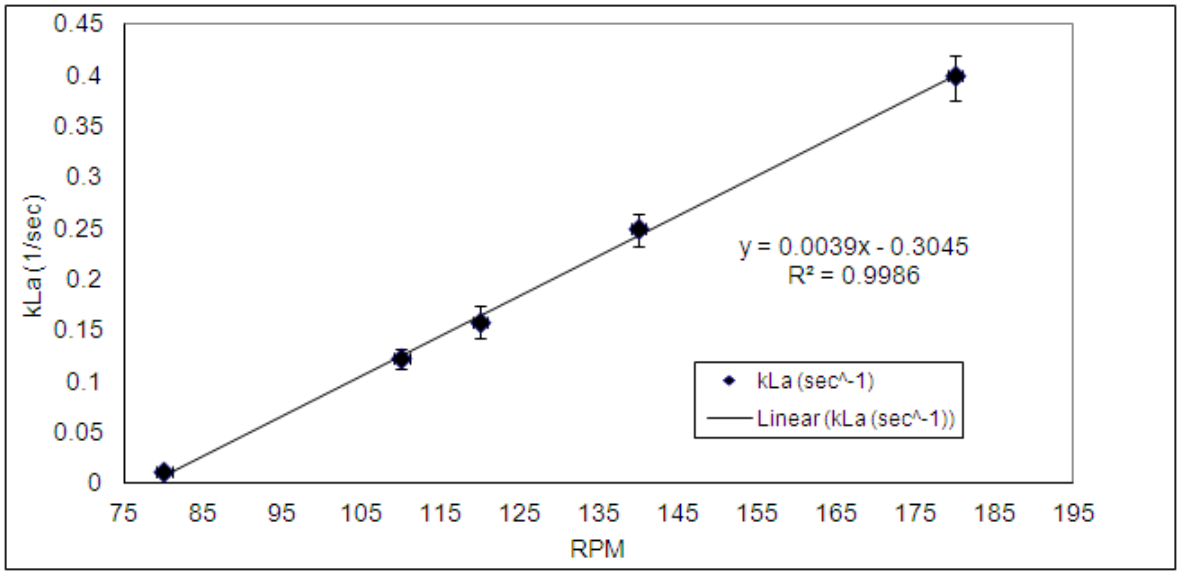

Figure 7.4: The Overall Volumetric Mass Transfer Coefficient vs. rpm (for 400-L MeOH fill level)

7.3.2 Pilot Plant Reaction Scale-up Under N_2 Atmosphere

Hydrogen uptake was measured as a function of time for the plant reaction and comparatively for the lab reaction. Figure 7.5 illustrates the hydrogen uptake between the lab and plant scale reaction. Results showed that the plant scale reaction was much slower compared to the lab reaction at a similar mass transfer rate (k_La of ~0.15 1/s), reaction temperature (25°C), and the catalyst loading (10-wt %). Since the reaction conditions and the mass transfer rate were similar between the lab and plant scale reactions, the catalyst for the plant reaction was deemed inhibited by some external factors. The reaction profile at the end of the reaction was higher in des-F content, at 0.18% (AUC), than the specification (< 0.15% AUC). In order to scale the reaction in the pilot plant reactor successfully, the des-F levels had to be maintained below 0.15% AUC. It was necessary to understand the catalyst behavior at plant scale.

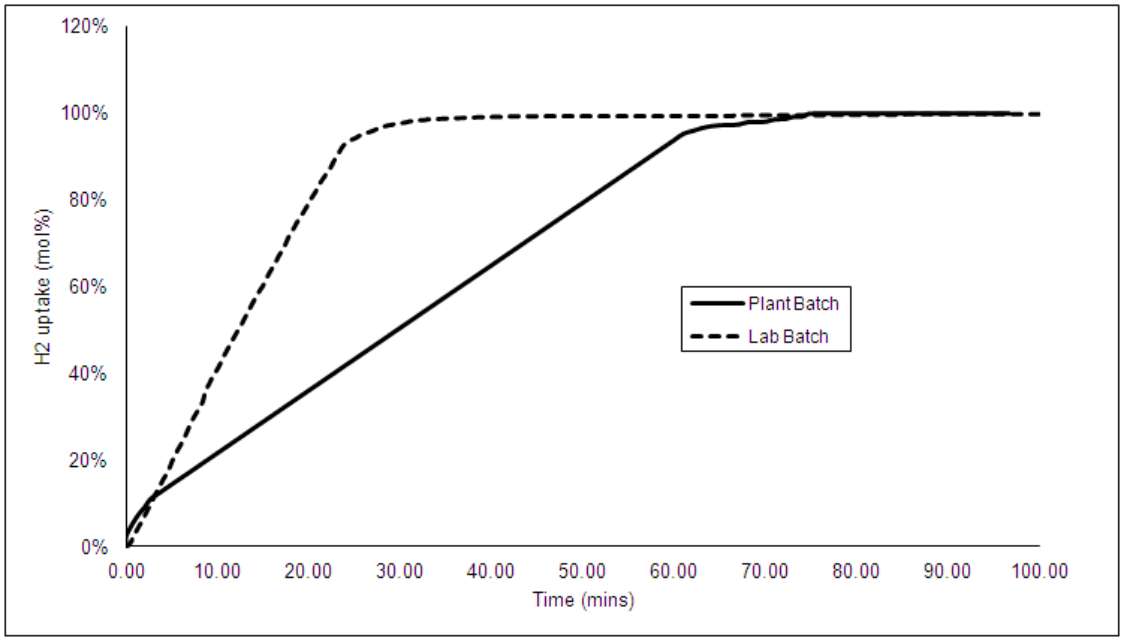

Figure 7.5: Pilot Plant and Lab Scale Reactions at 0.15 k_La (1/s)

7.3.2.1 Understanding Catalyst Inhibition

Figure 7.5 illustrates that both the lab and plant runs had similar reaction rates for the first three minutes, after which the plant reaction rate was almost half for the rest of the reaction. In addition, the des-F impurity was higher than the specification and, thus, it was vital to understand the cause for the catalyst inhibition. Comparisons between the two different k_La of 0.10 and 0.15 1/s reactions in the lab were made to the plant run, as seen in Figure 7.6. During the start of the plant reaction, the H_2 uptake is similar for the first three minutes when compared to the lab reaction at the same k_La of 0.15 (1/s). However, after the first three minutes of the reaction, it slowed to the point that now the rate of the reaction became similar to the one obtained in the lab reaction that was run at 0.10 k_La (1/s).

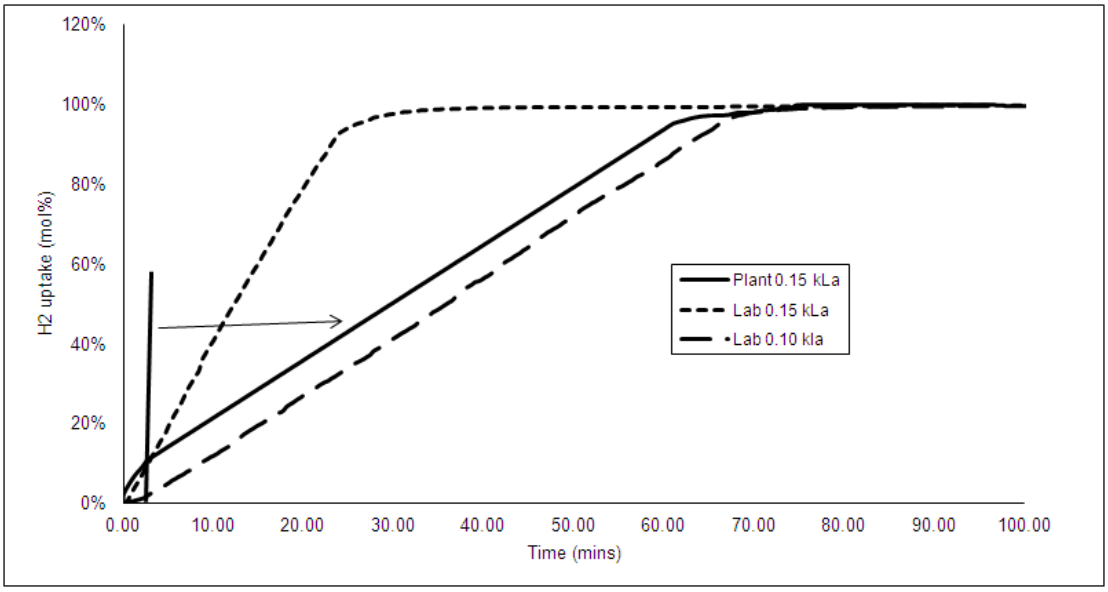

Figure 7.6: Comparison of H_2 Uptake Between the Lab and Plant Reactions

This change from a kinetic limited reaction (at 0.15 k_La) to the mass transfer limitation (at 0.10 k_La) as shown in Chapter 5, is indicative of catalyst poisoning or inhibition of some sort. In order to identify this phenomenon, several reactions were run in the lab at k_La of 0.15 (1/s), 10-wt % catalyst

loading, and at 25°C, but varying the hydrogen pressure, with and without nitrogen present in the headspace. Refer to Table 7.1 for the experimental details.

Table 7.1: Reactions with Varying Amounts of H_2 Pressure and With/without N_2

Experiment	$P(N_2)$ bara	$P(H_2)$ bara	Reaction rate (mol/L/min)	des-F (%)
1	0	5	0.00124	0.08
2	0	4	0.00097	0.11
3	0	3	0.00075	0.15
4	1	5	0.00043	0.20
5	1	4	0.00034	0.23
6	1	3	0.00027	0.29

The results clearly indicate the following conclusions:

1. The reaction rate decreases with the decrease in hydrogen pressure (with or without nitrogen present); and
2. The des-F impurity increases with a decrease in the hydrogen pressure; however, the des-F increases significantly in the presence of nitrogen in the headspace at the same hydrogen pressure.

The results indicate that the presence of nitrogen in the headspace actually inhibits the reaction rate at the same hydrogen pressure (refer to Figure 7.7). In order to comprehend the potential of catalyst poisoning the catalyst would be further characterized.

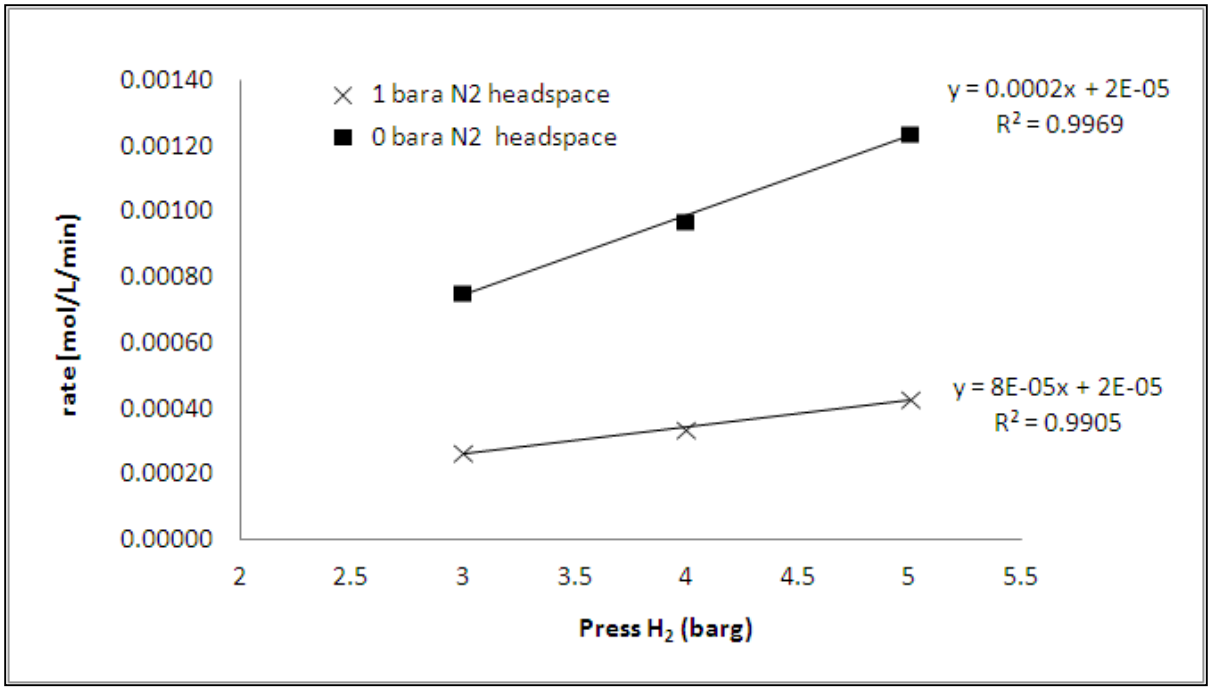

Figure 7.7: Reaction Rate vs. H_2 Pressure (with/without N_2 headspace)

7.3.2.2 Catalyst Characterization using Quantachrome Autosorb Instrument

In order to understand the catalyst inhibition as shown above, it was desired to characterize the catalyst using physi- and chemisorption methods as discussed in Chapter 3, Section 3.4.3. The spent catalyst was filtered and analyzed by physi- and chemisorption techniques, using Quantachrome Autosorb automated gas sorption system [7] hooked to a mass spectrometer to measure off-gassing from the catalyst, and compared to that of the virgin catalyst.

7.3.2.2.1 Physisorption Analysis

The purpose of physisorption was to determine the changes in the surface area and the total pore volume for the virgin and the spent catalyst from the reaction media. The catalyst samples (virgin and spent) were outgassed at 300°C for at least one hour before nitrogen physisorption measurements were taken (as detailed in Section 3.4.3.1). The results for the surface area and total pore volume for several lots of catalysts are summarized in Table 7.2.

7.3.2.2.2 Chemisorption Analysis

The aim of chemisorption experiments is to determine the number of active sites present on a given sample (as detailed in Section 3.4.3.2). Several lots of the catalyst were characterized, using this technique, and were found to be identical with respect to metal dispersion, active surface area, and crystallite size, as summarized in Table 7.2. Once the reaction was completed, the catalyst was re-tested. The catalyst was filtered and vacuum dried to remove any organic material. The spent catalyst was then analyzed and compared to the fresh (virgin) catalyst, which indicated that the spent catalyst gave the same percent metal dispersion of 2.5% Pd, along with crystallite size of ~454°A, compared to the virgin catalyst, thus confirming that the catalyst did not lose its activity during the course of the reaction.

Table 7.2: Catalyst Characterization Results

Lot #	ASA (m^2/g)	Dispersion (% D)	Avg. Cryst. Size d (°A)	Multi-point BET Surface Area (m^2/g)	Total Pore Volume (cm^3/g)
Virgin Catalyst	1.10	2.46	454	854.9	0.7948
Spent cat 1	1.08	2.39	448	856.3	0.8113
Spent cat 2	1.10	2.52	451	852.8	0.8037
Spent cat 3	1.11	2.53	454	849.3	0.7868

7.3.2.3 Mass Spectrometer Analysis

Mass spectrometry was used to measure the off gassing during the physi- and chemisorption analysis, for both the virgin and the spent catalyst. For the reactions that were run under H_2

headspace (no partial N_2 present), the virgin and the spent catalyst showed presence of three peaks in the mass spec during the helium drying process; water vapor, oxygen and helium. However, for the spent catalyst, which was run under a partial nitrogen atmosphere during the reaction, mass spec analysis indicated presence of a couple of additional peaks during the helium drying cycle, as shown in Figure 7.8. These two new peaks were later identified as carbon monoxide and carbon dioxide based on the molecular weight obtained from the mass spec. These findings indicate the presence of small amounts of CO in the nitrogen supply stream.

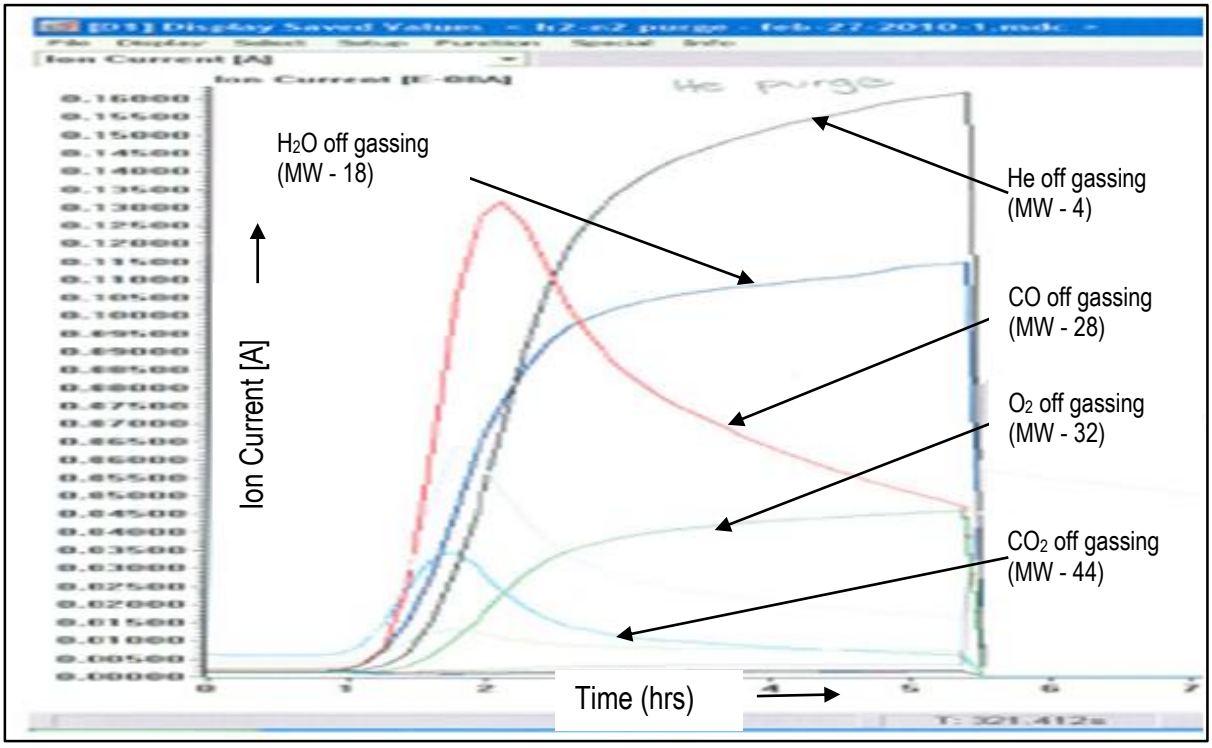

Figure 7.8: Mass Spec Profile during Helium Drying for Spent Catalysts Run under N_2 Atmosphere Reaction Conditions

As the drying of the catalyst continued, the CO and CO_2 peaks reached a maximum value and then started to decrease after two hours; whereas, the water peak was still rising as the catalyst was

over 50% water wet (w/w %). The catalyst was dried until the water peak started to decrease and reached a low-level equilibrium.

A small sample of N_2 from the supply tank was directly injected into the gas chromatography (GC) instrument. The result illustrated in Figure 7.9 (a) showed a small peak after the nitrogen (large) peak on the shoulder. In addition, a nitrogen sample from the ultra pure supply tank containing 99.999% pure nitrogen was also injected into the GC. This sample only indicated the presence of nitrogen in the GC and did not have this small shoulder CO peak near the end (refer to Figure 7.9 (b)). This indicated the presence of small amounts of CO in the N_2 supply, which might have had a larger impact on the observed reaction rate.

It can be postulated that when the reaction is run under slight N_2 headspace, due to the presence of small amounts of CO in the nitrogen stream, the CO adsorbs onto the catalyst and, thereby, reduces the number of sites available for reaction. Also, from hydrogen pressure vs. the reaction rate plot (Figure 7.7), it can be postulated that the rate of catalyst poisoning is first order w.r.t. concentration of CO present in N_2, thereby, reducing the total active site $[\theta_*]$ balance to Equation 7.1. Where C_{CO} is the concentration of CO (ppm) in the reactor headspace, K_i is the equilibrium rate constant for species "I"; and [A], [C], and [D] are the species concentrations.

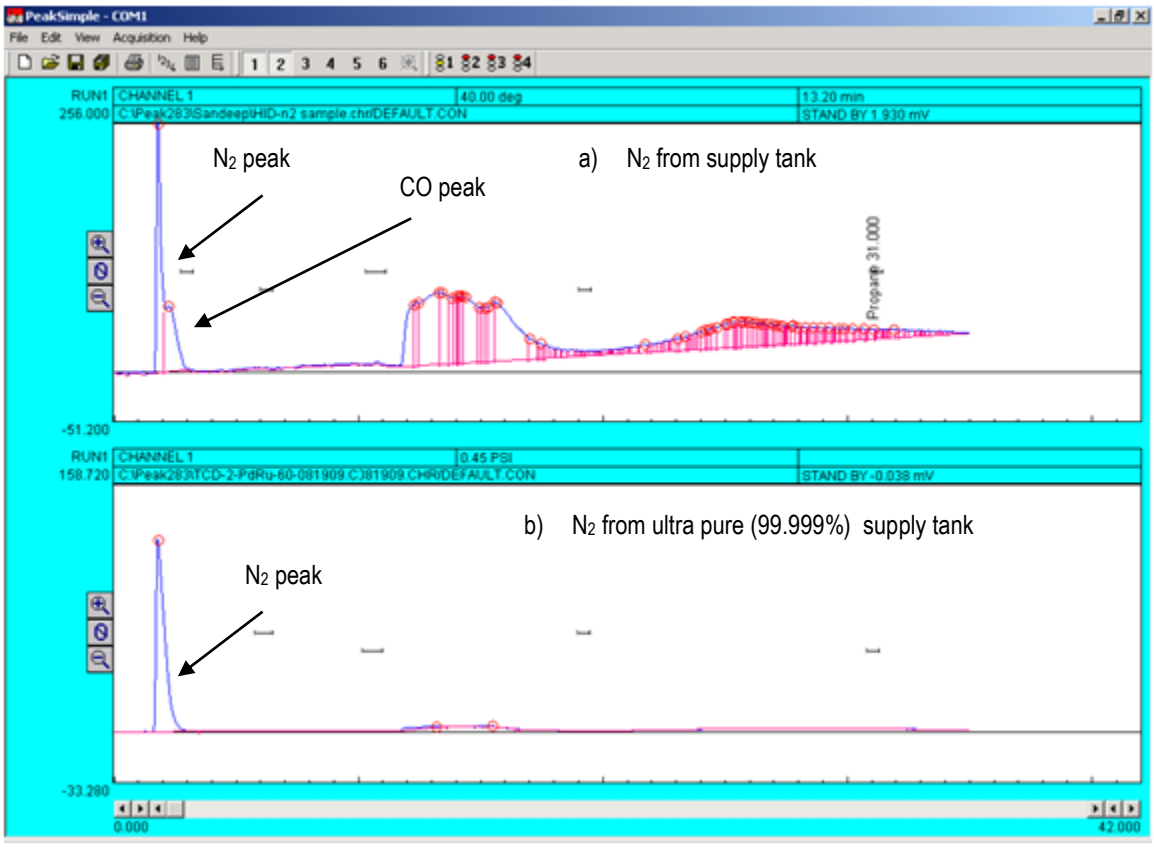

a) sample indicates presence of small amounts of CO in the N_2 supply;
b) sample indicates no CO in the ultra pure N_2 injection below.

Figure 7.9: Gas Chromatography of Nitrogen Sample

$$[\theta_*] = \frac{1 - C_{CO}}{(1 + K_A[C_{Al}] + K_C[C_{Cl}] + K_D[C_{Dl}])} \qquad [7.1]$$

To verify this claim, a series of experiments were run in the lab using a pre-mixed CO (50 and 100 ppm) in the nitrogen supply tank to purge the reactor. Initially, once all the materials were charged, no H_2 purge sequence was applied. The reactor was then pressurized to 4-barg of H_2, and H_2 uptake measurements were collected as the reaction progressed (Refer to Table 7.3 for the reaction conditions). As can be examined from the controlled reaction (with H_2 purge sequence), the reaction

rate decreases as the amount of CO increases from 50 to 100 ppm in the reactor headspace (experiments 2 through 4). The reaction that was run with 1-bara (bar atmospheric) of ultra pure nitrogen (no CO present) and 4-bara of hydrogen was found to be indistinguishable when compared to the reaction that was run in the absence of nitrogen and 4-bara of hydrogen (experiments 1 and 5).

Table 7.3: Controlled Reaction vs. Reaction Rates

Experiment	Reaction Conditions	H_2 pressure (bara)	N_2 pressure (bara)	CO (ppm)	Reaction rate (mol/L/min)
1	H_2 in headspace	4	0	0	0.0010
2	N_2 in headspace	4	1	50	0.0006
3	N_2 in headspace (plant)	4	1	?	0.0003
4	N_2 in headspace	4	1	100	0.0002
5	N_2 in headspace	4	1	0	0.0010
6	N_2 in headspace	4	1	125	0.0000

Experiments 2, 4, and 5 were plotted vs. the reaction rate, demonstrating a linear relationship between the amounts of CO present in the nitrogen stream, as illustrated in Figure 7.10. Based on this linear relationship, the carbon monoxide for the plant reaction was calculated to be ~ 83 ppm. The suppliers for the lab and the plant N_2 were the same and found to contain similar amounts of carbon monoxide. In addition, it can also be observed that, at 125 ppm of CO, the reaction rate would reduce to zero. To confirm this claim, a pre-mixed nitrogen cylinder with 125 ppm of CO was used to purge the reaction mixture, and was run under 4-bar of H_2 and 1 bar of N_2 pressure (as shown in Table 7.3, experiment 6). This reaction did not progress even after being for 4-hours under the reaction condition. Since the use of ultra pure nitrogen is cost prohibitive on a plant scale, it was recommended that the headspace be evacuated after the N_2 purge with H_2, prior to start of the reaction, in order to successfully scale up the reaction and control the des-F impurity formation. In case of an emergency

(i.e. thermal runaway reaction), the agitation could be stopped to prevent a thermal runaway, thereby, maintaining a safe environment in the pilot plant reactors. This procedure was also demonstrated in the lab reactor and shown to control the thermal runaway in case of an emergency.

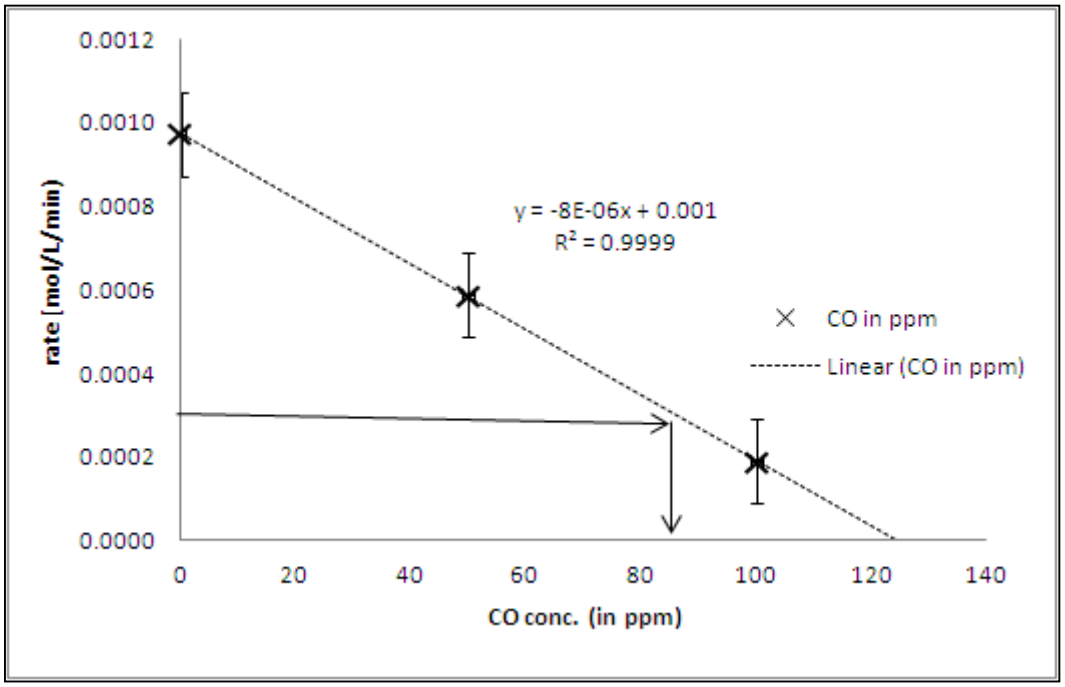

Figure 7.10: Reaction Rate vs. Concentration of CO (ppm)

The Equation 7.1 is re-written as follows from the above experimental data to incorporate the deactivation of catalyst as:

$$[\theta_*] = \frac{1 - \frac{C_{CO}}{125}}{(1 + \mathrm{K_A}[C_{Al}] + \mathrm{K_C}\,[C_{Cl}] + \mathrm{K_D}\,[C_{Dl}])} \qquad [7.2]$$

This equation shows that all the vacant sites are fully occupied by carbon monoxide at 125-ppm concentration present in the headspace of the reactor, to shut-off the reaction completely.

7.3.3 Pilot Plant Reaction Scale-up Under H_2 Atmosphere

The procedure is followed as described in Section 7.3.2, with the exception of nitrogen present in the headspace prior to the start of the reaction. The reactor was pressure purged with hydrogen, to evacuate the nitrogen from the headspace, once all materials were charged and fully dissolved.

Two batches were manufactured using this procedure. The agitation was set to 123 rpm (with a +/- 5 rpm variance). Hydrogen uptake was measured as a function of time for the plant reaction and compared to that for the lab reaction. Figure 7.11 depicts the hydrogen uptake between the lab and plant scale reaction. Results indicated that both of the reactions were identical. In addition, the reaction rate for these reactions was similar when compared to the lab runs between a k_La of 0.15 and 0.25 1/s. The reaction profile at the end of the reaction was similar in des-F content at 0.08-.010% (AUC) for the two batches and met the product specification of < 0.15% (AUC). This indicated that the reaction inhibition was well understood, and the controls were put in place in order to safely scale-up these hydrogenation reactions, producing good quality materials from lab to plant scale.

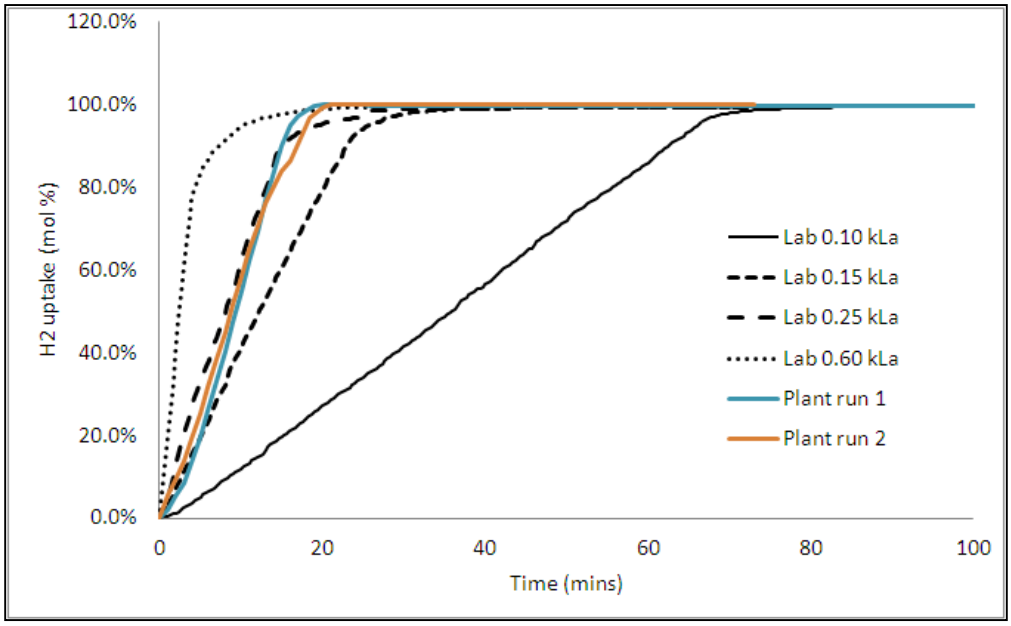

Figure 7.11: Reaction Rate for Lab and Plant Scale Reactions vs. Time
Plant runs 1 & 2 were run at a k_La value of ~0.20 (1/s)

7.4 Conclusions

The reactions were scaled up into the pilot plant reactors by maintaining analogous k_La from the lab scale based on a non-reactive methanol/hydrogen system as described in Chapter 4. Although the reactions were scaled based on comparable k_La, the reaction rate was found to be much slower than that of the lab reaction. Upon investigation, it was found that the issue was caused by the presence of nitrogen headspace in the reactor, according to the plant safety procedures. Even though nitrogen is considered to be an innocuous substance, it somehow resulted in catalyst inhibition issues. Later results, discovered by physi- and chemisorption measurements, along with mass spectrometer and gas chromatography instruments, indicated that the plant nitrogen contained small amounts of carbon monoxide present in the nitrogen supply stream. From a series of controlled experiments, using various amounts of CO present in the nitrogen supply stream (0, 50, 100 and 125 ppm), it was illustrated that CO adsorbs onto the catalyst sites during the course of the reaction, thereby, diminishing the reaction rate. In the absence of CO (by utilizing ultra pure nitrogen in the headspace), the reaction rates were analogous to the one without nitrogen in the headspace. However, due to the excessive cost of using ultra pure nitrogen for the plant reactions, the plant reactor was operated without nitrogen in the headspace. The reactor agitation was shown to act as the safety control in the plant reactor in case of a thermal runaway reaction. Finally, the pilot plant reactions were scaled up safely and successfully under hydrogen atmosphere (no N_2), producing good quality material required for on-going clinical trials.

References

1 F. Stoessel, Experimental study of thermal hazards during hydrogenation of nitroaromatics; J. Loss. Prev. Process Ind., 1993, Vol. 6 (2), p. 79-85.

2 A. Schumpe, Y. T. Shah, and R. S Albal, Mass Transfer in Multiphase Agitated Contractors, The Chemical Engineering Journal, 1983, Vol. 27, p. 61-80.

3 W. R. Tong, R.L. Seagrove, and R. Wiederhorn, 3-4-Dichloroaniline Autoclave Incident, AIChE Loss Prev., 1977, Vol. 11, p. 71-75.

4 A. Z. Francesconi and J. H. dAngelo, Gas-Liquid Solubility of Hydrogen in n-Alcohols; J. Chem. Eng. Data, 2001, Vol. 46, p. 671-674.

5 R. V. Chaudhari, M. S. Kulkarni, M. J. Vaidya, M. J., Synthesis of p-Aminophenol by Catalytic Hydrogenation of p-Nitrophenol, Organic Process Research & Development, 2003, Vol. 7, p. 202-208.

6 Catalyst Screening was performed to find the optimum selectivity and reactivity. Refer to Chapter 3 for details on catalyst selection.

7 Autosorb 1C was purchased from Quantachrome Instruments, Boynton Beach, FL.

CHAPTER 8: CONCLUSIONS AND RECOMMENDATIONS

8.1 Conclusions

Reduction of halo-nitroaromatic to halo-aniline is an industrially important reaction carried out over a heterogeneous catalyst in a batch slurry reactor. One such reduction product, the halo-aniline, is a key intermediate for the manufacture of an Active Pharmaceutical Ingredient (API) in late-stage clinical trials. Such a reaction involves multiple intermediate steps [1]; but, the relationships between intrinsic kinetics, mass transfer rate, and the mechanistic pathway are not well understood. This research supports the probable mechanistic pathway the reaction takes by means of kinetic profiling. In addition, results highlight the relationship between intrinsic kinetics and mass transfer rate, which plays a vital role in understanding the mechanistic pathway. It also elucidates the formation and control of the highly energetic intermediate - the hydroxylamine and the des-F impurity for safely scaling up the desired reaction.

A set of forty-eight catalysts, varying in precious metal types (Pd, Pt, etc.), deposition types (eggshell, uniform, etc.), percent metal loading (5%, 10%, etc.), and various metal combinations (i.e., mono vs. bi-metallic), were chosen to test the performance of these individual catalysts under the reaction conditions to yield the desired selectivity and activity for the reaction. Catalysts were rapidly evaluated using a high-throughput screening technique from a diverse group of 48 catalysts available, down to a single catalyst. The selection criteria were based on the reactivity, selectivity and availability of the catalyst for scale-up in the pilot facilities. The catalyst screening results showed that the catalysts containing palladium metal were superior in terms of reactivity and selectivity of the reaction, when compared to platinum or other bimetallic catalysts, which was in direct contradiction to the published literature for such reactions [2]. One postulated theory could be that the acidic nature of the

reaction solution resulted in this deviation from the norm [3]. The chosen catalyst (E101NE/W) was classified as an eggshell catalyst by Evonik Ind., which was further characterized using Autosorb equipment by chemisorption and physisorption techniques.

It was essential to develop and measure mass transfer rate for the reaction in lab scale reactors, prior to scaling it up in the pilot and manufacturing facilities. An experimental technique was utilized to calculate the overall mass transfer coefficient (k_La) as described by Shah et al. [4]. Also, as most of the nitro reductions are carried out in a water and/or alcohol system, methanol was chosen as the standardized non-reactive solvent to conduct the mass transfer studies, due to its high dielectric values and hydrogen solubility [5]. The experimental method also gave a direct measurement of hydrogen solubility in the solvent system, along with k_La values. The overall equilibrium concentration of hydrogen in methanol was calculated and found to be 1.74×10^{-2} mol/L with a standard deviation of 9.03×10^{-4} mol/L. The measured solubility was found to be in close agreement with literature values [4], thereby, validating the methodology used. The overall volumetric mass transfer coefficient was calculated and found to be a linear function with respect to reactor agitation rate, as seen in Chapter 4. In addition, k_La was found to be a linear function of liquid level in the reactor. This is particularly useful, as one can predict the k_La values for the desired liquid fill volume and rpm. For the given system, it was found that k_La was constant over the pressure range, however, was found to decrease over increase in temperature. This methodology was used to scale-up mass transfer coefficient from lab to plant scale reactors.

In addition, for simple systems, the CST method is in agreement with the measured value of hydrogen solubility in the solvent system, even for the systems which do not have readily available Henry's constant data. Also, the hydrogen solubility in methanol was found to increase with increase in temperature and pressure. With the degree of accuracy for hydrogen solubility, such data can be

generated very quickly without the need to do experiments, and then can be verified in the lab for the system of interest, thus saving process development timelines.

Chapter 5 elucidates the dominant pathway for the desired reaction, to establish a kinetic model. Results proved that the dominant pathway for the generic reaction schematic, as shown in Figure 5.1, was the reduction of nitroaromatic to hydroxylamine and, then, the hydrogenolysis of hydroxylamine to aniline. This mechanistic pathway was then utilized to postulate a kinetic model, considering the various kinetic reactions: gas-liquid mass transfer and liquid-solid mass transfer that need to take place during such heterogeneous catalysis.

In addition, the postulated kinetic rate model, based on several calculations and by kinetic measurement, established that intrinsic kinetics rather than gas-liquid or liquid-solid mass transfer resistances limited the reaction rate. Furthermore, results show that the reaction behaves first order in both the hydrogen concentration (i.e., partial pressure of hydrogen in the reactor headspace) as well as the catalyst concentration. A new methodology to test catalyst robustness (i.e., catalyst poisoning, inhibition, or degradation) was established, using reaction progress analysis, which showed that the given catalyst was robust for the given reaction conditions. Rate constants obtained from reaction data sets were used to validate catalyst robustness, by normalizing the reaction rate w.r.t. catalysts.

Hydroxylamine formation was found to be a mass transfer limited process, whereas, the hydrogenolysis of hydroxylamine was found to be kinetically limited. In order to control the rate and the maximum concentration of hydroxylamine in the reaction, both mass transfer rates and the desired reaction temperature were required. A shift in the rate-limiting step was postulated for the mass transfer limited process, which resulted in hydroxylamine formation as rate limiting, to a kinetically limited process, which resulted in hydrogenolysis as the rate-limiting step. For the current example and choice of the catalysts system, vanadium promoters were found to be ineffective in reducing the overall accumulation of hydroxylamine in the reaction mixture.

Des-F impurity formation was found to be a function of both the mass transfer rate, as well as the reaction temperature. The dehalogenated impurity was formed as a result of competitive reduction between the nitroaromatic and the halo- functional group on the nitroaromatic ring during the mass transfer limited process. The rate of dehalogenation was found to increase with lower catalyst loadings or lower mass transfer rates (i.e., lower adsorption of hydrogen onto the catalyst site available to reduce the nitro group), as well as with the increase in the reaction temperature. Initially, due to the presence of the electron-withdrawing group on the aromatic ring, such as the nitro-, it stabilizes the incipient negative charge developed on the aromatic ring during the hydrogenolysis of carbon sp^2-substituted halogen bond. Once the electron-withdrawing group was reduced to the electron-rich group, such as the hydroxylamine, aniline, etc., then the rate of hydrogenolysis of C-X (halogen) drops. It was found that the dehalogenated impurity only occurred in the presence of nitroaromatic, and it did not increase during the hydrogenolysis of hydroxylamine or in the presence of aniline under the reaction conditions. Both the temperature and mass transfer rates were critical in order to meet the product specification for the des-F impurity. A detail kinetic model was also presented for both the hydroxylamine and the des-F formation, in order to understand and control the respective concentrations with respect to both, the mass transfer coefficient and the intrinsic kinetics.

The reactions were scaled up into the pilot plant reactors by maintaining analogous k_La from the lab scale based on a non-reactive methanol/hydrogen system as described in Chapter 4. Although the reactions were scaled based on comparable k_La, the reaction rate was found to be much slower than that of the lab reaction. Upon investigation, it was found that the issue was caused by the presence of nitrogen headspace in the reactor, according to the plant safety procedures. Even though nitrogen is considered to be an innocuous substance, it somehow resulted in catalyst inhibition issues. Later results, discovered by physi- and chemisorption measurements, along with mass spectrometer and gas chromatography instruments, indicated that the plant nitrogen contained small amounts of

carbon monoxide present in the nitrogen supply stream. From a series of controlled experiments, using various amounts of CO present in the nitrogen supply stream (0, 50, 100, and 125 ppm), it was illustrated that CO adsorbs onto the catalyst sites during the course of the reaction, thereby, diminishing the reaction rate. In the absence of CO (by utilizing ultra pure nitrogen in the headspace), the reaction rates were analogous to the one without nitrogen in the headspace. However, due to the excessive cost of using ultra pure nitrogen for the plant reactions, the plant reactor was operated without nitrogen in the headspace. The reactor agitation was shown to act as the safety control in the plant reactor in case of a thermal runaway reaction. Finally, the pilot plant reactions were scaled up safely and successfully under hydrogen atmosphere (no N_2), producing good quality material required for on-going clinical trials.

8.2 Future Recommendations

Although the corresponding states theory method predicts the hydrogen solubility within five percent of the measured value, some fluids exhibit higher start deviation for hydrogen solubility between the experimental and CST method. Higher deviations are generally caused by stronger hydrogen bonding. Future work can explore equations of state based on the statistical associating fluid theory (SAFT) in order to minimize the standard deviation between the measured and calculated values.

New catalysts can be designed, which will be less prone to poisoning due to the presence of small amounts of carbon monoxide found in the nitrogen stream in the plant environment. Thereby, avoiding the catalyst inhibition that is caused during the course of the reaction, and providing considerable plant savings in terms of cycle time, catalyst cost, batch deviations, as well as avoiding higher costs of ultra purified nitrogen stream than would be required for the current catalyst system.

References

1 J. Wisniak et al., Reduction of Nitrobenzene to Aniline, Ind. Eng. Chem. Prod. Res. Dev., 1984, Vol. 23 (1), p. 44–50.

2 H. Greenfield, Platinum metal sulfides in catalytic hydrogenations, Annals New York Academy of Sciences, 1967, Vol. 145, p. 108-115.

3 J. Kosak, Catalytic Hydrogenation of Aromatic Halonitro Compounds, Annals New York Academy of Sciences, 1970, Vol. 172, p. 175-184.

4 Y.T. Shah, A. Deimling, B.M. Karandikar, and N.L. Carr, Solubility and mass transfer of CO and H_2 in Fischer—Tropsch liquids and slurries, The Chemical Engineering Journal, 1984, Vol. 29 (3), p. 127-140.

5 A. Z. Francesconi and J. H. dAngelo, Gas-Liquid Solubility of Hydrogen in n-Alcohols; J. Chem. Eng. Data, 2001, Vol. 46, p. 671-674.

APPENDIX

9.1 Mass Transfer Coefficient (k_La)

The mass transfer rate (k_La) can be measured experimentally, as described by Shah et al. [1]. The experimental technique involves a batch reactor in which gas absorption in the liquid takes place due to surface aeration. The liquid is added to the batch reactor, and the reactor is pressurized with the gas (hydrogen) and sealed. Upon initiation of agitation in the reactor, the pressure in the reactor headspace decreases with time because of the absorption of gas in the liquid phase. This decrease in pressure with time allows the estimation of mass transfer rate and volumetric mass transfer coefficient (k_La). The total pressure decrease, until equilibrium is reached, gives us the dissolved equilibrium concentration (C*). The following assumptions were used by Shah to derive k_La and (C*) equations:

1. In the pressure range of operation, the ideal gas assumption is valid.
2. Absorption of gas in the liquid phase can be described by Henry's Law.
3. The temperature of gas and liquid are equal and constant.
4. While pressurizing the reactor with gas, there is no absorption of gas before the stirrer is set in motion and aeration takes place.
5. The time required for the achievement of constant gas entrainment and gas holdup during the start of the absorption is negligibly short compared to the absorption time required for saturation.
6. The vapor pressure of the solvent is small compared to total system pressure (usually less than five percent of the total pressure).
7. Mass transfer resistance in the gas phase is negligible.
8. The liquid in the reactor is well mixed and has a uniform concentration (C_L) at any given time.

With these assumptions, the equilibrium concentration (C*) can easily be obtained from the total uptake of gas by the liquid and can be calculated by using the ideal gas law as follows:

$$P_1 - P_2(\text{psi}) = \left(n_{G_1} - n_{G_2}\right)\frac{RT}{V_G} \qquad [9.1]$$

where P denotes the system pressure, n_G denotes the moles of hydrogen, V_G is the molar gas volume of hydrogen, R is the universal gas constant and T is the temperature. The initial and final conditions are denoted by subscripts "1" and "2", respectively.

The drop in number of moles of hydrogen in the gas phase into the liquid phase is given by:

$$\left(n_{G_1} - n_{G_2}\right)[moles] = C^*\, V_L \qquad [9.2]$$

where V_L denotes the liquid volume and C* is the equilibrium hydrogen concentration.

Re-arranging Equations 9.1 & 9.2 above gives us a way to measure equilibrium solubility of hydrogen:

$$C^*\left(\frac{mol}{L}\right) = (P_1 - P_2)\frac{V_G}{V_L}\frac{1}{RT} \qquad [9.3]$$

The differential mass balance for hydrogen in the liquid phase during the adsorption process takes the form

$$\frac{dC_L}{dt}\left(\frac{mol}{L * min}\right) = k_L a(C^* - C_L) \qquad [9.4]$$

With $C_L = n_L/V_L$ moles in liquid volume, and using Henry's Law (C*) = P/H, we get

$$\frac{dn_L}{dt}\left(\frac{mol}{min}\right) = V_L\, k_L a\, \left(\frac{P}{H} - \frac{n_L}{V_L}\right) \qquad [9.5]$$

A differential form of Equation 9.1 gas law can be used to relate pressure changes to liquid concentration changes as:

$$\frac{dP}{dt}\left(\frac{atm}{min}\right) = \left(\frac{RT}{V_G}\frac{dn_G}{dt}\right) = -\left(\frac{RT}{V_G}\frac{dn_L}{dt}\right) \quad [9.6]$$

Equation 9.6 can be integrated to derive an expression for the time dependence of the total pressure P as follows:

$$(n_L - n_{L0})[moles] = \frac{V_G}{RT}(P_1 - P) \quad [9.7]$$

where *P* and P_1 are the pressures at time 't=t' and at t=0, respectively. The subscripts "L_0" and "*L*" denotes the moles of hydrogen at time 't=t' and at t=0, respectively.

Inserting Equations 9.6 and 9.7 into Eq. 9.5, we obtain

$$\frac{dP}{dt}\left(\frac{\text{atm}}{\text{min}}\right) = -k_L a\ V_L \frac{RT}{V_G}\left[\frac{P}{H} - \frac{1}{V_L}\frac{V_G}{RT}(P_1 - P) - \frac{n_{L0}}{V_L}\right] \quad [9.8]$$

Defining α = $V_L \frac{RT}{H\,V_G}$ and $n_{L0} = V_L \frac{P_0}{H}$ in the above equation we get

$$\frac{dP}{dt}\left(\frac{atm}{min}\right) = -k_L a\ \ [P(\alpha + 1) - P_1 - \alpha P_0] \quad [9.9]$$

We now define $X = \{P(\alpha + 1) - P_1 - \alpha P_0\}$ and $\{dP(\alpha + 1) = \text{dX}\}$ into Eq. 9.9 we get the following equation:

$$\frac{dX}{[X]} = -k_L a(\alpha + 1)dt \quad [9.10]$$

Integrating Eq. 9.10 results in the linearized equation below:

$$[lnX] = [-k_L a(\alpha + 1)t] \quad [9.11]$$

Applying the limit @ t=0, P=P_1 we get

$$k_L a(\alpha+1)t = \ln[\frac{P_1(\alpha+1) - P_1 - \alpha P_0}{P(\alpha+1) - P_1 - \alpha P_0}] = \ln[\frac{P_1(\alpha+1) - P_1 - \alpha P_0}{P(\alpha+1) - P_1 + P_0 - P_0 - \alpha P_0}] \quad [9.12]$$

$$k_L a(\alpha+1)t = \ln[\frac{\alpha(P_1 - P_0)}{(P - P_0)(\alpha+1) - (P_1 - P_0)}] \quad [9.13]$$

From Henry's law $\{n_L = P_2 V_L / H\}$ and using Eq. 9.7 along with the definition of n_{L0}, we get

$$\left(\frac{P_2 V_L}{H} - \frac{V_L P_0}{H}\right) = \frac{V_G}{RT}(P_1 - P_2) \quad [9.14]$$

And using the definition of $\alpha = V_L \frac{RT}{H V_G}$ yields

$$\alpha(P_2 - P_0) = (P_1 - P_2) \quad [9.15]$$

Rearrange Eq. 9.15 to get α as follows:

$$\alpha = \frac{(P_1 - P_2)}{(P_2 - P_0)} \quad [9.16]$$

Substituting this value of α into Eq. 9.13 results in the linearized equation below:

$$k_L a\left(\frac{(P_1 - P_2)}{(P_2 - P_0)} + 1\right)t = \ln[\frac{\frac{(P_1 - P_2)}{(P_2 - P_0)}(P_1 - P_0)}{(P - P_0)\left(\frac{(P_1 - P_2)}{(P_2 - P_0)} + 1\right) - (P_1 - P_0)}]$$

$$k_L a\left(\frac{(P_1 - P_2) + P_2 - P_0}{(P_2 - P_0)}\right)t = \ln[\frac{\frac{(P_1 - P_2)}{(P_2 - P_0)}(P_1 - P_0)}{(P - P_0)\left(\frac{(P_1 - P_2) + P_2 - P_0}{(P_2 - P_0)}\right) - (P_1 - P_0)}]$$

$$k_L a\left(\frac{P_1 - P_0}{P_2 - P_0}\right) t = \ln[\frac{\frac{(P_1 - P_0)}{(P_2 - P_0)}(P_1 - \mathrm{P}_2)}{(P - P_0)\left(\frac{P_1 - P_0}{P_2 - P_0}\right) - (P_1 - \mathrm{P}_0)}]$$

$$k_L a\left(\frac{P_1 - P_0}{P_2 - P_0}\right) t = \ln[\frac{\frac{(P_1 - P_0)}{(P_2 - P_0)}(P_1 - P_2)}{(P_1 - P_0)[\left(\frac{P - P_0}{P_2 - P_0}\right) - 1]}]$$

$$k_L a\left(\frac{P_1 - P_0}{P_2 - P_0}\right) t = \ln[\frac{\frac{(P_1 - P_0)}{(P_2 - P_0)}(P_1 - P_2)}{(P_1 - P_0)[\left(\frac{P - P_0 - P_2 + P_0}{P_2 - P_0}\right)]}]$$

The equation finally simplifies to the equation shown below:

$$[k_L a]\,\mathrm{t} = \frac{(P_2 - P_0)}{(P_1 - P_0)} \ln\left[\frac{P_1 - P_2}{P - P_2}\right] \qquad [9.17]$$

where P_1 & P_2 are the initial and final pressures, respectively; P is the pressure of system at time t; and P_0 is the pre-saturation pressure (or vapor pressure of solvent at the system temperature). This vapor pressure is usually very small, and can be neglected. The volumetric mass transfer rate ($k_L a$) is calculated from Eq. 9.17 by measuring the pressure drop of the system as a function of time.

9.2 Hydrogen Gas Solubility based on Corresponding States Theory (CST)

Hydrogen solubility in simple and mixed solvent systems can be calculated as described by Shaw [2] and Sebastian et al. [3]. Hydrogen gas solubility cannot be expressed by simple relationship, such as Henry's Law, at temperatures and pressures above 298ºK and 0.10 MPa, or when one of the components is supercritical, as described by Brandani and Prausnitz [4]. A hydrogen solubility correlation, employing corresponding states theory (CST), was developed by Shaw, by equating the fugacity of the dissolved hydrogen equal to fugacity of gas in equilibrium, calculated from an equation of state as in Eq. 9.18.

$$\left[\frac{f'}{x}\right] = \left[\frac{f}{x}\right] \; exp\,[\frac{PV}{RT}] \qquad [9.18]$$

where f and f' are the fugacities in the reference state and vapor phase, respectively; x is the mole fraction of the solute; P is the hydrogen partial pressure; V is the molar volume; R is the universal gas constant; and T is temperature.

An expression for the gas solubility, using CST, was obtained using the following assumptions:

1. Hydrogen solubility is primarily a function of the T_r (reduced temperature) of solvent.
2. The mole fraction of hydrogen in solvent is low, and the impact of hydrogen on T_c of liquid can be neglected. The pseudo critical temperature of n-component mixtures can be established by mixing rule proposed by Reid et al. [5] as given the form:

$$[Tc] = [\textstyle\sum_i^n x_i \, T_{ci}^2/P_{ci}] \; /[\sum_i^n x_i \, T_{ci}/P_{ci}] \qquad [9.19]$$

where T_c is the critical temperature; P_c is the critical pressure; and x is the mole fraction of solute.

3. The solute molecule occupies the free volume that is within the ensemble of larger solvent molecules. The fluid free volume per mole of solvent is proportional to the molar volume and inversely proportional to the fluid density. On a unit mass basis, free volume is inversely proportional to the square of the density.
4. The concentration of dissolved hydrogen (C*) is given as:

$$[\mathrm{C}*] = \mathrm{S}\,(\mathrm{P})\left(\frac{mol\ of\ H_2}{kg_{solvent}}\right) \qquad [9.20]$$

where S is the solubility coefficient and P is the hydrogen partial pressure.

The fugacity in the gas and liquid phases are equal for hydrogen; hence, we get:

$$\left[\frac{f'}{P}\right] - \left[\frac{f}{P}\right] = [C^*]\,\gamma\,\left[\frac{f}{P}\right] \qquad [9.21]$$

where γ is the activity coefficient

Shaw approximated the fugacity coefficient in the gas phase [f'/P] and in reference state [f/P], using the Redlich-Kwong equation of state as:

$$\frac{P'V}{R\,T} = \frac{V}{V-b}\,\frac{\Omega_a}{\Omega_b}\,\frac{b\,F}{(V+b)} \qquad [9.22]$$

where P' = total pressure; Ω_a = 0.42478; Ω_b = 0.08664; b = (Ω_b R T_c / P_c); and F = fugacity function, which approaches zero asymptotically at higher temperatures.

Furthermore, the fugacity coefficients were calculated by Shaw as:

$$\ln\left[\frac{f'}{P}\right] \cong \frac{b_i}{b_m}(Z_m - 1) - \ln Z_m + \ln\left[\frac{V_m}{V_m - b_m}\right] + \frac{\Omega_a}{\Omega_b} F_m \left[\frac{b_i}{b_m}\right] - 2\sum\left(1 - K_{ij}\right)Y_j \frac{(b_i b_j F_i F_j)^{0.5}}{b_m F_m} \ln\left[\frac{V_m + b_m}{V_m}\right] \quad [9.23]$$

$$\ln\left[\frac{f}{P}\right] \cong -\ln\left[\frac{V-b}{V}\right] + \frac{\Omega_a}{\Omega_b} F \ln\left[\frac{V+b}{V}\right] + \frac{V}{V-b} - \frac{\Omega_a}{\Omega_b}\frac{bF}{(V+b)} - \ln\left[\frac{V}{V-b}\right] - \frac{\Omega_a}{\Omega_b}\frac{bF}{(V+b)}\Big] \quad [9.24]$$

where Z = compressibility factor; K_{ij} = iteration parameter; and Y = mole fraction of hydrogen in gas phase.

Ignoring the less significant terms and linearizing Eqs. 9.23 and 9.24, and inserting EOS Eq. 9.22 into Eq. 9.21 yields:

$$\left[\frac{f'}{P}\right] - \left[\frac{f}{P}\right] \cong \left[\frac{b_m}{Z_m RTY} - \frac{b}{ZRT} - \frac{\Omega_a}{\Omega_b}\left(\frac{F_m}{Z_m RTY} - \frac{F}{ZRT}\right)\right] P = S(P)\gamma \left[\frac{f}{P}\right] \quad [9.25]$$

As the concentration of the vapor phase is nearly constant with pressure, the product of S γ $[\frac{f}{P}]$ is constant over a wide range of pressures. Shaw experimentally fitted the infinite solubility coefficient (S_0) to the relation as follows:

$$S_0 = S\left[\frac{f}{P}\right]\left(\frac{mol\ of\ H_2}{kg_{solvent} * atm}\right) \quad [9.26]$$

where S and S_0 are is the solubility coefficient and is the solubility coefficient at zero pressure.

Shaw also suggested that the activity coefficient in the liquid phase would remain independent of the hydrogen concentration, thereby, redefining the solubility (S*) per free unit volume as

$$(S^*) = S\left[\frac{f}{P}\right]\rho_{ref}^2\left(\frac{mol\ of\ H_2}{kg_{solvent}\ *\ atm\ *\ L^{\ 2}_{solvent}}\right) \quad [9.27]$$

where S* = normalized solubility of hydrogen, and ρ = specific gravity of reference solvent.

Shaw further calculated the fugacity coefficient in reference state at elevated temperatures ($T_r \geq 8$) and at moderate pressures (where $b \ll V$) as:

$$\left[\frac{f}{P}\right] \cong exp\left[\frac{(\Omega_b - \ \Omega_a\ F)}{\frac{T_r}{2\ P_r} + \frac{T_r}{2\ P_r}\left[1 - \frac{P_r}{T_r}\ \Omega_a\ F\right]^{0.5}}\right] \quad [9.28]$$

Theoretically, the 'F' function approaches zero asymptotically at elevated temperatures in the above equation, and the T_{soave} shares this property, where F_{soave} was suggested by Shaw as:

$$F_{Soave} = \ T_r^{-1}\left[1 + (0.48 + 1.574\omega - 0.176\ \omega^2)\ (1 - T_r^{0.5})\right]^2 \quad [9.29]$$

where ω = Pitzer acentric factor (= - 0.22 for hydrogen); and T_r and P_r are the reduced temperature and pressure, respectively.

Shaw found that the plot of ln (S*) vs. T_r (solvent) was linear, except near the critical region. Hence, a scaling function (T* solvent) was introduced by Shaw to maintain the linear correlation of Ln (S*) vs. T_r (solvent) in the critical region as

$$T^*_{solvent} = \frac{T_{r\ solvent}}{(1 - \ T_{r\ solvent)}^{\ 0.132}} \quad [9.30]$$

Furthermore, Shaw fitted the experimental value with the new T* solvent w.r.t. Ln (S*) and derived a simplified version for solubility as:

$$\ln(S^*) = \frac{A_1}{\rho_{ref}^{0.5}} T^* + \frac{A_2}{\rho_{ref}^{0.5}} + A_3 + A_4 \Delta\rho_s \qquad [9.31]$$

where the constants were regressed as A_1 = 2.17587; A_2 = -1.81836; A_3 = -5.23139; A_4 = 1.500; and ρ_s is the density difference between the two phases set to zero for simple solvents.

The resulting solubility of hydrogen [C*] in the given solvent system, is the simplified version from the above equations to

$$[C^*] = \frac{P}{\rho_{ref}^2} S^* \left[\frac{f}{P}\right]^{-1} \left(\frac{mol}{kg_{solvent}}\right) \qquad [9.32]$$

where normalized hydrogen solubility (S*) is given by Eq. 9.31 and [f/P] is given by Eq. 9.28.

9.3 Liquid-Solid (L-S) Mass Transfer Effect

To confirm that the liquid-solid (L-S) mass transfer coefficient ($k_L s$) for both [A] and [H_2] were not rate limiting, these $k_L s$ were estimated using the correlation given by Roberts [6-7] and Satterfield [8]. The expression for $k_L s$ is given by:

$$\left[\frac{k_L s \ d_p}{D}\right]^2 = 16 + 4.84 \left[\frac{g \ {d_p}^3 \ (\rho_a - \rho_l)}{18 \ \mu \ D}\right]^{\frac{2}{3}} \qquad [9.33]$$

where d_p is the diameter of the catalyst particle (d_{50} of 28 μm – obtained from the manufacturer); D is the effective diffusivity of [A] or [H_2] in cm^2/sec; g is the gravitation force (9.81 m/s^2); ρ_l is the liquid density (=0.85 g/cc); and μ is the liquid viscocity (1.08 X 10^{-4} poise).

The apparent density for the catalyst (ρ_a) was calculated, as given by Roberts [9] as:

$$\rho_a = \frac{\varepsilon}{V_p} + \varepsilon \ \rho_l \quad = 1.155 \frac{g}{cc} \qquad [9.34]$$

where ε (=0.55) is the catalyst porosity given by the manufacturer; Vp (=0.80 cm^3/g) is the pore volume measured by the physisorption analysis (Table 3.3); and ρ_l(=0.85 g/cm^3) is the liquid density of the reaction solvent system.

Effective diffusivity (D) was calculated, using the expression given by Wilke and Chang [10]:

$$D_A \ or \ D_{H2} \left(\frac{cm^2}{s}\right) = 7.4 \ x \ 10^{-10} \frac{T \ (\zeta \ M_2)^{0.5}}{\mu \ (V_b)^{0.6}} \qquad [9.35]$$

where D_A or D_{H2} are the diffusion coefficients for [A] and [H_2], respectively; T is temperature in Kelvin; ζ is the association parameter (=2.05 from [10]); M_2 is the molecular weight of the solvent; μ is the viscosity in poise (=1.08 X 10^{-4} poise); and V_b is the molar volume of diffusing solute in cm^3/g-mol.

The molar volumes (V_b) for [A] and [H_2] are calculated from the values given by Satterfield [10] and found to be 473.4 cm^3/g-mol and 3.7 cm^3/g-mol, respectively.

Substituting these values into Eq. 9.35, the effective diffusivities are calculated as:

$$D_A = 4.13\ x\ 10^{-4}\ \left(\frac{cm^2}{s}\right) \qquad [9.36]$$

$$D_{H2} = \ 75.8\ x\ 10^{-4}\ \left(\frac{cm^2}{s}\right) \qquad [9.37]$$

Substituting the values from Equations 9.34– 9.37, into Eq. 9.33, the L-S mass transfer coefficients for [A] and [H_2]are obtained as:

$$[k_L s]_{\ A} = 88.1\ \left(\frac{m}{s}\right) \qquad [9.38]$$

$$[k_L s]_{H2} = 1175.1\ \left(\frac{m}{s}\right) \qquad [9.39]$$

Mills and Chaudhari [15] proposed that the liquid-solid (L-S) mass transfer can be neglected, if the ratio of the observed reaction rate (r_H) to the maximum L-S mass transfer rate (γ_2) is < 0.1. The ratio (γ_2) is expressed as:

<u>L-S mass transfer insignificant if:</u>

$$\gamma_2 = \frac{r_H}{[k_L s]_{A\ or\ H2}\ *\ a_p\ *\ H_2\ [sat]} < 0.1 \qquad [9.40]$$

where a_p is the ratio of the external surface of the catalyst to the slurry volume (cm^2/cm^3) and was calculated, as given by Bartholomew [8]:

$$a_p = \frac{6 * \text{g of catalyst}}{\rho_a * d_p * \text{V (slurry volume)}} \frac{\text{cm}^2}{\text{cm}^3} \qquad [9.41]$$

$$a_p = 18.55 \frac{cm^2}{cm^3}$$

References

1 Y.T. Shah, A. Deimling, B.M. Karandikar, and N.L. Carr, Solubility and mass transfer of CO and H_2 in Fischer—Tropsch liquids and slurries, The Chemical Engineering Journal, 1984, Vol. 29 (3), p. 127-140.

2 J. M. Shaw, A Correlation for Hydrogen Solubility in Alicyclic and Aromatic Solvents; The Canadian Journal of Chemical Engineering, 1987, Vol 65, p. 293-298.

3 H. M. Sebastian, H. M. Lin and K. C. Chao, Correlation of Solubility of Hydrogen in Hydrocarbon Solvents, AIChE J., 1981, Vol. 27, p. 138-148.

4 V. Brandani and J. M. Prausnitz, Thermodynamics of Gas Solubility in Liquid Solvents and Solvent Mixtures, Fluid Phase Equilibria, 1981, Vol. 7, p. 259-274.

5 R. C. Reid, The properties of gases and liquids, McGraw-Hill Publications, 1977, 3rd Edition.

6 G. W. Roberts, The Influence of Mass and Heat Transfer on the Performance of Heterogeneous Catalysis in Gas/Liquid/Solid Systems, Catalysis in Organic Synthesis, Academic Press: New York, 1976.

7 G. W. Roberts, D. Xu, R. G. Carbonell, and D. J. Kiserow, Kinetics, Catalysis and Reaction Engineering, Ind. Eng. Chem. Res., 2003, Vol. 42, p. 3509-3515.

8 C. N. Satterfield, Mass Transfer in Heterogeneous Catalysis, Robert E. Krieger Publishing Company, Malabar, FL., 1981.

9 G. W. Roberts, Chemical Reactions and Chemical Reactors, John Wiley & Sons, Inc., 2009.

10 C. R. Wilke and P. Change, Correlation of Diffusion Coefficients in Dilute Solutions, A.I.C.H.E. J., 1955, Vol. 1 (2), p. 264-270.